UNIVERSITY OF CALIFORNIA SAN DIEGO

Interpreting New Galaxy Large-Scale Structure Measurements and the Galaxy–Halo Connection

A dissertation submitted in partial satisfaction of the
requirements for the degree
Doctor of Philosophy

in

Physics

by

Angela Berti

Committee in charge:

Professor Alison Coil, Chair
Professor Dusan Keres
Professor Barney Rickett
Professor Karin Sandstrom
Professor Mark Thiemens

2020

The dissertation of Angela Berti is approved, and it is acceptable in quality and form for publication on microfilm and electronically:

_____

_____

_____

_____

_____

Chair

University of California San Diego

2020

EPIGRAPH

As the astronomers unanimously teach, the circuit of the whole earth,

which to us seems endless, compared with the greatness of the universe

has the likeness of a mere tiny point.

—Ammianus Marcellinus,
Roman historian ca. 330–395
in *The Chronicle of Events*

TABLE OF CONTENTS

LIST OF FIGURES

LIST OF TABLES

ACKNOWLEDGEMENTS

This dissertation would not have been possible without the mentorship of my advisor, Dr. Alison Coil, Dr. Phil Choi of Pomona College, and the steadfast support of my parents and my partner Andrew.

Thanks are also due to Dr. Susan Lea, Dr. Andi Mahdavi, Dr. Ron Marzke, and Dr. Adrienne Cool of San Francisco State University, and to the entire staff of the Morrison Planetarium at the California Academy of Sciences in San Francisco, where I was working nine years ago when I decided I did want to give that whole graduate school thing a go after all.

Chapter 2, in full, is a reprint of material previously published in The Astrophysical Journal, 2017, Vol. 834, as "PRIMUS: One- and Two-Halo Galactic Conformity at $0.2 < z < 1$" by A. M. Berti, A. L. Coil, P. S. Behroozi, D. J. Eisenstein, A. D. Bray, R. J. Cool, and J. Moustakas. The dissertation author was the primary investigator and author of this paper.

Chapter 3, in full, is a reprint of material previously published in The Astrophysical Journal, 2019, Vol. 884, as "PRIMUS: Clustering of Star-forming and Quiescent Central Galaxies at $0.2 < z < 0.9$" by A. M. Berti, A. L. Coil, A. P. Hearin, and J. Moustakas. The dissertation author was the primary investigator and author of this paper.

Chapter 4, in part, is currently being prepared for submission for publication in The Astrophysical Journal as "Main Sequence Scatter is Real: The Joint Dependence of Galaxy Clustering on Star Formation and Stellar Mass" by A. M. Berti, A. L. Coil, A. P. Hearin, and P. S. Behroozi. The dissertation author was the primary investigator and author of this material.

VITA

2008	B.S. Physics, Harvey Mudd College, Claremont, California
2014	M.S. Astrophysics, San Francisco State University, California
2020	Ph.D. Physics, University of California San Diego

PUBLICATIONS

Berti, A. M., Coil, A. L., Hearin, A. P., Moustakas, J. "PRIMUS: Clustering of Star-forming and Quiescent Central Galaxies at $0.2 < z < 0.9$." The Astrophysical Journal, 884:76, 2019.

Berti, A. M., Coil, A. L., Behroozi, P. S., Eisenstein, D. J., Bray, A. D., Cool, R. J., Moustakas, J. "PRIMUS: One- and Two-Halo Galactic Conformity at $0.2 < z < 1$." The Astrophysical Journal, 834:87, 2017.

Arnold, T. J., Martini, P., Mulchaey, J. S., Berti, A. M., Jeltema, T. E. "Active Galactic Nuclei in Groups and Clusters of Galaxies: Detection and Host Morphology." The Astrophysical Journal, 707:1691-1706, 2009.

ABSTRACT OF THE DISSERTATION

Interpreting New Galaxy Large-Scale Structure Measurements and the Galaxy–Halo Connection

by

Angela Berti

Doctor of Philosophy in Physics

University of California San Diego, 2020

Professor Alison Coil, Chair

The galaxy distribution in the joint space of stellar mass and star formation rate (SFR) is observed to be bimodal, with distinct star-forming (high SFR) and quiescent (low SFR) populations across many orders of magnitude in stellar mass. The absence of a significant population of intermediate-stage galaxies implies that galaxies tend to cease star formation and become quiescent relatively rapidly, and the physical origins of this rapid quenching are an open question in the field of galaxy evolution.

Recent progress in cosmological simulations of dark matter structure evolution, as well as in statistical modeling of how galaxies inhabit dark matter halos, suggest a nuanced coevolutionary

relationship between galaxies and the dark matter halos galaxies reside in (the "galaxy–halo connection"), in which the statistical galaxy content of a halo depends on more than halo mass. One class of these galaxy–halo connection models are those that incorporate *galaxy assembly bias*, a general term for the dependence of galaxy properties on halo properties other than mass. For example, distinct stellar-to-halo mass relations for star-forming and quiescent *central* galaxies is a form of galaxy assembly bias that could manifest as an anticorrelation of galaxy SFR with clustering amplitude, if the trend is independent of stellar (or halo) mass.

In this dissertation we present the first measurements of galactic conformity, or the tendency of neighboring galaxies to share the star formation properties of an adjacent central galaxy, on two-halo scales beyond the local universe (to $z \sim 1$). We then measure the clustering of isolated galaxies as a proxy for central galaxies, separately for star-forming and quiescent galaxies, to test predictions of galaxy–halo models reflecting galaxy assembly bias. Finally, we measure the joint dependence of clustering on stellar mass and SFR. With mock galaxy catalogs derived from simulations and an empirical galaxy evolution model we quantify and compensate for the effects of systematic biases on these measurements. A parallel theme of this dissertation is demonstrating how existing galaxy surveys beyond the local universe are at the cusp of probing the volumes needed for statistically significant tests of theoretical predictions of various models of galaxy evolution.

1 Introduction

Extragalactic astrophysics is a relatively new field. For most of humanity's history our knowledge of the cosmos was limited to what could be seen with the naked eye: the brightest and closest stars in our galaxy, some of the planets in our solar system, and the occasional comet or meteor. The first telescopes expanded our observations to the most distant planets in the solar system, and to the fuzzy, extended objects scattered among the stars in the night sky that were dubbed "nebulae" for their cloud-like appearance. Only within the past century have we come to understand that the Milky Way galaxy—itself home to hundreds of billions of stars, as well as interstellar gas and dust—is only one of (at least) hundreds of billions of other galaxies in the universe.

The discovery that many of the so-called nebulae are actually other galaxies entirely outside our own by Hubble (1926) (and independently by Lemaître, 1931) in the early twentieth century revolutionized modern astronomy by vastly expanding the size and complexity of the known universe. Not only did Hubble show that the Milky Way galaxy is not unique and the universe is far larger than all prior evidence indicated, his work also led to the discovery that the universe is expanding. This conclusion follows from Hubble's demonstration that the farther away a galaxy is, the faster it appears to be moving away from us. Now known as Hubble's Law, the linear relation between the distances to and radial velocities of other galaxies also implies the universe had a beginning in time. What's more, an expanding universe with a temporal origin is one that evolves with time.

1.1 The Discovery of Large-scale Structure in the Universe

The early work of Hubble and Lemaître launched an ongoing effort to map the spatial distribution of galaxies, beginning with studies of the two-dimensional angular clustering of galaxies on the plane of the sky. Angular clustering describes the probability that a randomly chosen pair of galaxies in a sample is separated by an angle θ. For galaxies scattered randomly on the sky this would be a Poisson distribution. Deviation from a Poisson distribution at given value of θ indicates the galaxy sample is clustered at that angular scale, with the clustering strength proportional to the magnitude of the deviation. Shapley & Ames (1932) note the "general unevenness" in the projected distribution of their catalog of over $1,200$ bright galaxies. Using the same data Hubble (1934) found deviations from a random distribution on angular scales of $\theta \lesssim 10^{\circ}$.

Seldner et al. (1977) used the Lick catalog (Shane & Wirtanen, 1967) of approximately one million galaxies to show the angular clustering of galaxies has a sponge-like structure with open regions (called "voids") surrounded by extended chains of galaxies (called "filaments"). A series of papers published throughout the 1970s led by Peebles (e.g. Peebles, 1973; Hauser & Peebles, 1973; Groth & Peebles, 1977; Seldner & Peebles, 1977; Fry & Peebles, 1978) developed the statistical methodology for quantifying the large-scale structure of galaxies (the three-dimensional analog of this method is described in §1.3 below), and found that the magnitude of angular clustering deviations follows a power law (i.e. is proportional to θ^n, where the value of n is determined from the data) on scales of $\theta \lesssim 5^{\circ}$.

At the same time efforts were underway to extend maps of galaxy distributions into three dimensions (e.g. Gregory & Thompson, 1978; Jôeveer et al., 1978; Davis et al., 1982). While humans have been mapping the sky in two dimensions as seen from Earth for millennia, measuring the *distances* to astrophysical objects is notoriously difficult. Geometric measurements of the distances of nearby stars in our own galaxy are possible by exploiting parallax as Earth

orbits the Sun, but distances to farther objects can only be inferred. For galaxies, their apparent motion away from us is largely due to the expansion of the universe. They are not moving away from us *through* the universe, but rather are carried apart as the fabric of space between them stretches.

From our vantage point in the Milky Way we are left to learn what we can about other galaxies by observing from Earth the visible light and other wavelengths of electromagnetic radiation they emit. Because the speed of light is finite, in the time it takes light emitted by distant galaxies to reach us the universe has expanded such that those galaxies are now farther away than they were when they emitted the light we receive from them. As light travels through an expanding universe its wavelengths are stretched, or *redshifted*. For example, shorter wavelengths of blue light emitted by stars in another galaxy may have been stretched toward the longer wavelengths of red light by the time they reach our detectors. As various physical processes are known to generate electromagnetic radiation with characteristic spectra (intensity of light as a function of wavelength), spectroscopy enables us to quantify the magnitude of this shift toward longer wavelengths, i.e. to measure the redshift of light emitted by a galaxy.

Both the distance to a galaxy and the age of the universe when the galaxy emitted the light we observe today are functions of the galaxy's redshift, denoted by z, for a chosen set of cosmological parameter values. A redshift of $z = 0$ corresponds to the present time, $z = 1$ to when the age of the universe was roughly 6 Gyr, or a little less than half its current age, and z approaches infinity as the age of the universe approaches zero.

Redshifts can be estimated from multi-wavelength photometric observations, but spectroscopic redshifts are more precise than photometric estimates. The tradeoff is that individual spectra for large numbers of galaxies are more time-consuming and expensive to obtain than multi-wavelength photometry, in which many galaxies are observed simultaneously. It wasn't until the end of the twentieth century that technological advances enabled the collection of high-resolution galaxy spectra in sufficient numbers for robust statistical analysis of the galaxy distribution in

three dimensions. The Two Degree Field Galaxy Redshift Survey (2dFGRS; Colless et al., 2001) contains over $220,000$ spectroscopic redshifts, while the Sloan Digital Sky Survey (SDSS; York et al., 2000) expanded that number more than fourfold to nearly one million spectroscopic galaxy redshifts to $z \sim 0.2$ over one-third of the entire sky.

A galaxy with a redshift of $z \simeq 0.2$ is one that we observe as it was roughly 2.5 Gyr ago. This is however only $\sim 20\%$ of the 13.8 Gyr evolutionary history of the universe. Extending our knowledge of the large-scale structure of galaxies—as well as how that structure has evolved—farther back in time requires deep surveys that obtain representative samples of galaxies at higher redshifts than the SDSS. This dissertation uses data from two such surveys: the DEEP2 Galaxy Redshift Survey (Newman et al., 2013) and the PRIsm MUlti-object Survey (PRIMUS; Coil et al., 2011; Cool et al., 2013). DEEP2 contains over $38,000$ spectroscopic galaxy redshifts to $z \sim 1.2$ and covers 2.8 deg^2 ($\sim 0.007\%$ of the sky). PRIMUS doubles the survey area of DEEP2 and contains $\sim 60,000$ galaxy redshifts at $0.2 < z < 1$. Both surveys are by design sufficiently deep to observe galaxies with typical luminosities, as opposed to targeting only the brightest galaxies which, while easier to observe, do not represent the bulk of the full galaxy population.

That deep surveys like DEEP2 and PRIMUS sample such small areas compared to the broad coverage of shallow surveys like SDSS is a consequence of how apparent luminosity decreases with increasing distance. Regardless of their intrinsic brightness, galaxies in the distant universe appear fainter to us and are therefore more difficult to observe than their closer counterparts. While it is of course possible to measure the redshifts of the brightest distant galaxies throughout the entire sky, such a sample provides little insight into properties of the full galaxy population at a given redshift. It would be akin to drawing conclusions about the entire human species by studying only the very oldest or tallest people from all over world.

The expansion of the universe complicates how we describe distances to and between galaxies because the distance to a galaxy that we infer by measuring its redshift is not the same as its distance *when it emitted the light we use to measure that redshift*. While on the

largest scales the universe is expanding, on (comparatively) smaller scales gravity overcomes this expansion, binding galaxies together in groups and clusters. These localized collections of galaxies are described as having decoupled from the *Hubble Flow*, the bulk motion of galaxies due to the expansion of the universe. The *comoving* distance is defined so as to "factor out" the large-scale expansion of the universe, allowing us to describe the relative positions of galaxies independent of the Hubble Flow. Comoving distances are usually expressed in units of $h^{-1}\,\mathrm{Mpc}$ ($1\ \mathrm{Mpc} \simeq 3 \times 10^{19}$ km), where h is defined in terms of the Hubble constant, H_0. The Hubble constant is the proportionality factor of Hubble's Law at the present time (i.e. $z = 0$), and relates a galaxy's distance, d, to its recessional velocity, v: $v = H_0\, d$.[1] The experimentally determined value of H_0 continues to be refined, but current estimates place it at $\sim 70\ \mathrm{km\ s^{-1}\,Mpc^{-1}}$ (Planck Collaboration et al., 2016). In terms of H_0, $h = H_0/(100\ \mathrm{km\ s^{-1}\,Mpc^{-1}}) \simeq 0.7$.

1.2 The Missing Mass Problem and Dark Matter

The term "dark matter" reflects our incomplete understanding of the phenomenon it attempts to describe: additional sources of gravity—the existence of which is inferred from directly observable behavior of baryonic (i.e. "normal" or "luminous") matter—are due to yet unknown species of particles that do not emit light or otherwise engage in electromagnetic interactions. As of this writing particle dark matter continues to elude all attempts at direct detection, although indirect evidence of its existence dates back nearly as far as Hubble's and Lemaître's discovery of other galaxies beyond the Milky Way.

Zwicky (1933) found an apparent order-of-magnitude discrepancy between the observed and estimated velocity dispersion of galaxies in the Coma Cluster. Making a set of reasonable assumptions about the cluster's size and the total mass of its galaxies, Zwicky used the virial

[1] H_0 is a special case of the *Hubble parameter*, $H(z)$, which is a function of redshift: $H_0 \equiv H(z = 0)$.

theorem[2] to predict an average velocity dispersion for Coma Cluster galaxies of roughly 100 km s^{-1}, while the measured value was larger by a factor of 10. This led Zwicky to the conclusion that were his results confirmed, "we would get the surprising result that dark matter is present in much greater amount than luminous matter."

Further evidence of luminous matter behaving as if under the gravitational influence of additional unseen matter came in the 1970s in a series of papers by Vera Rubin and several colleagues (e.g. Rubin et al., 1976, 1978). Rubin measured the rotation rates of the disks of spiral galaxies as a function of distance from the center of the disk, and found that stars toward the outer part of the disk orbit much too fast for their motion to be due entirely to the observed mass of the galaxy. Spiral galaxies must have substantial additional mass providing the extra gravity needed to keep the outer regions of their disks from flying apart as they rotate.

Walsh et al. (1979) published observations of two quasistellar objects (QSOs), 0957+561 A and B, separated on the sky by just $5.7''$ ($1^\circ = 3,600''$). Their proximity to each other, combined with their suspiciously similar spectra and redshifts, led the authors to hypothesize that the two objects were actually separate images of a single source created by a gravitational lens. As with more familiar lenses, a gravitational lens effectively bends the path traveled by light. However, instead of light rays refracting at the boundary between two different media, gravitational lenses alter the trajectory of light by distorting the fabric of spacetime through which light travels.

Depending on the amount and distribution of the lensing matter, and the alignment of the lens relative to the otherwise unaltered path from source to observer, gravitational lensing is either weak (causing slight distortions to the apparent shapes of individual objects and only detectable statistically) or strong (creating multiple, highly distorted images of a single source that may arc around the inferred center of the lens). Lynds & Petrosian (1989) describe further early observations of strong gravitational lensing in their paper "Luminous arcs in clusters of galaxies," in which they conclude the most likely explanation is that the "features are images of

[2]The virial theorem states that the average kinetic energy $\langle K \rangle$ of a system (such as a cluster of galaxies) is equal to negative one half of the average potential energy $\langle U \rangle$ of the system: $\langle K \rangle = -\frac{1}{2}\langle U \rangle$.

more distant objects produced by the gravitational field of the intervening clusters."

The same phenomena that reveal dark matter's existence also make it possible to infer *how* it behaves, even without knowing *what* it is.[3] For example, measuring the lensing of light from distant objects by the dark matter that binds galaxies in foreground clusters together enables us to reconstruct the distribution of dark matter within those clusters. Such inferences place constraints on the properties of dark matter, which in turn inform theoretical models and simulations of the evolution of its large-scale structure throughout the history of the universe.

The predominate ΛCDM cosmological model describes a universe composed of 5% normal matter, 25% cold dark matter (CDM), and 70% dark energy[4] (e.g. Planck Collaboration et al., 2016). Despite not knowing what dark matter is, significant progress has been made in studying its properties with increasing resolution and larger volumes over the past quarter century. At the same time the development of the "halo model" of dark matter (e.g. Peacock & Smith, 2000; Smith et al., 2003) has provided a framework for describing dark matter in terms of halos: (approximately) spherical ensembles of dark matter particles that have collapsed under their own gravity and decoupled from the Hubble Flow. The halo model simplifies the analysis of dark matter clustering on larger scales because halos become the fundamental units that cluster, akin to studying the behavior of a group of people without having to consider the individual atoms each person in the group is comprised of.

Under the simplifying assumption of spherical symmetry, a dark matter halo is defined at a given redshift by (among other properties) its mass, radius, maximum circular velocity, and the shape of its radial density profile, usually modeled as a power law with separate slopes for the inner and outer regions of the halo (e.g. Navarro et al., 1997). Because the density profile is a smooth function of radius with no definite boundary, the radius within which the virial theorem

[3]There are alternatives to the predominate particle theory of dark matter, such as modified Newtonian dynamics (MoND; e.g. Milgrom, 1983), which proposes modifications to Newtonian dynamics on galactic and larger scales.

[4]The term "dark energy" can be understood as a placeholder for the yet unknown cause of the accelerating expansion of the universe (e.g. Riess et al., 1998; Perlmutter et al., 1999). Λ represents an explanation for this acceleration in the form of a cosmological constant, i.e. a constant energy density of space.

applies to the halo, $R_{\rm vir}$, is commonly used to define halo size:

$$M_{\rm vir} = \frac{4\pi}{3} R_{\rm vir}^3 \Delta \rho_{\rm m}. \tag{1.1}$$

Here $M_{\rm vir}$ is a halo's *virial mass*, $\rho_{\rm m}$ is the mean density of dark matter (which evolves as the universe expands), and the value of Δ is usually around 200, although other values can be used. Equation 1.1 defines $R_{\rm vir}$ to be the radius within which a halo's mass density is Δ times greater than the mean.

The evolutionary picture of the large-scale structure of dark matter that has emerged from *N*-body cosmological simulations over the past several decades describes hierarchical structure formation. Particles coalesce into small clumps of dark matter, which merge to create progressively larger clumps, eventually forming the smallest halos that are accreted by and become "subhalos" within the virial radius of larger, more massive halos. On the largest scales the structure of dark matter resembles that of a three-dimensional web or sponge, in which the largest halos contain many subhalos and are connected by long filaments of dark matter that trace the boundaries of voids, vast empty regions of the universe. This structure was seeded by minute variations in the density and temperature of the very early universe, before complex structures of baryonic matter such as galaxies or even stars had formed. The underlying web of dark matter provides the scaffolding for the observed distribution of galaxies, which form within the gravitational potential wells of dark matter halos.

1.3 Quantifying Large-scale Structure: Clustering and Bias

The large-scale spatial properties of galaxies (as well as of dark matter particles or halos) can be described in terms of the two-point correlation function, denoted by $\xi(r)$, which quantifies the excess probability dP (above that of a purely random spatial distribution) of finding two objects separated by a distance r within a differential volume dV. The distribution of pairwise separations

of objects scattered randomly in a finite volume is Poissonian. Gravitational clustering of galaxies or halos yields a probability distribution with amplitudes larger than a Poisson distribution on small scales, and correspondingly smaller amplitudes at large scales. Mathematically $\xi(r)$ is expressed in terms of dP, dV, and the mean number density of galaxies, n, as $\mathrm{d}P = n(1+\xi(r))\mathrm{d}V$.

Measuring $\xi(r)$ for a given galaxy sample requires knowing the volume the sample occupies, a choice of estimator function, and a catalog of random points that cover the equivalent survey area on the sky and have the same (smoothed) redshift distribution as the galaxy sample.[5] The random catalog must also be large enough that any random statistical errors it introduces are subdominant to those of the galaxy data. The most commonly used estimators for $\xi(r)$ are given below, and each have advantages and disadvantages in terms of the magnitude of statistical errors, the computational time required to count pairs, and their sensitivity to the size of random catalog used.

$$\text{Davis \& Peebles (1983):}\ \ \xi(r) = \left(\frac{n_\mathrm{R}}{n_\mathrm{D}}\right)\frac{DD}{DR} - 1 \tag{1.2}$$

$$\text{Hamilton (1993):}\ \ \xi(r) = \frac{DD\,DR}{(DR)^2} - 1 \tag{1.3}$$

$$\text{Landy \& Szalay (1993):}\ \ \xi(r) = \frac{DD}{RR}\left(\frac{n_\mathrm{R}}{n_\mathrm{D}}\right)^2 - \frac{2\,DR}{RR}\left(\frac{n_\mathrm{R}}{n_\mathrm{D}}\right) + 1 \tag{1.4}$$

In the above estimators n_D and n_R are the number densities of objects in the data and random catalogs, respectively, and DD, DR, and RR are counts of data-data, data-random, and random-random pair separations, respectively, and are each a function of scale. $\xi(r)$ is typically measured in comoving coordinates (h^{-1} kpc or h^{-1} Mpc; 1 Mpc $= 10^3$ kpc).

Because the peculiar velocities[6] of galaxies affect the line-of-sight component of distance (Fisher et al., 1994), in practice pair separations are counted both projected onto the plane of the

[5] Constructing a random catalog for a mock galaxy catalog—based on a distribution of halos from a cosmological N-body simulation and a model of how galaxies occupy halos—is simpler because the catalog only needs to cover the cubic volume of the simulation.

[6] A galaxy's peculiar velocity is the (subdominant) component of its velocity that is not due to the Hubble Flow.

sky (denoted by $r_{\rm p}$) and along the line of sight (denoted by π). The projected correlation function, $\omega_{\rm p}(r_{\rm p})$, is the integral of $\xi(r_{\rm p}, \pi)$ over π:

$$\omega_{\rm p}(r_{\rm p}) \equiv \int_{-\infty}^{\infty} \xi(r_{\rm p}, \pi)\, {\rm d}\pi \approx 2 \int_{0}^{\pi_{\rm max}} \xi(r_{\rm p}, \pi)\, {\rm d}\pi \tag{1.5}$$

Typical values of $\pi_{\rm max}$ are between ~ 20 and $\sim 80\ h^{-1}$ Mpc, depending on the properties of the dataset for which $\omega_{\rm p}(r_{\rm p})$ is being measured.

The relative clustering amplitude of a galaxy sample to that of the underlying dark matter distribution (usually averaged over a given length scale) is the bias, b, of the galaxy sample, defined as the square root of the ratio of the galaxy to dark matter correlation functions over a given scale: $b \equiv \sqrt{\xi_{\rm gal}/\xi_{\rm DM}}$. The typical halo mass of a given galaxy population can be inferred from an estimate of the bias (see §1.5 below). To compare the clustering properties of separate galaxy samples—for example with different mean luminosities, stellar masses, star formation rates, etc.—the *relative bias* of two galaxy samples is the square root of the ratio of the samples' correlation functions, again at a specified scale. An advantage of relative bias is that it can be estimated purely from observations, and so does not require any assumptions about the underlying dark matter.

1.4 The Bimodality of Galaxy Properties

All matter in the universe obeys the rules of gravity, but unlike dark matter the relatively small amount of normal matter that composes everything we *directly* observe is also governed by electromagnetism and the strong and weak nuclear forces. The relevant consequence for this work is that the many physical processes that drive the evolution of individual galaxies are both complex and interrelated. Galaxies are rich ecosystems in which generations of stars are formed from the gravitational collapse of pockets of sufficiently dense, cold gas. The masses of stars span many orders of magnitude, and their lifetimes are inversely proportional to their mass. When stars

exhaust their capacity to generate the nuclear energy that sustains them and either fade slowly and quietly into planetary nebulae, or quickly and violently as supernovae, they shed some of their mass back into the interstellar medium to be recycled into new stars and solar systems.

The galaxy population is observed to divide into two broad categories: those actively forming stars, and those that are *quiescent*, with little to no ongoing star formation. The physical causes of this bimodality are not well understood, and remain a major question in the field of galaxy evolution. Moreover, the star-forming/quiescent galaxy bimodality extends to many other galaxy properties, including color—which is closely associated with star formation rate (SFR)—gas and dust content, shape, and amount of internal structure (e.g. Strateva et al., 2001; Kauffmann et al., 2003; Baldry et al., 2004; Balogh et al., 2004). Galaxies with high rates of star formation have more bright, young blue stars, and tend to be disk-shaped, with multiple features such as spiral arms and extended clumps of light-obscuring dust. They also have larger gas fractions than quiescent galaxies, which tend to be redder due to their older stellar populations, elliptical in shape, and have little substructure. Absent from the overall galaxy population are substantial numbers of galaxies in an intermediate state of evolution between star-forming and quiescent, which suggests that galaxies generally tend to cease star formation (i.e. "quench") relatively rapidly.

The simplest quenching process is the depletion of gas reserves by ongoing star formation without replenishment via accretion from the intergalactic medium. Dying stars are an internal source of new fuel, but the fact that so many galaxies remain quiescent indicates that other quenching mechanisms must play an important role in producing the quiescent population. Other mechanisms involve the heating of available gas to temperatures above which it can collapse under its own gravity. This heating could be caused by internal processes within the galaxy, such as feedback by active galactic nuclei (AGN; e.g. Croton et al., 2006; Hopkins et al., 2006), highly emissive regions at the centers of galaxies where accretion by a supermassive black hole produces enormous amounts of radiation. Gas can also be "shock" heated during infall onto a galaxy (e.g.

White & Rees, 1978), or when galaxies collide and merge. Gas can even be removed entirely by the strong tidal forces of interactions between galaxies in clusters, a process called "tidal stripping" (e.g. Merritt, 1983).

The predictions of ΛCDM about galaxy clustering generally agree with observations. Additionally, the dependence of galaxy clustering on stellar mass, luminosity, and color is now well-established at $z \sim 0$ (Norberg et al., 2001; Norberg et al., 2002; Zehavi et al., 2002, 2005; Li et al., 2006; Zehavi et al., 2011), in no small part due to the wealth of data collected by the SDSS. These dependencies have also been studied to $z \sim 1$ (Coil et al., 2006, 2008; Mostek et al., 2013; Skibba et al., 2014; Coil et al., 2017), although the data here are limited as it is more difficult to obtain both sufficiently large and statistically complete samples at higher redshift, particularly of fainter and less massive galaxies. Galaxy clustering amplitude increases with luminosity (Norberg et al., 2001), which indicates that more luminous galaxies reside in more massive halos as galaxy clustering, halo clustering, and halo mass are all positively correlated (see §1.5 below). Red, low-SFR galaxies are also observed in the local universe ($z \sim 0$) to cluster more strongly than blue, high-SFR galaxies (Madgwick et al., 2003; Zehavi et al., 2005). As galaxies with lower SFRs tend to be older than those with higher SFRs, the interpretation is that the earliest galaxies formed in the most massive halos present at that epoch in the history of the universe.

While blue galaxies follow the same luminosity-clustering relation as the full galaxy population, the luminosity dependence of clustering for red galaxies is more complicated. The galaxy luminosity function describes the density of galaxies as a function of luminosity (Schechter, 1976), and is described by (among other parameters) a characteristic luminosity L^* that represents a turning point in the shape of the luminosity function. Faint red galaxies—i.e. red galaxies with $L \lesssim L^*/2$—are *more* strongly clustered than red galaxies with $L \sim L^*$, while the clustering amplitude of red galaxies increases again for $L > L^*$ (Zehavi et al., 2011). As discussed in §1.5 below, this is related to the fact that faint red galaxies tend to reside within galaxy clusters.

The dependencies of galaxy clustering on luminosity and color seen at $z \sim 0$ have also

been observed at higher redshift (to $z \sim 1$). Trends with galaxy color are stronger than with luminosity both locally and at $z \sim 1$. However, trends that are consistent across much of the history of the universe do not necessarily have the same physical explanations at different redshifts. The evolution of galaxy clustering is influenced not only by gravity increasing clustering over time, but also by the expansion of the universe, which itself depends on cosmological parameters such as Λ, the dark energy or cosmological constant responsible for the expansion of the universe, and $\Omega_{\rm m}$, the amplitude of the universe's mean matter density.

Cosmological parameters also affect the evolution of halo clustering. For example, larger values of Λ would yield larger voids in the cosmic web. The hierarchical structure formation of ΛCDM (see §1.2 above) means that the earliest galaxies (those that form at high redshifts) form in the earliest-forming halos, which—as discussed in §1.5—are more strongly clustered than halos that form later. The oldest galaxies are therefore a more biased tracer of the universe's overall matter distribution than younger galaxies. Coil et al. (2006) present evidence consistent with this interpretation using data from the DEEP2 survey: galaxy bias on two-halo scales ($\sim$ 1–10 h^{-1} Mpc; see §1.5) correlates with luminosity. Also using DEEP2 data Coil et al. (2008) find that the relative bias of red to blue galaxies is as large at $z \sim 1$ as it is today. This indicates that the greater clustering amplitude of red galaxies compared to blue galaxies observed locally cannot result entirely from the effects of gravity acting over time; additional physical processes must play a role.

1.5 The Galaxy–Halo Connection

In a ΛCDM universe galaxies form in collapsing overdense regions of cold dark matter that attract sufficient normal matter to reach the densities, temperatures, and pressures required to ignite fusion and form stars. But not only does dark matter play a crucial role in galaxy formation, the evolution of galaxies—their potential for star formation and the triggers of quenching—is

inextricably tied to dark matter as well.

As dark matter is unaffected by baryonic physics, the evolution of its structure is in some sense simpler to study than that of galaxies. The clustering properties of halos are primarily studied with cosmological simulations, which demonstrate that halo mass is the dominant variable affecting halo clustering (Sheth & Tormen, 1999), with clustering amplitude increasing with larger halo mass. This is unsurprising as dark matter only interacts with itself and with baryonic matter via gravity.[7]

The mass of a typical halo for a particular galaxy population can be inferred from (1) measurements of the populations's large-scale clustering amplitude combined with (2) the large-scale clustering amplitude of halos as a function of halo mass. The latter is obtained from N-body simulations and assumed values of cosmological parameters. Together (1) and (2) provide an estimate of the galaxy population's large-scale bias. These galaxies are then assumed to occupy halos of a given mass that have the same bias as that given by (2).

Gao et al. (2005) used the Millennium simulation (Springel et al., 2005) to show that halo age—and thus the age of the universe when a halo began to form—also correlates with halo clustering amplitude, independent of halo mass: older halos are more strongly clustered than younger halos of the same mass. Since the Gao et al. (2005) result many studies have explored other possible dependencies of halo clustering in addition to age, including concentration (related to halo internal mass distribution), occupation (the galaxy population of a halo), spin (related to angular momentum), and environment (Wechsler et al., 2006; Croton et al., 2007; Gao & White, 2007; Zentner, 2007; Tinker et al., 2008; Hahn et al., 2009; Lacerna & Padilla, 2011, 2012; Sunayama et al., 2016; Lee et al., 2017; Villarreal et al., 2017; Johnson et al., 2018; Mao et al., 2018; Salcedo et al., 2018; Mansfield & Kravtsov, 2019). The general concept of halo clustering correlating with other halo properties besides mass is known as *halo assembly bias*.

The earliest statistical models prescribing how galaxies occupy halos presumed that halo

[7] A theory of self-interacting dark matter has been proposed by Spergel & Steinhardt (2000).

mass determines the probability that a halo hosts one or more galaxies (Peacock & Smith, 2000; Benson et al., 2000; Berlind & Weinberg, 2002). Similar models utilize *abundance matching*, a technique that involves rank-ordering halos by mass, and galaxies by stellar mass or luminosity, and pairing the most massive (or luminous) galaxies with the most massive halos.

The HOD model of Peacock & Smith (2000) depends on the halo occupation number (the mean number of galaxies in a halo of a given mass) and the location of the galaxies within the halo. It places one galaxy at the center of a halo (the "central" galaxy) and assumes that other galaxies in the same halo ("satellite" galaxies) are embedded within the halo according to its radial dark matter distribution, which is modeled as an NFW profile[8] (Navarro et al., 1997). Benson et al. (2000) proposed a similar model that includes a minimum halo mass ($M_{\rm min}$) required for a halo to host a central galaxy. In both models the clustering of galaxies within a single halo defines the "one-halo" term ($r \lesssim 1\ h^{-1}\,$Mpc) of the galaxy correlation function $\xi(r)$, while the "two-halo" term ($1 \lesssim r \lesssim 10\ h^{-1}\,$Mpc) represents contributions from galaxies in separate halos. The combination of these two terms yields a power law $\xi(r)$.

The Berlind & Weinberg (2002) model defines the probability $P(N|M_{\rm h})$ that a halo of mass $M_{\rm h}$ hosts N galaxies, where $P(N|M_{\rm h})$ has two parameters: $M_{\rm min}$ and the slope of $P(N|M_{\rm h})$ for satellite galaxies, which determines the halo occupation number for satellites. To apply this model halos are first identified in the result of an N-body simulation, then galaxies are assigned to halos according to $P(N|M_{\rm h})$.

Closely related to HOD models are conditional luminosity function (CLF) models (e.g. Yang et al., 2003), which relate galaxy luminosity to halo mass. Both frameworks have been refined to incorporate prescriptions for satellite galaxies in subhalos within larger "parent" halos (Kravtsov et al., 2004; Zehavi et al., 2004), as well as expanded to accommodate additional galaxy properties that have been shown to correlate with galaxy clustering (van den Bosch et al., 2003; Vale & Ostriker, 2004; Hearin & Watson, 2013; Watson & Conroy, 2013; Hearin et al., 2014;

[8]The NFW profile models the radial mass density of a halo as $\rho(r) = \rho_0 (r/r_{\rm s})^{-1}(1 + r/r_{\rm s})^{-2}$ with free parameters ρ_0 and scale radius $r_{\rm s}$.

Campbell et al., 2015; Zu & Mandelbaum, 2015). For example, Zehavi et al. (2004) found that the galaxy correlation function $\xi(r)$ for SDSS data deviates slightly from a power law: there is a change in the slope of $\xi(r)$ at the scale corresponding to the transition from the one-halo to the two-halo term. Their model adds as a third parameter the minimum mass required for a halo to host a satellite galaxy.

The parameters of HOD models vary for different galaxy populations, which provides insight into physical explanations of the observed clustering dependencies of galaxies. Zehavi et al. (2011) find via HOD modeling that at $z \sim 0$ a much lower fraction of blue galaxies are satellites ($\sim 25\%$) compared to the satellite fraction for red galaxies ($\sim 60\%$). They also demonstrate that the median mass of halos that host blue galaxies is lower than for red galaxies. While galaxy color is *not* found to correlate strongly with halo mass *at a given luminosity*, the relation between galaxy color and median halo mass is explained by a larger satellite fraction for red galaxies. Similarly, the greater clustering amplitude of faint red galaxies relative to that of their brighter quiescent counterparts (see §1.4) can be explained by faint red galaxies being satellites of a bright, quiescent central galaxy in the same massive halo (Berlind et al., 2005).

While halo assembly bias is a well-established prediction of ΛCDM, the role of *galaxy* assembly bias in the relationship between galaxies and dark matter halos is an open question. Galaxy assembly bias refers to the direct dependence of galaxy properties on properties of halos other than halo mass (Zentner et al., 2014), and is inconsistent with the assumption of HOD and CLF models that the (statistical) galaxy content of a halo is predicted by halo mass alone.

Models of the galaxy–halo connection that incorporate galaxy assembly bias are difficult to test empirically because the observational signatures of galaxy assembly bias are consistent with alternative explanations, at least within the limits of existing data. Two such signatures explored in this dissertation are galactic conformity on two-halo scales, and the differential clustering of star-forming and quiescent central galaxies independent of stellar mass.

1.6 Dissertation Outline

Galactic conformity, first observed by Weinmann et al. (2006) in the SDSS, is the tendency of neighboring galaxies to "conform" to the star formation properties of an adjacent central galaxy, i.e. star-forming central galaxies are more likely to have have star-forming satellites, and likewise for quiescent galaxies. As we demonstrate in Chapter 2, galactic conformity is a small statistical effect and thus highly sensitive to systematic errors, as well as cosmic variance (inhomogeneities in the density of the universe on certain large scales).

Chapter 2 presents measurements of galactic conformity at $0.2 < z < 1$ on length scales greater than that of a single halo, which is the scale most relevant for testing galaxy assembly bias. These measurements are the first of their kind and utilize a dataset uniquely suited for robust detections of a conformity signal at intermediate redshift. We compare both our method and results to the few other studies of galactic conformity, and show how existing galaxy survey data is at the cusp of what is required for statistically significant tests of theoretical predictions of both the stellar mass and redshift dependence of galactic conformity.

In Chapter 3 we measure the clustering dependence of central galaxies on specific SFR (sSFR, or SFR per unit stellar mass) at intermediate redshift to determine the extent to which analogous measurements of the full galaxy population are attributable to satellite galaxies (as opposed to centrals, which are the dominant tracers of the underlying distribution of halos). Disentangling the relative contributions of centrals and satellites to the observed correlation between galaxy sSFR and clustering amplitude is essential for interpreting such measurements in the context of galaxy assembly bias.

Chapter 3 also presents an analysis of the completeness and contamination of the samples of central galaxies we use by testing our selection criteria on mock galaxy catalogs designed to replicate the observational effects present in our galaxy survey data. We identify a new systematic bias, *environmental incompleteness*, and demonstrate the critical importance of using mock

catalogs to understand and compensate for such biases.

In Chapter 4 we expand measurements of the joint dependence of galaxy clustering on sSFR and stellar mass at intermediate redshift to include the local universe ($z \sim 0$). With these novel measurements we compare observations to a state-of-the-art empirical model of galaxy evolution over $0 < z < 1.2$, more than 8 Gyr of cosmic history. We show how galaxy bias at fixed sSFR is a new constraint for these types of models, and identify an improvement to the existing best-fit model at $z = 0$. The analysis of Chapter 4 concludes with a comparative study of *intra-sequence relative bias*—differential clustering *within* the star-forming and quiescent galaxy populations—in the data and model to improve the physical interpretation of this phenomenon.

We conclude in Chapter 5 with a discussion of possibilities for future work, including the limitations of forthcoming spectroscopic galaxy redshift surveys for studies of galaxy evolution.

2 One- and Two-halo Galactic Conformity at $0.2 < z < 1$

Abstract

We test for galactic conformity at $0.2 < z < 1.0$ to a projected distance of 5 Mpc using spectroscopic redshifts from the PRism MUlti-object Survey (PRIMUS). Our sample consists of $\sim 60,000$ galaxies in five separate fields covering a total of ~ 5.5 square degrees, which allows us to account for cosmic variance. We identify star-forming and quiescent "isolated primary" (i.e. central) galaxies using isolation criteria and cuts in specific star formation rate. We match the redshift and stellar mass distributions of these samples, to control for correlations between quiescent fraction and redshift and stellar mass. We detect a significant ($> 3\sigma$) one-halo conformity signal, or an excess of star-forming neighbors around star-forming central galaxies, of $\sim 5\%$ on scales of 0–1 Mpc and a 2.5σ two-halo signal of $\sim 1\%$ on scales of 1–3 Mpc. These signals are weaker than those detected in SDSS and are consistent with galactic conformity being the result of large-scale tidal fields and reflecting assembly bias. We also measure the star-forming fraction of central galaxies at fixed stellar mass as a function of large-scale environment and find that central galaxies are more likely to be quenched in overdense environments, independent of stellar mass. However, we find that environment does *not* affect the star formation efficiency of central galaxies, as long as they are forming stars. We test for redshift and stellar mass dependence of the conformity signal within our sample and show that large volumes and multiple fields are required at intermediate redshift to adequately account for cosmic variance.

2.1 Introduction

The distributions of many related galaxy properties are bimodal, including color, star formation rate (SFR), gas fraction, and morphology (e.g. Strateva et al., 2001; Kauffmann et al., 2003; Baldry et al., 2004; Balogh et al., 2004). Galaxies with lower star formation rates are usually redder and exhibit "early-type" morphologies, while those with higher star formation rates tend to be bluer and have "late-type" morphologies. The existence of this bimodality is consistent with star formation in galaxies turning off, or quenching, rapidly, as quenching over longer timescales would result in flatter distributions of color and SFR (e.g. Tinker & Wetzel, 2010; Wetzel et al., 2013).

Numerous mechanisms for quenching have been proposed, including but not limited to the shock heating of infalling gas (e.g. White & Rees, 1978; Dekel & Birnboim, 2006), stellar and AGN feedback (e.g. Croton et al., 2006; Hopkins et al., 2006), and gas heating and/or removal caused by galaxy mergers or harassment (e.g. Moore et al., 1996). Agreement on which of these mechanisms plays the largest role remains elusive in the absence of definitive evidence, although it is likely that the relative importance of these various mechanisms depends on stellar or halo mass, as well as on large-scale environment.

The recently-discovered phenomenon of galactic conformity may provide additional insights into and constraints on the quenching mechanism, and more broadly, the dependence of galaxy evolution on large-scale structure. Galactic conformity refers to correlations between the colors and SFRs of massive central galaxies and their nearby neighboring galaxies. It was first identified by Weinmann et al. (2006) in the Sloan Digital Sky Survey (SDSS; York et al., 2000) at $z < 0.03$. Weinmann et al. (2006) identified galaxy groups in SDSS—defined as the ensemble of galaxies residing in the same dark matter halo—using a group-finding algorithm (Yang et al., 2005). They define central galaxies as the brightest galaxy in each group, and dub all other group members satellite galaxies. Group halo masses are estimated by assuming a correlation between

group luminosity and halo mass. Weinmann et al. (2006) found that the quiescent fraction of satellite galaxies is higher for quiescent central galaxies than for star-forming central galaxies residing in halos of the same mass, and that this correlation exists for halo masses spanning three orders of magnitude, from 10^{12} to 10^{15} $M_\odot$.

Kauffmann et al. (2013) compared the specific star formation rates of central SDSS galaxies and their neighbor galaxies at fixed *stellar* mass from 5×10^9 to 3×10^{11} $M_\odot$ and found evidence of conformity at projected distances up to ~ 4 Mpc from the central galaxy, well beyond the virial radius of a single halo. The Kauffmann et al. (2013) result motivated the distinction of "one-halo" and "two-halo" conformity (Hearin, Watson, & van den Bosch, 2015), referring to correlations between central galaxies and their satellite galaxies within a single halo and between central galaxies and neighboring galaxies in adjacent halos, respectively. Kauffmann et al. (2013) also concluded that the scale dependence of conformity is correlated with the stellar mass of the central galaxy. Specifically, they found that two-halo conformity exists for low-mass central galaxies ($9.7 < \log(M_*/M_\odot) < 10.3$) and is greatest at large separations (> 1 Mpc). For high-mass central galaxies ($10.7 < \log(M_*/M_\odot) < 11.3$) the signal is confined to one-halo scales.

Galactic conformity (especially two-halo conformity) is further evidence that standard halo occupation model (Berlind & Weinberg, 2002), which presumes that the properties of a halo's galaxy population are determined solely by present-day halo mass, does not represent the full picture of galaxy and halo clustering (e.g. Kravtsov et al., 2004). Correlations between the colors and SFRs of central galaxies and their satellites *at fixed halo mass* is a clear contradiction of the assumptions of mass-only halo occupation models.

The additional dependence of halo clustering on properties beyond halo mass, such as formation epoch and large-scale environment, is referred to as *assembly bias* (e.g. Gao et al., 2005; Wechsler et al., 2006; Croton et al., 2007; Gao & White, 2007; Zentner, 2007; Dalal et al., 2008; Tinker et al., 2008; Sunayama et al., 2016). Theoretical models provide evidence that

galactic conformity may be a natural result of *galaxy assembly bias*.

Hearin et al. (2015) tests for two-halo conformity with three different (sub)halo abundance matching (SHAM) models of halo occupation statistics by assigning galaxies to halos in the N-body Bolshoi simulation (Klypin et al., 2011), which follows the evolution of 2048^3 particles in a 250 h^{-1} Mpc periodic box. Both the standard halo occupation model, in which the quenching of central and satellite galaxies depends only on halo mass, and the delayed-then-rapid model (Wetzel et al., 2013), in which satellite galaxy quenching depends on both time since accretion and halo mass at accretion time, exhibit zero two-halo conformity. The age matching SHAM model, in which central and satellite galaxy quenching depends on halo mass and (sub)halo formation time, and the lowest SFR galaxies are assigned to the oldest halos, *does* exhibit two-halo conformity comparable to that seen by Kauffmann et al. (2013) in SDSS.

Hearin et al. (2015) also shuffles the SFRs of only satellite and only central galaxies in the age matching model, and finds that shuffling satellite galaxy SFRs has little effect on the conformity signal, while shuffling the SFRs of central galaxies erases it entirely. This result focuses the likely connection to one between two-halo conformity and *central* galaxy assembly bias.

In a follow-up paper Hearin et al. (2016) conclude that conformity and assembly bias are alternative descriptions of the same underlying phenomenon. Because halos that assembled earlier are more strongly clustered than more recently-assembled halos of the same mass (e.g. Hahn et al., 2009), older (younger) halos inhabit more (less) dense environments and are therefore subjected to stronger (weaker) large-scale tidal fields. Strong tidal effects inhibit the rate at which dark matter is accreted into halos, giving rise to what Hearin et al. (2016) dubs *halo accretion conformity*: the clustering of halos at fixed mass with high (lower) dark matter accretion rates.

Hearin et al. (2016) finds evidence of halo accretion conformity in the Bolshoi simulation, and proposes that two-halo galactic conformity follows from halo accretion conformity if gas and dark matter accretion rates are sufficiently coupled (e.g. Wetzel & Nagai, 2015). The same work

also proposes that present-day one-halo conformity may be a direct result of two-halo conformity at higher redshift, since many satellite galaxies were their own centrals at an earlier epoch.

Additionally, Hearin et al. (2016) clearly predicts halo accretion conformity strength should diminish both with increasing redshift and with increasing halo mass, as more massive halos are less sensitive to tidal effects. For example, for 10^{11} $M_{\odot}$ secondary halos surrounding a 10^{12} $M_{\odot}$ primary halo Hearin et al. (2016) predicts that a normalized halo accretion conformity signal at 3 Mpc of $\sim 20\%$ at $z = 0$ would equate to a signal of $\sim 4\%$ at $z \sim 1$, and to just $\sim 0.5\%$ by $z \sim 2$.

Both strong one-halo and weaker two-halo conformity have been found by Bray et al. (2016) in the hydrodynamical *Illustris* simulation (Vogelsberger et al., 2014). Bray et al. (2016) also detect "halo age conformity" to $R \sim 10$ Mpc, in which less massive old (young), "secondary" halos are preferentially found in the vicinity of more massive old (young), "primary" halos.

However, Paranjape et al. (2015) argue that the two-halo conformity signal in SDSS found at fixed *stellar* mass in Kauffmann et al. (2013) is not conclusive evidence that two-halo galactic conformity is the result of halo assembly bias. Such a signal could also be due to one-halo conformity "leaking" to large scales when averaging over a range of halo masses, as scatter in the stellar mass-halo mass relation means that some galaxies with the same stellar mass inevitably reside in halos of different masses.

Kauffmann (2015) proposes "pre-heating" as an alternative explanation for galactic conformity. In the pre-heating scenario, feedback from an early generation of accreting black holes heats gas over large scales at an early epoch, causing coherent modulation of cooling and star formation among galaxies on the same large scales. As evidence, Kauffmann (2015) cites an excess number of very massive galaxies out to 2.5 Mpc around quiescent central galaxies in the same SDSS sample used in Kauffmann et al. (2013). Kauffmann (2015) also finds that massive galaxies in the vicinity of low sSFR central galaxies at $z = 0$ are 3–4 times more likely to host radio-loud active galactic nuclei (AGN) than those around a control sample of higher

sSFR central galaxies. While not explicitly stated in Kauffmann (2015), if pre-heating by an early generation of AGN is responsible for two-halo conformity, the signal strength will most likely *increase* with redshift, which is the opposite of the Hearin et al. (2016) prediction.

Measuring a statistical effect like galactic conformity at $z > 0.2$ requires very deep, relatively large-volume surveys with precise redshifts. Not surprisingly, observational studies of conformity have until recently been limited to the redshift range of SDSS. Searching for evidence of conformity over a much larger range of cosmic time is a valuable test of assembly bias, and may play an important role in constraining the quenching mechanism(s) at work at certain stellar masses and in certain environments.

As of this writing only a few studies have tested for conformity or a related effect at $z > 0.2$. Using photometric redshifts from three fields totaling 2.37 deg^2 Kawinwanichakij et al. (2016) test for one-halo conformity in four redshift bins over the range $0.3 < z < 2.5$ for central galaxies with $M_* > 10^{10.5}$ M$_\odot$. Kawinwanichakij et al. (2016) estimate the average quiescent fraction of satellite galaxies in fixed apertures for stellar mass-matched samples of quiescent and star-forming central galaxies. If we define the magnitude of a conformity signal to be the percent difference between the fraction of star-forming satellites surrounding star-forming and quiescent central galaxies, Kawinwanichakij et al. (2016) find a conformity signal of $\sim$ 10–30% at $0.6 < z < 1.6$ on scales of $\lesssim$ 300 projected comoving kpc, and a $\sim$ 10% signal at $0.3 < z < 0.6$.

Hartley et al. (2015) also use photometric redshifts to look for one-halo conformity in a sample of $10^{10.5} < M_* < 10^{11.0}$ M$_\odot$ central galaxies in the 0.77 deg^2 UKIDSS UDS field at $0.4 < z < 1.9$. They measure the radial density profiles of quiescent satellite galaxies for mass-matched samples of quiescent and star-forming central galaxies. Hartley et al. (2015) find a conformity signal of $\sim$ 50% on scales of $\sim$ 10–350 projected kpc at $0.4 < z < 1.9$.

Both Campbell et al. (2015) and Paranjape et al. (2015) have shown that systematic error can create an artificial conformity signal. Contamination from interlopers (galaxies not physically associated with a central galaxy that are falsely classified as satellites, or satellite

galaxies falsely classified as centrals) can also bias measurements of conformity (for a detailed explanation see §2.2 of Hearin et al., 2015). Spectroscopic redshifts are therefore crucial for measuring conformity robustly. Additionally, cosmic variance may impact a conformity signal, but the effect can be mitigated by using a large survey volume and multiple fields. We achieve this using data from the PRIsm MUlti-object Survey (PRIMUS; Coil et al., 2011; Cool et al., 2013).

With a survey area of ~ 9 deg^2, a redshift precision of $\sigma_z = 0.005\,(1+z)$, and four spatially-distinct fields, PRIMUS is uniquely suited for investigating one- and two-halo conformity at $0.2 < z < 1$. While previous studies of conformity at $z > 0.2$ have necessarily used photometric redshifts, spectroscopic redshifts allow us to much more cleanly identify isolated central-like galaxies, which is critical for a robust measurement of conformity. PRIMUS also allows us to test the effects of cosmic variance and the need for large areas in multiple fields at intermediate redshift, and to investigate the redshift and mass dependence of one- and two-halo conformity.

In a related forthcoming paper, Bray et al. (in preparation) perform a complimentary analysis with cross-correlations between the PRIMUS spectroscopic and photometric galaxy samples. Bray et al. measure the fraction of quiescent galaxies around all PRIMUS spectroscopic galaxies (not just central galaxies) to $\sim 1\ h^{-1}\,$Mpc.

The structure of this chapter is as follows. In §2.2 we describe the survey used for this study and the details of sample selection. Our results are presented in §2.3. In §2.4 we discuss the implications of our results in the context of other conformity studies and the predictions from simulations and theory. We summarize our findings and conclusions in §2.5. Throughout this chapter we assume $H_0 = 70$ km s$^{-1}\,$Mpc^{-1}, $\Omega_{\rm m} = 0.3$, and $\Omega_\Lambda = 0.7$.

2.2 Data

In this section we describe the PRIMUS redshift survey data, how we identify star-forming and quiescent galaxies, and how we define the isolated primary samples used to measure the

conformity signal within PRIMUS.

2.2.1 The PRIMUS Redshift Survey

The PRIsm MUlti-Object Survey (PRIMUS) is the largest spectroscopic faint galaxy redshift survey completed to date. The survey was conducted with the IMACS spectrograph (Bigelow & Dressler, 2003) on the Magellan I Baade 6.5-meter telescope at Las Campanas Observatory, using slitmasks and a low-dispersion prism. The design allowed for $\sim 2,000$ objects per slitmask to be observed simultaneously with a spectral resolution of $\lambda/\Delta\lambda \sim 40$ in a ~ 0.2 deg^2 field of view. Objects were targeted to a maximum depth of $i \geq 23$, and typically two slitmasks were observed per pointing on the sky. PRIMUS obtained robust redshifts ($Q \geq 3$; see Cool et al., 2013) for $\sim 120,000$ objects at $0 < z < 1.2$ with a redshift precision of $\sigma_z/(1+z) \sim 0.005$.

The total survey area of PRIMUS is 9.1 deg^2 and encompasses seven distinct science fields: the Chandra Deep Field South-SWIRE field (CDFS; Lonsdale et al., 2003), the 02hr and 23hr DEEP2 fields (Newman et al., 2013), the COSMOS field (Scoville et al., 2007), the European Large Area ISO Survey-South 1 field (ES1; Oliver et al., 2000), the Deep Lens Survey (DLS; Wittman et al., 2002) F5 field, and two spatially-adjacent subfields of the XMM-Large Scale Structure Survey field (XMM-LSS; Pierre et al., 2004). The XMM subfields are the Subaru/XMM-Newton DEEP Survey field (XMM-SXDS; Furusawa et al., 2008) and the Canada-France-Hawaii Telescope Legacy Survey (CFHTLS) field (XMM-CFHTLS). These two fields are adjacent but are treated separately in our analysis as they were targeted by PRIMUS using different photometric catalogs (Coil et al., 2011). Full details of the survey design, targeting, and data summary can be found in Coil et al. (2011), while details of data reduction, redshift fitting, precision, and survey completeness are available in Cool et al. (2013).

Here we use the PRIMUS fields that have deep multi-wavelength ultraviolet (UV) imaging from the Galaxy Evolution Explorer (GALEX; Martin et al., 2005), mid-infrared imaging from the Spitzer Space Telescope (Werner et al., 2004) Infrared Array Camera (IRAC; Fazio et al.,

2004), and optical and near-IR imaging from various ground-based surveys. These include the CDFS, COSMOS, ES1, XMM-CFHTLS, and XMM-SXDS fields, covering ~ 5.5 deg^2 on the sky.

2.2.2 Full Galaxy Sample and Targeting Weights

Objects in PRIMUS are classified as galaxies, stars, or broad-line AGN by fitting the low-resolution spectra and multi-wavelength photometry for each source with an empirical library of templates. The best-fit template defines both the redshift and the type of the source. We exclude AGN from this study and keep only those objects defined as galaxies with robust redshifts ($Q \geq 3$) in the redshift range $0.2 < z < 1.0$. We also only keep galaxies with well-defined targeting weights (these are termed "primary" galaxies in Coil et al. (2011); we do not use that naming here, to avoid confusion with our isolated primary sample defined below in §2.2.5). These galaxies have a well-understood spatial and targeting selection function, defined by both a density-dependent weight and a magnitude-dependent sparse-sampling weight. In combination with a third, post-targeting weight that accounts for redshift incompleteness (see below) these weights allow a statistically complete galaxy sample to be recovered, which is suitable for analysis on two-point statistics, such as performed here.

PRIMUS targeting weights are described in detail in Coil et al. (2011) and Cool et al. (2013). Briefly, density-dependent weights account for sources that PRIMUS could not target in dense survey regions, as galaxies are sufficiently clustered in the plane of the sky to the PRIMUS flux limit that even two slitmasks per pointing could not target every galaxy below the magnitude limit in each field (as spectra would overlap on the detector). Sparse-sampling weights are magnitude-dependent and ensure that the PRIMUS target catalog is not dominated by the faintest objects within the survey flux limit. Sparse-sampling weights were used to randomly select roughly a third of galaxies in the faintest 0.5 mag interval above the primary sample targeting limit.

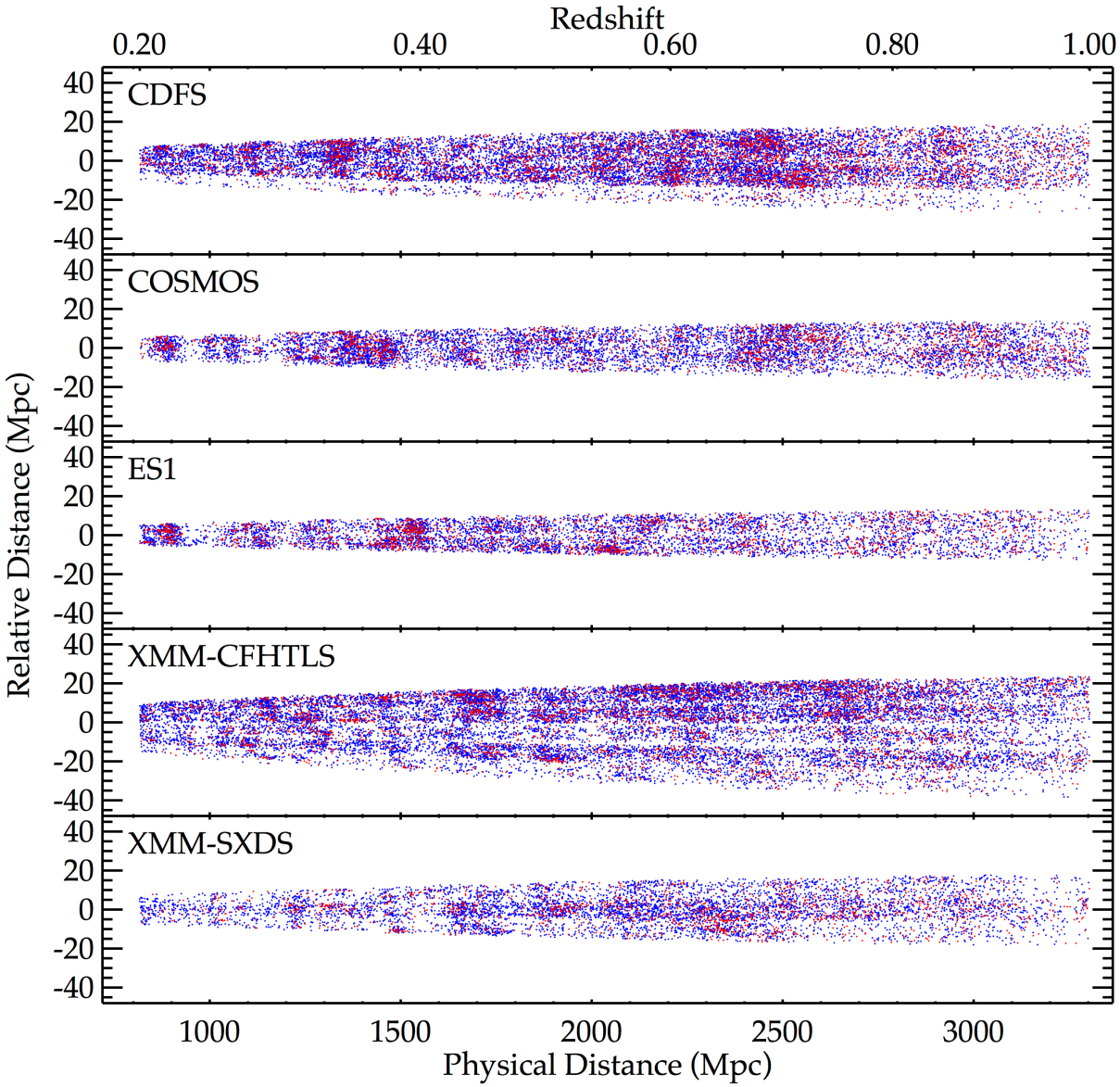

Figure 2.1: Redshift space distributions of PRIMUS galaxies as a function of physical distance along the line-of-sight and physical distance in the right ascension (RA) direction, relative to the median RA of the field. Only galaxies with robust redshifts ($Q \geq 3$) are shown. Star-forming galaxies are shown in blue and quiescent galaxies in red (see §2.2.4). Large-scale differences in the observed density of galaxies, for example, as a function of RA, reflect the number of slitmasks and targeting density.

Skibba et al. (2014) measured galaxy clustering in PRIMUS and tested the recoverability of two-point statistics with mock galaxy catalogs covering the PRIMUS survey volume. They applied the same process used to select the PRIMUS target sample and calculate density-dependent and sparse-sampling weights to a mock catalog, and generated a weighted mock sample. Skibba et al. (2014) then compared the correlation function of all galaxies in the mock catalog to that of the weighted mock sample and found no systematic difference between the two. Thus when PRIMUS targeting weights are applied target selection does not impact the results presented in §2.3 below.

A third, post-targeting weight (described in detail in Cool et al., 2013) accounts for the fact that not all PRIMUS spectra yielded reliable ($Q \geq 3$) redshifts. As shown in §7 of Cool et al. (2013), the PRIMUS redshift success rate is primarily a function of *i*-band magnitude and does *not* depend strongly on galaxy color. Taken together, the three weights described above allow for the recovery of a statistically complete galaxy sample from the targeted sources with reliable redshifts.

The full sample used here includes $60,071$ galaxies in the five fields discussed above with robust redshifts between $0.2 < z < 1.0$ and well-understood selection weights. Below we test the sensitivity of our results to these targeting and completeness weights.

2.2.3 Stellar Mass and Star Formation Rate Estimates

Stellar masses and star formation rates (SFRs) of PRIMUS galaxies are obtained with SED fitting, a widely adopted method for estimating the physical properties of galaxies. A complete description of the SED fitting process using `iSEDfit` can be found in Moustakas et al. (2013), but we summarize the relevant points here.

`iSEDfit` is a suite of routines written in the `IDL` programming language that uses galaxy redshifts and photometry to compute the statistical likelihood of a large ensemble of model SEDs for each galaxy. Model SEDs are generated using population synthesis models, and

span a wide range of observed colors and physical properties (age, metallicity, star formation history, dust content, etc.). `iSEDfit` uses a Monte Carlo technique to randomly select values of model parameters from user-defined parameter distributions and compute a posterior probability distribution function (PDF). PDFs of stellar mass and SFR are found by marginalizing over all other parameters, and the median value of the marginalized PDF is taken as the best estimate of the stellar mass or SFR of each galaxy.

To test how the uncertainties on the stellar mass and SFR estimates described above affect our classification of galaxies as either star-forming or quiescent, we randomly sampled individual stellar masses and SFRs for each galaxy in the full sample 100 times from normal distributions with widths equal to the stellar mass or SFR error for that galaxy. Over 100 trials there is an average change in the star-forming fraction of $< 1\%$. Below in §2.3.2 we discuss how this small difference may affect our conformity results.

2.2.4 Identifying Star-forming and Quiescent Galaxies

We divide our sample into star-forming and quiescent galaxies based on each galaxy's position in the SFR–stellar mass plane. Figure 2.2 shows SFR versus stellar mass in six redshift bins from $z = 0.2$–1 for the PRIMUS galaxy sample. The dashed line (Eq. 2.1) in each panel traces the minimum of the bimodal galaxy distribution in that bin and is given by the following linear relation:

$$\log(\mathrm{SFR}) = -1.29 + 0.65\log(M-10) + 1.33(z-0.1) \tag{2.1}$$

where SFR has units of $\mathrm{M}_{\odot}\,\mathrm{yr}^{-1}$ and M has units of $\mathrm{M}_{\odot}$. The slope of this line is defined by the slope of the star-forming main sequence (Noeske et al., 2007) as measured in the PRIMUS dataset using `iSEDfit` SFR and stellar mass estimates. Each galaxy is classified as star-forming or quiescent based on whether it lies above or below the cut defined by Equation 2.1, evaluated at

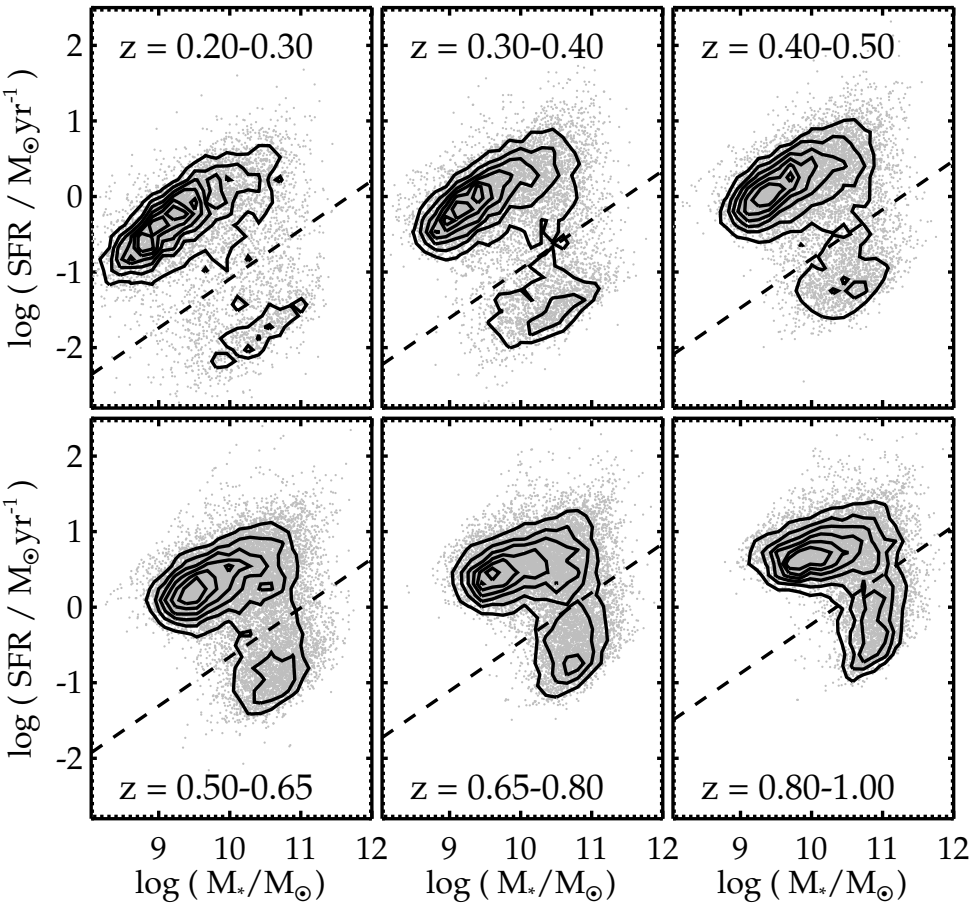

Figure 2.2: Star formation rate (SFR) versus stellar mass for PRIMUS galaxies in six redshift bins from $z = 0.2$–1. Galaxies in our sample are classified as star-forming or quiescent according to whether they lie above or below the dashed line, respectively. This line runs parallel to the star-forming main sequence, traces the minimum in the galaxy SFR bimodality, and evolves with redshift according to Equation 2.1.

the redshift of the galaxy.

2.2.5 Isolated Primary Galaxy Sample

In order to measure galactic conformity we must first identify isolated galaxies around which to search for the signal. We follow Kauffmann et al. (2013), who selected in SDSS a volume-limited sample of galaxies with $\log(M_*/\mathrm{M}_\odot) > 9.25$ and $0.017 < z < 0.03$. They then defined "central" galaxies of stellar mass M_* as those in their sample with no other galaxies with stellar mass greater than $M_*/2$ within a projected radius of 500 kpc and with a velocity difference

less than 500 km s^{-1}. Any galaxy in our full sample (defined above) is considered an isolated primary (IP) if there are no other galaxies (i) within a projected physical distance of 500 kpc from the IP candidate, (ii) within $\pm 2.0\sigma_z(1+z_{\rm IP})$ in redshift space from the IP candidate (this includes as many true neighbors as possible while simultaneously minimizing interlopers and integrates over peculiar velocities), and (iii) with stellar mass greater than half the stellar mass of the IP candidate. Additionally, IPs can be neighbors (see §2.3.1) of other IPs, and all galaxies can be a neighbor of multiple IPs.

It is possible for galaxies near the edge of the survey area to be incorrectly classified as isolated if they have a sufficiently massive neighbor within a projected physical distance of 500 kpc that lies outside the survey area. This could lead to contamination of our IP samples. To test for this potential effect we visually inspected the distribution of IPs near the survey edges and concluded that false detections near edges do not significantly impact our IP sample, in that the spatial density of IPs does not rise substantially at the survey edges.

Stellar Mass Completeness Limits

Because PRIMUS is a flux-limited survey targeted in the *i* band, galaxies with higher SFRs (i.e. bluer galaxies) can be more easily detected at lower stellar mass than galaxies with lower SFR (i.e. redder galaxies). This introduces a bias towards star-forming galaxies in the PRIMUS sample at lower stellar masses. To account for this bias we define a stellar mass limit above which at least 95% of all galaxies can be detected, regardless of SFR. This stellar mass completeness limit is a function of redshift, galaxy type (star-forming or quiescent), and also varies slightly between fields (due to the different photometry used for targeting in each field). Details of the calculation of PRIMUS mass completeness limits can be found in Moustakas et al. (2013). Briefly, we compute the stellar mass each galaxy would have if its apparent magnitude were equal to the survey magnitude limit, $M_{\rm lim}$. We then construct the cumulative distribution of $M_{\rm lim}$ for the 15% faintest galaxies in redshift bins of width $\Delta z = 0.04$, and calculate the minimum

Table 2.1: Stellar mass completeness limits for star-forming and quiescent galaxies as a function of redshift. At least 95% of all galaxies above these stellar mass limits can be detected regardless of SFR.

	CDFS	COSMOS	ES1	XMM-CFHTLS	XMM-SXDS
Redshift Range			$\log(M_*/\mathrm{M}_\odot)$		
			Star-forming		
$0.20-0.30$	9.60	8.68	9.58	8.80	8.79
$0.30-0.40$	9.92	9.05	9.94	9.06	9.13
$0.40-0.50$	10.19	9.38	10.25	9.30	9.44
$0.50-0.65$	10.44	9.75	10.59	9.58	9.77
$0.65-0.80$	10.63	10.12	10.90	9.89	10.10
$0.80-1.00$	10.69	10.46	11.14	10.21	10.38
			Quiescent		
$0.20-0.30$	9.65	9.23	9.80	9.17	9.35
$0.30-0.40$	9.92	9.58	10.06	9.52	9.61
$0.40-0.50$	10.17	9.89	10.30	9.85	9.85
$0.50-0.65$	10.44	10.22	10.55	10.22	10.13
$0.65-0.80$	10.71	10.52	10.79	10.60	10.43
$0.80-1.00$	10.96	10.75	10.99	10.96	10.73

stellar mass that includes 95% of the objects. The limiting stellar mass versus redshift is fit with a separate quadratic polynomial for all, star-forming, and quiescent galaxies, and the fit is evaluated at the center of each redshift interval (see Moustakas et al., 2013).

In addition to the isolation criteria described above, all IPs must have stellar masses above the stellar mass completeness threshold specific to the IP's field, redshift, and type (star-forming or quiescent; see Table 2.1). When identifying IPs, for each field and each redshift range in Table 2.1 we eliminated any star-forming (quiescent) galaxy with stellar mass below the limiting value for star-forming (quiescent) galaxies in that field and redshift range.

Of the $60,071$ galaxies in the full sample, $14,888$ star-forming and $6,847$ quiescent galaxies meet the isolation and stellar mass completeness criteria to be IPs.

Matching Stellar Mass and Redshift

While our star-forming and quiescent IP populations are statistically complete (after applying the targeting and completeness weights), even above the stellar mass completeness limits the median stellar masses and redshifts of the two populations differ, as the stellar mass functions of star-forming and quiescent galaxies are different.

Figure 2.3 shows the redshift distributions of all star-forming (solid blue line) and quiescent (dashed red line) IPs, and the star-forming fraction of all PRIMUS galaxies in the full sample as a function of redshift. Our star-forming and quiescent IP populations have median stellar masses of $\log(M_*/\mathrm{M}_\odot) = 10.44$ and 10.86, respectively, and median redshifts of $z = 0.55$ and 0.60.

Several recent studies (as well as this work) caution that systematic errors can in some cases create an artificial conformity signal. For example, Campbell et al. (2015) found that while

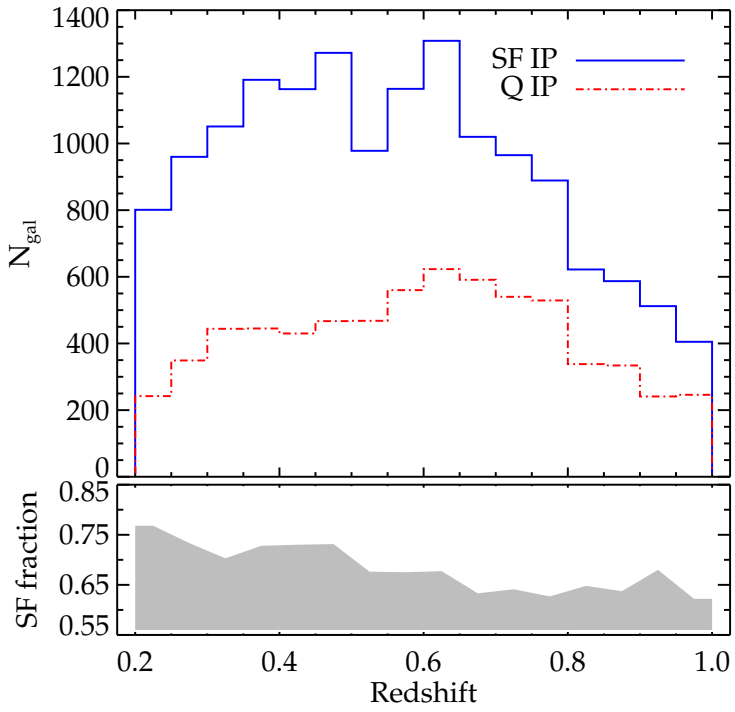

Figure 2.3: Top panel: Redshift histograms of all star-forming (solid blue line) and quiescent (dash-dot red line) IPs. Bottom panel: Star-forming fraction of all PRIMUS galaxies in the full sample as a function of redshift.

Table 2.2: Upper stellar mass limit for galaxies in the matched IP sample.

Redshift Range	$\log(M_{\rm max}/{\rm M}_\odot)$
$0.20-0.30$	11.154
$0.30-0.40$	11.208
$0.40-0.50$	11.255
$0.50-0.65$	11.241
$0.65-0.80$	11.308
$0.80-1.00$	11.324

group-finding algorithms do a good job of recovering one-halo galactic conformity in mock catalogs, they also have a tendency to introduce a weak conformity signal when none is present.

As discussed below, to compare the star-forming fraction of neighbors around star-forming and quiescent IP galaxies we require the star-forming and quiescent IP samples to have the same stellar mass and redshift distributions. To obtain these "matched" IP samples we first apply to our IP samples an *upper* stellar mass cut derived from the PRIMUS stellar mass function (SMF, denoted by Φ; see Moustakas et al., 2013) for star-forming galaxies. This upper cut is required as there are fewer star-forming galaxies at high stellar mass ($\log(M_*/{\rm M}_\odot) > 11$) than quiescent galaxies. Therefore the high-mass end of the star-forming galaxy SMF defines the upper stellar mass limit of our matched IP samples. Specifically, we eliminate all IPs (both star-forming and quiescent) with stellar masses greater than the stellar mass at which $\log(\Phi \,/\, 10^{-4}\,{\rm Mpc}^{-3}\,{\rm dex}^{-1}) \leq -3.7$, interpolated at the redshift of each galaxy. These upper mass limits are listed in Table 2.2.

We then create a two-dimensional histogram of the stellar mass and redshift distribution of the remaining quiescent IP population, in bins of 0.2 dex in stellar mass and 0.05 in redshift. For each of our five fields, in each bin we randomly select with replacement the same number of star-forming as there are quiescent IPs. This selection is done separately in each field to account for field-to-field variations in the stellar mass and redshift distributions of the IP populations. Our final matched IP sample (hereafter "matched sample") contains 6,197 unique quiescent and 4,185

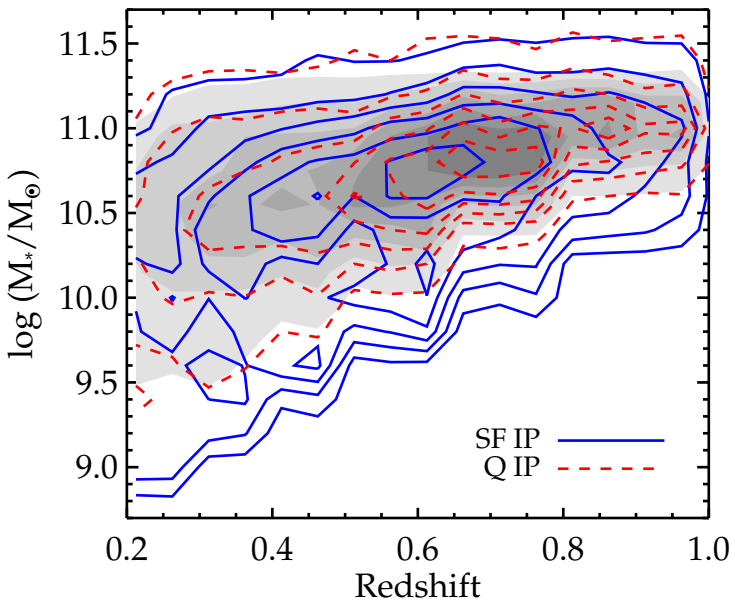

Figure 2.4: Stellar mass and redshift distribution for all star-forming (blue solid contours) and quiescent (red dashed contours) IPs in the full sample. Gray shaded contours show the matched sample, in which star-forming and quiescent IPs have the same stellar mass and redshift distributions.

unique star-forming IPs. Each star-forming IP is assigned a weight equal to the number of times it was randomly selected while matching the distribution of the quiescent IP sample. The sum of all star-forming IP weights therefore equals the total number of unique quiescent IPs. Figure 2.4 shows the stellar mass and redshift distributions of all star-forming and quiescent IPs in the full sample, as well as the stellar mass and redshift distributions of the matched sample.

2.3 Results

In this section we discuss the importance of matching star-forming and quiescent IP samples in both stellar mass and redshift, and we present the one- and two-halo conformity signal in the matched PRIMUS sample. We discuss the effects of cosmic variance on measures of conformity and the need for jackknife errors at intermediate redshifts, and we investigate the redshift and stellar mass dependence of conformity within the PRIMUS sample.

2.3.1 Effects of Matching Redshift and Stellar Mass on the Conformity Signal

As discussed above, galactic conformity is the observed tendency of neighbor galaxies to have the same star-formation type (star-forming or quiescent) as their associated IP galaxy. One-halo conformity refers to conformity between an IP and the neighbors within the same dark matter halo (i.e. within ~ 0.5 Mpc of the IP), while two-halo conformity refers to conformity between an IP and neighbors in other adjacent halos (i.e. at distances greater than ~ 0.5 Mpc from the IP).

We therefore want to measure how the fraction of neighbors that are star-forming differs between star-forming and quiescent IP hosts as a function of projected radius from the IP. To do this, for each IP in our matched sample we count all neighbors within concentric cylindrical shells of length $2 \times 2\sigma_z(1+z_{\rm IP})$ and cross-sectional area $\pi[(R_{\rm proj}+dR_{\rm proj})^2 - R_{\rm proj}^2]$, where $R_{\rm proj}$ is the 2D projected radius from the IP in (physical) Mpc, and $dR_{\rm proj}$ is the shell width in Mpc. The star-forming fraction of neighbors of star-forming IPs in a cylindrical shell at projected radius $R_{\rm proj}$ to $(R_{\rm proj}+dR_{\rm proj})$, $f_{\rm SF}^{\text{SF-IP}}(R_{\rm proj})$ is defined to be the sum of the targeting weights (see §2.2.2) of the star-forming neighbors of star-forming IPs in the shell, divided by the sum of the targeting weights of *all* neighbors of star-forming IPs in the shell:

$$f_{\rm SF}^{\text{SF-IP}}(R_{\rm proj}) = \frac{\sum_{i=1}^{N_{\text{SF-IP}}} \sum_{j=1}^{N_{{\rm SF},i}} w_j}{\sum_{i=1}^{N_{\text{SF-IP}}} \sum_{k=1}^{N_{{\rm tot},i}} w_k}, \tag{2.2}$$

and likewise for quiescent IPs. $N_{\text{SF-IP}}$ is the total number of star-forming IPs, $N_{{\rm SF},i}$ is the number of star-forming neighbors of IP i in the shell, $N_{{\rm tot},i}$ is the total number of neighbors of IP i in the shell, and w_j and w_k are PRIMUS targeting weights of the neighbors. We are therefore essentially computing star-forming neighbor fractions for star-forming and quiescent IPs by stacking the neighbors of all IPs of each type.

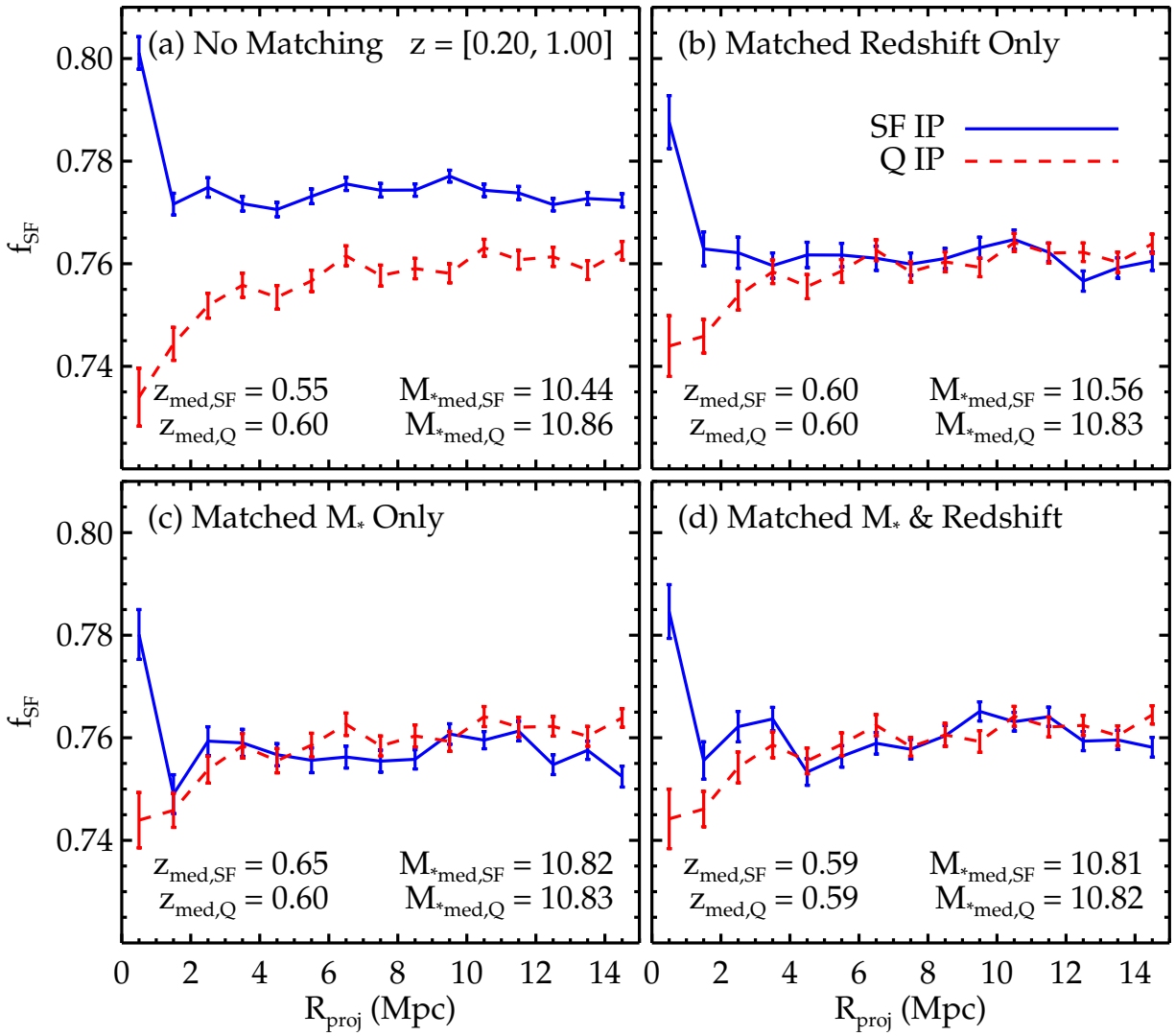

Figure 2.5: The fraction of star-forming neighbor galaxies around star-forming and quiescent IPs, to a projected distance of $R_{\rm proj} < 15$ Mpc, for four different IP samples: (a) all IP candidates above the Moustakas et al. (2013) mass completeness limit (§2.2.5); (b) IP candidates that also have the same redshift distribution for the star-forming and quiescent IPs; (c) IP candidates that have the same stellar mass distribution; (d) IPs that have both matched stellar mass and redshift distributions. The median redshift and stellar mass of each IP sample are shown in each panel. Errors are computed by bootstrap resampling as described in the text.

The importance of matching both the stellar mass and redshift distributions of our IP sample is clearly illustrated in Figure 2.5, which shows how the star-forming fractions of neighbors around star-forming and quiescent IPs differ when different IP samples are used. Figure 2.5 shows the fraction of neighbors of star-forming and quiescent IPs that are star-forming as a function of projected radius from the IP in 1 Mpc annuli out to 15 Mpc for four different IP samples.

In panel (a) all IP candidates above the Moustakas et al. (2013) mass completeness limit (§2.2.5) are included. Here the median stellar mass of the quiescent IP population is 0.42 dex greater than that of the star-forming IP population, and the median redshift is greater by 0.05. This difference in the stellar mass distribution in particular means that star-forming IPs are preferentially located at lower redshift, where the star-forming fraction of *all* PRIMUS galaxies (the "full" sample; see §2.2.2) is larger than at higher redshifts. The star-forming fraction of the full sample declines steadily from ~ 0.80 at $z \sim 0.2$ to ~ 0.73 at $z \sim 1.0$, causing us to overestimate the star-forming neighbor fraction for star-forming IPs at all projected radii. The result is a relatively fixed offset between the solid and dashed lines in the upper left panel of Figure 2.5 that persists to the largest projected radii we measure with PRIMUS, mimicking a conformity signal. We therefore measure a "false" conformity signal in this sample.

In panel (b) we select star-forming and quiescent IP samples with matched redshift distributions using the method described in §2.2.5. This eliminates the large-scale offset, but there is still a 0.3 dex difference in the median stellar masses of the IP samples. Since star-forming fraction depends on stellar mass, this is not ideal.

In panel (c) we select star-forming and quiescent IP samples with matched stellar mass distributions; this results in a star-forming IP sample with a higher median redshift than that of the quiescent IP sample (by 0.05). In this case the systematic bias mimics the opposite of a conformity signal: the solid line moves closer to the dashed line at all projected radii, actually dropping below it at $\gtrsim 5$ Mpc.

Finally, panel (d) shows results for our matched stellar mass and matched redshift IP

sample. Failing to control for differences in stellar mass and/or redshift distributions can introduce bias into the relative star-forming neighbor fractions of star-forming and quiescent IPs. Only by matching both the stellar mass and redshift distributions of our star-forming and quiescent IP samples do we eliminate systematic biases in star-forming neighbor fraction measurements that could masquerade as a conformity signal.

For the remainder of this chapter, the IP samples matched in both stellar mass and redshift are referred to as the "matched" sample.

2.3.2 One- and Two-halo Conformity Signals in the Matched Isolated Primary Galaxy Sample

Stacked star-forming neighbor fractions for the matched sample of star-forming and quiescent IPs are shown in Figure 2.6, here using finer radial bins. The errors here and above are estimated by bootstrap resampling, where for each radial bin we randomly select with replacement

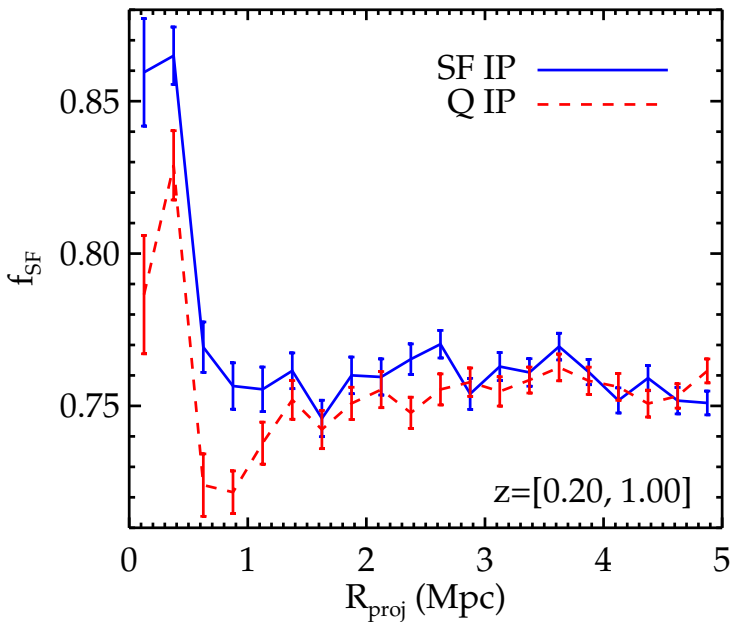

Figure 2.6: The fraction of star-forming neighbor galaxies around star-forming and quiescent IPs to a projected distance of $R_{\rm proj} < 5$ Mpc for IP samples matched in both stellar mass and redshift. Here we use finer radial bins ($dR_{\rm proj} = 0.25$ Mpc) for all star-forming (blue solid line) and quiescent (red dashed line) IPs in the matched sample. Errors are computed by bootstrap resampling.

90 percent of all star-forming or quiescent IPs 200 times, and compute $f_{\rm late}$ for each of the 200 samples. The bootstrap error is the standard deviation of the $f_{\rm late}$ distribution. Below in §2.3.3 we discuss the merits of estimating error with jackknife versus bootstrap resampling.

In Figure 2.6 the one-halo component of the conformity signal is clearly visible as the 4–7% difference between $f_{\rm late}$ for star-forming and quiescent IPs at $R_{\rm proj} < 1$ Mpc. Within this range $f_{\rm late}$ for both IP types is greatest at $R_{\rm proj} < 0.5$ Mpc: $\sim 86\%$ for star-forming and $\sim 80\%$ for quiescent IPs. At $R_{\rm proj} = 0.5$ Mpc $f_{\rm late}$ for both IP types drops sharply by at least 8% to $\sim 76\%$ for star-forming and $\sim 72\%$ for quiescent IPs.

This break at 500 kpc is an artifact of the isolation criteria used to identify isolated primaries (see §2.2.5), and the fact that the fraction of all galaxies in our full sample that are star-forming is a decreasing function of stellar mass. Because we require IP galaxies (regardless of type) to have no other galaxies more massive than half the stellar mass of the IP within 500 projected kpc, the median stellar mass of galaxies within 500 kpc will automatically be lower than the median stellar mass of galaxies beyond this distance. The star-forming fraction of neighboring galaxies within 500 kpc will therefore be greater than the star-forming fraction of neighbors within $0.5 < R_{\rm proj} < 5$ Mpc.

To confirm that this feature of Figure 2.6 is a direct result of our choice of a projected radius of 500 kpc when identifying IPs, we also measured $f_{\rm late}$ for redshift and stellar mass-matched samples of star-forming and quiescent IPs selected using 250 and 750 kpc as the projected radius for our isolation criteria. As expected, when 250 kpc is used to identify IPs, the break in $f_{\rm late}$ for both star-forming and quiescent IPs occurs at 250 kpc, and likewise for 750 kpc. Because conformity is the *difference* between $f_{\rm late}$ for star-forming and quiescent IPs and does not depend on the absolute star-forming neighbor fraction for either IP type, this break at 500 kpc does not affect our result.

Over $R_{\rm proj} \simeq 1$–1.5 Mpc $f_{\rm late}$ for quiescent IPs increases to ~ 0.75, while for star-forming IPs $f_{\rm late}$ begins to level off at ~ 0.76. This $\sim 1\%$ difference between the two fractions is a

two-halo conformity signal that persists to to roughly 3 Mpc. At $3 \lesssim R_{\rm proj} < 5$ Mpc $f_{\rm late}$ for both IP types is effectively constant and nearly equal, such that no conformity signal is present beyond $R_{\rm proj} \simeq 3$ Mpc.

Within a particular radial bin (or shell around each IP), this stacking method weights IPs with more neighbors more heavily than those with fewer or no neighbors. To assess whether this will bias our results, we recompute the star-forming neighbor fraction, now assigning equal weight to each IP by computing the star-forming fraction individually for each IP and then taking the median of the distribution of all non-zero fractions for both IP types, within each 1 Mpc radial bin. The result is shown in Figure 2.7, which also shows the mean individual star-forming neighbor fraction for both IP types in each radial bin (again using only non-zero fractions), and the interquartile range ($25^{\rm th}$ to $75^{\rm th}$ percentile) of the combined $f_{\rm late}$ distribution for both IP types.

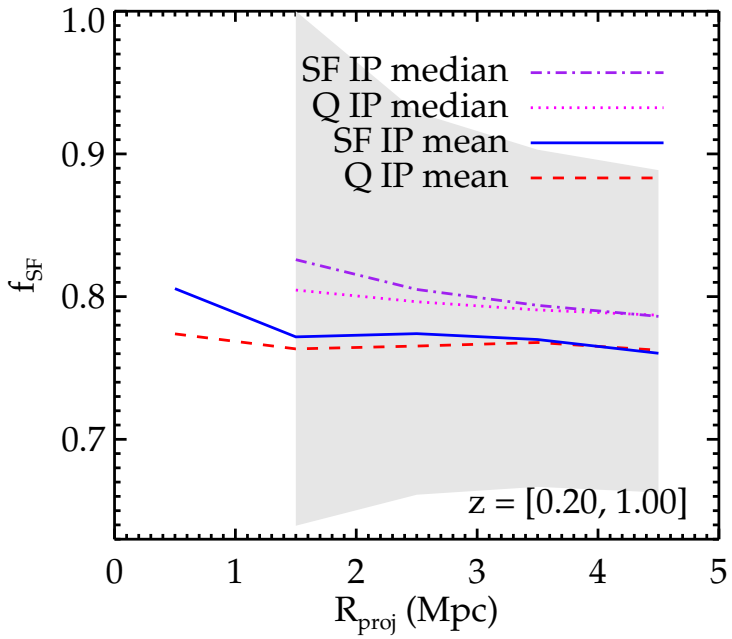

Figure 2.7: Similar to Figure 2.6, except here $f_{\rm late}$ is the median of the distribution of non-zero individual star-forming neighbor fractions for each IP type as a function of $R_{\rm proj}$. This effectively gives equal weight to each IP, instead of upweighting the IPs with more neighbors, as shown in Figure 2.6. Also shown is the mean of the non-zero star-forming neighbor fraction distributions of star-forming and quiescent IPs (purple dash-dot and magenta dotted lines), and the interquartile range of the combined distribution for both IP types (gray shaded region).

Above $R_{\rm proj} = 1$ Mpc the large spread in the interquartile range indicates that three quarters of IPs have a star-forming neighbor fraction of at least 65%, while for one quarter of IPs the star-forming fraction is over 90%. Median and interquartile range values are not shown for $R_{\rm proj} < 1$ Mpc because in that bin the median (and 75$^{\rm th}$ percentile) value of $f_{\rm late}$ for both IP types is 1.

In the $R_{\rm proj} < 1$ Mpc bin the only meaningful measure of conformity is the mean values of the $f_{\rm late}$ distributions, which vary from $\sim 81\%$ for star-forming IPs to $\sim 77\%$ for quiescent IPs. The difference between the mean values of $f_{\rm late}$ decreases on scales of 1–3 Mpc and disappears entirely on larger scales.

The difference between star-forming neighbor fractions for star-forming and quiescent IPs is comparable for equal weighting of IPs as shown here and when each IP is weighted proportionally to its number of neighbors, as shown in Figure 2.6.

We define the normalized conformity signal, $\xi_{\rm norm}$, at a projected radius of $R_{\rm proj}$ as the difference between the star-forming neighbor fractions of star-forming and quiescent IPs, divided by the mean of these two fractions:

$$\xi_{\rm norm}(R_{\rm proj}) = \frac{\left| f_{\rm SF}^{\text{SF-IP}} - f_{\rm SF}^{\text{Q-IP}} \right|}{\left(f_{\rm SF}^{\text{SF-IP}} + f_{\rm SF}^{\text{Q-IP}} \right)/2} \tag{2.3}$$

We note that the choice to define $\xi_{\rm norm}$ in terms of the star-forming instead of the quiescent neighbor fraction is arbitrary. Were we to instead define $\xi_{\rm norm}$ as the normalized difference in *quiescent* neighbor fraction $f_{\rm Q} = 1 - f_{\rm SF}$ then Equation 2.3 would be

$$\frac{\left| f_{\rm Q}^{\text{SF-IP}} - f_{\rm Q}^{\text{Q-IP}} \right|}{\left(f_{\rm Q}^{\text{SF-IP}} + f_{\rm Q}^{\text{Q-IP}} \right)/2} = \frac{\left| f_{\rm SF}^{\text{SF-IP}} - f_{\rm SF}^{\text{Q-IP}} \right|}{\left[1 - \left(f_{\rm SF}^{\text{SF-IP}} + f_{\rm SF}^{\text{Q-IP}} \right)/2 \right]}.$$

Defining a normalized conformity signal serves two important purposes. First, it enables us to clearly demonstrate the significant effects that cosmic variance can have on conformity

Table 2.3: Normalized conformity signal $\xi_{\rm norm}$ for the matched sample in two redshift bins and in two stellar mass bins for three ranges of projected radius: $R_{\rm proj} = 0$–1, 1–3, and 3–5 Mpc. Errors shown are computed by jackknife resampling. The significance of all signals is shown for both jackknife ($\sigma_{\rm JK}$) and bootstrap $\sigma_{\rm BS}$ errors.

$N_{\rm IP}$				$0 < R_{\rm proj} < 1$ Mpc			$1 < R_{\rm proj} < 3$ Mpc			$3 < R_{\rm proj} < 5$ Mpc		
SF [a]	Q	z [b]	$\log(M_*/{\rm M}_\odot)$ [c]	$\xi_{\rm norm}$	$\sigma_{\rm JK}$	$\sigma_{\rm BS}$	$\xi_{\rm norm}$	$\sigma_{\rm JK}$	$\sigma_{\rm BS}$	$\xi_{\rm norm}$	$\sigma_{\rm JK}$	$\sigma_{\rm BS}$
Matched Sample												
4,185	6,197	0.2–1.0	9.1–11.3	0.053 (0.015)	3.6	6.8	0.011 (0.005)	2.5	3.5	0.002 (0.005)	0.3	0.6
Redshift Bins												
2,241	3,096	0.2–0.59	9.1–11.3	0.052 (0.013)	4.0	4.9	0.010 (0.006)	1.7	2.5	−0.003 (0.005)	0.7	1.1
1,945	3,101	0.59–1.0	10.1–11.3	0.056 (0.026)	2.1	4.5	0.015 (0.009)	1.6	2.8	0.011 (0.008)	1.2	2.7
Stellar Mass Bins												
2,385	3,069	0.2–1.0	9.1–10.8	0.039 (0.013)	2.9	3.7	0.008 (0.006)	1.5	1.9	0.000 (0.005)	0.0	0.0
1,801	3,128	0.2–1.0	10.8–11.3	0.070 (0.021)	3.3	5.9	0.015 (0.005)	2.8	3.0	0.003 (0.007)	0.4	0.8

[a] Number of *unique* star-forming isolated primary galaxies, which are upweighted such that the sum of the weights equals the total number of quiescent isolated primary galaxies.
[b] Redshift range of isolated primary galaxy (sub)sample.
[c] Stellar mass range of isolated primary galaxy (sub)sample

measurements, which we show in Figures 2.8 and 2.9 and discuss below in §2.3.3 and §2.3.4. Second, it is a metric we can use to *quantitatively* compare the magnitude of the conformity signal we detect to the results of other conformity studies, as we do in §2.4 below.

Table 2.3 presents the normalized conformity signal in the matched sample in integrated radial bins of $R_{\rm proj} = 0$–1, 1–3, and 3–5 Mpc. Over the full redshift range $0.2 < z < 1.0$ we find a normalized one-halo conformity signal of 5.3% and a two-halo signal of 1.1%. We emphasize that galactic conformity is a very small effect, especially at two-halo scales, making it highly sensitive to observational uncertainty. Galactic conformity therefore cannot be accurately measured without a sufficiently large sample volume. The above measurements were made using over 60,000 galaxies in $\sim 2 \times 10^7$ comoving Mpc^3 spanning over 5 Gyr of cosmic time.

In §2.2.3 above we note that the uncertainty of our stellar mass and SFR estimates introduces an uncertainty in the star-forming fraction of the full sample of $\sim 1\%$. To test how this error affects our measurement of $\xi_{\rm norm}$ we recomputed the normalized conformity signal (Figure 2.8) for the matched sample 10 times, each time drawing individual stellar masses and SFRs for each galaxy in the full sample (instead of using the median values) from a normal distribution with a width equal to the galaxy's stellar mass or SFR error. The mean normalized one-halo conformity signal (0–1 Mpc) increased by 0.2σ and the two-halo signal (1–3 Mpc) increased by 1.4σ. This clearly indicates that the stellar mass and SFR errors are subdominant.

2.3.3 Bootstrap Versus Jackknife Errors

In Table 2.3 we estimate the uncertainty in $\xi_{\rm norm}$ using both bootstrap and jackknife resampling, and quote the significance we find using each method as $\sigma_{\rm BS}$ and $\sigma_{\rm JK}$, respectively. We compute bootstrap errors by selecting 90% of the data randomly with replacement 200 times, and then taking the standard deviation of the 200 results. To compute jackknife errors we divide the survey area of the matched sample into 10 regions of approximately 0.5 deg^2 each. We then compute $\xi_{\rm norm}$ 10 times, systematically excluding one of the 10 jackknife samples each time, and

take the standard deviation of the 10 results as the error.

Each method gives information about a different type of variation in our sample. Bootstrap resampling provides an estimate of the variation of $f_{\rm late}$ for the entire matched IP sample *as a whole*. It does not, however, take into account that our matched sample contains four spatially-distinct fields of different sizes on the sky.

Jackknife resampling estimates the uncertainty in $f_{\rm late}$ *due to field-to-field variation* (i.e. cosmic variance) within the matched sample. As seen in Table 2.3, jackknife resampling yields errors that are at least as large as bootstrap errors at all projected radii, and which usually exceed bootstrap errors by a factor of ~ 2. Cosmic variance is therefore the dominate source of uncertainty in our result.

We emphasize that any meaningful measurement of conformity at $z > 0.2$ should accurately account for cosmic variance by using multiple spatially-distinct fields and jackknife errors. Bootstrap resampling is sufficient to estimate the uncertainty of a conformity signal *within a*

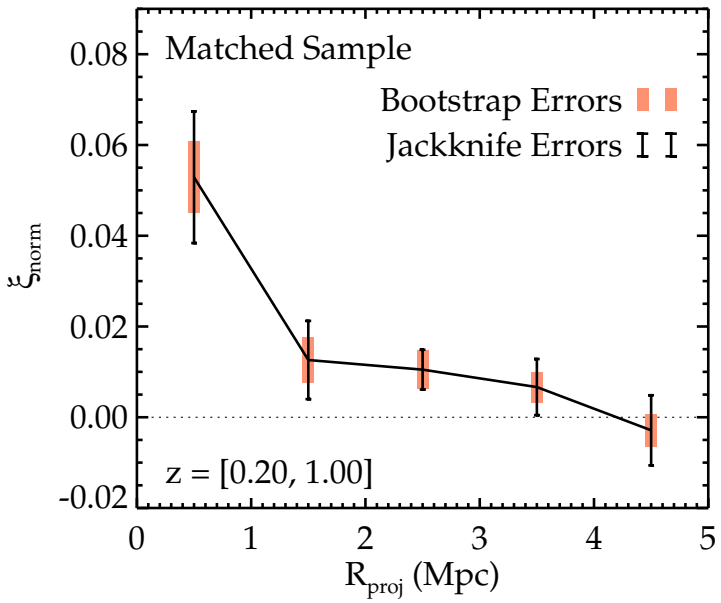

Figure 2.8: Normalized conformity signal, $\xi_{\rm norm}$, for the matched sample to $R_{\rm proj} < 5$ Mpc. Both bootstrap (orange) and jackknife errors (black) are shown. The jackknife errors exceed the bootstrap errors by up to a factor of ~ 2.

single field, but the result obtained with any one field cannot realistically be extrapolated to draw conclusions about conformity on larger scales (see also §2.3.4).

Figure 2.8 shows $\xi_{\rm norm}$ for the matched sample in $dR_{\rm proj} = 1$ Mpc bins with both jackknife and bootstrap errors. In the matched sample we find that for $0 < R_{\rm proj} < 1$ Mpc the bootstrap error of $\xi_{\rm norm}$ is ± 0.008, which yields a significance of $\sigma_{\rm BS} = 6.8$, while the jackknife error is ± 0.015, with a significance of $\sigma_{\rm JK} = 3.6$.

The above result uses all star-forming and quiescent IPs in the matched sample, regardless of specific SFR (sSFR). To test whether the conformity signal is sensitive to the magnitude of the difference in sSFR between star-forming and quiescent IPs, we also measure one- and two-halo conformity with only the extreme high and low ends of the IP sSFR distribution. Specifically, we compute $\xi_{\rm norm}$ for the highest and lowest quartiles of IP sSFR (also matched in stellar mass and redshift distribution).

One-halo conformity over the full redshift range increases slightly to 5.5%, while the uncertainty decreases to 1.2%. This increases $\sigma_{\rm JK}$ to 4.7, even though the sample is half the size of the matched IP sample. Two-halo conformity increases slightly to 1.5%, but the uncertainty also increases to 0.9%, which decreases $\sigma_{\rm JK}$ to 1.7.

2.3.4 Variance Among Different Fields

Errors estimated with jackknife resampling account for variation in the magnitude of the conformity signal among spatially-distinct regions of the sky. The fact that $\sigma_{\rm JK}$ is significantly less than $\sigma_{\rm BS}$ for every conformity signal measurement in Table 2.3 illustrates the importance of accounting for cosmic variance in any conformity measurement.

We further investigate how the conformity signal in PRIMUS is sensitive to cosmic variance by measuring one- and two-halo conformity in each field individually. The results are shown in Table 2.4 and Figure 2.9. The errors on the individual field measurements in Figure 2.9 are computed by bootstrap resampling within the field, and represent the uncertainty of the

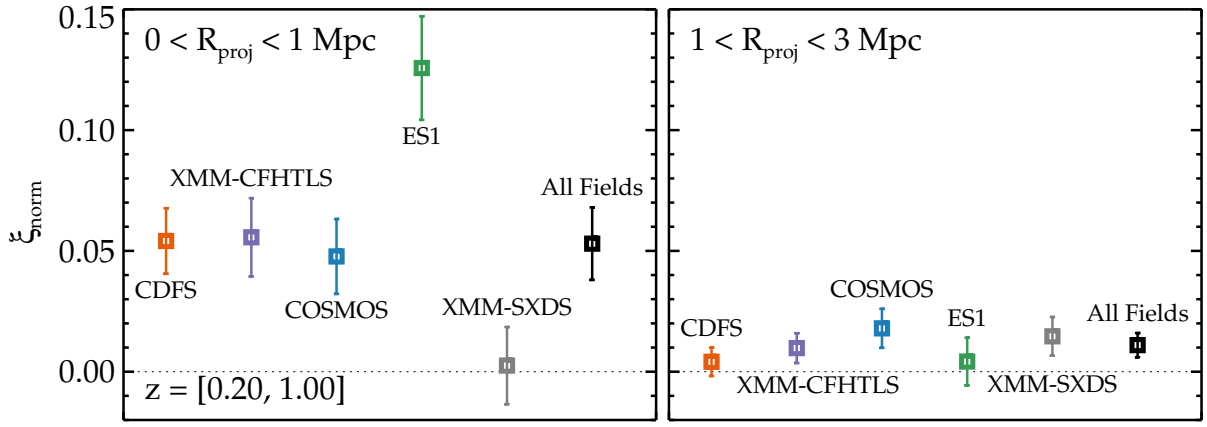

Figure 2.9: One-halo ($R_{\rm proj} < 1$ Mpc, left) and two-halo ($1 < R_{\rm proj} < 3$ Mpc, right) conformity signals for each field and for the matched sample ("All Fields"). Individual field errors are estimated by bootstrap resampling within the field and the matched sample error is estimated by jackknife resampling.

conformity signal *in that field*. The error on the signal measured over all five fields is computed by jackknife resampling from all fields, and represents the uncertainty of the conformity signal due to variation *among* different fields.

The field-to-field variation within PRIMUS is substantial. Among the five fields in the matched sample the one-halo conformity signal varies from over 12% with $\sigma_{\rm BS} = 5.9$ in ES1, to $\sim 5\%$ in CDFS, COSMOS, and XMM-CFHTLS, to 0% with $\sigma_{\rm BS} \simeq 0$ in XMM-SXDS. The two-halo signal has similar field-fo-field variation relative to its smaller overall magnitude of $\sim 1\%$. This variation clearly indicates the importance of measuring conformity in multiple fields. A large dispersion exists in the strength of conformity among PRIMUS fields, and the signal in any one field can differ significantly from the mean.

2.3.5 Redshift and Stellar Mass Dependence

Hearin et al. (2016) predicts that conformity strength (specifically two-halo) should decrease with both increasing central galaxy halo mass and increasing redshift, weakening significantly by $z \sim 1$ and disappearing entirely by $z \sim 2$. With PRIMUS we can test for trends in conformity signal strength with redshift to $z = 1$, and with halo mass using IP stellar

Table 2.4: Significance of the one-halo conformity signal in individual fields.

Field	$N_{\rm IP}$[a]	$N_{\rm IP(SF)}$[b]	$N_{\rm IP(Q)}$	$\sigma_{\rm BS}$[c]
CDFS	2,837	1,139	1,698	4.0
COSMOS	1,830	731	1,099	3.1
ES1	1,011	390	621	5.9
XMM-CFHTLS	3,222	1,325	1,897	3.4
XMM-SXDS	1,482	600	882	0.2
Satched Sample[c]	10,392	4,185	6,207	3.6

[a] Total number of unique isolated primary galaxies.
[b] Number of *unique* star-forming isolated primary galaxies.
[c] The significance of the Matched Sample is computed via jackknife resampling.

mass as a proxy for halo mass. We further divide the matched sample into two redshift bins and two stellar mass bins to investigate the dependence in the magnitude of the signal on redshift or stellar mass. In Figure 2.10 we divide the matched IP sample into two redshift bins, $0.2 < z < 0.59$ and $0.59 < z < 1$, and two stellar mass bins, $9.13 < \log(M_*/\mathrm{M}_\odot) < 10.82$ and $10.82 < \log(M_*/\mathrm{M}_\odot) < 11.33$, each containing equal numbers of IPs. The upper panels show $f_{\rm late}$ for star-forming and quiescent IPs in each redshift or stellar mass bin, while the lower panels plot the corresponding values of $\xi_{\rm norm}$ for each radial bin. The normalized signal and significance are given in Table 2.3.

When dividing into redshift bins the one-halo conformity signal in both bins is comparable to the 5.3% signal observed over the full redshift range. The significance of the "low" redshift ($0.2 < z < 0.59$) one-halo conformity signal increases to $\sigma_{\rm JK} = 4.0$, while the significance of the "high" redshift one-halo conformity signal drops to $\sigma_{\rm JK} = 2.1$. The magnitude of the two-halo conformity signal in each bin also remains comparable to the full redshift range signal of 1.1%, but the uncertainty in each bin also increases, reducing $\sigma_{\rm JK}$ from 2.5 for the full redshift range to 1.7 and 1.6 for the low and high redshift bins, respectively.

Dividing the matched sample into two stellar mass bins containing equal numbers of IPs, we find a significant one-halo conformity signal in both stellar mass bins: $\sim 4\%$ in the lower-mass

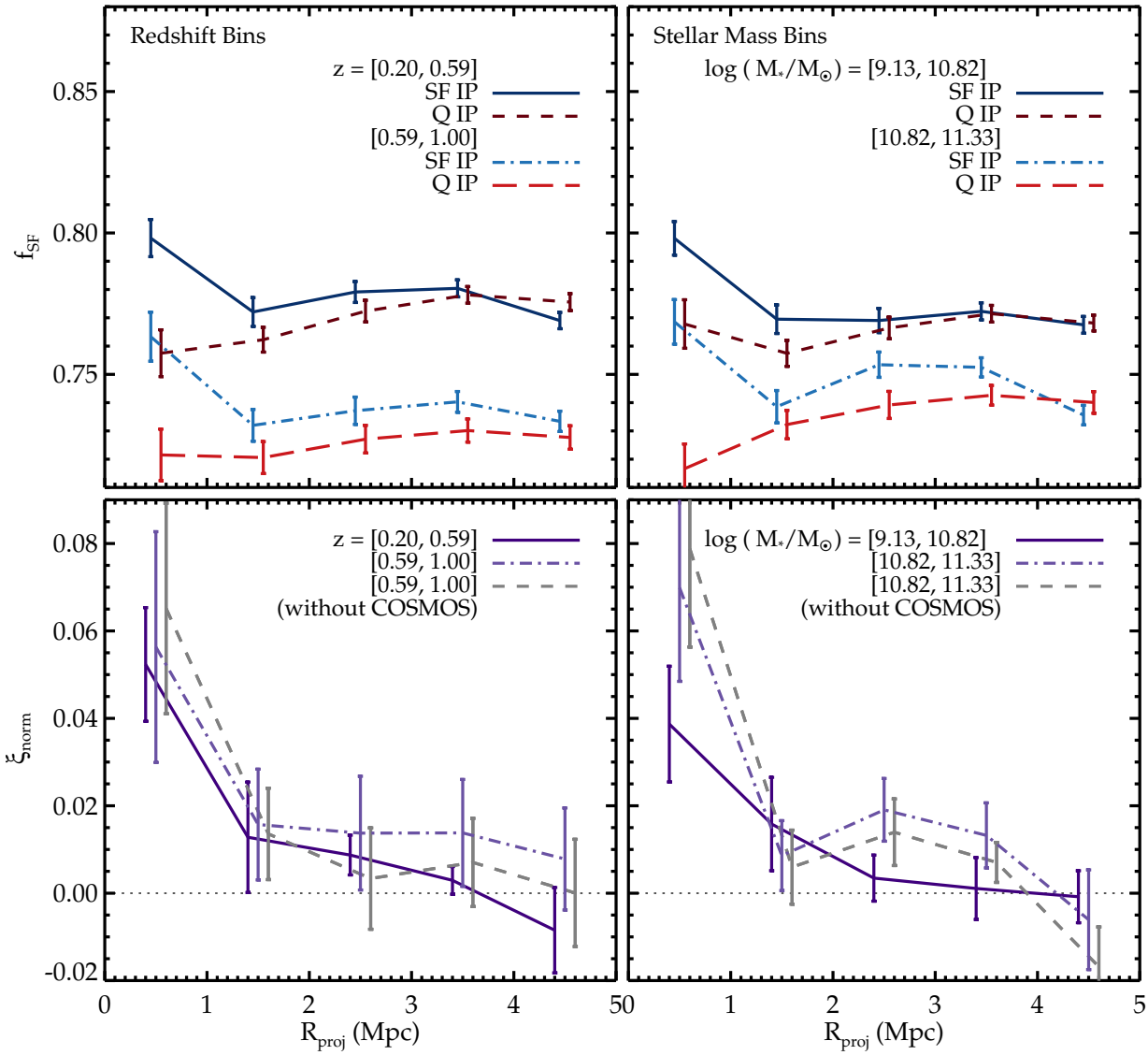

Figure 2.10: Top panels: Star-forming neighbor fractions for star-forming (solid and dash-dot blue lines) and quiescent (dashed red lines) IPs in our matched sample divided into two redshift bins (left) and two stellar mass bins (right). Errors are computed by bootstrap resampling and are offset for clarity. Bottom panels: $\xi_{\rm norm}$ for the corresponding redshift and stellar mass divisions in the top panels. Errors are computed by jackknife resampling. The bottom panels also show $\xi_{\rm norm}$ for the higher redshift bin (left) and higher stellar mass bin (right) computed *without* the COSMOS field (dashed gray line).

bin ($9.13 < \log(M_*/\mathrm{M}_\odot) < 10.82$), and $\sim 7\%$ in the higher-mass bin ($10.82 < \log(M_*/\mathrm{M}_\odot) < 11.33$). We also find that two-halo conformity is stronger at higher than at lower stellar mass, although the significance of this trend is low due to the large error of our lower-mass two-halo signal.

While ideally one would use narrower stellar mass bins to test the stellar mass dependence of the conformity signal, our sample size restricts us to a lower-mass bin width of 1.7 dex. If conformity is intrinsically stronger at lower stellar mass, averaging over too wide a range in stellar mass would dilute a strong signal contribution from lower masses.

Assuming that galaxy stellar mass is tightly coupled with host halo mass, our results appear to contradict the Hearin et al. (2016) prediction that conformity strength should decrease with increasing halo mass. However, the Hearin et al. (2016) prediction is specifically for two-halo conformity, where we do not have significant results as a function of stellar mass. Therefore, we can not test the two-halo stellar mass dependence of conformity with our sample.

The Effect of the COSMOS Field

The COSMOS field contains substantial large-scale structures at $z \sim 0.35$ and $z \sim 0.7$ (e.g. McCracken et al., 2007; Meneux et al., 2009; Kovač et al., 2010), presenting another opportunity to test the impact of field-to-field variation on our results. As Figure 2.9 and Table 2.4 show, one-halo conformity in the COSMOS field alone agrees well with the one-halo signal in the matched sample. However, we also measure two-halo conformity for each field individually, and find that it is stronger in COSMOS than in any other field. Additionally, when we divide the matched sample into two redshift and two stellar mass bins, two-halo conformity is stronger in both the higher redshift and higher stellar mass bin (see Figure 2.10 and Table 2.3).

To investigate the degree to which COSMOS contributes to the higher redshift and higher stellar mass two-halo conformity signal we recomputed ξ_{norm} for these bins using all of the matched sample *except* COSMOS. The result is shown in the lower panels of Figure 2.10 (dashed

gray lines). In both cases (higher redshift and higher stellar mass) two-halo conformity *without* COSMOS is weaker than the result for all fields. However, the results including and excluding COSMOS are each within the uncertainty of the other for both the higher stellar mass and higher redshift bins.

We conclude that the 1.5 $(\pm 0.5)\%$ two-halo conformity signal we observe at higher stellar mass ($10.8 \lesssim \log(M_*/\mathrm{M}_\odot) \lesssim 11.3$) is not dominated by a single field, but it is likely inflated by COSMOS. The two-halo signal strength trend with stellar mass we observe is *less* at odds with the prediction of Hearin et al. (2016) if the COSMOS field is excluded. However, this is not a statement about COSMOS specifically, but about the degree to which conformity measurements are sensitive to cosmic variance in general. Surveys larger than the 5.5 deg^2 of our matched sample, with comparable depth and sampling density, are required to confidently test existing predictions about the relationship between conformity strength and both redshift and mass.

2.3.6 The Relationship Between Isolated Primary Galaxy Quenching and Environment

If two-halo conformity is due to large-scale tidal fields and adjacent halos being similarly affected by larger-scale overdensities, then we would expect to observe a correlation between the quenched fraction of central galaxies and large-scale environment.

Behroozi et al. (in preparation as of this writing; hereafter PB) measure central galaxy quenched fraction versus environment for a sample of SDSS galaxies at $0.01 < z < 0.057$ with $10 < \log(M_*/\mathrm{M}_\odot) < 10.5$. Within this sample, PB define "central" galaxies as those with no larger (in stellar mass) neighbors within a projected distance of 500 kpc and 1000 km s^{-1} in redshift. PB define neighbors as galaxies of stellar mass M_{neigh} where $0 < (M_{\mathrm{central}} - M_{\mathrm{neigh}}) < 0.5$ dex, and within a projected distance of 0.3–4 Mpc and 1000 km s^{-1} in redshift from the central galaxy. These cuts reduce any correlation between environment and central galaxy stellar mass, in that the median stellar mass of the central galaxies is only very weakly, if at all, correlated with

environment. PB find that the star-forming fraction of central galaxies is negatively correlated with environment, decreasing by about a factor of two as the number of neighbors increases by an order of magnitude from ~ 10 to ~ 100. PB also find that the mean sSFR of *star-forming* central galaxies does *not* depend on environment.

We test for the same relationships in PRIMUS by comparing the star-forming fraction with environment for a subset of isolated primaries. To ensure that both our IP and neighbor samples are complete, we consider only IPs with stellar masses 0.5 dex *greater* than the completeness limits described in §2.2.5. We use the same definition of neighbors as PB, except we use $\Delta z = 2\sigma_z$ instead of PB's 1000 km s^{-1} to account for our sample's larger uncertainty in redshift. At the redshift range of our sample $2\sigma_z \approx 3000$ km s^{-1}. For accurate environment measurements our neighbor sample must be complete to 0.5 dex below the minimum IP stellar mass for a particular redshift range, field, and galaxy type. Following PB, our measure of environment is $N_{\rm neigh}$, the sum of the statistical weights (see §2.2.2) of all neighbors of an IP galaxy, which need not be an integer.

We select IP galaxies in three bins in stellar mass, each of which spans $0.2 < z < z_{\rm max}$: $\log(M_{\rm IP}/{\rm M}_\odot) = 10.1$–$10.4$ ($z_{\rm max} = 0.65$), 10.4–10.7 ($z_{\rm max} = 0.8$), and 10.7–11.0 ($z_{\rm max} = 1$). These bins are narrower than the 0.5 dex width used by PB because the PRIMUS mass completeness limits depend strongly on redshift; for $z > 0.65$ ($z > 0.8$) our neighbor sample is only complete for IP masses greater than $10^{10.4}$ ($10^{10.7}$) ${\rm M}_\odot$. Narrow bins allow us to measure the relationship between IP quenched fraction and environment over the full PRIMUS redshift range.

Figure 2.11 shows the star-forming fraction of IPs (top left), median IP stellar mass (top right), and mean sSFR for star-forming IPs (bottom left), each as a function of environment for three bins in IP stellar mass. The top right panel is a check that the IP stellar mass distribution within each bin is independent of environment: as shown, IPs with few as well as many neighbors have the same stellar mass. Similarly, the bottom left panel shows only weak correlation between the sSFR of star-forming IPs and environment, and no correlation for the lowest mass bin. This

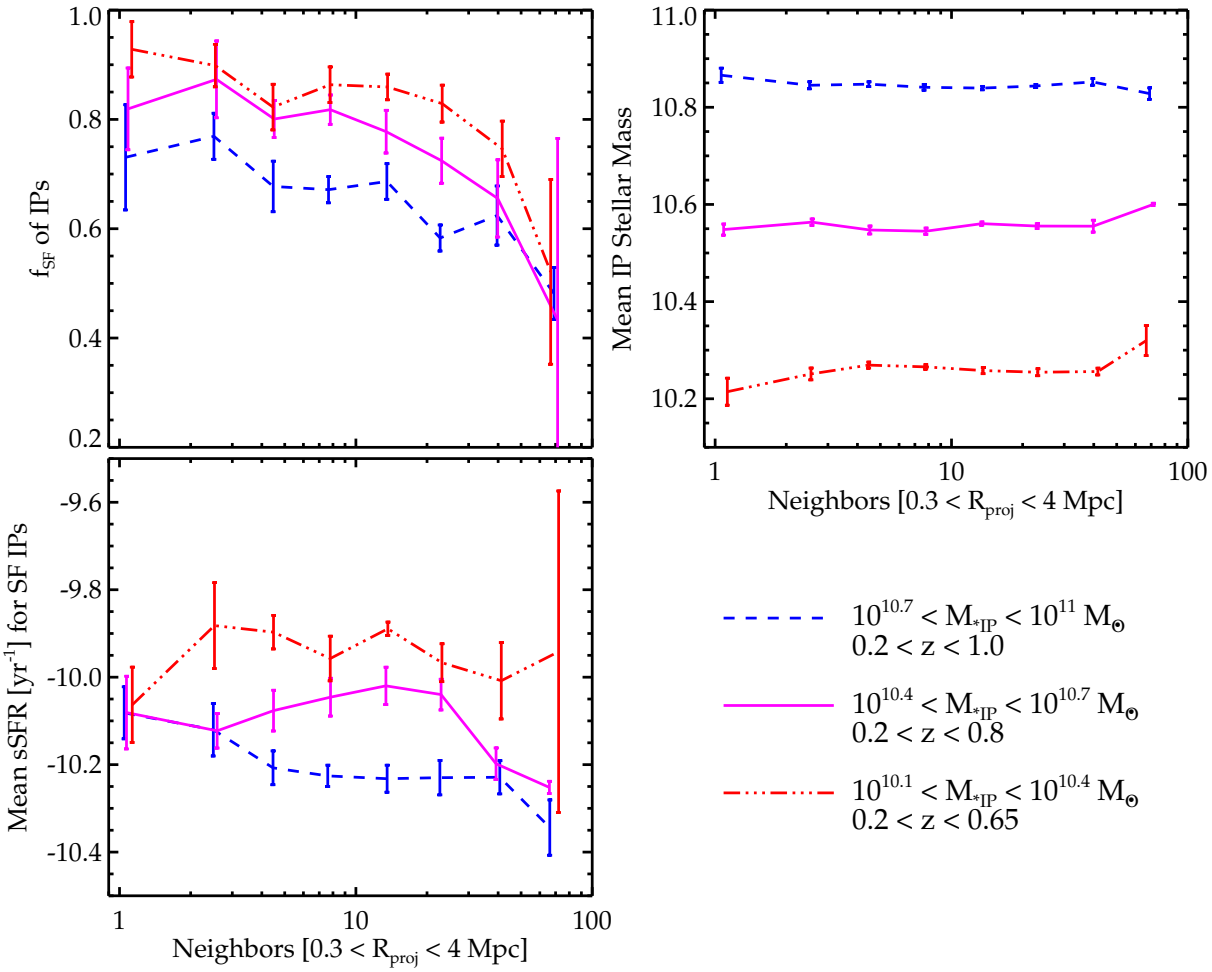

Figure 2.11: Star-forming fraction of IPs (top left), median IP stellar mass (top right), and mean sSFR of star-forming IPs (bottom left), each as a function of environment for three bins in IP stellar mass: $10.1 < \log(M_{\rm IP}/{\rm M}_\odot) < 10.4$ (dash-dot red line), $10.4 < \log(M_{\rm IP}/{\rm M}_\odot) < 10.7$ (solid magenta line), and $10.7 < \log(M_{\rm IP}/{\rm M}_\odot) < 11.0$ (dashed blue line). Neighbors are defined as galaxies of stellar mass $M_{\rm neigh}$, where $0 < (M_{\rm IP} - M_{\rm neigh}) < 0.5$ dex, within $0.3 < R_{\rm proj} < 4$ Mpc and $2\sigma_z$ in redshift space from the IP. Errors are computed by jackknife resampling.

clearly indicates that as long as a galaxy is forming stars, the sSFR is not strongly (if at all) dependent on the large-scale environment of the galaxy.

However, for all three stellar mass bins, the star-forming fraction of IPs is roughly constant for $N_{\rm neigh} \lesssim 10$, then falls off as $N_{\rm neigh}$ increases. The difference in IP star-forming fraction between IPs with $N_{\rm neigh} < 10$ and $N_{\rm neigh} > 30$ is $\sim 13\%$ (2.1σ) for $10.1 < \log(M_{\rm IP}/{\rm M}_\odot) < 10.4$, $\sim 20\%$ (3.4σ) for $10.4 < \log(M_{\rm IP}/{\rm M}_\odot) < 10.7$, and $\sim 10\%$ (1.8σ) for $10.7 < \log(M_{\rm IP}/{\rm M}_\odot) <$

11.0. The difference is statistically significant only for the middle stellar mass bin.

We can increase the signal-to-noise in this measurement by considering the decrease in IP star-forming fraction between IPs with $N_{\rm neigh} < 10$ and $N_{\rm neigh} > 30$ for wider stellar mass bins. For $10.1 < \log(M_{\rm IP}/{\rm M}_{\odot}) < 10.7$ ($z_{\rm max} = 0.65$) the IP star-forming fraction decreases by $\sim 15\%$ (4.9σ), while for $10.4 < \log(M_{\rm IP}/{\rm M}_{\odot}) < 11.0$ ($z_{\rm max} = 0.8$) we find a decrease of $\sim 11\%$ (2.9σ).

Two conclusions can be drawn from Figure 2.11. The first is that *at fixed stellar mass* central galaxies are more likely to be quenched in large-scale (~ 4 Mpc) environments. This may be a consequence of the known correlations between halo mass and greater quenched fraction, and between halo mass and large-scale environment.

The second conclusion is not due to known correlations, and it is that as long as a central galaxy in a dense environment is forming stars, it does so *as efficiently* as a star-forming central galaxy of the same stellar mass in a low-density environment.

These results are consistent with PB and indicate that the higher probability that a central galaxy is quenched when residing in a large-scale overdensity persists to $z \sim 0.5$–1. This measurement can also be made at higher significance than the usual "conformity" signal (as presented above).

To further investigate the relationship between central galaxy sSFR and environment, in Figure 2.12 we plot the mean sSFR for all IPs and for star-forming IPs only as a function of stellar mass in three bins of environment, $N_{\rm neigh} < 10$, $10 < N_{\rm neigh} < 30$, and $N_{\rm neigh} > 30$, in the mass range $10^{10.1} < M_{\rm IP} < 10^{11.0}$ M$_{\odot}$ and redshift range $0.2 < z < 0.65$.

Specific SFR is negatively correlated with IP stellar mass in all three environment bins. This trend is highly significant ($\geq 4\sigma$) both for all IPs and for star-forming IPs alone, with the exception of the $N_{\rm neigh} > 30$ bin of star-forming IPs, where $\sigma \sim 2.3$. This bin also contains the fewest galaxies, which likely contributes to the lower significance.

There is no statistical difference between the low and intermediate density bins, although this could be a result of our inability to robustly measure environment. Additionally, there

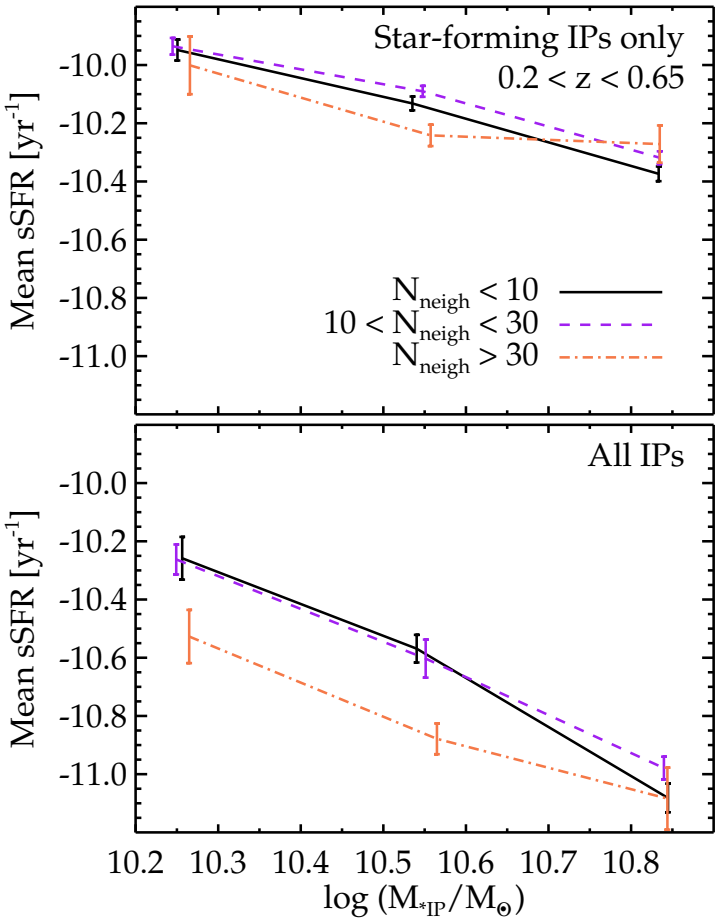

Figure 2.12: Mean sSFR for star-forming (top panel) and all (bottom panel) IP galaxies as a function of stellar mass for three bins in environment: $N_{\rm neigh} < 10$ (solid black line), $10 < N_{\rm neigh} < 30$ (dashed purple line), and $N_{\rm neigh} > 30$ (dash-dot orange line). Errors are computed by jackknife resampling.

are no statistical differences among the three environment bins for IPs of high stellar mass ($M_{\rm IP} \gtrsim 10^{10.7}$ M$_\odot$), again for both all IPs and star-forming IPs only.

Considering just the bottom panel of Figure 2.12, a statistically significant difference of $\sim$0.3 dex in sSFR does exist between low- and intermediate-mass IPs ($10^{10.1} < M_{\rm IP} < 10^{10.7}$ M$_\odot$) in very dense environments ($N_{\rm neigh} > 30$) and those with $N_{\rm neigh} < 30$. At higher stellar mass ($M_{\rm IP} \gtrsim 10^{10.7}$ M$_\odot$) and within the errors, *as long as a central galaxy is forming stars* its rate of star formation is *not* influenced by large-scale environment. However, overdense environments are clearly correlated with central galaxy quenching.

2.4 Discussion

We have presented a significant detection of both one-halo and two-halo galactic conformity at $0.2 < z < 1.0$ using the largest faint galaxy spectroscopic redshift survey completed to date. Ours is currently the only study of galactic conformity at intermediate redshift performed with spectroscopic redshifts, and is the first detection of two-halo conformity at $z > 0.2$. In this section we compare our results with existing conformity studies, both at low ($z < 0.2$) and higher ($0.2 < z < 2.5$) redshift, and discuss the physical implications of our results.

2.4.1 Comparison to Previous Low Redshift Studies

The original discovery of conformity, Weinmann et al. (2006), measured the star-forming satellite fraction for quiescent and star-forming central galaxies at fixed halo mass. Their estimates of the star-forming satellite fraction range from $\sim 20\%$ to $\sim 65\%$ for quiescent centrals, and $\sim 45\%$ to $\sim 80\%$ for star-forming centrals, depending on halo mass, central galaxy luminosity, and whether galaxy type was determined by color or by sSFR. If we apply Equation 2.3 to these star-forming fractions, the magnitude of the one-halo signal found by Weinmann et al. (2006) is $\sim 20\%$ at $M_{\rm halo} \sim 10^{12}{\rm M}_{\odot}$ (roughly corresponding to $M_* \sim 10^{10}{\rm M}_{\odot}$) compared to the 5.3% we find at higher redshift, which is qualitatively consistent with the Hearin et al. (2016) prediction that conformity strength decrease with increasing redshift.

We note that if we define the normalized conformity signal (Equation 2.3) to be in terms of quiescent neighbor fraction instead of star-forming fraction then the Weinmann et al. (2006) signal is $\sim 35\%$ at $M_{\rm halo} \sim 10^{12}{\rm M}_{\odot}$ while our signal would be $\sim 17\%$. Because the overall star-forming fraction of galaxies in our sample is $\sim 75\%$ a difference in star-forming neighbor fraction between star-forming and quiescent IPs of 5% is smaller *relative to the mean star-forming fraction* than to the mean quiescent fraction. However the fundamental result is unchanged: Weinmann et al. (2006) find a stronger conformity signal at $z < 0.2$ than the signal we find at higher redshift. We

emphasize that throughout this work the physical interpretation of our results does *not* depend on whether the normalized conformity signal is defined in terms of star-forming or quiescent neighbor fraction.

We also compare our results with those of Kauffmann et al. (2013), whose methodology for defining isolated central galaxies is used in this work. Unlike Weinmann et al. (2006) and our study, Kauffmann et al. (2013) did not measure the star-forming fraction, but instead compared the median satellite galaxy sSFR for quartiles of isolated primary (i.e. "central") galaxy sSFR at fixed stellar mass. Kauffmann et al. (2013) found a significant galactic conformity signal across the full central galaxy stellar mass range studied (5×10^9 M$_\odot$ to 3×10^{11} M$_\odot$) in a sample of SDSS galaxies with $0.017 < z < 0.03$. Our main result of $\gtrsim 3\sigma$ detections of one- and two-halo conformity at $0.2 < z < 1$ is consistent with the signal Kauffmann et al. (2013) find at lower redshift.

Kauffmann et al. (2013) also compared low-mass ($9.7 < \log(M_*/\mathrm{M}_\odot) < 10.3$) and high-mass ($10.7 < \log(M_*/\mathrm{M}_\odot) < 11.5$) samples of central galaxies and found that the scale dependence of the conformity signal depends on the central galaxy stellar mass. Specifically, Kauffmann et al. (2013) find that at low redshift two-halo conformity exists for low-mass central galaxies, while for high-mass central galaxies conformity is confined to one-halo scales.

Contrary to Kauffmann et al. (2013), within PRIMUS we do not detect significant differences in the measured conformity signal with stellar mass; however, as discussed above, the error bars on our measurements may be too large to detect such a signal. Additionally, the stellar mass ranges we study differ from those of Kauffmann et al. (2013). To keep our sample sizes large and minimize uncertainty, our low-mass bin spans 1.7 dex from $9.1 \lesssim \log(M_*/\mathrm{M}_\odot) \lesssim 10.8$, which is a much wider range than that of Kauffmann et al. (2013). Our high-mass bin ($10.8 \lesssim \log(M_*/\mathrm{M}_\odot) \lesssim 11.3$) spans only 0.5 dex, and is a subset of the high-mass bin Kauffmann et al. (2013) use.

As mentioned above, Kauffmann et al. (2013) compare quartiles of central galaxy sSFR

instead of using a binary classification of galaxies as either star-forming or quiescent, as we do here. However, as discussed in §2.3.3 above, we do not find different results within our sample if we compare quartiles in sSFR instead of using a binary galaxy type classification. Indeed, as we showed in §2.3.6, what appears to be driving the conformity signal is whether a galaxy is indeed quenched. Therefore, using quartiles in sSFR or a binary classification should yield similar results.

Kauffmann et al. (2013) find a two-halo conformity signal to a projected distance of ~ 4 Mpc, while the two-halo signal we measure disappears by ~ 3 Mpc. This is consistent with the prediction of Hearin et al. (2016) that the scale dependence of conformity (i.e. the relative signal strength at a given distance) should weaken with increasing redshift, and also supports the idea that galactic conformity is an indirect result of large-scale tidal fields. However, we note that in PRIMUS we have larger error bars than in SDSS, which could make it more difficult to detect a signal on larger scales.

2.4.2 Comparison to Previous Higher Redshift Studies

We now compare our results with the two existing studies of conformity at higher redshift, Hartley et al. (2015) and Kawinwanichakij et al. (2016).

Hartley et al. (2015) used photometric redshifts to search for one-halo conformity at $0.4 < z < 1.9$ in the 0.77 deg^2 UKIRT Infrared Deep Sky Survey (UKIDSS; Lawrence et al., 2007) Ultra Deep Survey (UDS) field, which overlaps with our XMM-SXDS field. They estimated the redshift uncertainty of their sample to be $0.014 \lesssim \sigma_z \lesssim 0.088$ and corrected for background contamination using the method described in Chen et al. (2006).

Hartley et al. (2015) defined central galaxies as those with no other galaxies within 450 projected kpc and $\sqrt{2}\sigma_z(1+z)$ that have stellar mass more than 0.3 dex (their expected uncertainty in stellar mass) greater than the mass of the central galaxy. Instead of star-forming (or quiescent/passive) *fractions* of satellite galaxies, Hartley et al. (2015) measured the radial density

profiles (number per kpc^2) of quiescent and all satellite galaxies for mass-matched samples of quiescent and star-forming central galaxies in logarithmic radial bins to a projected distance of 1 Mpc, and claim to detect one-halo conformity at $> 3\sigma$ to $z \sim 2$.

By our definition the normalized conformity signal (Equation 2.3) Hartley et al. (2015) find is an order of magnitude larger than our one-halo result. (As in §2.4.1 we note that if we define the normalized conformity signal to be in terms of quiescent neighbor fraction instead of star-forming fraction then the Hartley et al. (2015) signal exceeds 100% while our signal is $\sim 17\%$. The fundamental result that the magnitude of Hartley et al. (2015)'s one-halo signal is much larger than ours is unchanged.) This discrepancy is especially puzzling considering that the Hartley et al. (2015) field, XMM-SXDS, is the only field in which we measure *no* one-halo conformity, although our redshift range only partially overlaps with theirs. Given the large uncertainties of their photometric redshifts, interlopers likely have a significant effect on their results. For example, as Hartley et al. (2015) note, because they count and background-correct their quiescent and all satellite galaxy samples separately they in some cases obtain quiescent satellite fractions that are negative or greater than unity.

Using photometric redshifts from three surveys totaling 2.37 deg^2, UltraVISTA (McCracken et al., 2012), UKIDSS (Lawrence et al., 2007) UDS (Almaini et al., in prep.), and the FourStar Galaxy Evolution Survey (ZFOURGE; Spitler et al., 2012), Kawinwanichakij et al. (2016) tested for one-halo conformity in four redshift bins over the range $0.3 < z < 2.5$ for central galaxies with $M_* > 10^{10.5}$ M$_\odot$. They defined central galaxies as those without any more massive galaxies within a projected distance of 300 comoving kpc (ckpc). Satellite galaxies were defined as those with $M_* > 10^{10.2}$ M$_\odot$ and a redshift difference of $\Delta z \leq 0.2$ from a the central galaxy. Kawinwanichakij et al. (2016) estimated the average quiescent fraction of satellite galaxies within 300 projected ckpc for stellar mass-matched samples of quiescent and star-forming central galaxies. They did *not* match the redshift distributions of their quiescent and star-forming central galaxy samples because the difference between the mean redshifts of these two samples is comparable to

the redshift uncertainty $(0.01 \lesssim \sigma_z \lesssim 0.05)$ in each redshift interval they studied.

We can compare our results with those of Kawinwanichakij et al. (2016) at $0.3 < z < 0.6$ and $0.6 < z < 0.9$, where they claim "less significant" (1.4σ) and "strong" (4.5σ) detections, respectively. Our results broadly agree over both redshift intervals combined, but in terms of significance we find the opposite: our one-halo conformity signal has $\sigma_{\rm JK} = 4$ at $0.2 < z < 0.59$, and only $\sigma_{\rm JK} = 2.1$ at $0.59 < z < 1$.

The *magnitude* of the observed conformity effect is quite different when measured with photometric versus spectroscopic redshifts. Hartley et al. (2015) found a difference in raw quiescent fractions for quiescent and star-forming central galaxies of up to $\sim$ 50–60% in their lower redshift bin ($0.4 < z < 1.3$). In Kawinwanichakij et al. (2016) the difference is as much as $\sim 10\%$ at $0.3 < z < 0.6$ and up to $\sim 30\%$ at $0.3 < z < 0.6$. These numbers correspond to normalized conformity signals (defined by Equation 2.3) that are *at least an order of magnitude* greater than the $\sim 5\%$ one-halo conformity signal we find with spectroscopic redshifts alone. Even more puzzling is that the larger uncertainties of photometric redshifts would be expected to *dilute* a conformity signal, not enhance the effect.

Other factors could affect the measured star-forming satellite fractions of star-forming and quiescent primary galaxies, including differences in both central and satellite galaxy selection criteria, as well as how galaxies are classified as either star-forming or quiescent. In the former case, both Kawinwanichakij et al. (2016) and especially Hartley et al. (2015) use isolation criteria different from ours to select primary galaxies and their satellites; they adopt smaller projected radii, larger σ_z, and less conservative stellar mass limits on galaxies within the spatial boundary for isolation.

Hartley et al. (2015) and Kawinwanichakij et al. (2016) both used a cut in rest-frame $V - J$ versus $U - V$ color to divide their samples into star-forming and quiescent galaxies, while Bray et al. used a redshift-dependent cut in M_g versus $(u - g)$ color to divide their photometric sample. As galaxy type distributions are bimodal for a variety of parameters, the precise method

used to divide a sample should not have a strong effect on the outcome, provided the estimates of the parameters used (color, sSFR, etc.) are robust.

Bray et al. performed a complimentary study to ours using cross-correlation measurements between the PRIMUS spectroscopic and (deeper) photometric galaxy samples. Specifically, they measured the overdensities of quiescent PRIMUS photometric galaxies within a physical deprojected distance of $\sim 1\ h^{-1}$ Mpc using PRIMUS spectroscopic galaxies in three redshift bins of over $0.2 < z < 0.8$, and bins of spectroscopic galaxy stellar mass in the range $9.5 < \log(M_*/\mathrm{M}_\odot) < 12$. Unlike all previous conformity studies, Bray et al. did not utilize isolation criteria to select "isolated primary" or "central" galaxies, and therefore did not measure the same conformity statistic as in this work and other studies. However, we can qualitatively compare our one-halo results to theirs.

For spectroscopic galaxies of stellar mass comparable to our high-mass bin ($10.8 < \log(M_*/\mathrm{M}_\odot) < 12$) Bray et al. find a difference in the overdensity of quiescent galaxies only at $0.4 < z < 0.6$, while for spectroscopic galaxies of stellar mass comparable to our low-mass bin ($9.5 < \log(M_*/\mathrm{M}_\odot) < 10.8$) they find a difference in quiescent galaxy overdensity over the full redshift range they test at this mass: $0.2 < z < 0.6$. This is qualitatively consistent with our one-halo results, although the *magnitude* of the signal is much larger than our $\sim 5\%$ one-halo conformity signal.

2.4.3 The Physical Driver of Two-halo Galactic Conformity

If large-scale tidal fields are the cause of two-halo conformity it should be possible to detect a correlation between the quenched fraction of central galaxies and large-scale environment. In §2.3.6 above we look for such a correlation in a sample of IP galaxies in the stellar mass range $10.1 < \log(M_*/\mathrm{M}_\odot) < 11.0$ using the same methods as PB, and find the same trend that PB observed at low redshift in SDSS: central galaxies are more likely to be quenched in overdense environments, *independent of stellar mass*. We also detect this correlation with greater significance

than the typical measure of two-halo conformity described above in §2.3.2.

At a given stellar mass, large-scale environment evidently either *does* impact central galaxy quenching or at least correlates with something that does. While this correlation does not necessarily imply a causal connection, it is consistent with the Hearin et al. (2016) description of two-halo conformity being an indirect effect of large-scale tidal fields. As such, it is likely observational evidence of assembly bias.

Interestingly, we also find that *as long as a central galaxy is forming stars*, the efficiency of star formation does *not* depend strongly (if at all) on large-scale environment. Darvish et al. (2016) find a similar result for a mass-complete sample of galaxies in the COSMOS field at $z \lesssim 3$: the median sSFR of *star-forming* galaxies does *not* vary significantly with environment, regardless of redshift and stellar mass. However, because Darvish et al. (2016) study all galaxies (not just central galaxies) their result is dominated by satellites in overdense environments. We have shown that this result is true of just central galaxies as well.

Our result is *not* solely due to the known relation between galaxy clusters and increased quenched fraction (e.g. Cooper et al., 2007). Roughly 8% of the IPs in our sample reside in very overdense environments (i.e. they have > 30 neighbors within ~ 4 projected Mpc), *at all stellar masses* in the range we studied, and these IPs are not exclusively located in clusters; they often lie along the large-scale filaments seen in Figure 2.1, as well as in more typical cluster-type environments.

Additionally, if our result that central galaxies are preferentially quenched in overdense environments were due to cluster-specific processes the magnitude of the effect should be greater for larger halo mass (and thus also for larger central galaxy stellar mass). However, Weinmann et al. (2006) found that the one-halo conformity signal in SDSS is independent of halo mass, and the two-halo SDSS signal found by Kauffmann et al. (2013) is *stronger* at *lower* stellar mass.

2.4.4 The Importance of Large Survey Volume

As we have shown, cosmic variance dominates the uncertainty—and therefore the significance—of any conformity signal measured at intermediate to high redshift, due to the relatively small volume of sufficiently deep observational data currently available. While a conformity signal in one or two small fields may be a robust measurement *within that field*, we caution against drawing broad conclusions about any observed dependence of conformity on redshift or stellar mass from existing studies. Simply put, more data are needed, and in particular, much larger volumes need to be surveyed with spectroscopic redshifts to faint depths in order to robustly test predictions of how conformity should evolve with cosmic time.

The Baryon Oscillation Spectroscopic Survey (BOSS; Dawson et al., 2013) has obtained 1.5 million spectroscopic redshifts for luminous galaxies to $z \sim 0.7$, but the mass distribution of this sample peaks at $M_* \sim 10^{11.3}$ $M_\odot$, and the sample contains almost no galaxies with stellar masses below $10^{10.5}$ $M_\odot$ (Maraston et al., 2013).

The upcoming Dark Energy Spectroscopic Instrument (DESI; Flaugher & Bebek, 2014; Eisenstein & DESI Collaboration, 2015) survey is expected to obtain a 14,000 deg^2 nearly complete sample of 10^7 bright $(r < 19.5)$ galaxies, but only to $z \sim 0.4$. This will extend the current SDSS-type studies to $z = 0.4$, but deep, wide-area spectroscopic surveys are still needed at $z > 0.4$ to test the theoretical predictions of Hearin et al. and more accurately constrain galaxy evolution models across cosmic time.

The best current candidate for studying conformity at intermediate to high redshift is an upcoming survey with the Subaru Prime Focus Spectrograph (PFS; Takada et al., 2014). This survey will observe 16 deg^2 of color-selected galaxies and AGN at $1 < z < 2$ to a depth of $J \simeq 23.4$, obtaining a statistically complete sample of galaxies with stellar masses greater than $\sim 10^{10}$ $M_\odot$ at $z \sim 2$.

2.5 Conclusions

The existence of galactic conformity, or the observed correlation between the fraction of isolated, "central" galaxies that are quenched or have low sSFR and the fraction of neighboring "satellite" galaxies that are also quenched, indicates that there is physics beyond the standard halo model of galaxy evolution. In particular, whether a central galaxy ceases to form stars must depend on more than just the mass of the dark matter halo that that galaxy resides in.

While the existence of galactic conformity was first measured ten years ago in SDSS galaxies at $z < 0.2$, it has only very recently been measured at intermediate and high redshift. Measurements of galactic conformity at higher redshifts is a very powerful tool for constraining how halo occupation models should move beyond the standard HOD model, and in particular for constraining what the quenching mechanism behind conformity must be.

Previous measurements of conformity at $z > 0.2$ relied on photometric redshifts; however, the large uncertainties of such measurements and the possibility of contamination of isolated galaxy samples using photometric redshifts calls into question their usefulness. These studies also only probed so-called one-halo conformity, between central and satellite galaxies within a given dark matter halo. In SDSS there are clear indications that conformity exists on larger scales, between halos (i.e., two-halo conformity).

Here we have tested for one- and two-halo galactic conformity at $0.2 < z < 1$ with a 5.5 deg^2 sample of $\sim 60,000$ $M_* \gtrsim 10^{9.3}$ M$_\odot$ galaxies from PRIMUS, the largest existing spectroscopic redshift survey of faint galaxies to $z \sim 1$. Covering four spatially distinct fields, our sample allows us to probe a large cosmic volume and also account for the effect of cosmic variance on the conformity signal, which we have shown can vary substantially between fields. The primary conclusions of this work are:

1. We detect a one-halo conformity signal at 3.6σ, and a two-halo signal at 2.5σ. The amplitude of the conformity signal is very small: only 5.3% on one-halo scales and 1.1% on

two-halo scales. Given the small size of the effect, it is critical to perform robust studies that take into account various possible systematic effects, including matching galaxy samples in both redshift and stellar mass, as well as using well-defined isolation criteria to identify central galaxies.

2. That the conformity signal in PRIMUS is weaker than the signal observed in SDSS is consistent with the idea that galactic conformity is due to large-scale tidal fields, which predicts that the amplitude of the signal should decrease with increasing redshift. This result is likely observational evidence for assembly bias.

3. We observe a two-halo effect more robustly by measuring the star-forming fraction of central galaxies at fixed stellar mass as a function of large-scale environment, and find that central galaxies are more likely to be quenched in denser environments, independent of stellar mass. Interestingly, the star formation efficiency of star-forming central galaxies does *not* significantly decline in high-density environments. However, environment does either help abruptly shut off star formation, or correlate with something that does.

4. Ours is the largest area intermediate redshift conformity study to date, and the only measurement of conformity at $z > 0.2$ performed with spectroscopic redshifts. It is also the only detection of two-halo conformity at $z > 0.2$. While our detections are robust, the fact that a survey the size of PRIMUS is only large enough to detect a $\sim$1% two-halo conformity signal at the 2.5σ level illustrates the need for a next generation of deep, wide-field spectroscopic redshift surveys at $z > 0.2$ to advance our understanding of galaxy and halo evolution. Current predictions of the dependence of the strength of the conformity signal with mass and redshift to $z \sim$ 1–2 cannot be conclusively tested without spectroscopic data of comparable depth from additional fields.

Acknowledgements

We gratefully acknowledge Andrew Hearin for thoughtful feedback on a draft of this work. We also thank the CFHTLS, COSMOS, DLS, and SWIRE teams for their public data releases and/or access to early releases. This chapter includes data gathered with the 6.5-meter Magellan Telescopes located at Las Campanas Observatory, Chile. We thank the support staff at LCO for their help during our observations, and we acknowledge the use of community access through NOAO observing time. Some of the data used for this project are from the CFHTLS public data release, which includes observations obtained with MegaPrime/MegaCam, a joint project of CFHT and CEA/DAPNIA, at the Canada-France-Hawaii Telescope (CFHT) which is operated by the National Research Council (NRC) of Canada, the Institut National des Science de l'Univers of the Centre National de la Recherche Scientifique (CNRS) of France, and the University of Hawaii. This work is based in part on data products produced at TERAPIX and the Canadian Astronomy Data Centre as part of the Canada-France-Hawaii Telescope Legacy Survey, a collaborative project of NRC and CNRS.

Funding for PRIMUS has been provided by NSF grants AST-0607701, 0908246, 0908442, 0908354, and NASA grant 08-ADP08-0019. ALC acknowledges support from the NSF CAREER award AST-1055081.

Chapter 2, in full, is a reprint of material previously published in The Astrophysical Journal, 2017, Vol. 834, as "PRIMUS: One- and Two-Halo Galactic Conformity at $0.2 < z < 1$" by A. M. Berti, A. L. Coil, P. S. Behroozi, D. J. Eisenstein, A. D. Bray, R. J. Cool, and J. Moustakas. The dissertation author was the primary investigator and author of this paper.

3 Clustering of Star-forming and Quiescent Central Galaxies at $0.2 < z < 0.9$

Abstract

Previous work has demonstrated that at a given stellar mass, quiescent galaxies are more strongly clustered than star-forming galaxies. The contribution to this signal from central, as opposed to satellite, galaxies is not known, which has strong implications for galaxy evolution models. To investigate the contribution from central galaxies, here we present measurements of the clustering of isolated primary (IP) galaxies, used as a proxy for central galaxies, at $0.2 < z < 0.9$ with data from the PRIMUS galaxy redshift survey. Using a sample of spectroscopic redshifts for $\sim 60,000$ galaxies with $M_* \gtrsim 10^9$ $M_\odot$ covering 5 deg^2 on the sky, we define IP galaxies using isolation cuts in spatial proximity and stellar mass of nearby galaxies. We find that at fixed stellar mass, quiescent IP galaxies are more strongly clustered than star-forming IP galaxies at $z \sim 0.35$ (10σ). Using mock galaxy catalogs based on recent halo occupation models of Behroozi et al. (2019) and designed to replicate the parameters of the PRIMUS survey dataset, we find that these clustering differences are due in part to quiescent central galaxies being more strongly clustered than star-forming central galaxies. This is consistent with either distinct stellar-to-halo mass relations for quiescent and star-forming central galaxies, and/or central galaxy assembly bias. We additionally use mock catalogs to assess the dependence of both incompleteness and satellite galaxy contamination in the IP galaxy samples on redshift, galaxy type, and stellar mass, and demonstrate how isolation criteria yield biased subsamples of central galaxies via *environmental*

incompleteness, or the preferential exclusion of central galaxies in overdense environments.

3.1 Introduction

In the current ΛCDM paradigm, galaxies form at the centers of overdense regions where density fluctuations in the early universe have collapsed to form dark matter halos (White & Rees, 1978). The assembly of halos and their clustering properties can be modeled across cosmic time with cosmological simulations, while the clustering of galaxies is measured using large galaxy surveys. Theoretical models for how galaxies populate halos thus provide a bridge between observations of galaxy clustering and simulations of dark matters halos.

Historically, the first statistical models for the galaxy–halo connection were predicated upon the assumption that present-day halo mass determines the galaxy content of a halo (e.g. Peacock & Smith, 2000; Seljak, 2000; Berlind & Weinberg, 2002). This assumption has proven to be remarkably powerful. Subsequent refinements of these models, such as the Halo Occupation Distribution (HOD), the Conditional Luminosity Function (CLF), and abundance matching have shown that a wide variety of large-scale structure measurements are consistent with the existence of a tight scaling relation between central galaxy stellar mass (or luminosity) and host halo mass (Tinker et al., 2005; Zehavi et al., 2005; Yang et al., 2003; Coil et al., 2006; Cacciato et al., 2013; Kravtsov et al., 2004; Conroy et al., 2006; Wake et al., 2011; Reddick et al., 2013; Leauthaud et al., 2012). Moreover, in the HOD and CLF, the total number of satellite galaxies brighter than some threshold scales simply as a power law with halo mass.

In addition to the above trends based on stellar mass or luminosity, it has been known for many years that two-point clustering and weak lensing has additional, strong dependence upon broadband color (e.g. Coil et al., 2008; Zehavi et al., 2011; Mandelbaum et al., 2016, and references therein). To capture these trends, models of the HOD and CLF have been extended such that more massive dark matter halos host larger fractions of quenched (red) galaxy populations

(e.g. van den Bosch et al., 2003). This basic modeling assumption has been strikingly successful at fitting the color-dependence of two-point clustering (Zehavi et al., 2011), galaxy–galaxy lensing (Tinker et al., 2013; Zu & Mandelbaum, 2016), and a wide variety of other measurements (for a recent review see Wechsler & Tinker, 2018).

While galaxy clustering dependencies historically have been demonstrated in broad bins of luminosity, stellar mass, or color, recent work has shown that the dependence of galaxy clustering on specific star formation rate (sSFR, or SFR per unit stellar mass) remains strong when measured at *fixed* stellar mass, both at $z \sim 0.1$ (Watson et al., 2015) and at higher redshift with the PRIMUS survey (Coil et al., 2017). Additionally, weak gravitational lensing studies have found that at fixed stellar mass, red quiescent galaxies reside in more massive halos than blue star-forming galaxies (Velander et al., 2013; Rodriguez-Puebla et al., 2015; Mandelbaum et al., 2016).

As models of the relationship between galaxies and their halos continue to be refined, a natural question is whether, and to what extent, various galaxy properties depend on properties of halos besides mass. This question first arose after the discovery of so-called "halo assembly bias": at fixed halo mass, the clustering of simulated halos shows strong dependence on halo formation time (Gao et al., 2005), halo concentration, and other properties (Wechsler et al., 2006; Dalal et al., 2008; Villarreal et al., 2017; Mao et al., 2018; Salcedo et al., 2018; Johnson et al., 2018; Mansfield & Kravtsov, 2019). Thus if the true statistical connection between galaxies and halos has additional dependence on halo assembly, then the standard "halo mass only" assumption of the HOD can lead to misinterpretation of galaxy clustering measurements, a phenomenon referred to as "galaxy assembly bias" (Zentner et al., 2016; Wechsler & Tinker, 2018).

The relationship between galaxy clustering and sSFR was largely unexplored until recently (e.g. Watson et al., 2015). Coil et al. (2017) measured the dependence of galaxy clustering on sSFR at fixed stellar mass to $z \sim 1.2$ with the PRIMUS and DEEP2 spectroscopic galaxy redshift surveys, and found that at a given stellar mass quiescent (low sSFR) galaxies are more strongly clustered than star-forming (high sSFR) galaxies. They also showed that within each of the

star-forming and quiescent galaxy populations, galaxies with lower sSFR are more strongly clustered, at a given stellar mass. Their results comparing the clustering dependence on both sSFR and stellar mass imply that clustering depends as strongly on sSFR as it does on stellar mass.

It is not yet known whether the observed correlation between clustering strength and sSFR is primarily due to central or satellite galaxies, or a combination of both. The strong clustering dependence with sSFR reported in Coil et al. (2017) could, in principle, be entirely due to satellite galaxies: relative to central galaxies of the same stellar mass, satellites have a larger quiescent fraction (Wetzel et al., 2012) and reside in more massive halos (Watson & Conroy, 2013). This degeneracy highlights the potential constraining power of robust and precise measurements of *central* galaxy clustering. Resolving the sSFR dependence of galaxy clustering on central versus satellite galaxies has strong implications for halo occupation models, as it could imply that the stellar-to-halo mass relation depends on galaxy sSFR.

Here, to investigate the extent to which the correlation between clustering strength and sSFR at a given stellar mass may exist for central galaxies, we measure the relative bias (i.e. the ratio of clustering amplitudes) on two-halo scales ($1 < r_{\rm p} < 10\ h^{-1}\,{\rm Mpc}$) of quiescent and star-forming "isolated primary" (IP) galaxies at $0.2 < z < 0.9$ with data from the PRIMUS galaxy redshift survey. An IP galaxy has no other galaxies above a given stellar mass threshold within a cylindrical volume specified by a projected radius and line-of-sight distance, and are commonly used as an observational proxy for central galaxies. We also measure the clustering and relative bias of star-forming (quiescent) IP galaxies above and below the star-forming (quiescent) sequence at $0.2 < z < 0.7$ to probe whether clustering amplitude depends on sSFR for central galaxies *within* each sequence. Using PRIMUS-like mock catalogs based on UNIVERSEMACHINE (Behroozi et al., 2019), we carefully scrutinize potential biases that may be caused by (i) satellite galaxies contaminating our IP galaxy samples, and (ii) systematically incomplete sampling of the distribution of large-scale environments of true central galaxies, a phenomenon we dub

environmental incompleteness.

The structure of this chapter is as follows. In §3.2 we present details of the PRIMUS spectroscopic redshift survey data used here and summarize the properties of our PRIMUS IP galaxy samples. §3.3 presents details of our PRIMUS-like mock galaxy catalogs and the mock galaxy samples. The methods we use to measure clustering and relative galaxy bias are described in §3.4, and the results presented in §3.5. In §3.6 we quantify the completeness and contamination of our galaxy samples, and discuss the implications of these systematic sources of error on studies that utilize isolation criteria to select central galaxy samples. We summarize our main results and discuss their implications in §3.7. Throughout this chapter we assume a standard ΛCDM cosmology with $\Omega_{\rm m} = 0.3$, $\Omega_\Lambda = 0.7$, and $H_0 = 70$ km s^{-1} Mpc^{-1}.

3.2 Data and Galaxy Samples

In this section we describe the PRIMUS redshift survey data and the mock galaxy catalogs we create to compare with the clustering results from PRIMUS. We describe how we identify star-forming and quiescent galaxies and how we define isolated primary galaxies in both the PRIMUS dataset and the mock catalogs.

3.2.1 PRIMUS

The PRIsm MUlti-Object Survey (PRIMUS) is the largest spectroscopic faint galaxy redshift survey completed to date. The survey was conducted with the IMACS spectrograph (Bigelow & Dressler, 2003) on the Magellan I Baade 6.5-meter telescope at Las Campanas Observatory, using slitmasks and a low-dispersion prism. The design allowed for $\sim 2,000$ objects per slitmask to be observed simultaneously with a spectral resolution of $\lambda/\Delta\lambda \sim 40$ in a ~ 0.2 deg^2 field of view. Objects were targeted to a maximum depth of $i \geq 23$, and typically two slitmasks were observed per pointing on the sky. PRIMUS obtained robust redshifts ($Q \geq 3$; see Cool et al.,

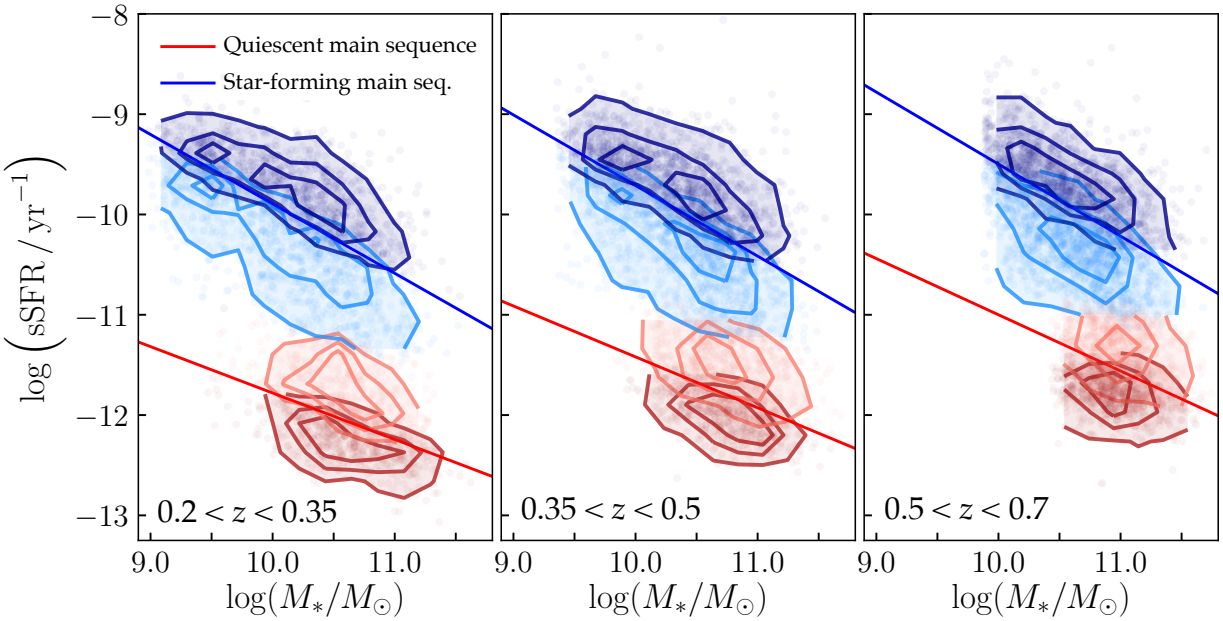

Figure 3.1: Stellar mass versus specific star formation rate (sSFR) for the four PRIMUS main sequence split IP galaxy samples (see §3.2.7) in three redshift bins: $0.2 < z < 0.35$ (left), $0.35 < z < 0.5$ (middle), and $0.5 < z < 0.7$ (right). Galaxies are divided into star-forming (blue) and quiescent (red) populations via Equation 3.1, a cut in the stellar mass-SFR plane that evolves with redshift and intersects the minimum of the bimodal galaxy distribution. Solid blue and red lines in each panel show the cuts dividing IP galaxies into samples above (SF-above; dark blue) and below (SF-below; light blue) the star-forming main sequence (Eq. 3.4) and above (Q-above; light red) and below (Q-below; dark red) the quiescent main sequence (Eq. 3.5) evaluated at the mean redshift of that panel.

2013) for $\sim 120,000$ objects at $0 < z < 1.2$ with a redshift precision of $\sigma_z/(1+z) \sim 0.005$.

The total survey area of PRIMUS is 9.1 deg^2 and encompasses seven distinct science fields. Here we use the PRIMUS fields that have deep multi-wavelength ultraviolet (UV) imaging from the Galaxy Evolution Explorer (GALEX; Martin et al., 2005), mid-infrared imaging from the Spitzer Space Telescope (Werner et al., 2004) Infrared Array Camera (IRAC; Fazio et al., 2004), and optical and near-IR imaging from various ground-based surveys. These include the Chandra Deep Field South-SWIRE field (CDFS; Lonsdale et al., 2003), the COSMOS field (Scoville et al., 2007), the European Large Area ISO Survey-South 1 field (ES1; Oliver et al., 2000), and two spatially-adjacent subfields of the XMM-Large Scale Structure Survey field (XMM-LSS; Pierre et al., 2004). The XMM subfields are the Subaru/XMM-Newton DEEP

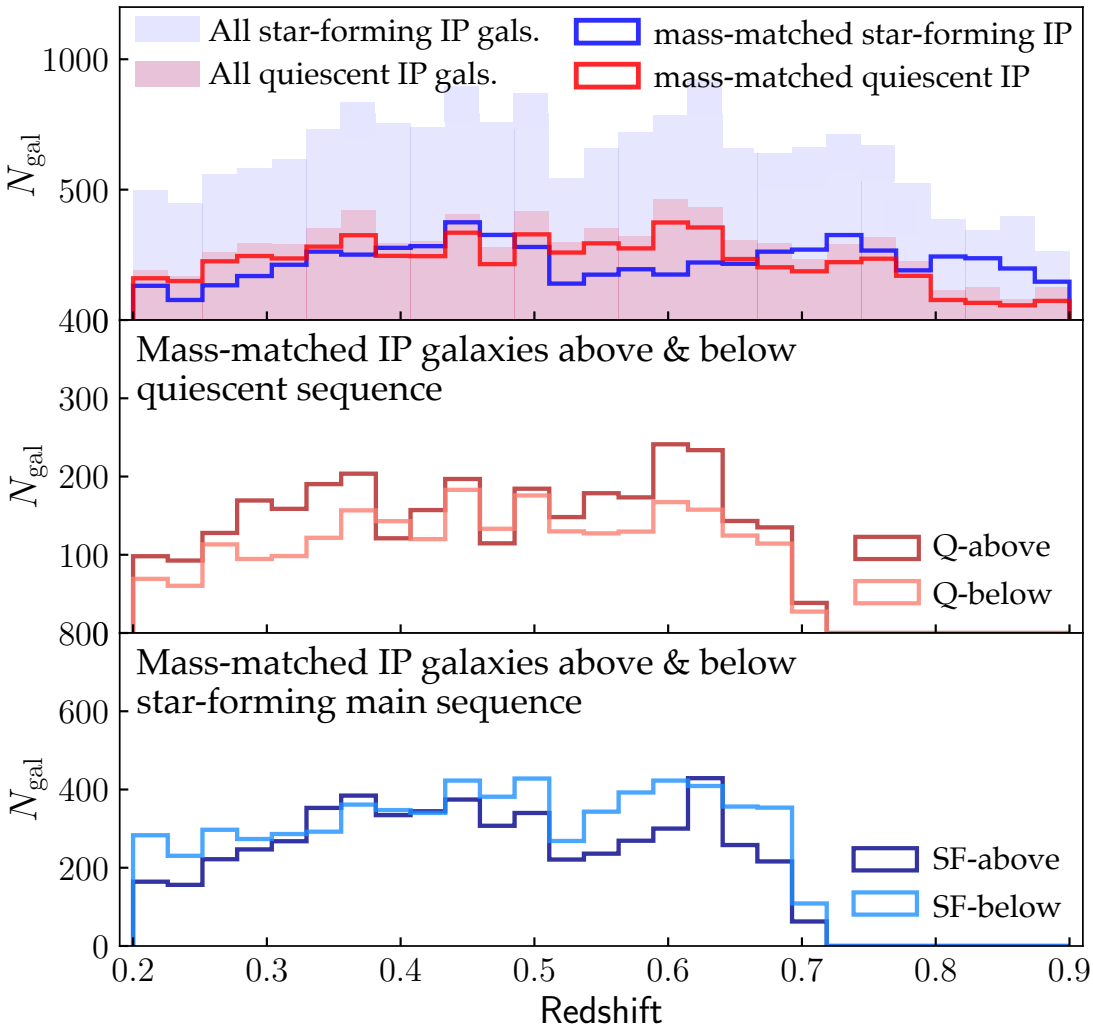

Figure 3.2: Top panel: Filled histograms show the redshift distributions of *all* quiescent (red) and star-forming (blue) PRIMUS isolated primary (IP; see §3.2.6 for details) galaxies from $0.2 < z < 0.9$. Unfilled histograms show stellar mass and redshift-matched quiescent and star-forming IP galaxy samples, each of which is a subset of the corresponding filled histogram samples. Middle panel: Stellar mass-matched quiescent PRIMUS IP galaxies divided into samples above (light red; "Q-above") and below (dark red; "Q-below") the quiescent main sequence (see §3.2.7 for details). Bottom panel: Stellar mass-matched star-forming PRIMUS IP galaxies divided into samples above (dark blue; "SF-above") and below (light blue; "SF-below") the star-forming main sequence.

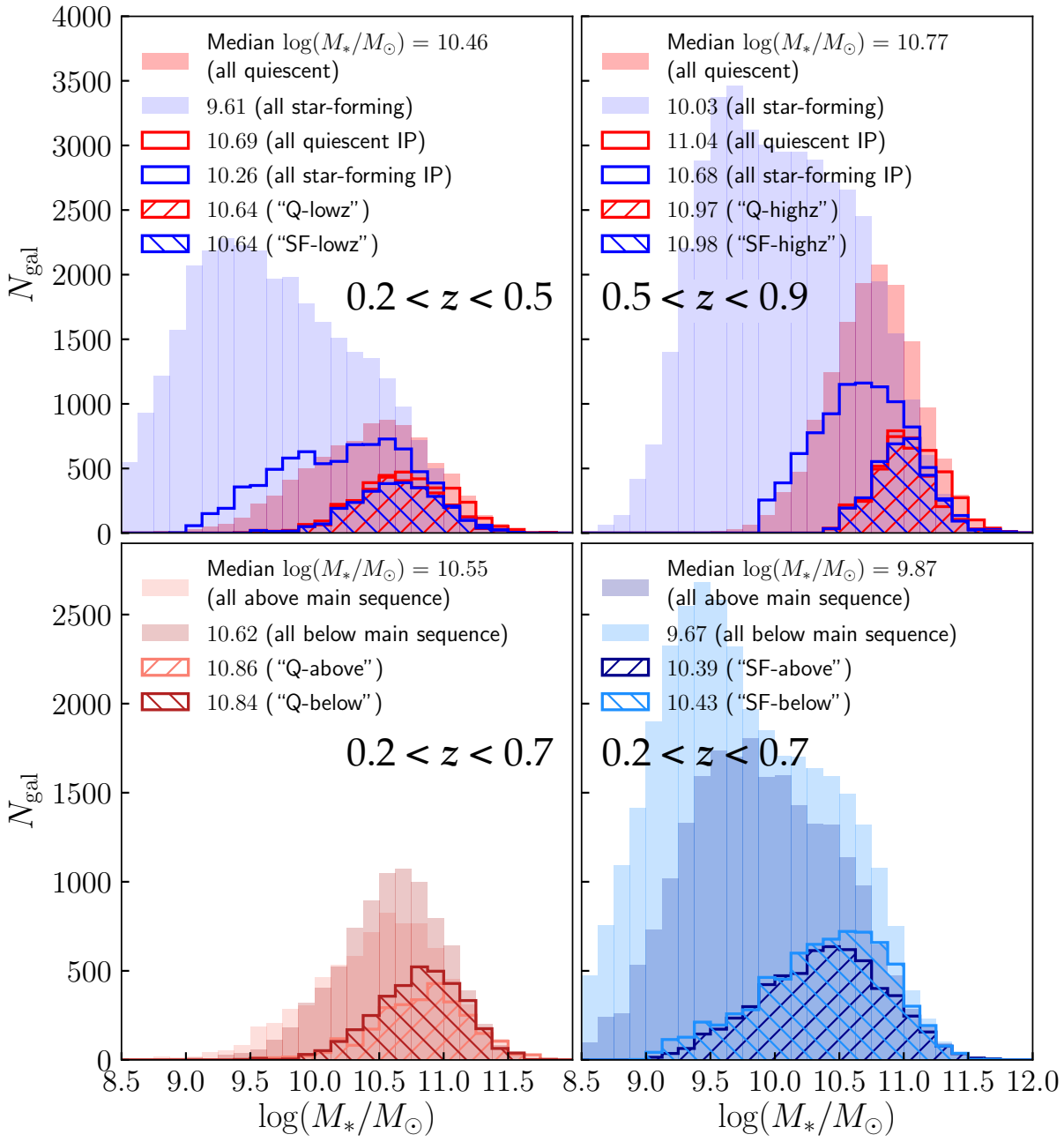

Figure 3.3: Top panels: Stellar mass distributions of all star-forming and quiescent PRIMUS galaxies (filled blue and red histograms), all IP galaxies (unfilled blue and red histograms), and stellar mass-matched distributions of star-forming and quiescent IP galaxies ("star-forming/quiescent split" samples; hatched blue and red histograms) in low ($0.2 < z < 0.5$; left) and high ($0.5 < z < 0.9$; right) redshift bins. Bottom panels: Filled histograms show the stellar mass distributions of all PRIMUS galaxies above and below the quiescent (left) and star-forming (right) main sequences at $0.2 < z < 0.7$. Hatched histograms show the stellar mass distributions of corresponding PRIMUS IP galaxy samples ("main sequence split" samples). Also shown is the median stellar mass of each galaxy sample.

Survey field (XMM-SXDS; Furusawa et al., 2008) and the Canada-France-Hawaii Telescope Legacy Survey (CFHTLS) field (XMM-CFHTLS). The data used here cover a total of ~ 5.5 deg^2 on the sky.

Full details of the survey design, targeting, and data summary can be found in Coil et al. (2011), while details of data reduction, redshift fitting, precision, and survey completeness are available in Cool et al. (2013).

3.2.2 Full Galaxy Sample and Targeting Weights

Objects in PRIMUS are classified as galaxies, stars, or broad-line AGN by fitting the low-resolution spectra and multi-wavelength photometry for each source with an empirical library of templates. The best-fit template defines both the redshift and the type of the source. We exclude AGN from this study, where the optical light is dominated by the AGN and we therefore can not determine host properties. We keep only those objects defined as galaxies with robust redshifts ($Q \geq 3$) in the redshift range $0.2 < z < 1.0$. We also only use galaxies with well-defined targeting weights (these are termed "primary" galaxies in Coil et al. (2011); we do not use that naming here, to avoid confusion with our isolated primary samples defined below in §3.2.7). These galaxies have a well-understood spatial and slitmask targeting selection function, defined by both a density-dependent weight and a magnitude-dependent sparse-sampling weight. In combination with a third, post-targeting weight that accounts for redshift incompleteness (see below) these weights allow a statistically complete galaxy sample to be recovered, which is suitable for analysis on two-point statistics, such as performed here. PRIMUS targeting weights are described in detail in Coil et al. (2011) and Cool et al. (2013). Briefly, density-dependent weights account for sources that PRIMUS could not target in dense survey regions, as galaxies are sufficiently clustered in the plane of the sky to the PRIMUS flux limit that even two slitmasks per pointing could not target every galaxy below the magnitude limit in each field (as spectra would overlap on the detector). Sparse-sampling weights are magnitude-dependent and ensure

that the PRIMUS target catalog is not dominated by the faintest objects within the survey flux limit. Sparse-sampling weights were used to randomly select roughly a third of galaxies in the faintest 0.5 mag interval above the primary sample targeting limit.

Skibba et al. (2014) measured galaxy clustering in PRIMUS and tested the recoverability of two-point statistics with the PRIMUS dataset using mock galaxy catalogs. They applied the same process used to select the PRIMUS target sample and calculate density-dependent and sparse-sampling weights to a mock catalog, and generated a weighted mock sample. Skibba et al. (2014) then compared the correlation function of all galaxies in the mock catalog to that of the weighted mock sample and found no systematic difference between the two. Thus when PRIMUS targeting weights are applied to the survey data, two-point statistics can be accurately recovered.

A third, post-targeting weight (described in detail in Cool et al., 2013) accounts for the fact that not all PRIMUS spectra yielded reliable ($Q \geq 3$) redshifts. As shown in §7 of Cool et al. (2013), the PRIMUS redshift success rate is primarily a function of *i*-band magnitude and does *not* depend strongly on galaxy color. Taken together, the three weights described above allow for the recovery of a statistically complete galaxy sample from the targeted sources with reliable redshifts.

3.2.3 Stellar Mass and Star Formation Rate Estimates

Stellar masses and star formation rates (SFRs) for PRIMUS galaxies are obtained using SED fitting, a widely-adopted method for estimating the physical properties of galaxies. A complete description of the `iSEDfit` fitting process used here can be found in Moustakas et al. (2013), and we summarize the relevant points here.

`iSEDfit` is a suite of routines written in the `IDL` programming language that uses galaxy redshifts and photometry to compute the statistical likelihood of a large ensemble of model SEDs for each galaxy. Model SEDs are generated using population synthesis models that assume a universal Chabrier (2003) initial mass function (IMF) from $0.1 - 100$ $M_{\odot}$, and span a wide range

of observed colors and physical properties (age, metallicity, star formation history, dust content, etc.). `iSEDfit` uses a Monte Carlo technique to randomly select values of model parameters from user-defined parameter distributions and compute a posterior probability distribution function (PDF). PDFs of stellar mass and SFR are found by marginalizing over all other parameters, and the median value of the marginalized PDF is taken as the best estimate of the stellar mass or SFR of each galaxy.

Berti et al. (2017) tested how the uncertainties on the stellar mass and SFR estimates described above affect the classification of galaxies as either star-forming or quiescent by randomly sampling individual stellar masses and SFRs for each galaxy in the full sample 100 times from normal distributions with widths equal to the stellar mass or SFR error for that galaxy, and found is an average change in the star-forming fraction of $< 1\%$.

3.2.4 Identifying Star-forming and Quiescent Galaxies

To divide our sample into star-forming and quiescent galaxies we use a cut in the SFR–stellar mass plane that evolves with redshift. This cut traces the minimum of the bimodal PRIMUS galaxy distribution seen in this plane, in six redshift bins from $z = 0.2$–1.0 (see Figure 2 of Berti et al., 2017), and is given by the following linear relation:

$$\log(\mathrm{SFR}) = -1.29 + 0.65\log(M_* - 10) + 1.33(z - 0.1) \tag{3.1}$$

where SFR has units of $\mathrm{M}_\odot\,\mathrm{yr}^{-1}$ and M_* has units of $\mathrm{M}_\odot$. The slope of this line is defined by the slope of the star-forming main sequence (e.g. Noeske et al., 2007) as measured in the PRIMUS dataset using `iSEDfit` SFR and stellar mass estimates. Each galaxy is classified as star-forming or quiescent based on whether it lies above or below the cut defined by Equation 3.1, evaluated at the redshift of the galaxy. Figure 3.1 shows stellar mass versus specific SFR for PRIMUS galaxies in three redshift bins between $z = 0.2$ and $z = 0.7$. Blue and red contours represent star-forming

and quiescent galaxies, respectively. The light and dark shades of red and blue are described in §3.2.7 below.

3.2.5 Stellar Mass Completeness Limits

Because PRIMUS is a flux-limited survey targeted in the *i* band, star-forming galaxies can be more easily detected at lower stellar mass than quiescent galaxies. This results in a disproportionate number of star-forming galaxies at lower stellar masses. To account for this we define a stellar mass limit above which at least 95% of all galaxies can be detected, regardless of their SFR. This stellar mass completeness limit is a function of redshift, galaxy type (star-forming or quiescent), and also varies slightly between fields (due to the different photometry used for targeting in each field). Details of the calculation of PRIMUS mass completeness limits can be found in Moustakas et al. (2013). When selecting isolated primary (IP) galaxies (see §3.2.6 below) we only consider a galaxy to be an IP candidate if its stellar mass is at least twice the mass completeness limit for that galaxy. This ensures we avoid misclassifying as isolated galaxies that *may* have one or more sufficiently massive yet undetected neighboring galaxies such that the IP candidate should not be considered isolated.

3.2.6 Isolated Primary Selection

To select isolated primary (IP) galaxies we use a method similar to that of Kauffmann et al. (2013), who selected a volume-limited sample of galaxies with $\log(M_*/\mathrm{M}_\odot) > 9.25$ and $0.017 < z < 0.03$ from SDSS. They then defined "central" galaxies of stellar mass M_* as those in their sample with no other galaxies with stellar mass greater than $M_*/2$ within a projected radius of 500 kpc and with a velocity difference less than 500 km s^{-1}.

Here we use the following selection criteria to identify IP galaxies in PRIMUS: IP *candidates* must have at least twice the stellar mass of the mass completeness limit M_{lim}

(see Moustakas et al., 2013) for their redshift and galaxy type (star-forming or quiescent): $M_* \geq M_{\rm lim}(z, \text{galaxy type}) - \log(m_{\rm frac})$ where $m_{\rm frac} = 0.5$. We then define IP *galaxies* as IP candidates with no neighbors with $M_* > m_{\rm frac} M_{\rm IP}$ within a projected distance of 500 comoving kpc (ckpc) and $\pm 2\sigma_z$ in redshift space, where σ_z is defined by the correspondence between PRIMUS redshifts and higher-resolution spectroscopic redshifts in PRIMUS fields (for details see Coil et al., 2011).

These isolation criteria are chosen because they yield IP samples that balance the competing needs of a large sample size and high completeness (the fraction of true central galaxies correctly identified as isolated), while minimizing sample contamination (the fraction of galaxies identified as isolated but which are actually satellite galaxies). Below in section §3.6 we estimate the completeness and contamination of PRIMUS IP samples as a function of redshift and stellar mass for different values of $r_{\rm p}$, $m_{\rm frac}$, and multiples of σ_z by applying the same isolation criteria to mock catalogs designed to match PRIMUS data.

It is possible for galaxies near the edge of the survey area to be incorrectly classified as isolated if in reality they have a sufficiently massive neighbor that would be within a projected distance of 500 ckpc that happens to lie outside the survey area. Berti et al. (2017) investigated the potential for this effect to contaminate IP samples in PRIMUS by visually inspecting the distribution of IPs near the survey edges. They found that the spatial density of IPs does not rise substantially near the survey edges and concluded that false detections near edges do not significantly impact IP selection.

3.2.7 Galaxy Samples

A main goal of this work is investigate the dependence of clustering amplitude on both stellar mass and sSFR for IP galaxies (which we use a proxy for central galaxies) at $z \sim 0.5$ in PRIMUS. After classifying all PRIMUS galaxies in the full sample as star-forming or quiescent as described in §3.2.4, and then selecting IP galaxies from the full sample, we next divide IP

galaxies into various samples for which we measure clustering amplitude and absolute bias on two-halo scales (see §3.4).

The "star-forming/quiescent split" run divides IP galaxies into star-forming and quiescent samples in two redshift bins to compare the clustering of star-forming versus quiescent IP galaxies at fixed stellar mass. The "main sequence split" run further divides IP galaxies within the star-forming and quiescent main sequences into samples above and below each main sequences. This allows us to test the dependence of clustering amplitude on sSFR at fixed stellar mass for IP galaxies *within* the star-forming and quiescent main sequences.

Coil et al. (2017) make similar measurements for all PRIMUS galaxies, and the IP galaxy samples we use here are analogous to their Run 1 ("star-forming/quiescent split") and Run 2 ("main sequence split") samples. Because here we are concerned with IP galaxies and the density of identifiable IP galaxies in PRIMUS decreases significantly with redshift, the maximum redshift of any of our samples is $z = 0.9$. Histograms of the redshift and stellar mass distributions of all IP galaxy samples are shown in Figures 3.2 and 3.3, respectively. Table 3.1 summarizes the properties of all galaxy samples.

Star-forming/Quiescent Split

We first define samples of star-forming and quiescent IP galaxies above the PRIMUS mass completeness limits in "low" ($0.2 < z < 0.5$) and "high" ($0.5 < z < 0.9$) redshift bins. Galaxies are classified as star-forming or quiescent by the same criteria used in Coil et al. (2017) and Berti et al. (2017): a galaxy with redshift z is star-forming (quiescent) if it lies above (below) Equation 3.1 in the stellar mass–sSFR plane.

While our star-forming and quiescent IP galaxy populations are statistically complete (after applying the targeting and completeness weights described above), and while we require IP galaxies to be above the stellar mass completeness limits of the survey, the median stellar masses and redshifts of the star-forming and quiescent IP populations differ, due to differences in the

stellar mass functions of star-forming and quiescent galaxies (see Moustakas et al., 2013).

The filled blue and red histograms in the top panel of Figure 3.2 show the redshift distributions of *all* star-forming and quiescent PRIMUS IP galaxies, respectively. The unfilled histograms show stellar mass-matched and redshift-matched star-forming and quiescent IP galaxy samples, each of which is a subset of the corresponding filled histogram.

The top panels of Figure 3.3 show the stellar mass distributions of all star-forming and quiescent PRIMUS galaxies in low ($0.2 < z < 0.5$) and high ($0.5 < z < 0.9$) redshift bins, all star-forming and quiescent IP galaxies in each redshift bin, and stellar mass-matched samples of star-forming and quiescent IP galaxies within each bin. For example, the low redshift star-forming and quiescent IP galaxy samples have median stellar masses of $10^{10.3}$ $M_{\odot}$ and $10^{10.7}$ $M_{\odot}$, respectively, while the stellar mass-matched IP galaxy samples both have a median stellar mass of $\sim 10^{10.6}$ $M_{\odot}$. We obtain stellar mass-matched IP galaxy samples by selecting all galaxies within the intersection of the stellar mass histograms of all star-forming IP galaxies and all quiescent IP galaxies. For the rest of this chapter we use the stellar mass-matched IP galaxy samples for the "star-forming/quiescent split" run (hatched histograms in the top panels of Figure 3.3 and outlined red and blue histograms in the top panel of Figure 3.2).

Main Sequence Split

To investigate the clustering amplitude dependence of IP galaxies *within* the star-forming and quiescent main sequences we divide the star-forming and quiescent IP galaxy populations in the redshift range $0.2 < z < 0.7$ each into two samples of approximately equal size and with the same median redshift (see the lower panels of Figure 3.2) and stellar mass (see the lower panels of Figure 3.3). Because here we split the IP galaxy population into four samples we use a wider redshift range than either used for the star-forming/quiescent split IP galaxy samples to maintain sufficiently large sample sizes and reduce uncertainty.

We split the star-forming IP galaxy population into "star-forming above" (SF-above) and

"star-forming below" (SF-below) samples based on whether each galaxy is above or below the redshift-dependent star-forming main sequence (Eq. 3.4; solid blue lines in Figure 3.1) evaluated at the redshift of that galaxy. The quiescent population is similarly divided into "quiescent above" (Q-above) and "quiescent below" (Q-below) based on whether each galaxy falls above or below the redshift-dependent quiescent main sequence (Eq. 3.5; solid red lines in Figure 3.1).

To identify the star-forming and quiescent main sequences as a function of redshift we first divide the star-forming and quiescent populations into redshift bins of width $\Delta z = 0.1$ from $z = 0.2$ to $z = 0.7$. Within each redshift bin we divide the star-forming and quiescent populations separately into narrow bins in stellar mass, and then find the median sSFR separately for star-forming and quiescent galaxies within each stellar mass bin. For each galaxy type (star-forming or quiescent) in each redshift bin we fit a linear relation between median sSFR and mean stellar mass:

$$\log(\mathrm{sSFR})^{\mathrm{SF}}_{\mathrm{med}} = a_0^{\mathrm{SF}}(z)\log(\mathrm{M}_\odot/M_*) + a_1^{\mathrm{SF}}(z) \tag{3.2a}$$

$$\log(\mathrm{sSFR})^{\mathrm{Q}}_{\mathrm{med}} = a_0^{\mathrm{Q}}(z)\log(\mathrm{M}_\odot/M_*) + a_1^{\mathrm{Q}}(z). \tag{3.2b}$$

To account for the redshift dependence of the coefficients $a_i^{\mathrm{SF}}(z)$ and $a_i^{\mathrm{Q}}(z)$ in Equation 3.2 (where $i = 0, 1$) we fit a second set of linear relations between the mean redshift in each bin and the fitted values of $a_i^{\mathrm{SF}}(z)$ and $a_i^{\mathrm{Q}}(z)$ at each mean redshift:

$$a_0^{\mathrm{SF}}(z) = b_0^{\mathrm{SF}} z + c_0^{\mathrm{SF}} \qquad a_1^{\mathrm{SF}}(z) = b_1^{\mathrm{SF}} z + c_1^{\mathrm{SF}} \tag{3.3a}$$

$$a_0^{\mathrm{Q}}(z) = b_0^{\mathrm{Q}} z + c_0^{\mathrm{Q}} \qquad a_1^{\mathrm{Q}}(z) = b_1^{\mathrm{Q}} z + c_1^{\mathrm{Q}} \tag{3.3b}$$

Combining Eqs. 3.2a and 3.2b with Eqs. 3.3a and 3.3b gives the final redshift-dependent equations for the star-forming and quiescent main sequences. Star-forming IP galaxies are classified as above or below the star-forming main sequence based on whether they fall above or below the

Table 3.1: PRIMUS isolated primary galaxy samples.

Run	Sample Name	$N_{\rm gal}$	Redshift			$\log(M_*/\mathrm{M}_\odot)$			$\log(\mathrm{sSFR/yr}^{-1})$		
			min	mean	max	min	mean	max	min	mean	max
Star-forming/ quiescent split	Q-lowz	2,892	0.2	0.36	0.5	9.47	10.63	11.61	-13.07	-11.86	-10.89
	SF-lowz	2,706	0.2	0.38	0.5	9.38	10.63	11.55	-11.46	-10.24	-8.06
	Q-highz	3,179	0.5	0.66	0.9	10.43	10.98	11.88	-12.68	-11.50	-10.63
	SF-highz	3,331	0.5	0.71	0.9	10.38	10.98	11.99	-11.13	-10.17	-8.49
Main sequence split	Q-below	3,106	0.2	0.47	0.7	9.47	10.79	11.75	-13.37	-11.98	-11.23
	Q-above	2,447	0.2	0.47	0.7	9.56	10.82	11.76	-12.40	-11.46	-10.83
	SF-below	6,598	0.2	0.47	0.7	8.98	10.36	11.67	-11.46	-10.28	-9.30
	SF-above	5,486	0.2	0.46	0.7	8.99	10.35	11.70	-10.82	-9.63	-7.94

following cut in the stellar mass–sSFR plane:

$$\begin{aligned}\log(\mathrm{sSFR})^{\mathrm{SF}}_{\mathrm{MS}} &= \left(b_0^{\mathrm{SF}} z + c_0^{\mathrm{SF}}\right) \log\left[\frac{M_*}{\mathrm{M}_\odot}\right] + b_1^{\mathrm{SF}} z + c_1^{\mathrm{SF}} \\ &= 2.02z - (0.08z + 0.67) \log\left[\frac{M_*}{\mathrm{M}_\odot}\right] - 3.53. \end{aligned} \tag{3.4}$$

Similarly, the cut in the stellar mass–sSFR plane that divides quiescent IP galaxies into samples above and below the quiescent main sequence is given by

$$\begin{aligned}\log(\mathrm{sSFR})^{\mathrm{Q}}_{\mathrm{MS}} &= \left(b_0^{\mathrm{Q}} z + c_0^{\mathrm{Q}}\right) \log\left[\frac{M_*}{\mathrm{M}_\odot}\right] + b_1^{\mathrm{Q}} z + c_1^{\mathrm{Q}} \\ &= 5.4z - (0.3z + 0.38) \log\left[\frac{M_*}{\mathrm{M}_\odot}\right] - 8.64. \end{aligned} \tag{3.5}$$

Figure 3.1 shows stellar mass versus sSFR for the four main sequence split IP galaxy samples (SF-above, SF-below, Q-above, Q-below) in three redshift bins: $0.2 < z < 0.35$, $0.35 < z < 0.5$, and $0.5 < z < 0.7$, and the star-forming and quiescent main sequence cuts (Eqs. 3.4 (solid blue lines) and 3.5 (solid red lines), respectively) evaluated at the mean redshift of each bin.

3.3 Mock Galaxy Catalogs

We create mock galaxy samples to help interpret our observational results. The mock galaxy catalogs we use are based on UNIVERSEMACHINE (Behroozi et al., 2019). By empirically modeling the dependence of galaxy SFR as a function of halo mass, halo accretion rate, and redshift, the UNIVERSEMACHINE makes predictions for the star formation history of galaxies across time, connecting these histories to the assembly history of dark matter halos. Predicting star formation history by modeling galaxy–halo co-evolution has a long history in the field of semi-analytic modeling (e.g., Kauffmann et al., 1993; Somerville & Primack, 1999; Benson, 2012; Somerville & Davé, 2015). Recent progress in empirically modeling galaxy formation has enabled a new generation of data-driven models to self-consistently predict galaxy assembly histories across cosmic time (Becker, 2015; Cohn, 2017; Moster et al., 2018). As shown in Behroozi et al. (2019), the UNIVERSEMACHINE model has sufficient flexibility to capture a wide range of statistics summarizing the observed galaxy distribution across redshift, including stellar mass functions, quiescent fractions, and two-point galaxy clustering.

We use the publicly available UNIVERSEMACHINE code to generate synthetic galaxies populating snapshots in the MDPL2 simulation (Klypin et al., 2016).[1] The snapshots we use are at the mean redshifts of our low and high redshift star-forming/quiescent split PRIMUS IP galaxy samples: $z = 0.35$ and $z = 0.7$, respectively.

In each snapshot, every subhalo identified by ROCKSTAR in MDPL2 is populated with a synthetic galaxy.[2] Briefly, star-formation histories of UNIVERSEMACHINE galaxies are modeled as follows. First, at each redshift, the distribution of SFRs of synthetic galaxies is modeled with a double Gaussian, one for quenched galaxies and one for star-forming galaxies. The locations and relative heights of the two SFR peaks have a parameterized dependence on both $V_{\rm max}$ (the maximum circular halo velocity) and redshift. At fixed $V_{\rm max}$ UNIVERSEMACHINE allows for

[1] In practice we use a $250 \times 250 \times 400\ h^{-1}$ Mpc cutout of MDPL2.

[2] UNIVERSEMACHINE mock catalogs include an additional treatment of orphan galaxies that reside in subhalos no longer identified by ROCKSTAR; see Appendix D of Behroozi et al. (2019) for further details.

the possibility that galaxy SFR is correlated with (sub)halo $\Delta V_{\rm max}|_{\tau_{\rm dyn}}$, the change in $V_{\rm max}$ over the last dynamical time, $\tau_{\rm dyn} \equiv \left(\frac{4}{3}\pi G \rho_{\rm vir}\right)^{-1/2}$, where $\rho_{\rm vir}$ is the virial overdensity. Conditional Abundance Matching (CAM) is used to implement the correlation between SFR and $\Delta V_{\rm max}|_{\tau_{\rm dyn}}$, while the strength of this correlation is parameterized to allow for possible dependence upon both halo mass and redshift. We then tailor these mock galaxy catalogs to mimic PRIMUS galaxy targeting with the process described in §3.3.1 below. Throughout this chapter we refer to these mock galaxy catalogs (after matching them to observed PRIMUS data) as our "standard" mocks.

Figure 3.4 shows $\omega_{\rm p}(r_{\rm p})$ separately for star-forming and quiescent PRIMUS galaxies at fixed stellar mass in low ($0.2 < z < 0.5$) and high ($0.5 < z < 0.9$) redshift bins. Also shown for comparison is $\omega_{\rm p}(r_{\rm p})$ for the corresponding mock galaxy samples from the $z = 0.35$ and $z = 0.7$

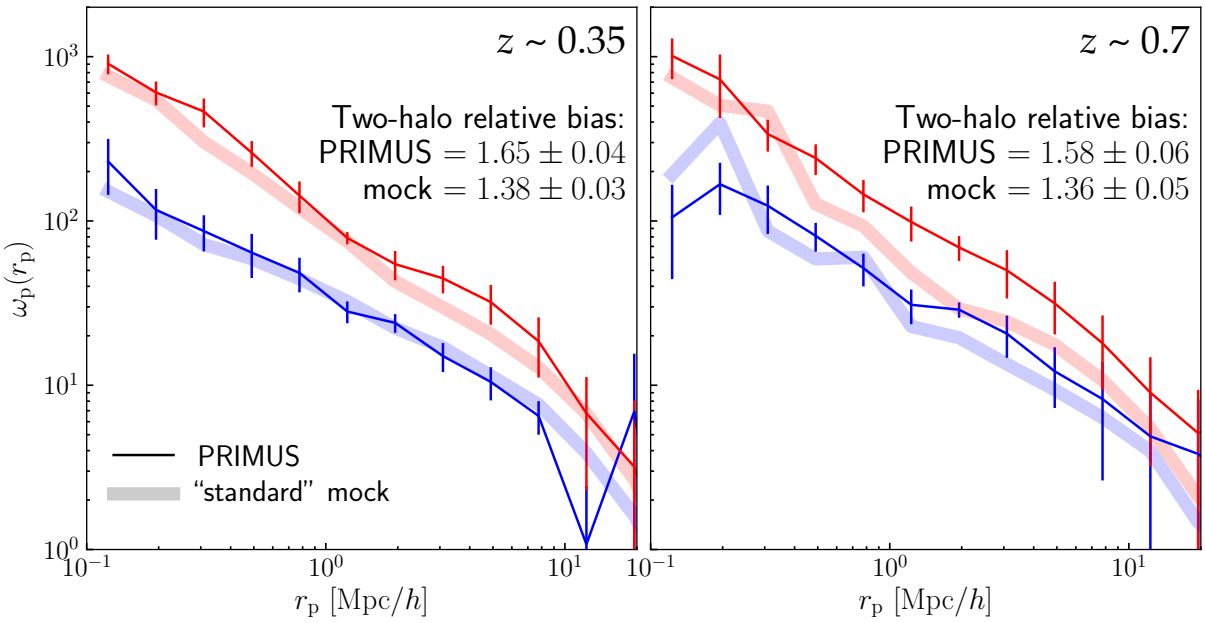

Figure 3.4: Clustering amplitude, $\omega_{\rm p}(r_{\rm p})$, for stellar mass-matched samples of all star-forming (thin blue lines) and all quiescent (thin red lines) PRIMUS galaxies at $0.2 < z < 0.5$ (left) and $0.5 < z < 0.9$ (right). Also shown is $\omega_{\rm p}(r_{\rm p})$ for all star-forming (thick blue lines) and quiescent (thick red lines) mock galaxy samples from the PRIMUS-matched "standard" mock galaxy catalogs at $z = 0.35$ (left) and $z = 0.7$ (right) in the same stellar mass ranges as PRIMUS samples. The clustering of all galaxies in the PRIMUS-matched mock catalog agrees with PRIMUS at low redshift. At high redshift galaxies in the PRIMUS-matched mock catalog are less clustered than PRIMUS galaxies, but the *relative* bias of quiescent versus star-forming galaxies at fixed stellar mass agrees with PRIMUS within uncertainty.

"standard" mock galaxy catalogs. At low redshift ($z \sim 0.35$) the relative bias on two-halo scales of all quiescent to all star-forming PRIMUS galaxies at fixed stellar mass is 1.65 ± 0.04, while in the "standard" mock catalog the relative bias is 1.38 ± 0.03. At high redshift ($z \sim 0.7$) this two-halo relative bias is 1.58 ± 0.06 in PRIMUS and 1.36 ± 0.05 in the "standard" mock catalog. While the relative biases in the PRIMUS galaxy samples and the mock galaxy samples are not identical, they are similar, and the clustering properties of the mock catalogs are sufficient for the purposes used here.

In this work we use IP galaxies in PRIMUS as an observational proxy for central galaxies. Our investigation will benefit from mock galaxy catalogs with a strong intrinsic signal[3] so that we can conduct a systematic study of how various measurement choices weaken or change the underlying clustering difference between quiescent and star-forming central galaxies. To facilitate such testing, we create an alternate version of the best-fit UNIVERSEMACHINE model and an associated "modified" mock galaxy catalog at $z = 0.35$, in which we enhance the strength of the correlation between central galaxy SFR and host halo accretion rate ($\mathrm{d}M_{\mathrm{halo}}/\mathrm{d}t$). The observable effect of this enhancement is a correlation between galaxy sSFR and clustering amplitude at fixed stellar mass for galaxies *within* the quiescent main sequence (and to a lesser extent within the star-forming main sequence), consistent with the observations of Coil et al. (2017) for PRIMUS galaxies. The relative bias between star-forming and quiescent galaxies is unchanged compared to the "standard" $z = 0.35$ mock galaxy catalog.

We use CAM to model this enhanced correlation (see Hearin et al., 2014; Watson et al., 2015). At fixed stellar mass, and separately for star-forming and quiescent centrals, we assume that sSFR varies monotonically with halo accretion rate, with stochasticity such that sSFR and $\mathrm{d}M_{\mathrm{halo}}/\mathrm{d}t$ exhibit a 50% rank-order correlation coefficient. The bin-free implementation of CAM in `Halotools` (Hearin et al., 2017) exactly preserves $P(\mathrm{SFR}|M_*)$, and so the one-point correlation functions in our mock are in exact statistical agreement with the best-fit UNIVERSEMACHINE

[3]By "signal" we mean specifically a difference in clustering amplitude between quiescent and star-forming galaxies at fixed stellar mass.

model. The two-halo relative bias of quiescent versus star-forming galaxies at fixed stellar mass in the "modified" mock is 1.38 ± 0.03, in precise agreement with the "standard" $z = 0.35$ mock catalog.

3.3.1 Matching Mock Galaxy Catalogs to PRIMUS Data

To compare the clustering of PRIMUS IP galaxies to that of IP and central galaxies in mock catalogs we require mock catalogs that match the PRIMUS dataset at a given redshift as closely as possible. Specifically, mock catalogs should have the same stellar mass and sSFR distributions, galaxy number density, and line-of-sight position (related to redshift) uncertainty as PRIMUS data.

We use the following process to match our mock catalogs to the PRIMUS survey dataset:

1. **Match the joint stellar mass and sSFR distribution.** For each mock catalog we create a normalized two-dimensional histogram of the joint stellar mass and sSFR distribution of all $z_{\rm quality} \geq 3$ PRIMUS galaxies within a given redshift range using bins of width 0.1 dex in stellar mass and 0.1 dex in sSFR. The redshift ranges used are $0.2 < z_{\rm PRIMUS} < 0.5$ and $0.5 < z_{\rm PRIMUS} < 0.9$ for the $z = 0.35$ and $z = 0.7$ "standard" mock galaxy catalogs, respectively. For the $z = 0.35$ "modified" mock catalog we use $0.2 < z_{\rm PRIMUS} < 0.7$, the redshift range of the main sequence split PRIMUS IP galaxy samples. We then randomly select from each bin the number of mock galaxies equal to the weight of that bin multiplied by the total number of mock galaxies in all bins with nonzero weight. This process eliminates mock galaxies with sufficiently low stellar mass and/or sSFR that they would not be PRIMUS targets and ensures that the remaining mock galaxies have the same stellar mass and sSFR distributions as PRIMUS galaxies within a given redshift range around the redshift of the mock.

2. **Match the mean galaxy number density.** We then randomly down-sample the mock

catalog so that it has the same number density as the mean observed PRIMUS number density over the relevant redshift range: $0.3 < z_{\rm PRIMUS} < 0.4$ for $z_{\rm mock} = 0.35$ and $0.65 < z_{\rm PRIMUS} < 0.75$ for $z_{\rm mock} = 0.7$. We use the mean density of the two largest PRIMUS fields: CDFS and XMM. In §3.5.3 below we test the effect of using higher and lower densities on IP galaxy selection and the relative bias of IP and central galaxy samples in the mock catalogs.

3. **Add PRIMUS-like redshift-space distortions.** While mock galaxy catalogs contain precise spatial information in three dimensions, PRIMUS redshifts have an uncertainty of $\sigma_z \simeq 0.005(1+z)$, which translates to an uncertainty in galaxy position in the comoving line-of-sight distance r_z. To emulate this uncertainty in the mock catalogs we add Δr_z ($h^{-1}\,$Mpc) to each mock galaxy's r_z coordinate such that $r_z^{\rm noisy} = r_z + \Delta r_z$, where Δr_z is randomly drawn from a normal distribution of width $\sigma_{r_z}(z)$ ($h^{-1}\,$Mpc). We compute $\sigma_{r_z}(z)$ by using the relationship between peculiar velocity $v_{\rm phys}$ and redshift to express the PRIMUS peculiar velocity uncertainty $\sigma_{v_{\rm phys}}$ in terms of redshift:

$$\begin{aligned} z \simeq v_{\rm phys}/c \rightarrow \sigma_{v_{\rm phys}} &= c\,\sigma_z \\ &= c \times 0.005(1+z). \end{aligned} \tag{3.6}$$

Physical distance $r_{z,\,\rm phys}$ is related to comoving line-of-sight distance r_z by the scale factor $a(z)$:

$$r_{z,\,\rm phys} = a(z)\,r_z, \tag{3.7}$$

and to peculiar velocity $v_{\rm phys}$ by $H(z)$:

$$r_{z,\,\rm phys} = v_{\rm phys}/H(z). \tag{3.8}$$

Combining the three equations above we have

$$\begin{aligned}\sigma_{r_z}(z) &= \frac{\sigma_{v_{\rm phys}}}{a(z)\,H(z)} \\ &= \frac{c \times 0.005(1+z)^2}{H_0\sqrt{\Omega_{\rm M}(1+z)^3+\Omega_k(1+z)^2+\Omega_\Lambda}}.\end{aligned} \tag{3.9}$$

For example, $\sigma_{r_z} \simeq 22.8\ h^{-1}\,$Mpc at $z = 0.35$ and $\sigma_{r_z} \simeq 29.4\ h^{-1}\,$Mpc at $z = 0.7$.

In §3.5.3 below we compare IP galaxy selection and clustering results in the mock catalogs with and without added PRIMUS redshift-space uncertainty.

3.3.2 Isolated Primary Galaxy Selection and Mock Galaxy Samples

IP galaxies were selected in the PRIMUS-matched "standard" and "modified" mock galaxy catalogs using the same criteria used to select IP galaxies in PRIMUS, where a cylinder depth of $\pm 2\sigma_{r_z}(z_{\rm mock})\ h^{-1}\,$Mpc was used instead of $\pm 2\sigma_z$ in redshift space because each mock is a snapshot at a single redshift.

IP galaxies from "standard" mock catalogs were divided into star-forming and quiescent samples, while IP galaxies from the "modified" mock catalog were divided into samples above and below the star-forming and quiescent main sequences. However, the same cuts used to divide star-forming and quiescent galaxies in PRIMUS do not precisely align with the PRIMUS-matched mock catalogs. This is shown in Figure 3.5 for the $z = 0.35$ "modified" mock catalog; solid lines show the PRIMUS cuts (Eq. 3.1), while the dashed lines show the redshift-dependent cuts that are fit to the minimum of the bimodal mock catalog stellar mass–sSFR distributions, which are given by the following relation:

$$\log({\rm sSFR}) = -0.64z + (0.13z - 0.31)\log\left[\frac{M_*}{{\rm M}_\odot}\right] - 7.77. \tag{3.10}$$

To divide star-forming and quiescent IP galaxies in the "modified" mock catalog into samples

Table 3.2: Mock galaxy samples.

Run	Sample Name	$N_{\rm gal}$	$z_{\rm mock}$	$\log(M_*/{\rm M}_\odot)$			$\log({\rm sSFR/yr}^{-1})$		
				min	mean	max	min	mean	max
Star-forming/ quiescent split ("standard" mock catalogs)	SF-lowz-IP	23,608	0.35	10.00	10.63	11.59	-10.98	-10.05	-8.75
	Q-lowz-IP	23,608	0.35	10.04	10.63	11.60	-13.04	-11.72	-10.80
	SF-highz-IP	4,141	0.7	10.80	11.03	11.59	-10.74	-9.87	-8.95
	Q-highz-IP	4,141	0.7	10.86	11.04	11.59	-12.76	-11.54	-10.62
	SF-lowz-cen	26,257	0.35	10.00	10.62	11.58	-10.98	-10.03	-8.85
	Q-lowz-cen	26,257	0.35	10.04	10.62	11.60	-13.02	-11.69	-10.79
	SF-highz-cen	3,843	0.7	10.80	11.02	11.59	-10.74	-9.86	-8.72
	Q-highz-cen	3,843	0.7	10.86	11.03	11.58	-12.76	-11.51	-10.62
	SF-lowz-all	42,321	0.35	10.00	10.58	11.59	-10.98	-10.02	-8.83
	Q-lowz-all	42,321	0.35	10.04	10.59	11.57	-13.03	-11.74	-10.79
	SF-highz-all	5,018	0.7	10.80	11.02	11.59	-10.74	-9.86	-8.64
	Q-highz-all	5,018	0.7	10.86	11.02	11.58	-12.76	-11.54	-10.62
Main sequence split ("modified" mock catalog)	SF-above-IP	22,140	0.35	9.81	10.42	11.57	-12.50	-9.66	-8.49
	SF-below-IP	22,140	0.35	9.81	10.42	11.57	-12.83	-10.13	-8.44
	Q-above-IP	11,187	0.35	10.04	10.73	11.69	-13.23	-11.43	-9.63
	Q-below-IP	11,187	0.35	10.04	10.73	11.62	-13.33	-12.03	-10.08
	SF-above-cen	29,562	0.35	9.81	10.40	11.57	-12.50	-9.65	-8.41
	SF-below-cen	29,562	0.35	9.81	10.40	11.57	-12.82	-10.11	-8.41
	Q-above-cen	11,989	0.35	10.04	10.70	11.69	-13.23	-11.41	-9.40
	Q-below-cen	11,989	0.35	10.04	10.70	11.65	-13.33	-12.00	-10.08
	SF-above-all	38,119	0.35	9.81	10.39	11.57	-12.50	-9.65	-8.54
	SF-below-all	38,119	0.35	9.81	10.39	11.57	-12.83	-10.12	-8.48
	Q-above-all	19,834	0.35	10.04	10.68	11.69	-13.23	-11.45	-9.40
	Q-below-all	19,834	0.35	10.04	10.68	11.66	-13.33	-12.06	-10.08

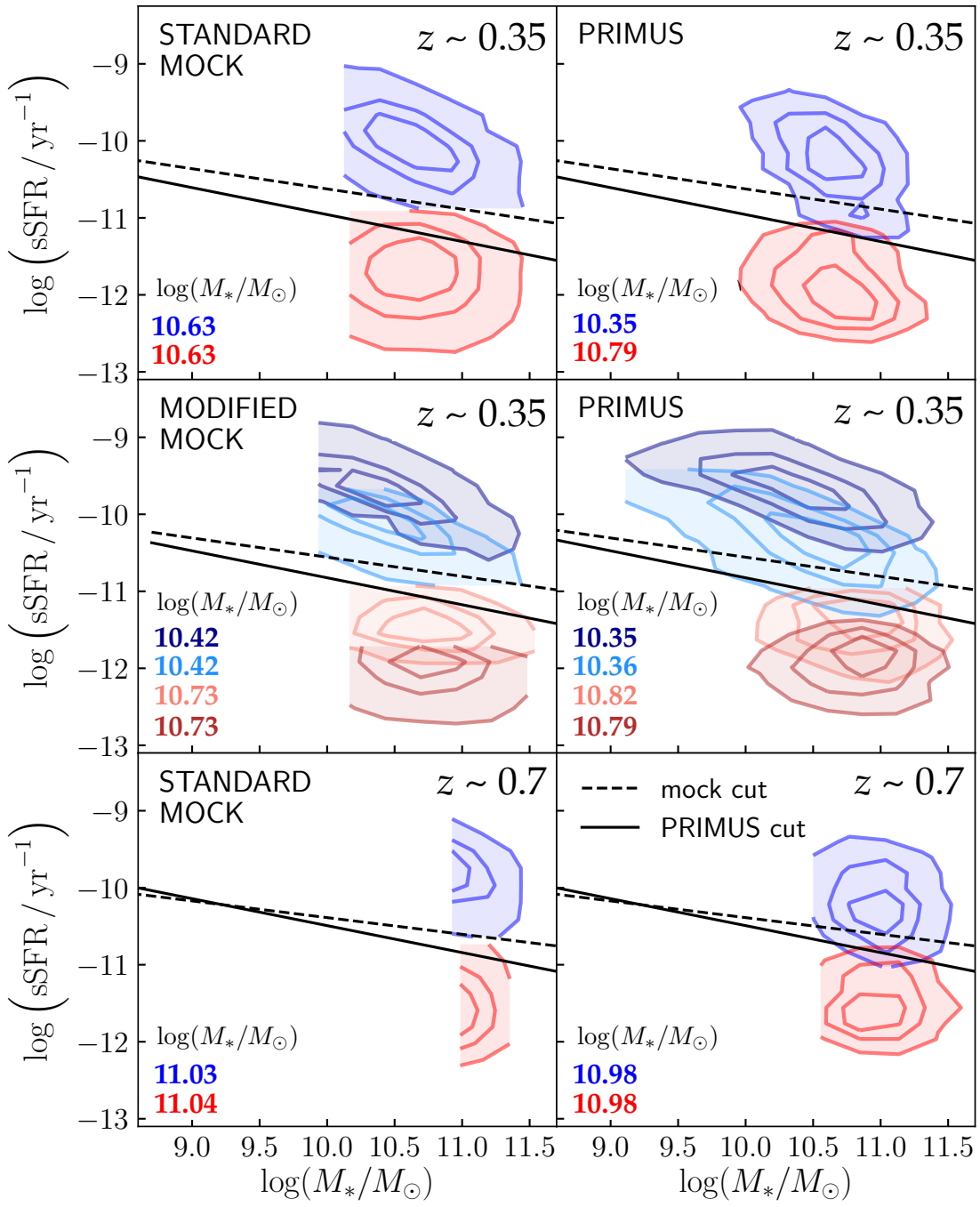

Figure 3.5: Stellar mass versus sSFR for the low redshift (top row) and high redshift (bottom row) "star-forming/quiescent split" IP galaxy samples and four "main sequence split" IP galaxy samples (middle row) in the PRIMUS-matched mock galaxy catalogs (left column) and in PRIMUS (right column). Each panel lists the median stellar mass of each galaxy sample. The PRIMUS galaxy type cut (Eq. 3.1; solid black line) does not quite fit the minimum of the bimodal stellar mass–sSFR distribution of the corresponding PRIMUS-matched mock catalog. We therefore use a slightly different cut (Eq. 3.10; dashed black line) to divide the PRIMUS-matched mock galaxy catalogs into star-forming and quiescent galaxy samples.

above and below the main sequence of each population we found the median stellar mass in each of a series of narrow mass bins for the star-forming (quiescent) mock IP galaxy population. The "SF-above" ("SF-below") mock IP galaxy sample consists of all star-forming mock IP galaxies with stellar masses above (below) the median star-forming IP galaxy stellar mass in for their mass bin. Similarly, the "Q-above" ("Q-below") mock IP galaxy sample is all quiescent mock IP galaxies with stellar masses above (below) the relevant median quiescent mock IP galaxy stellar mass. This method splits the star-forming and quiescent mock IP galaxy populations each into two samples of equal size and mean stellar mass. Table 3.2 summarizes all galaxy samples from the "standard" and "modified" mock galaxy catalogs.

3.4 Methods

3.4.1 Clustering Measurements

To quantify the clustering of IP galaxies we measure the two-point correlation function $\xi(r)$, which determines the excess probability above a random Poisson distribution of a pair of galaxies having a given physical separation.

Following the methods of Coil et al. (2017), we first measure the cross-correlation function (CCF) of a given IP galaxy sample with a "tracer" galaxy sample consisting of all PRIMUS galaxies with robust redshifts within the relevant redshift range. For CCF measurements we use the Davis & Peebles (1983) estimator: $\xi(r_{\rm p}, \pi) = GT/GR - 1$, where GT is the sum of the weighted pair counts of IP galaxies (G) and tracer galaxies (T) and GR is the sum of the weighted pair counts of IP galaxies and a random catalog that has the same projected spatial distribution and redshift distribution as the tracer sample. The random catalogs also account for the PRIMUS redshift success fraction discussed in §3.2.1 above. Weights account for target selection in PRIMUS (see §3.2.2) and allow us to create a statistically complete sample not subject to spatial biases. Pair counts are measured in bins of projected distance $r_{\rm p}$ and line-of-sight distance π.

We also measure the auto-correlation function (ACF) of the tracer sample in the same volume as each IP galaxy sample using the Landy & Szalay (1993) estimator: $\xi(r_{\rm p}, \pi) = (GG - 2GR)/RR + 1$, where *GG*, *GR*, and *RR* are weighted pair counts of galaxies in the galaxy-galaxy, galaxy-random, and random-random catalogs. Weights again are used to account for the PRIMUS target selection.

To account for redshift space distortions, we then obtain the projected correlation function $\omega_{\rm p}(r_{\rm p})$ by integrating all ACFs and CCFs along the line of sight to a maximum separation of $\pi_{\rm max} = 40\ h^{-1}\,{\rm Mpc}$, chosen because the signal-to-noise ratio of $\xi(r_{\rm p}, \pi)$ declines quickly for larger values of π.

Finally, we infer the ACF for a particular IP galaxy sample from the corresponding projected galaxy–tracer CCF, $\omega_{\rm GT}(r_{\rm p})$, and projected tracer ACF, $\omega_{\rm TT}(r_{\rm p})$:

$$\omega_{\rm GG}(r_{\rm p}) = \frac{\omega^2_{\rm GT}(r_{\rm p})}{\omega_{\rm TT}(r_{\rm p})}. \tag{3.11}$$

This method assumes that the spatial distributions of the IP and tracer galaxies in each sample are linearly related to the spatial distribution of the underlying dark matter, and that IP and tracer galaxies are well-mixed within dark matter halos. Coil et al. (2017) test this assumption by comparing the direct ACF of both star-forming and quiescent PRIMUS galaxies with the ACF inferred from the galaxy–tracer CCF and find excellent agreement on both small and large projected scales.

3.4.2 Relative Bias

In this chapter we focus on relative bias measurements to compare the clustering amplitudes of different galaxy samples at the same redshift. The relative bias of two galaxy samples is defined to be the square root of the ratio of their respective projected correlation functions and is a simple comparison of the clustering strengths of the two samples over a given length

scale. We estimate the relative bias $b_{\rm rel}$ between two IP galaxy samples on the "two-halo" scale of $1 < r_{\rm p} < 10\ h^{-1}\,{\rm Mpc}$ by taking the mean of $\sqrt{\omega_1(r_{\rm p})/\omega_2(r_{\rm p})}$ over the scales of interest, where ω_1 and ω_2 are the values of the projected auto-correlation functions of the two galaxy samples at each $r_{\rm p}$ bin value between 1 and 10 $h^{-1}\,{\rm Mpc}$.

3.4.3 Error Estimation

We estimate the uncertainty on $\omega_{\rm p}(r_{\rm p})$ using the jackknife resampling procedure described in Coil et al. (2017), which accounts for uncertainty due to cosmic variance. We use 10 jackknife samples across the four PRIMUS fields. The two larger fields, CDFS and XMM, are each divided along lines of constant RA and Dec into four subfields of roughly equal area on the sky. The smaller fields, COSMOS and ES1, are not subdivided as they are each approximately one fourth the size of the larger fields.

We calculate the projected correlation function $\omega_{\rm p}(r_{\rm p})$ for each jackknife sample j. The variance of $\omega_{\rm p}(r_{\rm p})$ is then

$$\sigma^2_{\omega_{\rm p}}(r_{\rm p}) = \frac{N-1}{N}\sum_{j}^{N}(\omega_{\rm p}(r_{\rm p}) - \omega_j(r_{\rm p}))^2, \tag{3.12}$$

where N is the total number of jackknife samples and $\omega_j(r_{\rm p})$ is the projected correlation function for a given jackknife sample. These errors are shown in figures of $\omega_{\rm p}(r_{\rm p})$ for individual bins in $r_{\rm p}$.

To estimate the uncertainty on the relative bias between two galaxy samples, we calculate $b_{\rm rel}$ for *each* jackknife sample j and measure the variance of the relative bias across the samples:

$$\sigma^2_{b_{\rm rel}} = \frac{N-1}{N}\sum_{j}^{N}(b_{\rm rel} - b_{{\rm rel},j})^2, \tag{3.13}$$

where $b_{{\rm rel},j}$ is the relative bias for a given jackknife sample. We therefore do not use the error bars on $\omega_{\rm p}(r_{\rm p})$ for each sample, but rather calculate the variance of the relative bias itself.

For the mock catalogs, to estimate the uncertainty on the two-halo scale relative bias for mock galaxy samples we repeat the pipeline described in §3.3.1 10 times to create 10 versions of the relevant PRIMUS-matched mock galaxy catalog, each with its own set of the relevant galaxy samples in Table 3.2. Then for a given sample or samples from each of the 10 versions of the mock galaxy catalog we calculate the relative bias, take the mean of all 10 values, and take the standard deviation of all 10 values as the error on the mean.

3.5 Isolated Primary Clustering Results

In this section we present two-halo relative bias measurements for the various IP galaxy samples from PRIMUS, and compare these results to the relative bias measurements for IP and central galaxy samples from the mock galaxy catalogs. We first present results for the "star-forming/quiescent split" samples in §3.5.1, and use the mock galaxy catalogs to refine the relative biases we measure in PRIMUS data. In §3.5.2 we present results for the "main sequence split" galaxy samples in PRIMUS and the mock catalogs. These galaxy samples are selected to investigate whether we detect any dependence of clustering amplitude on sSFR for IP galaxies separately within the star-forming and quiescent main sequences ("intra-sequence" relative bias). Finally in §3.5.3 we explore how factors such as galaxy number density and the presence of PRIMUS redshift errors affect the selection of IP galaxies and the relative biases of IP and central galaxies we measure in the mock galaxy catalogs.

3.5.1 Star-forming/Quiescent Split

A main goal of this work is to quantify the relative clustering strength of star-forming and quiescent IP galaxies as a proxy for star-forming and quiescent central galaxies at $0.2 < z < 0.9$. As shown in the top panels of Figure 3.6, quiescent IP galaxies are more strongly clustered than star-forming IP galaxies at fixed stellar mass in both redshift bins ($z \sim 0.35$ and $z \sim 0.7$). The

top panels show $\omega_p(r_p)$ for the star-forming/quiescent split PRIMUS IP galaxy samples at low ($0.2 < z < 0.5$) and high ($0.5 < z < 0.9$) redshift, and report the relative bias between quiescent and star-forming IP galaxies in each redshift bin. At low redshift the mean stellar mass of both quiescent and star-forming IP galaxies in the data is ~ 10.6 and the relative bias is 1.71 ± 0.07, while at high redshift ($0.5 < z < 0.9$) the mean stellar mass is ~ 11.0 and the relative bias is 1.31 ± 0.16.

Because IP galaxies in PRIMUS are only a proxy for true central galaxies, it is important to consider the extent to which the relative bias we measure for IP galaxies may differ from the value for galaxies in PRIMUS that are truly centrals. Any sample of IP galaxies selected using isolation criteria will have some degree of contamination (see §3.6 below) from satellite galaxies misclassified as isolated galaxies. One of the most robust results from HOD studies is

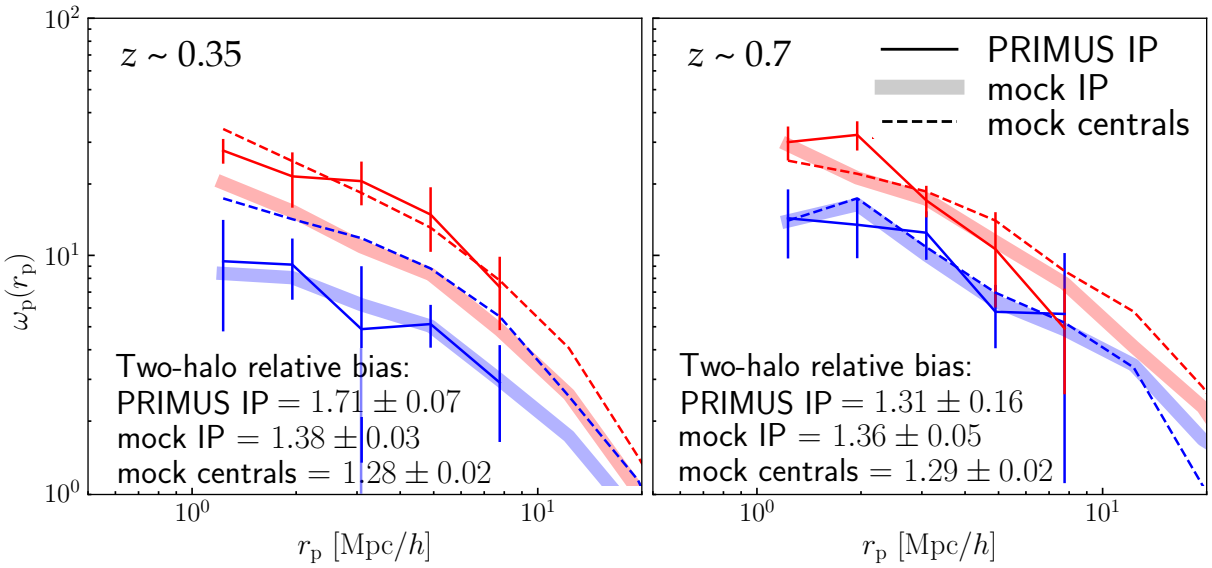

Figure 3.6: Clustering amplitude, $\omega_p(r_p)$, for star-forming (thin blue lines) and quiescent (thin red lines) PRIMUS IP galaxy samples at low ($0.2 < z < 0.5$; left) and high redshift ($0.5 < z < 0.9$; right). Also shown are star-forming and quiescent IP galaxies (dashed blue and red lines) and central galaxies (thick blue and red lines) in low ($z = 0.35$) and high ($z = 0.7$) redshift PRIMUS-matched "standard" mock galaxy catalogs. Within each redshift bin all PRIMUS and mock galaxy samples have the same stellar mass distribution: the mean stellar mass is $\sim 10^{10.6}$ $M_\odot$ at $0.2 < z < 0.5$ and $\sim 10^{11.0}$ $M_\odot$ at $0.5 < z < 0.9$ (see Tables 3.1 and 3.2). At fixed stellar mass quiescent IP galaxies are more strongly clustered on two-halo scales than star-forming IP galaxies.

that satellite galaxies are more strongly clustered than central galaxies of the same stellar mass; for example, the minimum mass for a dark matter to host a satellite galaxy is typically ~ 20 times larger than the minimum halo mass required to host a central (e.g. Zehavi et al., 2005; Leauthaud et al., 2012). A similarly robust result deriving from empirical modeling fits to galaxy clustering is that quiescent galaxies are more strongly clustered than star-forming galaxies at fixed stellar mass (e.g. Tinker et al., 2013).

Due to the combination of these effects working in concert, we must consider the possibility that the difference in clustering amplitude we observe between quiescent and star-forming PRIMUS IP galaxies is due not to an inherent dependence of *central* galaxy clustering strength on sSFR, but is instead a result of contamination by satellite galaxies when selecting IP galaxy samples.

We investigate this possibility by measuring the relative bias of quiescent versus star-forming galaxies for samples of IP and central galaxies, with the same stellar mass distribution as PRIMUS IP galaxies, from the "standard" mock galaxy catalogs. IP galaxies are selected by applying to the mock catalogs the same isolation criteria used to select IP galaxies in PRIMUS. Table 3.2 presents details of the mock IP and central galaxy samples, and clustering amplitudes and relative biases are shown in the bottom panels of Figure 3.6.

At low redshift ($z \sim 0.35$; bottom left panel) the relative bias of quiescent versus star-forming mock IP galaxies (thick red and blue lines) at fixed stellar mass is 1.38 ± 0.03, while for mock central galaxies (dashed red and blue lines) with the same stellar mass distribution the relative bias is 1.28 ± 0.02, or 7% less than IP galaxies. Thus while the relative bias for mock central galaxies is slightly lower than for mock IP galaxies, quiescent mock central galaxies are more strongly clustered than star-forming mock central galaxies at fixed stellar mass (for the stellar mass range probed here). Applying this 7% "correction" to the relative bias of PRIMUS IP galaxies yields an estimated value of 1.59 ± 0.06 for central galaxies in PRIMUS at $z \sim 0.35$.

We find similar results at high redshift (bottom right panel of Figure 3.6), where the

relative bias of quiescent versus star-forming mock galaxies is 1.36 ± 0.05 for mock IP galaxies, and 1.29 ± 0.02 for mock central galaxies. Applying this 5% difference results in an estimated relative bias for PRIMUS central galaxies at high redshift of 1.24 ± 0.12.

The simplest explanation of these results is distinct stellar-to-halo mass relations for star-forming and quiescent central galaxies, which Behroozi et al. (2019) also hints at for $z \gtrsim 1$. However we note the possibility that star-forming and quiescent central galaxies could have the same mean stellar mass at fixed halo mass, and that the scatter in the SMHM relation in combination with the strong positive correlation between quiescent fraction and halo mass (Mandelbaum et al., 2016), could imply that for a sample of central galaxies at fixed *stellar* mass the quiescent centrals have a larger mean halo mass than star-forming centrals.

3.5.2 Main Sequence Split

In the previous section we found a significant (10σ) difference in the clustering amplitude of quiescent versus star-forming IP galaxies in PRIMUS at $z \sim 0.35$ (for $\log(M_*/\mathrm{M}_\odot) \sim 10.6$), and a $\sim 2\sigma$ difference at $z \sim 0.7$ (for $\log(M_*/\mathrm{M}_\odot) \sim 11.0$). We now investigate whether the dependence of the clustering amplitude on sSFR that we find when comparing quiescent and star-forming IP galaxies in PRIMUS persists *within* the star-forming and quiescent main sequences separately. As before we compare the relative biases of IP galaxy samples in PRIMUS to the corresponding IP and central galaxy samples from a mock galaxy catalog.

Since we are now dividing PRIMUS IP galaxies into four samples—above and below each of the star-forming and quiescent main sequences—we use a single wider redshift bin ($0.2 < z < 0.7$) instead of the narrower low and high redshift bins used in §3.5.1, to increase the sample sizes. Additionally, as we are now investigating whether the clustering amplitude of IP galaxies *within* each main sequence depends on sSFR at fixed stellar mas, we no longer require the same stellar mass distribution between samples of star-forming and quiescent galaxies; we only need to constrain intra-sequence samples to have the same stellar mass distributions. This

enables us to use a larger fraction of the star-forming PRIMUS IP galaxy population than we could for the "star-forming/quiescent split" comparison, across a wider stellar mass distribution.

As the "standard" mock galaxy catalogs we use in the previous section do not incorporate the dependence of clustering amplitude on sSFR that Coil et al. (2017) find at fixed stellar mass for all galaxies *within* the star-forming and quiescent main sequences, in this section we use the "modified" mock galaxy catalog for comparison with PRIMUS. As described in §3.3, the "modified" mock catalog has an "intra-sequence" clustering amplitude dependence on sSFR for all galaxies intentionally built into the mock catalog, such that the "intra-sequence" relative bias—the relative bias of galaxies below versus above the star-forming or quiescent main sequence—agrees with what Coil et al. (2017) find for PRIMUS data.

This agreement is shown in Figure 3.7, which shows $\omega_p(r_p)$ for the "main sequence split"

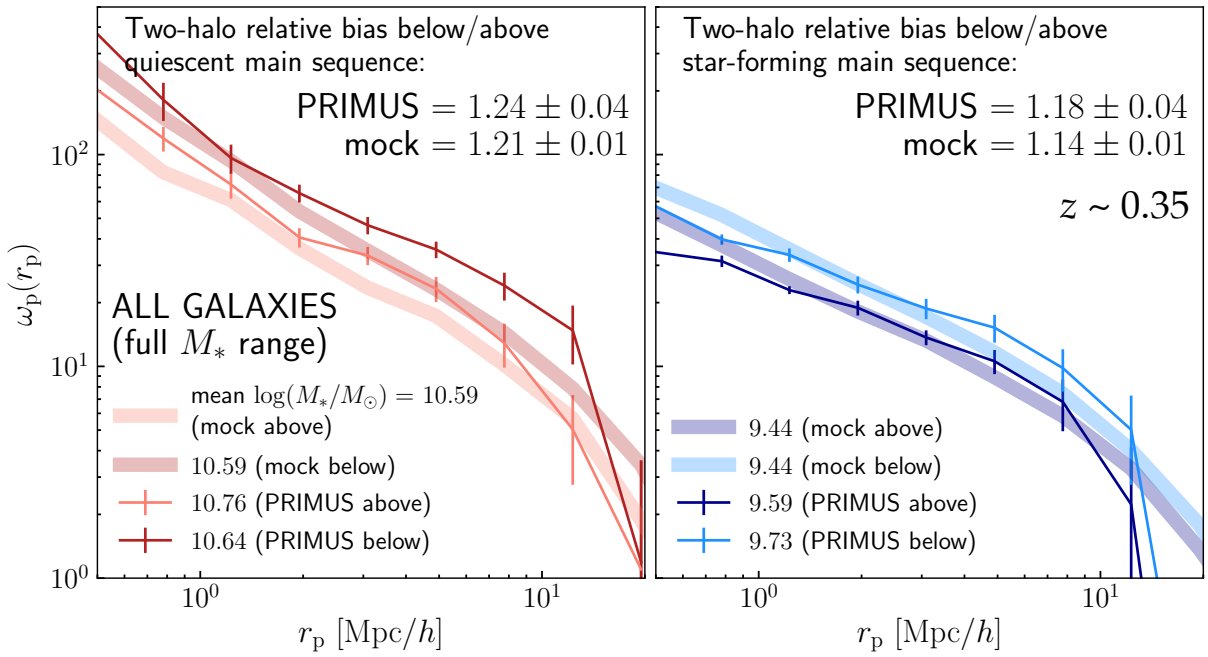

Figure 3.7: Clustering amplitude, $\omega_p(r_p)$, for main-sequence split samples of *all* PRIMUS galaxies and stellar mass-matched samples of all galaxies from the "modified" mock galaxy catalog. The left panel shows PRIMUS and mock galaxy samples above (thin and thick light red lines) and below (thin and thick dark red lines) the quiescent main sequence, while the right panel shows PRIMUS and "modified" mock samples above (thin and thick dark blue lines) and below (thin and thick light blue lines) the star-forming main sequence.

samples of *all* galaxies in both PRIMUS and the "modified" mock galaxy catalog. The left panel of Figure 3.7 shows PRIMUS and mock galaxy samples above (light red) and below (dark red) the quiescent main sequence, while the right panel shows PRIMUS and mock samples above (dark blue) and below (light blue) the star-forming main sequence. The intra-sequence relative bias of all quiescent galaxies is 1.24 ± 0.04 for PRIMUS and 1.21 ± 0.01 for the "modified" mock galaxies. For all star-forming galaxies the intra-sequence relative bias is 1.18 ± 0.04 for PRIMUS and 1.14 ± 0.01 for the "modified" mock galaxies.[4]

With agreement between PRIMUS and the "modified" mock galaxy catalog established for all galaxies, we next investigate whether the intra-sequence relative biases persist for IP galaxies, used as a proxy for central galaxies. The results are shown in Figure 3.8, which shows $\omega_p(r_p)$ for the "main sequence split" samples of PRIMUS IP galaxies (top panels), as well as for stellar mass-matched samples of IP and central galaxies from the "modified" mock galaxy catalog (bottom panels). We do not find an "intra-sequence" clustering amplitude dependence on sSFR (the "signal") for IP galaxies: the intra-sequence relative bias of PRIMUS IP galaxies is 0.99 ± 0.05 for quiescent and 0.99 ± 0.06 for star-forming galaxies.

However, in the "modified" mock galaxy catalog an intra-sequence clustering amplitude dependence on sSFR *is* present for both IP and central galaxies, with a relative bias of $\sim 1.25 \pm 0.03$ for both star-forming and quiescent mock IP and central galaxies.

Given the intra-sequence relative bias detected for mock IP galaxies, we might expect a similar signal for IP galaxies in PRIMUS. However we note that the "modified" mock galaxy catalog is intentionally designed to have intra-sequence relative bias present at all stellar masses for the sake of comparison with PRIMUS data; that intra-sequence relative bias persists in the

[4]We note that the mean stellar masses of the galaxy samples in Figure 3.7 differ between PRIMUS and the mock galaxy catalog by up to ~ 0.3 dex. This is because the clustering amplitude and intra-sequence relative bias measurements for the PRIMUS samples *in this figure* (all galaxies at $0.2 < z < 0.7$ in the full PRIMUS stellar mass range divided into samples above and below the star-forming and quiescent main sequences) are taken from Coil et al. (2017) and contain additional galaxies from DEEP2. The "modified" mock galaxy catalog we use here for comparison with PRIMUS is matched to only PRIMUS data, not to the slightly different combined dataset of PRIMUS and DEEP2 galaxies used by Coil et al. (2017).

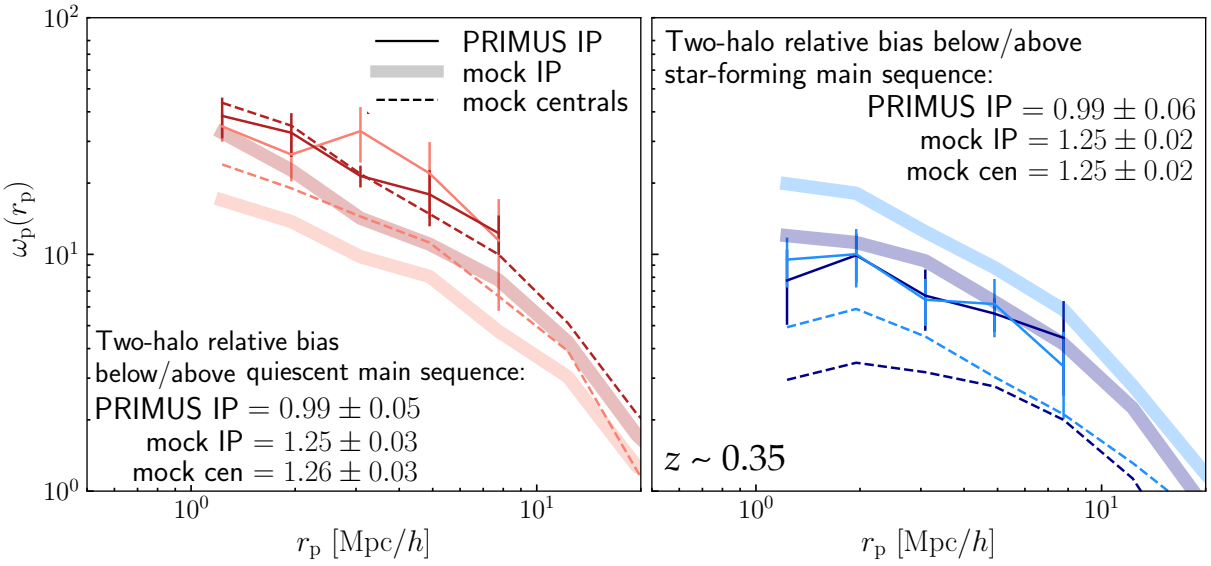

Figure 3.8: Clustering amplitude, $\omega_{\rm p}(r_{\rm p})$, for main-sequence split samples of PRIMUS IP galaxies (solid lines), and IP galaxies (thick lines) and central galaxies (dashed lines) in the "modified" mock galaxy catalog. IP galaxy samples above and below the quiescent main sequence (light and dark red lines) have the same stellar mass distribution ($\log(M_*/{\rm M}_\odot) \sim 10.8$), as do the IP galaxy samples above and below the star-forming main sequence (dark and light blue lines; $\log(M_*/{\rm M}_\odot) \sim 10.3$). The joint stellar mass and sSFR distribution of each IP galaxy sample is shown in Figure 3.1. Intra-sequence relative bias is *not* present for PRIMUS IP galaxies—i.e. we don't see clustering strength dependence on sSFR for IP galaxies *within* either the star-forming or quiescent main sequence. However, intra-sequence relative bias does persist for mock IP and central galaxies in the "modified" mock galaxy catalog.

mock catalog at higher stellar mass does not mean we should necessarily expect to observe a signal for the same stellar mass range in PRIMUS.

As Figure 3.8 shows, no such signal is observed in PRIMUS data, though this could be due to the PRIMUS mass completeness limits (see §3.2.5) necessarily constraining IP galaxy samples to relatively high stellar mass ($\log(M_*/{\rm M}_\odot) \gtrsim 10.8$ for quiescent and $\gtrsim 10.3$ for star-forming galaxies). This is illustrated in Figure 3.9, which is the same as Figure 3.7 except the stellar mass range of each "main sequence split" galaxy sample is now constrained to the higher stellar mass range of the corresponding IP galaxy sample. While Figure 3.7 shows the clustering amplitude and relative bias of "main sequence split" samples of all galaxies over the full PRIMUS stellar mass range, Figure 3.9 shows the same measurements for these samples *limited to a higher mean stellar mass*—the same stellar mass range as the "main sequence split" IP galaxy samples.

As discussed above, the clustering amplitude and relative bias of "main sequence split" samples of *all* galaxies agrees between the PRIMUS data and the "modified" mock galaxy catalog when sample galaxies are selected *from the full PRIMUS stellar mass range*, as seen in Figure 3.7. These intra-sequence relative biases remain consistent in the mock catalog when sample galaxies are constrained to the higher stellar mass range of PRIMUS IP galaxies ($\log(M_*/\mathrm{M}_\odot) \sim 10.7$ for quiescent and ~ 10.3 for star-forming galaxies). As shown in Figure 3.9, the intra-sequence relative biases for all "modified" mock galaxies at the IP galaxy stellar mass range is 1.21 ± 0.02 for quiescent and 1.20 ± 0.03 for star-forming galaxies. However, in the PRIMUS data these intra-sequence relative biases are only 1.09 ± 0.04 for all quiescent and 1.05 ± 0.04 for all star-forming galaxies, for the IP galaxy stellar mass range.

The fact that we do not observe a significant intra-sequence relative bias for PRIMUS

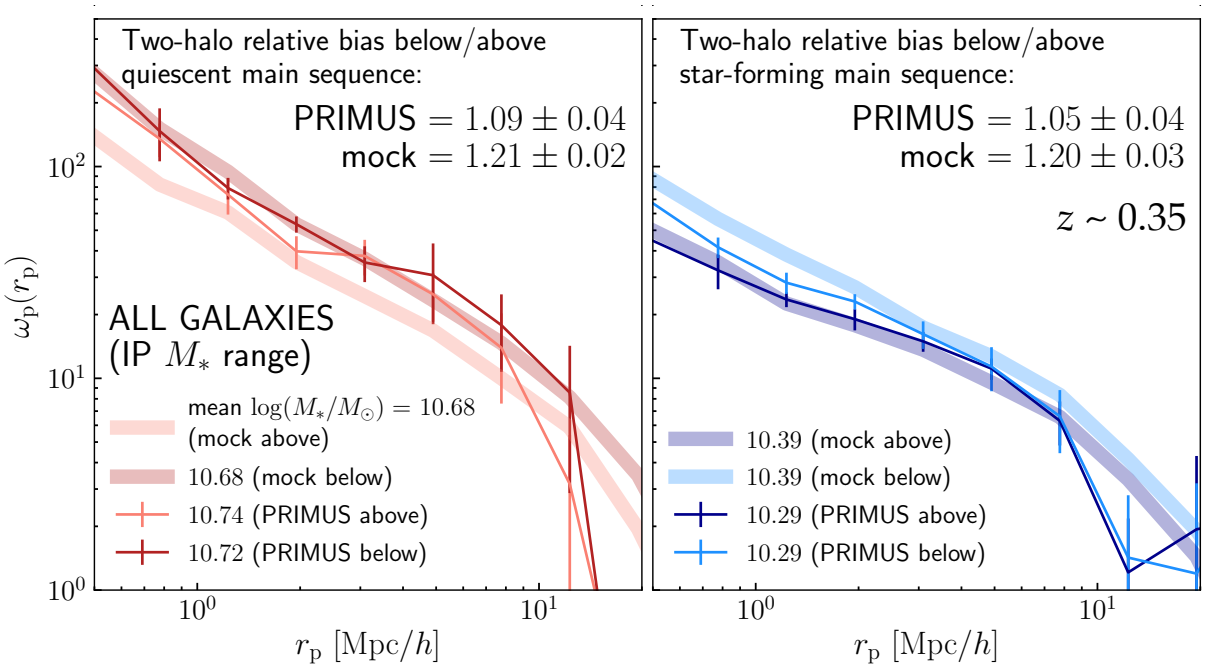

Figure 3.9: Same as Figure 3.7 except here the stellar mass range of each galaxy sample is limited to that of quiescent (left) and star-forming (right) PRIMUS IP galaxies. The clustering amplitude and intra-sequence relative bias of all galaxies in the "modified" mock galaxy catalog matches PRIMUS *over the full PRIMUS stellar mass range*. This agreement is no longer present when the same galaxy samples are constrained to the (higher) PRIMUS IP galaxy stellar mass range.

IP galaxies does not necessarily indicate that no signal exists, although it does indicate that a substantial component of the signal Coil et al. (2017) find for all PRIMUS galaxies is likely due to satellites. This result is also consistent with Zu et al. (2017), who find a hint of intra-sequence clustering differences in SDSS, although measurement uncertainties in their summary statistic are too large to conclusively quantify the true strength of the correlation.

In addition to the possible stellar mass-dependent effect of this signal, it is possible that our sample sizes are simply too small for a significant detection. IP galaxies are a subset of all galaxies in a given stellar mass range. In PRIMUS we find that the intra-sequence relative bias decreases in magnitude as the galaxy sample size also decreases from all galaxies ($N \sim 22,000$ for star-forming and $N \sim 6,000$ for quiescent galaxy samples) to all high mass galaxies ($N \sim 10,000$ for star-forming and $N \sim 5,000$ for quiescent) to IP galaxies ($N \sim 6,000$ for star-forming and $N \sim 3,000$ for quiescent), and for the smallest subset of PRIMUS "main sequence split" galaxies we detect no intra-sequence relative bias at all. In other words, the PRIMUS galaxy samples for which we measure no intra-sequence relative bias are 45% to 75% smaller than the galaxy samples where we do detect a signal.

We note that in the "modified" mock galaxy catalog all galaxy sample sizes are substantially larger than the corresponding PRIMUS galaxy sample. Even the smallest mock galaxy samples ("main sequence split" IP galaxies) are at least as large as the largest PRIMUS samples, and for quiescent galaxies the smallest mock samples are nearly twice the size of the largest PRIMUS samples.

3.5.3 Effects of Galaxy Number Density and PRIMUS Redshift Errors

The mock galaxy catalogs we use are randomly down-sampled to have the same galaxy number density as the mean density of the two largest PRIMUS fields at the redshift of each mock catalog (see §3.3.1). However, the galaxy number density of PRIMUS is a strong function of redshift, as it is a flux-limited survey. To test how galaxy number density affects IP galaxy

selection and the relative bias of mock IP and central galaxies mass we create "high" and "low" density versions of our $z = 0.35$ and $z = 0.7$ "standard" mock catalogs. High density $z = 0.35$ and $z = 0.7$ mock catalogs are matched to the mean galaxy number density of PRIMUS at $0.2 < z < 0.25$ and $0.5 < z < 0.55$, and are 47% and 31% denser than the mean density catalogs, respectively. Low density $z = 0.35$ and $z = 0.7$ mocks are matched to the density of PRIMUS at $0.45 < z < 0.5$ and $0.85 < z < 0.9$, and are 44% and 53% less dense than the mean density mock catalogs, respectively.

We find that our results are not substantially affected by changing the galaxy number density in the mock galaxy catalogs. At low redshift ($z \sim 0.35$) the relative bias of quiescent to star-forming mock IP galaxies decreases by just 1% for the low density mock catalog and increases by 1% for the high density mock catalog. For mock central galaxies the relative biases changes by less than a percent for both the low and high density mock catalogs.

Additionally, the uncertainties of these low and high density relative bias measurements are not substantially different from the mean density mock catalog: 17σ and 8σ for IP galaxies in the low and high density mock catalogs, respectively, and 9σ and 17σ respectively for central galaxies in the low and high density mock catalogs.

Our results are similarly insensitive to galaxy number density at high redshift ($z \sim 0.7$). The relative bias of mock IP galaxies increases by 2% (3.6σ) and for the low density case is unchanged for the high density mock catalog (5.5σ), while for central galaxies the relative bias increases 11% (3.1σ) and 6% (6σ), respectively, for the low and high density mock catalogs.

We also test the effect that PRIMUS redshift errors have on the relative bias of mock IP and central galaxies by comparing to results created from the "standard" mock galaxy catalogs *without* added PRIMUS redshift errors. For this test we follow the procedure described in §3.3.1 but ignore the third and final step of adding PRIMUS-like redshift-space distortions to the mock catalogs. We then select IP galaxies using the same isolation criteria we use to identify IP galaxies in the "standard" mock catalogs (with added redshift errors), and measure the relative bias of

these new IP galaxy samples that do not have redshift-space distortions.

Our results are not substantially different: the relative bias of quiescent versus star-forming mock IP galaxies selected in mock catalogs without PRIMUS redshift errors decreases by 9% (9σ) at low redshift and increases by 2% (2.3σ) at high redshift. For mock central galaxies the relative bias in mock catalogs without PRIMUS redshift errors increases by 4% (6.3σ) and 8% (2.9σ), respectively, at low and high redshift. These tests show that the relative biases in the mock galaxy catalogs are not sensitive to galaxy number density or to redshift errors of the magnitude present in PRIMUS data.

3.6 Effect of Isolation Criteria on Completeness and Contamination

Our goal in studying isolated primary galaxies in PRIMUS is to select a representative, unbiased sample of true central galaxies. However, as discussed in §3.5.1, the application of isolation criteria to the galaxy selection function introduces (unwanted) complications such as satellite contamination and biases in the distribution of environments sampled by the true centrals identified as IP galaxies. To address these effects, in this section we use mock galaxy catalogs to quantify how both sample completeness and contamination are affected by the choice of isolation criteria used to select IP galaxies in PRIMUS. We also demonstrate how isolation criteria yield biased galaxy samples that are not fully representative of the central galaxy population for which they are intended to be an observational proxy.

3.6.1 Completeness and Contamination

In §3.2.6 above we describe the various parameters used in the cylindrical isolation criteria we use to select IP galaxies: projected radius ($r_{\rm p}$), cylinder depth, and mass fraction ($m_{\rm frac}$), or the maximum stellar mass any galaxy within the cylinder can have for the IP candidate galaxy to be

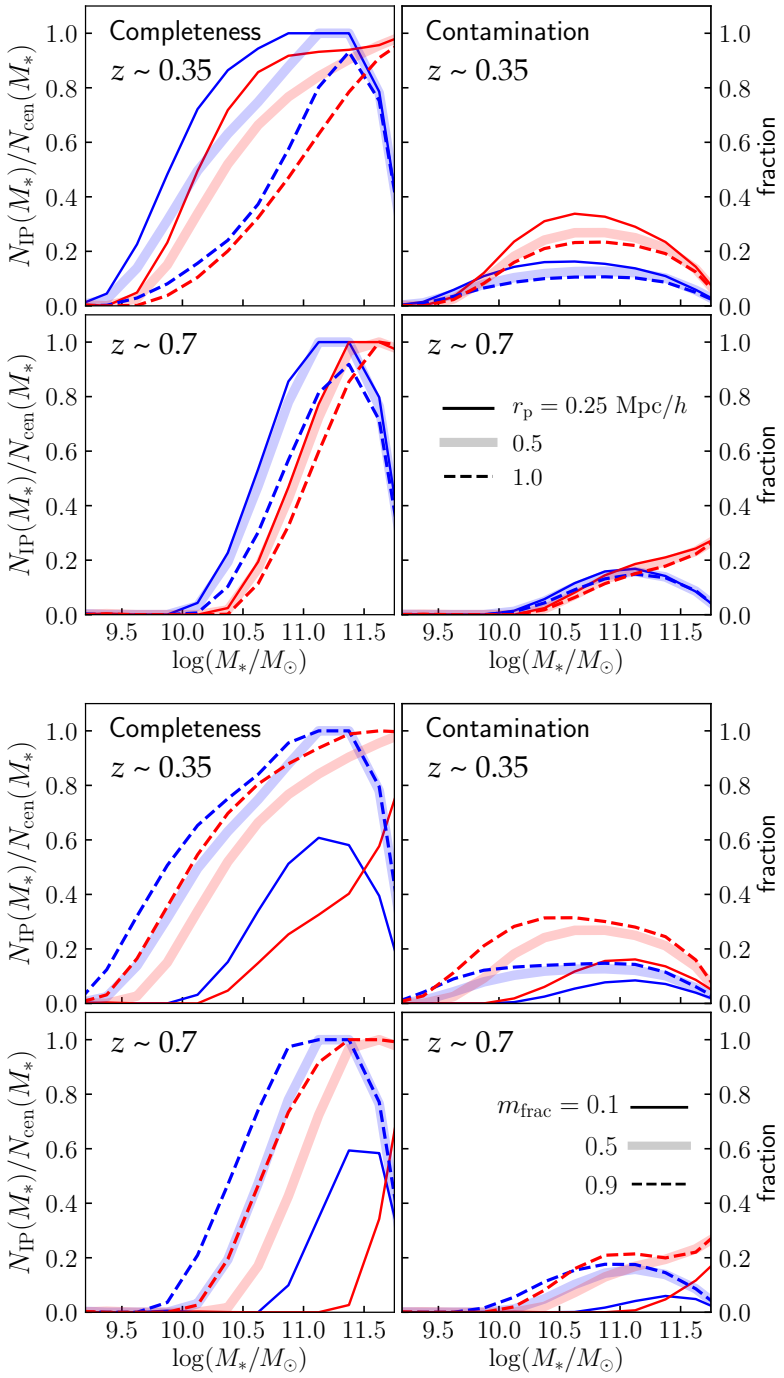

Figure 3.10: Completeness and contamination fractions of IP galaxy samples as a function of stellar mass for star-forming (blue) and quiescent (red) IP galaxy samples from the standard mock galaxy catalogs at $z = 0.35$ and $z = 0.7$ for $r_p = 0.25$, 0.5, and 1.0 h^{-1} Mpc (top four panels) and $m_{frac} = 0.1$, 0.5, and 0.9 (bottom four panels). IP galaxies are defined as those galaxies with no neighbors of mass $M_* > m_{frac} \times$ (IP stellar mass) within a projected radius r_p and within a line-of-sight distance of $\pm 2\sigma_{r_z}(z)$ (equivalent to $\pm 2\sigma_z$, or twice the PRIMUS redshift uncertainty). Different line styles show results for different values of r_p (left) and m_{frac} (right).

considered isolated (as a fraction of the IP galaxy candidate stellar mass). Each of these three parameters affects both the completeness and contamination of an IP galaxy sample, which in turn can affect any conclusions drawn about IP galaxies from that sample. Completeness (measured as a function of stellar mass and galaxy type) is defined as the fraction of central galaxies identified as IP galaxies:

$$f_{\rm comp}(M_*) \equiv \frac{N_{\rm (IP\ \&\ cen)}}{N_{\rm cen}}. \tag{3.14}$$

Contamination is defined as the fraction of galaxies identified as IP galaxies that are actually satellite and *not* central galaxies:

$$f_{\rm contam}(M_*) \equiv \frac{N_{\rm (IP\ \&\ sat)}}{N_{\rm IP}}. \tag{3.15}$$

Ideally an IP sample will have high completeness and low contamination.

To assess how $r_{\rm p}$, $m_{\rm frac}$, and cylinder depth affect the completeness and contamination of our IP galaxy samples, we reselect IP galaxies in the "standard" mock galaxy catalogs multiple times, varying each parameter over a range of values while holding the other parameters constant. We then compute the completeness and contamination of each sample as a function of stellar mass separately for star-forming and quiescent mock IP galaxy samples. The results are shown in Figure 3.10 for $r_{\rm p} = 0.25$, 0.5, and 1.0 h^{-1} Mpc (at $m_{\rm frac} = 0.5$; left panels), and $m_{\rm frac} = 0.1$, 0.5, and 0.9 (at $r_{\rm p} = 0.5$ h^{-1} Mpc; right panels), for a cylinder half-depth of $2\sigma_z$. Blue and red lines show star-forming and quiescent IP galaxies, respectively. We also test but do not show how the choice of cylinder half-depth affects completeness and contamination; we find no substantial differences over the stellar mass range of interest for cylinder half-depths between $1\sigma_z$ and $3\sigma_z$.

Ideally we would maximize completeness and minimize contamination to obtain IP galaxy samples which are maximally pure *and* represent the largest possible sample of central galaxies. This assumes that isolation criteria select a representative subsample of all central galaxies, which we address further in §3.6.2 below. In practice, while more lenient isolation criteria increase

completeness, they also increase contamination. As a main goal of this work is to assess the extent to which quiescent *central* galaxies are more strongly clustered than star-forming central galaxies at fixed stellar mass, reducing IP sample contamination by satellite galaxies is more important than maximizing completeness for our purposes. At the same time, completeness cannot be entirely disregarded because adequate sample sizes are essential to keep measurement uncertainty low.

To determine which value of $r_{\rm p}$ to use (left panels of Figure 3.10) we consider that the contamination for quiescent IP galaxies at $M_* \sim 10^{10.5}$ at $z = 0.35$ increases from $\sim 20\%$ for $r_{\rm p} = 1\ h^{-1}\,$Mpc to $\sim 35\%$ for $r_{\rm p} = 0.25\ h^{-1}\,$Mpc. While the most lenient choice of $r_{\rm p} = 0.25\ h^{-1}\,$Mpc would yield a larger IP galaxy sample (with higher completeness, as seen in the top left panel), the choice of $r_{\rm p} = 0.5\ h^{-1}\,$Mpc reduces contamination nearly 10 percentage points for quiescent IP galaxies at the peak stellar mass of the sample *without* substantially reducing sample completeness. We use $r_{\rm p} = 0.5\ h^{-1}\,$Mpc to select IP samples from the $z = 0.35$ mock galaxy catalog with relatively high completeness ($> 50\%$) while retaining relatively low contamination. For the $z = 0.7$ mock catalog completeness and especially contamination are less sensitive to the choice of $r_{\rm p}$ due to the lower catalog density.

As the right panels of Figure 3.10 show, both completeness and contamination are more sensitive to the choice of $m_{\rm frac}$ than to the choice of $r_{\rm p}$; both fractions span a wider range as $m_{\rm frac}$ varies from 0.1 to 0.9. While the most restrictive choice of $m_{\rm frac} = 0.9$ keeps the maximum contamination value below 20% for quiescent ($< 10\%$ for star-forming) IP galaxy samples at both low and high redshift, it also substantially reduces sample completeness to a maximum value of $\sim 60\%$ at $M_* \sim 10^{11}\ {\rm M}_\odot$ for star-forming IP galaxies at $z = 0.35$, and just $\sim 30\%$ for quiescent IP galaxies. Completeness is even lower for the $z = 0.7$ IP galaxy samples. Our choice of $m_{\rm frac} = 0.5$ substantially increases the sample size while only modestly increasing contamination to levels similar to what we obtain with the choice of $r_{\rm p} = 0.5\ h^{-1}\,$Mpc.

It should be noted that the intrinsic scatter in the stellar mass to halo mass (SMHM)

relation (Moster et al., 2013; Behroozi et al., 2013) places a floor on the obtainable level of contamination for any IP galaxy sample; the only way to eliminate contamination entirely is to use isolation criteria so conservative that completeness is also reduced to effectively zero.

By convolving the completeness and contamination fractions shown in Figure 3.10 as a function of stellar mass the with the stellar mass distributions of the "star-forming/quiescent split" PRIMUS IP galaxy samples, we estimate the overall completeness and contamination fractions of those samples. At low redshift ($0.2 < z < 0.5$) the completeness is 63.4 $(\pm 0.5)\%$ for quiescent IP galaxies and 71.5 $(\pm 0.5)\%$ for star-forming IP galaxies, and the contamination is 24.1 $(\pm 0.4)\%$ for quiescent IP galaxies and 11.3 $(\pm 0.4)\%$ for star-forming IP galaxies. The completeness at high redshift ($0.5 < z < 0.9$) is 57.1 $(\pm 0.6)\%$ for quiescent IP galaxies and 82.9 $(\pm 0.6)\%$ for star-forming IP galaxies, and the contamination is 17.4 $(\pm 0.6)\%$ for quiescent IP galaxies and 14.5 $(\pm 0.7)\%$ for star-forming IP galaxies.

Below in §3.6.2 we discuss the implications of these completeness and contamination levels for both our clustering results and more generally for other studies that utilize isolation criteria.

3.6.2 Biases of Isolation Criteria

An important question when considering the contamination of an IP galaxy sample is to what extent the fraction of interloper satellite galaxies affects any scientific conclusions drawn using the sample. As discussed above, at fixed stellar mass satellite galaxies are more clustered than central galaxies, such that the significant difference we observe in the clustering strength of star-forming and quiescent IP galaxies at fixed stellar mass could be in part due to satellite contamination. We addressed this question in §3.5.1 by using PRIMUS-like mock galaxy catalogs to quantify the difference in relative bias between mock IP and mock central galaxies at fixed stellar mass, and used this to infer the relative biases for central galaxies in PRIMUS. Even after accounting for the contributions of incompleteness and satellite galaxy contamination, we find

that quiescent central galaxies are more strongly clustered at fixed stellar mass than star-forming central galaxies. This implies that satellite contamination does *not* account for the entire signal we observe for IP galaxies, and the remaining signal is a real property of central galaxies in PRIMUS data.

After accounting for the effects of contamination, a remaining question regarding sample completeness is whether the IP galaxies identified by particular isolation criteria are a representative sample of all central galaxies, including those the isolation criteria missed, or whether some form(s) of selection bias yields an IP galaxy sample that is *not* a random subsample of the central galaxies it is intended to represent. To address this question we separate mock IP galaxies into two subsamples: (1) IP galaxies that are also central galaxies, and (2) IP galaxies that are satellite galaxies. We then measure the two-halo clustering amplitude separately for each subsample. The results are shown in Figure 3.11 for the following samples of quiescent and star-forming

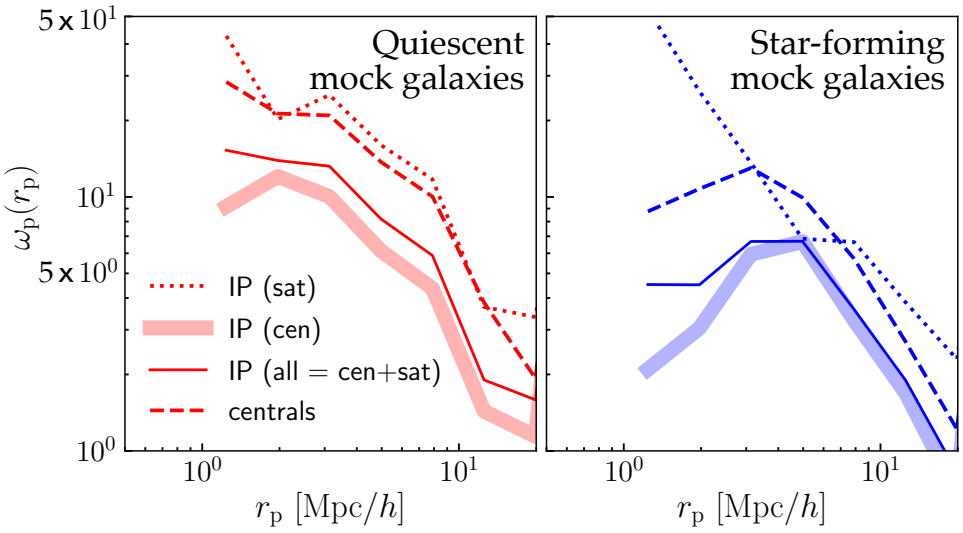

Figure 3.11: Clustering amplitude, $\omega_p(r_p)$, for quiescent (left) and star-forming (right) samples of all mock IP galaxies (thin red and blue lines) and all mock central galaxies (thick red and blue lines) in the $z = 0.35$ "standard" mock galaxy catalog. Also shown is $\omega_p(r_p)$ for only mock IP galaxies that are actually satellite galaxies (dashed red and blue lines) and which are central galaxies (dotted red and blue lines). At fixed stellar mass mock satellite galaxies misclassified as IP galaxies are *more* clustered than all mock IP galaxies (centrals + misclassified satellites), and all mock IP galaxies are *more* clustered than mock IP galaxies that are central galaxies. Mock IP galaxies that are centrals are *less clustered* than all mock central galaxies at fixed stellar mass.

galaxies in the $z = 0.35$ "standard" mock catalog: IP galaxies that are satellites (IP (sat); dotted red and blue lines), IP galaxies that are true centrals (IP (cen); thick red and blue lines), all IP galaxies (IP (all = sat + cen); thin red and blue lines), and all central galaxies (dashed red and blue lines). By design the samples of all IP galaxies and all central galaxies have the same stellar mass distributions (see top panels of Figure 3.12).

If IP galaxies were an unbiased proxy for central galaxies then we expect both samples to have the same clustering amplitude. However, as shown in Figure 3.11, all IP galaxies (a subset of all centrals + contaminating satellites; thick red and blue lines) are *less* clustered than all central galaxies (dashed red and blue lines).

Because satellite galaxies are generically more strongly clustered than central galaxies of the same stellar mass, the presence of contaminating satellite galaxies in an IP galaxy sample should *increase* the sample's clustering amplitude. This is consistent with our results: satellite galaxies misclassified as IP galaxies (dotted red and blue lines in Figure 3.11) are more clustered than all IP galaxies (thin red and blue lines).

However, Figure 3.11 also shows that all IP galaxies are *less* clustered than all central galaxies at fixed stellar mass. This indicates that our IP galaxy samples are incomplete in a way that biases them towards being less clustered; i.e. isolation criteria systematically miss the most strongly clustered central galaxies. Further, the clustering amplitude difference between all central and all IP galaxies is larger than the difference between all IP galaxies and the subset of IP galaxies that are also centrals. In other words, incompleteness has a stronger effect on the observed clustering amplitude of IP galaxies than does contamination by satellite galaxies: the presence of misclassified satellites increases the clustering amplitude of all IP galaxies much less than the exclusion of some central galaxies decreases the it.

The reasonable assumption of a direct mapping between clustering strength and host halo mass leads to the expectation that the host halo mass distributions of the various galaxy samples shown in Figure 3.11 follow the same trend: IP (sat) $>$ centrals $>$ IP (cen + sat) $>$ IP (cen).

Table 3.3: Summary chart of Figures 3.11 and 3.12. All central and IP central galaxies reside in host halos of the same mass, but all central galaxies are more strongly clustered than IP central galaxies due to environmental incompleteness associated with isolation criteria.

Clustering amplitude	Galaxy sample	Host halo mass	Galaxy sample
most clustered	IP (satellites)	most massive	IP (satellites)
$\Downarrow$	centrals IP (centrals + satellites)	$\Downarrow$	IP (centrals + satellites)
least clustered	IP (centrals)	least massive	centrals & IP (centrals)

This order of relative clustering amplitudes is summarized in Table 3.3, which also includes for comparison the same samples ordered from most to least massive mean host halo mass. In Figure 3.12 we plot histograms of the stellar mass (top panels) and host halo mass (bottom panels) distributions of the same mock galaxy samples shown in Figure 3.11 and Table 3.3. Because we are interested in characterizing the clustering properties of central galaxies at fixed stellar mass, all mock galaxy samples have the same stellar mass distribution and mean stellar mass (top panels of Figure 3.12) by design.

We find that the host halo mass distributions of the galaxy samples in Figure 3.11 (IP (sat), centrals, IP $(\mathrm{cen}+\mathrm{sat})$, and IP (cen)) do not follow the same hierarchy as the clustering amplitudes of those samples. Given that all central galaxies are more clustered than IP central galaxies at fixed stellar mass we would expect the mean halo mass of all central galaxies to be greater than that of IP central galaxies. However, the mean halo masses of all central and IP central galaxies are the same ($10^{12.2}$ $\mathrm{M}_{\odot}$ and $10^{11.9}$ $\mathrm{M}_{\odot}$ for quiescent and star-forming galaxies, respectively), indicating that the difference in clustering amplitude between all central and IP central galaxies is a function of a selection bias introduced by the isolation criteria used to select IP galaxies, and *not* the result of a difference in host halo mass. We refer to the effect of this selection bias as environmental incompleteness.

As shown in Figures 3.11 and 3.12, satellite galaxies misclassifed as IP galaxies have both the largest clustering amplitude and mean parent halo mass ($10^{12.9}$ $\mathrm{M}_{\odot}$ and $10^{12.7}$ $\mathrm{M}_{\odot}$ for

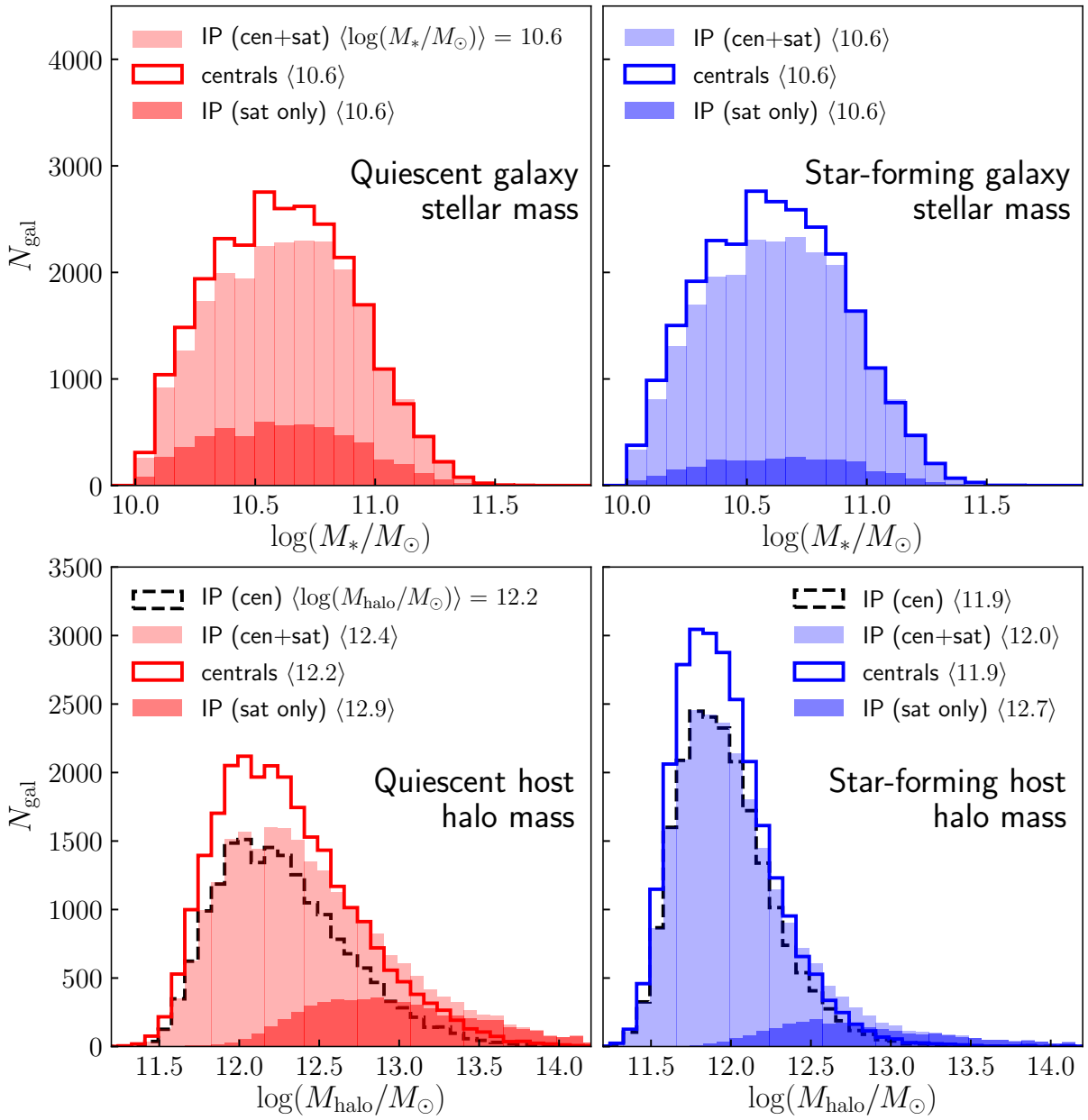

Figure 3.12: Stellar mass (top panels) and parent halo mass (bottom panels) distributions and mean masses for the following galaxy samples in the $z = 0.35$ "standard" mock catalog: all IP galaxies (subset of central galaxies + contaminating satellites; light red and blue filled histograms), only central galaxies (red and blue unfilled histograms), and IP galaxies that are actually satellites (dark red and blue filled histograms). The host halo mass histograms also include only IP galaxies that are also central galaxies (black dotted histograms).

quiescent and star-forming satellites, respectively). In the case of all IP galaxies compared to IP satellite galaxies, IP satellite galaxies reside in substantially more massive parent halos and are more clustered than all IP galaxies. Thus contamination of an IP galaxy sample by misclassified satellite galaxies increases both the sample's mean halo mass and clustering amplitude compared to pure IP central galaxies.

In summary, satellite galaxy contamination inflates the observed clustering of IP galaxies, while (environmental) incompleteness has the opposite effect, systematically excluding central galaxies in overdense environments. These inherent biases of isolation criteria have implications

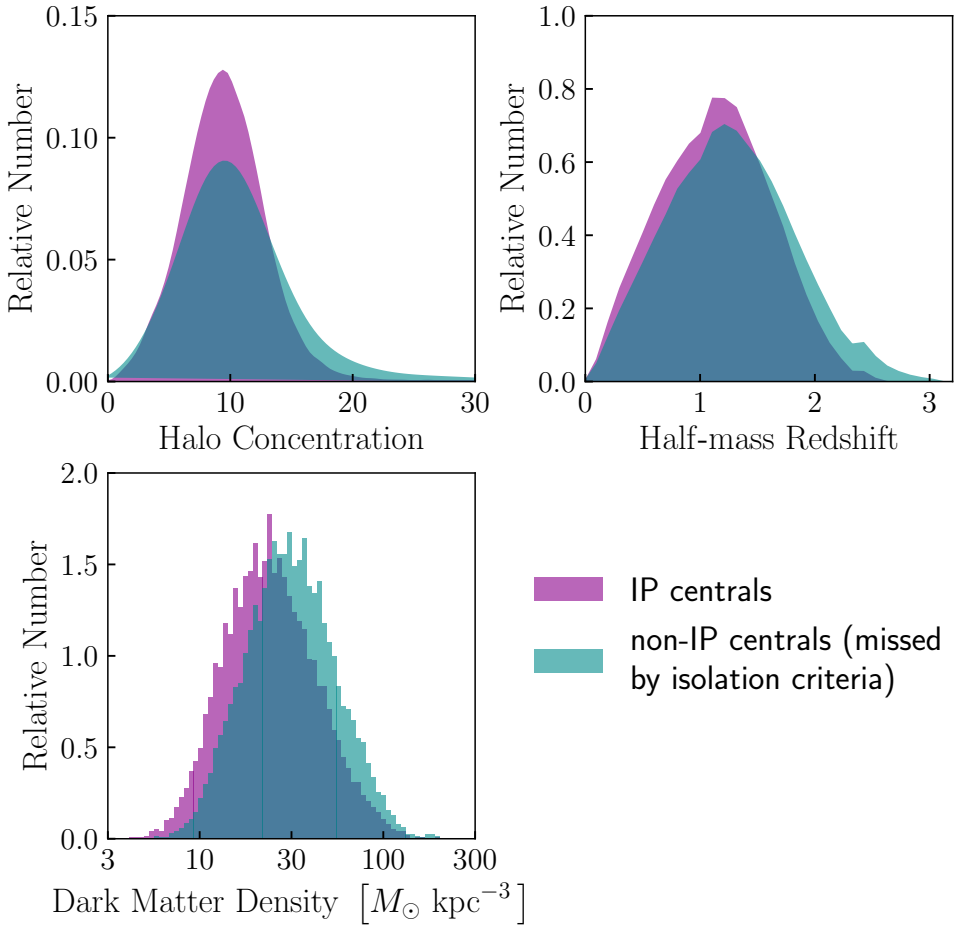

Figure 3.13: Distributions of mock IP galaxies that are also central galaxies ("IP centrals"; magenta) and central galaxies missed by the isolation criteria used to select IP galaxies ("non-IP centrals"; green) as a function of halo concentration (top left panel), half-mass redshift (top right panel), and large-scale dark matter density (bottom panel).

beyond the central galaxy clustering that is the focus of this work. Any study that relies on isolation criteria to identify central galaxies, such as measurements of galactic conformity (e.g. Kauffmann et al., 2013; Hartley et al., 2015; Kawinwanichakij et al., 2016; Berti et al., 2017), should not assume that such criteria generate a representative subsample of central galaxies, even after accounting for contamination by misclassified satellite galaxies.

Figure 3.13 provides further insight into the relationship between isolation criteria and environmental incompleteness. The three panels compare the distributions of mock IP galaxies that are also central galaxies ("IP centrals") and central galaxies missed by the isolation criteria used to select IP galaxies[5] ("non-IP centrals") as a function of three different parameters: halo concentration (top left panel), half-mass redshift (top right panel), and large-scale dark matter density $\rho_{\rm DM}$ (bottom panel). Note that Figure 3.13 explicitly does not consider satellite galaxies and focuses entirely on distinctions between central galaxies selected versus those excluded by isolation criteria.

As shown in the upper left panel of Figure 3.13, the distribution of halo concentrations of non-IP central galaxies (blue) has a long tail extending toward higher concentration that is absent from the distribution for IP central galaxies (magenta). While both distributions peak at a halo concentration of ~ 10, isolation criteria exclude central galaxies that reside in the most highly concentrated halos.

The upper right panel of Figure 3.13 shows the distributions of half-mass redshift (the redshift at which a halo had assembled half of its current virial mass) for IP central and non-IP central galaxies. The distribution for non-IP central galaxies has a similar tail toward higher half-mass redshift, corresponding to earlier halo half-mass assembly time (earlier halo formation epoch and older halo age). The IP central galaxy distribution is conversely shifted slightly toward younger halos with lower half-mass redshifts.

[5]Here we do not use the PRIMUS-like mock galaxy catalogs. Galaxy samples are instead selected from a $z = 0$ mock catalog without added PRIMUS-like redshift errors and limited to the stellar mass range $10.0 < \log(M_*/\mathrm{M}_\odot) < 10.25$. IP galaxies are those with no more massive galaxies within a spherical region of radius 1.5 Mpc.

The bottom panel of Figure 3.13 shows the distributions for IP central and non-IP central galaxies of the large-scale dark matter density, defined as the spherical shell with inner and outer radii of 5 Mpc and 10 Mpc, respectively. Both distributions approximate a normal distribution, but the peaks are slightly offset to either side of $\rho_{DM} \approx 30\ M_{\odot}\ kpc^{-3}$; IP centrals toward lower density and non-IP centrals toward higher density. Isolation criteria are more likely to exclude central galaxies that reside in regions of higher large-scale dark matter density beyond the scale of a single halo.

3.7 Summary and Discussion

We use the PRIMUS galaxy redshift survey to investigate the extent to which the known stronger observed clustering amplitude of quiescent galaxies compared to star-forming galaxies at a given stellar mass is due to clustering differences between central galaxies in these two populations. Using a total sample of $\sim 60,000$ spectroscopic redshifts at $0.2 < z < 0.9$, we identify "isolated primary" (IP) galaxies, using isolation cuts in spatial proximity and stellar mass of nearby galaxies. We then compare the clustering amplitudes of quiescent and star-forming IP galaxies at a given stellar mass, where IP galaxies are used as an observational proxy for central galaxies.

We further test for any dependence of the clustering amplitude on the specific SFR *within* each of the star-forming and quiescent main sequences (which we term "intra-sequence" relative bias). We also compare the observed clustering of IP galaxies in PRIMUS data with the same measurements for PRIMUS-like mock galaxy catalogs created from cosmological simulations, to understand how the clustering of *true* centrals may differ from that of IP galaxies. We use these mock catalogs to quantify the completeness and contamination of our IP galaxy samples and demonstrate that using isolation criteria to identify central galaxies creates biased subsamples of the true central galaxy population.

Our main results are:

1. At fixed stellar mass quiescent IP galaxies are more strongly clustered than star-forming IP galaxies in the PRIMUS dataset. The relative bias observed is 1.71 ± 0.07 (10σ) at $z \sim 0.35$ and 1.31 ± 0.16 (1.6σ) at $z \sim 0.7$. We use our PRIMUS-like mock catalogs to interpret the magnitude of this relative bias as being caused, in part, by quiescent *central* galaxies being more strongly clustered relative to star-forming centrals within these two populations. These differences are consistent with the recent halo occupation models of Behroozi et al. (2019), and can thus be accounted for by distinct stellar-to-halo mass relations for quenched versus star-forming centrals, and/or by central galaxy assembly bias.

2. We do not find evidence that the clustering strength of IP galaxies depends on specific SFR *within* either the star-forming or quiescent main sequence (so-called "intra-sequence relative bias"), which Coil et al. (2017) find for *all* galaxies in PRIMUS at fixed stellar mass. However, we cannot rule out the existence of intra-sequence relative bias for IP (or central) galaxies, in part because the sample sizes decrease when further subdividing the star-forming and quiescent populations, and because of the limited stellar mass range over which we can perform this test.

3. We used mock galaxy catalogs to study both incompleteness (true central galaxies excluded by isolation criteria used by observers) and contamination (satellite galaxies misclassified as isolated primary galaxies). We find that both incompleteness and contamination depend significantly on stellar mass, redshift, and galaxy type (star-forming or quiescent). In particular, the same isolation criteria applied to star-forming and quiescent galaxies yields IP galaxy samples with higher completeness for star-forming galaxies at all stellar masses and redshifts probed here. Completeness is also a strong positive function of stellar mass for both galaxy types. At low redshift, contamination is nearly twice as high for quiescent IP galaxies compared to star-forming IP galaxies, while the IP galaxy samples have similar

levels of contamination at higher redshift.

4. Both star-forming and quiescent mock IP galaxies are less clustered than true central galaxies at fixed stellar mass, even though they reside in equally massive halos. The isolation criteria often used by observers to select "central" (i.e. isolated) galaxies can yield biased samples by preferentially excluding true central galaxies in the most overdense regions, a phenomenon we refer to as *environmental incompleteness*. While contamination by satellite galaxies enhances the observed clustering of IP galaxies, environmental incompleteness decreases the clustering amplitude. This and other systematic biases that result from using isolation criteria to select proxies for central galaxies can be addressed by comparing observational data with mock galaxy catalogs, as is done here.

One of our principal findings is that the application of isolation criteria generically influences central versus satellite contributions to galaxy clustering, as well as modulates the role of central galaxy environment on the signal. Measurements of the clustering of IP galaxies thereby provide important, distinct information that is not contained in standard observations of the two-point clustering of all galaxies. Thus our new measurements of the two-point function of quiescent versus star-forming IP galaxies should be substantially constraining for galaxy evolution models (e.g. Benson, 2012; Becker, 2015; Lacey et al., 2016; Moster et al., 2018; Henriques et al., 2017; Behroozi et al., 2019). Looking forward, models of galaxy formation would benefit from measurements of IP clustering made with larger galaxy samples that probe lower stellar masses at intermediate redshift, which are currently unavailable with existing spectroscopic redshift surveys.

The potentially insidious effects of satellite galaxy contamination have been explored previously in the literature. In particular, it is common to design and apply isolation criteria with the primary goal of minimizing satellite contamination in pursuit of a pure sample of centrals (e.g. Tal et al., 2013; Planck Collaboration et al., 2013; Hartley et al., 2015; Anderson et al., 2015; Mandelbaum et al., 2016). A basic prediction of halo occupation statistics is that satellites

generically live in higher mass parent halos relative to centrals of the same stellar mass. Thus we should *generically* expect that satellite contamination boosts the clustering of putative centrals, which is consistent with our measurements of the relative bias of IP galaxies to true centrals. We thus confirm that contamination by satellite galaxies can indeed significantly bias attempts to measure the large-scale structure of true centrals.

On the other hand, environmental incompleteness can also substantially bias attempts to measure central galaxy clustering. Due to coupling between small and large scales, we should generically expect the application of isolation criteria to exclude centrals in overdense regions of the underlying matter density field. This is borne out in mock catalogs, as shown in Figure 3.13. Moreover, we find that IP galaxy samples preferentially exclude true centrals in high-concentration, early-forming halos. This has particularly important implications for efforts to observationally detect galaxy assembly bias, or more generally, to measure and constrain the co-evolution between galaxies and their halos. Recent progress in understanding the physical origin of assembly bias suggests that the bulk of the underlying halo assembly bias signal is driven by only $\sim 10\%$ of true host halos of a given mass (Mansfield & Kravtsov, 2019). Thus when attempting to observationally constrain central galaxy assembly bias by applying isolation criteria to a galaxy sample, if sufficiently aggressive criteria are applied, one could in principle entirely erase the effect by systematically discarding the sample of dark matter halos responsible for the signal. As shown in Lee et al. (2017, see their Figures 5 and 6), the possibility of such a bias is not limited to analyses based on the particular choice of halo property adopted in Mansfield & Kravtsov (2019). In fact, for *many* choices of secondary halo property, correlations with large-scale density only exist for those halos residing in the high-density tail of the distribution of environments.

The potential pitfalls of environmental incompleteness apply not just to isolation criteria, but also to methods based on group-finding algorithms. Galaxy group catalogs offer a closely related but alternative approach to identifying samples of central galaxies, and there are many

examples in the literature in which group-finding algorithms are used to exclude satellites from a subsequent measurement (e.g. Yang et al., 2005; Weinmann et al., 2006; Berlind et al., 2006; Yang et al., 2008; Lin et al., 2016). As shown previously (Duarte & Mamon, 2014; Campbell et al., 2015), systematic errors in group-finding algorithms can lead to significant biases in the trends inferred directly from a sample of group-finder-determined centrals. Here we point out that environmental incompleteness effects are not limited to samples selected with isolation criteria; this same systematic applies to central galaxy identification with a group-finding algorithm. Similarly, measurements of galactic conformity (e.g. Kauffmann et al., 2013; Hartley et al., 2015; Kawinwanichakij et al., 2016; Berti et al., 2017; Tinker et al., 2018) should not generally assume that such criteria create a fully representative subsample of central galaxies.

Observational studies that select subsamples dependent on spatial location from the full galaxy population should apply their selection methods to mock galaxy catalogs, created from N-body simulations combined with galaxy halo occupation models, to assess the completeness and contamination of their samples. Mock catalogs can additionally be useful in defining a statistic that is robust to the dominant systematics in the problem, as we have done here by tuning our isolation criteria (for another recent example see Calderon et al., 2018). Analyses with mock catalogs are also especially useful in determining whether galaxy samples are subject to unanticipated selection biases, as well as to address the effects of any biases by both refining selection criteria and quantifying differences between statistics obtained from real versus simulated data (e.g. Barton et al., 2007).

Acknowledgements

This chapter includes data gathered with the 6.5-meter Magellan Telescopes located at Las Campanas Observatory, Chile. We thank the support staff at LCO for their help during our observations, and we acknowledge the use of community access through NOAO observing

time. Funding for PRIMUS has been provided by NSF grants AST-0607701, 0908246, 0908442, 0908354, and NASA grant 08-ADP08-0019. Special thanks to Peter Behroozi for help with generating mock catalogs with UNIVERSEMACHINE, and to the PRIMUS survey team. AMB and ALC acknowledge support from the Ingrid and Joseph W. Hibben endowed chair at UC San Diego.

Chapter 3, in full, is a reprint of material previously published in The Astrophysical Journal, 2019, Vol. 884, as "PRIMUS: Clustering of Star-forming and Quiescent Central Galaxies at $0.2 < z < 0.9$" by A. M. Berti, A. L. Coil, A. P. Hearin, and J. Moustakas. The dissertation author was the primary investigator and author of this paper.

4 Joint Dependence of Galaxy Clustering on Star Formation and Stellar Mass

Abstract

We present new measurements of the clustering of stellar mass-complete samples of $\sim 40,000$ SDSS galaxies at $z \sim 0.03$ as a joint function of stellar mass and specific star formation rate (sSFR). Our results confirm what Coil et al. (2017) find at $z \sim 0.7$: galaxy clustering is a stronger function of sSFR at fixed stellar mass than of stellar mass at fixed sSFR. We also find that galaxies above the star-forming main sequence (SFMS) with higher sSFR are less clustered than galaxies below the SFMS with lower sSFR, at a given stellar mass. A similar trend is present within the quiescent galaxy population. This confirms that main sequence scatter, and scatter within the quiescent sequence, is real. We compare the resulting galaxy bias as a function of sSFR and *relative* bias versus sSFR *ratio* for different galaxy samples, across $0 < z < 1.2$ to mock galaxy catalogs based on the empirical galaxy evolution model of Behroozi et al. (2019). We find this model fits PRIMUS and DEEP2 clustering data well at intermediate redshift, but the agreement with SDSS is not as strong. We show that increasing the correlation between galaxy SFR and halo accretion rate at $z \sim 0$ in the model substantially improves the agreement with SDSS data. From the mock catalogs we conclude that the dependence of clustering on sSFR at a given stellar mass is predominantly due to a signal from central galaxies; it is not simply an effect of satellite galaxy fraction differences with stellar mass or sSFR. Our results are highly constraining for galaxy evolution models and shows that the stellar-to-halo mass relation (SHMR)

depends on sSFR.

4.1 Introduction

In the ΛCDM paradigm, galaxies form at the centers of collapsing overdensities in a cosmic web of dark matter that underlies the large-scale structure of the universe. Large N-body cosmological simulations model the predicted evolution of the structure of dark matter, while galaxy redshift surveys reveal the spatial distribution of observed galaxies.

Both early models for linking galaxies to halos like halo occupation distribution (HOD) and conditional luminosity function (CLF) (Benson et al., 2000; Peacock & Smith, 2000; Berlind & Weinberg, 2002; Yang et al., 2003), as well as later abundance matching models, use either stellar mass or luminosity as the primary determining characteristic of galaxy clustering (e.g. Kravtsov et al., 2004; Vale & Ostriker, 2004, 2006). The abundance matching technique involves rank-ordering separately rank-ordered by mass (or luminosity for galaxies), then pairing the most massive or luminous galaxies with the most massive halos. Theoretical models also typically differentiate between central galaxies (primary galaxies at the centers of their halos) and satellites galaxies (residing in subhalos within a larger, more massive parent halo). Although it is not always clear within observed galaxies populations if an individual galaxy is a central or satellite, this distinction has proven useful for galaxy–halo connection models because while centrals and satellites occupy the same parent halo they have different formation and evolutionary histories.

The best-fit parameters of HOD and CLF models are different for galaxy population split by properties such as luminosity and optical color. This offers insight into the physical processes responsible for the observed clustering properties of galaxies, which are the main constraints on models of the galaxy–halo connection.

The observed dependence of galaxy clustering on properties such as luminosity, stellar mass, and color have been thoroughly studied within the limits of existing survey data to $z \sim 1$.

Clustering amplitude positively correlates with luminosity, particularly for $L > L^*$, while the correlation is shallower for fainter galaxies (Benoist et al., 1996; Norberg et al., 2001; Coil et al., 2006; Pollo, A. et al., 2006; Meneux et al., 2009). Similar, although weaker, trends are observed with stellar mass, particularly for masses greater than $\sim M^*$ (Li et al., 2006; Meneux, B. et al., 2008; Wake et al., 2011; Leauthaud et al., 2012; Marulli, F. et al., 2013). Coupled with the known dependence of halo clustering amplitude on halo mass, this result implies a stellar-to-halo mass relation (SHMR), estimates of which at different redshifts provide insight into the evolution of star formation efficiency and galaxy evolution (Behroozi et al., 2010; Moster et al., 2010; Leauthaud et al., 2011; Durkalec, A. et al., 2015; Skibba et al., 2015).

In terms of optical color, at fixed luminosity red, quiescent galaxies are more clustered than blue, star-forming galaxies, both locally and to $z \sim 1$ (Norberg et al., 2002; Hogg et al., 2003; Coil et al., 2004; Zehavi et al., 2005; Meneux, B. et al., 2006). The luminosity dependence of red and blue galaxies has also been studied [refs], as well as the dependence of clustering on color *within* the red and blue populations (Coil et al., 2008; Zehavi et al., 2011; Skibba et al., 2014).

Galaxy clustering studies have more recently began exploring the dependence on star formation rate (SFR) and specific SFR (sSFR, or SFR per unit stellar mass), which while similar to optical color are more closely linked to the physical processes relevant for star formation. Heinis et al. (2009) divide star-forming SDSS galaxies into two bins in sSFR and find that clustering amplitude increases with decreasing sSFR. At higher redshift Mostek et al. (2013) find with data from the DEEP2 survey that clustering amplitude is stronger with increasing SFR and decreasing sSFR, although they acknowledge these trends are largely but not entirely attributable to the correlation between SFR and stellar mass, i.e. the star-forming main sequence (SFMS). Mostek et al. (2013) also find that within the star-forming population galaxies above the main sequence are less clustered than those below for a given stellar mass range, implying that galaxies evolve not only *along* the SFMS as they build up stellar mass, but also *across* it, from above to below.

Coil et al. (2017, hereafter C17) use the PRIMUS and DEEP2 datasets to further subdivide

galaxies in the stellar mass–sSFR plane at $z \sim 0.5$ and $z \sim 0.9$, and find that galaxy clustering depends as strongly on sSFR as on stellar mass. Specifically, C17 find a strong correlation between the relative clustering amplitudes of different galaxy samples and the ratio of their sSFRs at a given stellar mass ratio, but not vice versa: relative clustering strength shows little dependence on stellar mass ratio at fixed sSFR ratio. This indicates that stellar mass may not be the primary galaxy property relevant for clustering and the galaxy–halo connection.

Complimenting observations of galaxy clustering dependencies across cosmic time are studies of halo clustering properties performed with ΛCDM cosmological simulations. *Halo assembly bias* refers to the finding that halo clustering depends on factors beyond halo mass, including halo age (e.g. Gao et al., 2005) and concentration (Wechsler et al., 2006; Villarreal et al., 2017), among others (Dalal et al., 2008; Mao et al., 2018; Salcedo et al., 2018; Johnson et al., 2018; Mansfield & Kravtsov, 2019). Combined with the observed clustering dependencies of galaxy properties, this has led to hypotheses of *galaxy assembly bias*, the correlation of a secondary galaxy property (other than stellar mass), such as luminosity or star formation rate, with an additional tracer of halo assembly history, such as dark matter accretion rate or maximum circular velocity $V_{\rm max}$ (e.g. Zentner et al., 2016; Wechsler & Tinker, 2018).

While halo assembly bias is a well-established prediction of ΛCDM simulations, the role of galaxy assembly bias in the relationship between galaxies and halos is an open question. The direct dependence of galaxy properties on halo properties beyond mass is inconsistent with the basic assumption of HOD and CLF models that a halo's mass is sufficient to statistically predict its galaxy content, but definitive observational evidence is difficult to come by, especially at higher redshift. For example, C17's result that clustering does *not* depend on stellar mass *at a given sSFR* is consistent with the SHMR depending on galaxy sSFR, which if true would be a manifestation of galaxy assembly bias. However, C17 note they cannot eliminate the possibility their results are due to satellite galaxies, which are known to reside in more massive halos than central galaxies of the same stellar mass (Watson & Conroy, 2013) and also have a larger quiescent fraction than

central galaxies in less massive halos (Wetzel et al., 2012).

Watson et al. (2015) show that age matching—an implementation of abundance matching that links galaxy stellar mass and (sub)halo $V_{\rm peak}$, the greatest circular velocity achieved by a halo throughout its history—replicates the observed clustering and galaxy-galaxy lensing of star-forming and quiescent SDSS galaxies. Hearin et al. (2015) demonstrate how two-halo galactic conformity (correlations of galaxy properties across multiple halos; e.g. Kauffmann et al., 2013) is a prediction of galaxy–halo models that incorporate *central* galaxy assembly bias, specifically (sub)halo abundance matching that associates galaxy SFR with (sub)halo age (Hearin et al., 2013). Berti et al. (2017) test predictions of this model at $0.2 < z < 1.0$, and find that existing galaxy survey data pushes the limits of the sample size and depth required for robust measurements.

Using "isolated primary" galaxies in PRIMUS data as a proxy for centrals, Berti et al. (2019) investigate the joint clustering dependence of central galaxies on stellar mass and sSFR at $z \sim 0.35$ and $z \sim 0.7$. They compare their results to mock galaxy catalogs based on the empirical UNIVERSEMACHINE model of Behroozi et al. (2019) and find that C17's results for all galaxies also hold for centrals: quiescent central galaxies are significantly more clustered than star-forming centrals at fixed stellar mass. This is consistent with some combination of central galaxy assembly bias and distinct SHMRs for quiescent and star-forming central galaxies.

Observationally, the distinction between centrals and satellites cannot be drawn as cleanly as is possible with dark matter N-body simulations. Existing methods for distinguishing central galaxies from satellites in the data—such as group-finding algorithms, isolation criteria, and using proxies like brightest cluster galaxies—are each subject to systematic uncertainties that manifest as varying levels of sample incompleteness (missing true centrals) and contamination (misclassifying a satellite galaxy as a central). This makes it difficult for empirical models of the galaxy–halo connection to separately constrain these galaxy types. What is possible is to implement existing observational constraints for the entire galaxy population via empirical modeling, and see what novel implications about galaxy evolution—including correlations between properties of galaxies

and halos—emerge from a particular model (e.g. Behroozi et al., 2013, 2015).

In this chapter we first measure the joint dependence of galaxy clustering on stellar mass and sSFR at $z \sim 0$ using data from the tenth SDSS data release, extending C17's study of this joint dependence at $0.2 < z < 1.2$ to the local universe for the first time. We compare our and C17's measurements to mock galaxy catalogs created using the UNIVERSEMACHINE model of Behroozi et al. (2019) to test its agreement with observations—specifically clustering amplitude differences with sSFR within both the star-forming and quiescent populations, or *intra-sequence relative bias* (ISRB)—across $z \sim 0$ to $z \sim 1$. While we find strong agreement between the data and model at higher redshift, we demonstrate how the model can be updated to better fit SDSS data. We then use the simulations to assess the relative contributions of central and satellite galaxies to the ISRB observed at both $z = 0$ and to $z = 1$.

The structure of this chapter is as follows. In §4.2 we provide an overview of the data and mock galaxy catalogs we use, as well as the galaxy samples used for our clustering measurements. §4.3 describes our methods for measuring clustering amplitudes, absolute and relative biases, and estimating errors. In §4.4 we present our measurements of galaxy clustering as a joint function of sSFR and stellar mass at $z \sim 0$, and compare these results and C17's analogous measurements at higher redshift to mock catalogs. §4.5 describes how we modify UNIVERSEMACHINE model at $z = 0$ to improve agreement with observations, and in §4.6 we use simulations to investigate the sources of intra-sequence clustering amplitude differences. We summarize our results in §4.7. Throughout this chapter we assume a standard ΛCDM cosmology with $H_0 = 70$ km s^{-1} Mpc^{-1}. The cosmological parameters of the simulations used are given in §4.2.3.

4.2 Data and Simulations

In this section we describe the observational datasets, *N*-body dark matter simulations, and mock galaxy catalogs used in this study. We use data from the Sloan Digital Sky Survey

to report new galaxy clustering measurements at $z \sim 0$. We further use simulations to create mock catalogs to compare with these new $z \sim 0$ clustering measurements, as well as previously-published clustering measurements from the PRIMUS and DEEP2 galaxy redshift surveys at $z \sim 0.45$ and $z \sim 0.9$.

4.2.1 SDSS

We use galaxy redshifts from Data Release 10 of the Sloan Digital Sky Survey (SDSS; Ahn et al., 2014). Stellar mass and SFR measurements are taken from the MPA-JHU catalog (Kauffmann et al., 2003; Brinchmann et al., 2004). In this catalog, fiber SFRs are measured from Hα (for star-forming galaxies) and estimated from the D4000 break (for quiescent galaxies) for the light within the SDSS fiber. Light outside each galaxy's fiber is converted to an SFR assuming the same average SFR/luminosity ratio as other fibers with similar $g-r$ and $r-i$ colors. The total SFRs used here are the sum of the fiber and non-fiber SFRs.

To create stellar mass complete samples we use a modified version of the redshift-dependent r-band apparent magnitude completeness cut of Behroozi et al. (2015):

$$r < -0.25 - 1.9 \log\left[\frac{M_*}{\mathrm{M}_\odot}\right] + 5 \log\left[\frac{D_\mathrm{L}(z)}{10\,\mathrm{pc}}\right], \tag{4.1}$$

where $D_\mathrm{L}(z)$ is the luminosity distance. Behroozi et al. (2015) find that at least 96% of SDSS galaxies within $9.5 < \log(M_*/\mathrm{M}_\odot) < 10.0$ satisfy $M_r < -0.25 - 1.9\log(M_*/\mathrm{M}_\odot)$, where M_r is the galaxy's Petrosian r-band absolute magnitude. This completeness limit becomes Eq. 4.1 when expressed in terms of redshift and apparent r-band magnitude. Inverting Equation 4.1 with $r = 17.77$ gives the minimum stellar mass to which SDSS is $\gtrsim 96\%$ complete as a function of redshift. Our SDSS samples are complete to a minimum stellar mass of $M_* > 10^{9.75}$ $\mathrm{M}_\odot$ at $z < 0.0435$, which we use as the maximum redshift of our SDSS galaxy samples.

We note, however, that bluer, star-forming galaxies have greater mass-to-light ratios than

redder, quiescent galaxies of the same stellar mass. Thus while $10^{9.75}$ $M_\odot$ is an appropriate mass completeness limit for quiescent SDSS galaxies at $z < 0.0435$, this cut is unnecessarily conservative for star-forming galaxies. Our goal in this study is to probe as wide of a range of galaxy stellar mass as possible, while maintaining an adequately large sample size for robust statistics. Therefore we determine a lower stellar mass above which star-forming SDSS galaxy samples will be complete.

First we classify galaxies as star-forming or quiescent based on whether they fall above or below the following redshift-dependent cut in the stellar mass–sSFR plane:

$$\log\left[\frac{\mathrm{sSFR}}{\mathrm{yr}^{-1}}\right] = (0.37\,z - 0.48)\log\left[\frac{M_*}{\mathrm{M}_\odot}\right] + 3.45\,z - 6.10. \tag{4.2}$$

We obtain this cut by dividing the full SDSS sample into narrow redshift bins containing roughly equal numbers of galaxies, and plotting the stellar mass–sSFR distribution in each redshift bin. Next we fit a line of the form $\mathrm{sSFR} = \alpha \log(M_*/\mathrm{M}_\odot) + \beta$ to the star-forming main sequence (SFMS) in each redshift bin, and then shift this line downward in sSFR to intersect the minimum of the bimodal galaxy stellar mass–sSFR distribution in that bin. We then obtain linear fits to the slope α and intercept β versus the median redshift in each bin to estimate the redshift dependence of each, and substitute in these linear expressions for $\alpha(z)$ and $\beta(z)$ to obtain Equation 4.2.

To determine an appropriate stellar mass completeness cut for star-forming galaxies we measure in narrow redshift bins the fraction of quiescent galaxies above the Behroozi et al. (2015) stellar mass limit at the median redshift of each bin. We then identify the stellar mass $M^{\mathrm{SF}}_{\mathrm{min}}(z)$ at which the same fraction of star-forming galaxies in each bin satisfies $M_* \geq M^{\mathrm{SF}}_{\mathrm{min}}(z)$. We find that star-forming galaxies have the same completeness fraction as their quiescent counterparts at stellar masses 0.5–0.6 dex less than the quiescent galaxy limit of $10^{9.75}$ $M_\odot$ over the redshift range of our sample, with a mean value of 0.55 dex. We therefore adopt a stellar mass completeness limit for star-forming galaxies of $10^{9.25}$ $M_\odot$ at $z = 0.0435$.

Our resulting stellar mass complete SDSS sample contains 41,486 star-forming galaxies with $M_* \geq 10^{9.25}$ $M_\odot$ and 17,960 quiescent galaxies with $M_* \geq 10^{9.75}$ $M_\odot$ in the redshift range $0.02 < z < 0.0435$.

4.2.2 PRIMUS and DEEP2

A primary goal of this work is to compare the sSFR dependence of galaxy clustering in data and mock catalogs at $0 < z < 1.2$. C17 has measured this dependence at $0.2 < z < 1.2$ using data from both the PRIsm- MUlti-object Survey (PRIMUS Coil et al., 2011; Cool et al., 2013) and DEEP2 (Newman et al., 2013) spectroscopic galaxy redshift surveys.

We refer the reader to C17 for full details of the PRIMUS and DEEP2 galaxy samples used in that work—which are the basis for the SDSS and mock galaxy samples used here (see §4.2.4 below)—as well as for additional details about each survey. Briefly, PRIMUS is a low-resolution ($R \sim 40$) spectroscopic redshift survey covering ~ 9 deg^2 in seven fields. Conducted with the IMACS instrument (Bigelow & Dressler, 2003) on the Magellan I Baade 6.5-meter telescope, PRIMUS is the largest spectroscopic faint galaxy redshift survey completed to date. The survey utilized targeting weights to achieve a statistically complete sample of $\sim 120,000$ robust spectroscopic redshifts.

The DEEP2 survey was conducted with the DEIMOS spectrograph (Faber et al., 2003) on the 10 m Keck II telescope, and contains $\sim 17,000$ high-confidence redshifts ($< 95\%$ or $Q \geq 3$; see Newman et al., 2013).

The galaxy samples used in Coil+17 consist of robust ($z_{\rm quality} \geq 3$; see Coil et al., 2011) PRIMUS redshifts from the CDFS-SWIRE, COSMOS, ES1, and XMM-LSS fields, augmented with $Q \geq 3$ DEEP2 redshifts at $0.2 < z < 1.2$ from the EGS field. For the remainder of this chapter "PRIMUS data" refers to this combined dataset using the PRIMUS and DEEP2 surveys.

C17 estimate stellar masses and SFRs for PRIMUS galaxies by using `iSEDfit` (Moustakas et al., 2013) to fit spectral energy distributions (SEDs) with the population synthesis models of

Bruzual & Charlot (2003), assuming a Chabrier (2003) initial mass function from 0.1 to 100 $M_\odot$. We refer the reader to §2.3 of C17 and to Moustakas et al. (2013) for additional details about PRIMUS stellar mass and SFR estimates.

4.2.3 Simulations and Mocks

As the basis for mock galaxy catalogs to compare to observational data we use snapshots of dark matter *N*-body simulations at the median redshift of the corresponding data sample.

For $z = 0$ we use the Bolshoi simulation[1] (Klypin et al., 2011), which contains 2048^3 particles in a $(250h^{-1}\,\mathrm{Mpc})^3$ cubic volume, has a dark matter particle mass resolution of $1.35 \times 10^8\ M_\odot\ h^{-1}$, and uses $\Omega_\mathrm{m} = 0.27$, $\Omega_\Lambda = 0.73$, and $\sigma_8 = 0.82$. For $z = 0.45$ and $z = 0.9$ we use the Bolshoi-Planck simulation (Klypin et al., 2016), which is similar to the Boishoi simulation but uses Planck cosmological parameters of $\Omega_\mathrm{m} = 0.31$ and $\Omega_\Lambda = 0.69$.

We use the publicly-available UNIVERSEMACHINE (Behroozi et al., 2019) code to populate simulation snapshots at $z = 0$, 0.45, and 0.9 with synthetic galaxies to create mock galaxy catalogs to which we compare our observational results. In each snapshot (sub)halos are identified with the publicly available ROCKSTAR halo finder code (Behroozi et al., 2013). UNIVERSEMACHINE empirically models the dependence of galaxy SFR as a function of halo mass, halo accretion rate, and redshift to predict the star formation histories (SFHs) of individual galaxies over cosmic time and connect those SFHs to the assembly histories of dark matter halos. Halos are populated with synthetic galaxies based on the distributions of a variety of observed galaxy properties across redshifts from $z \sim 0$ to $z \sim 10$ (summarized in Table 1 of Behroozi et al., 2019).

Comparing observations with simulations requires mock galaxy catalogs that have the same joint stellar mass and sSFR distributions, galaxy number density, and line-of-sight positional uncertainty (analogous to redshift error in observational data) as the dataset of interest. To achieve

[1] https://www.cosmosim.org/cms/simulations/bolshoi/

this we use a procedure similar to the one described in §3.1 of Berti et al. (2019). Briefly, for each dataset we create a 2D kernel density estimate (KDE) of the joint distribution of galaxy stellar mass versus sSFR. We then select from the relevant synthetic galaxy population a sample with the same 2D distribution as the corresponding observational data. Next we randomly down-sample the selected synthetic galaxy population such that it has the same number density as that of the relevant dataset at its median redshift, i.e. we match the number density of the $z = 0$ snapshot to our SDSS sample, and of the $z = 0.45$ and $z = 0.9$ snapshots to the number density of PRIMUS data at $0.4 < z < 0.5$ and $0.85 < z < 0.95$, respectively.

Finally, we add noise to the line-of-sight coordinate r_z of all galaxies in the $z = 0.45$ and $z = 0.9$ mocks to simulate the redshift errors of the PRIMUS dataset. Specifically, we define a "noisy" line-of-sight coordinate $r_z^{\rm noisy} = r_z + \Delta r_z$, where Δr_z is drawn from a normal distribution with a dispersion equal to the distance in $h^{-1}\,$Mpc equivalent to the PRIMUS redshift error ($\sigma_z/(1+z) \approx 0.0033$) at the redshift of the mock. At $z = 0.45$ $\sigma_{r_z} \simeq 16.4\ h^{-1}\,$Mpc and at $z = 0.9$ $\sigma_{r_z} \simeq 21.5\ h^{-1}\,$Mpc. Redshift errors in SDSS are sufficiently small (York et al., 2000; Blanton et al., 2005) that we do not add additional line-of-sight position noise to the $z = 0$ mock.

We note that Coil et al. (2011) published estimated PRIMUS redshift errors of $\sigma_z \simeq 0.005\,(1+z)$, based on a comparison with higher resolution spectroscopic redshifts. However, Behroozi et al. (2019) found that $\sigma_z \simeq 0.0033\,(1+z)$ is a more accurate estimate of the true PRIMUS redshift errors (see Figure C6 of Behroozi et al. (2019) and the associated discussion). We test using both $\sigma_z/(1+z) = 0.0033$ and 0.005 to add line-of-sight position uncertainties to the $z = 0.45$ and $z = 0.9$ mocks. At both redshifts the clustering amplitudes and biases of the mocks are in better agreement with PRIMUS data if $\sigma_z/(1+z) = 0.0033$ is used; larger values of $\sigma_z/(1+z) = 0.005$ systematically lower the observed clustering as mock galaxies are overly scattered along the line-of-sight dimension.

Mock galaxies are divided into star-forming and quiescent populations with the following

cuts in the stellar mass–sSFR plane:

$$z = 0 \quad : \log(\mathrm{sSFR}) > -0.46 \log(M_*) - 6.24; \tag{4.3a}$$

$$z = 0.45 : \log(\mathrm{sSFR}) > -0.25 \log(M_*) - 8.06; \tag{4.3b}$$

$$z = 0.9 \quad : \log(\mathrm{sSFR}) > -0.19 \log(M_*) - 8.35, \tag{4.3c}$$

where sSFR is in units of yr^{-1} and M_* is in units of $\mathrm{M}_\odot$. These cuts are determined using an analogous method to that described in §4.2.1 for SDSS galaxies: finding a linear fit to the SFMS in the stellar mass–sSFR plane, and shifting this line downward in sSFR so that it intersects the minimum of the bimodal galaxy distribution in this plane.

4.2.4 Galaxy Samples

Two main goals of this work are (i) to measure the joint dependence of clustering on stellar mass and sSFR in the SDSS, and (ii) compare these measurements in data from both SDSS and PRIMUS to simulations by making analogous measurements in mock galaxy catalogs at $0 < z < 1.2$. C17 has measured the clustering dependence of galaxies on stellar mass and sSFR at $0.2 < z < 1.2$ with data from the PRIMUS and DEEP2 galaxy redshift surveys ("PRIMUS data" as described above), and their galaxy samples are the basis for both our SDSS samples (see Figure 4.1 and Table 4.1) and the mock galaxy samples we create at each redshift (see Figures 4.2 and 4.3 and Table 4.2). We therefore describe C17's samples and the rationale behind them in some detail.

C17 divide PRIMUS data into two redshift bins, $0.2 < z < 0.7$ and $0.7 < z < 1.2$. Within each redshift bin they create subsamples in four different ways to conduct distinct "runs" of their analysis. In their nomenclature, Run 1 ("star-forming/quiescent split") compares the clustering of stellar mass complete star-forming and quiescent galaxies within the same stellar mass range.

Run 2 ("main sequence split") divides the star-forming and quiescent populations within

a given stellar mass range into two subsamples each: those above and below the star-forming or quiescent main sequence in the stellar mass–sSFR plane. The goal with these samples is to compare the clustering of star-forming (or quiescent) galaxies with above average sSFRs to those with below average sSFRs at fixed stellar mass.

C17's Run 3 ("sSFR cuts") again limits the star-forming and quiescent populations in each redshift bin to specified ranges in stellar mass, and divides each population into three bins in sSFR. These samples are therefore defined by strict limits in sSFR.

Finally, Run 4 is designed to measure the dependence of clustering on sSFR at fixed stellar mass, as well as the dependence of clustering on stellar mass at fixed sSFR. C17 divide PRIMUS data into nine samples at $0.2 < z < 0.7$ and seven samples at $0.7 < z < 1.2$ with multiple cuts in both stellar mass and sSFR to create a grid in the stellar mass–sSFR plane. We refer readers to §3 in C17 for complete descriptions of the stellar mass, sSFR, and redshift cuts that define their samples.

SDSS Data Samples

As described above, C17's PRIMUS galaxy sample divisions are the basis for our comparable analysis of SDSS data. As PRIMUS is at higher redshift, only C17's "star-forming/quiescent split" samples are stellar mass complete. Here all of our SDSS samples (described below) are stellar mass complete, using the SDSS mass completeness limits described in §4.2.1 above.

Following C17, we divide the SDSS parent sample four ways, shown in Figure 4.1 and described below. Table 4.1 contains parameters for our SDSS galaxy sample cuts.

Star-forming/quiescent split. Here we divide the parent sample into star-forming and quiescent subsamples, both limited to $9.75 < \log(M_*/\mathrm{M}_\odot) < 10.5$, to compare the star-forming and quiescent populations at fixed stellar mass. Galaxies are classified as star-forming or quiescent based on Equation 4.2 (see §4.2.1).

Main sequence split. Here we divide the star-forming and quiescent sequences each

into two samples. We find the median sSFR of the star-forming population in narrow bins in stellar mass, and split the star-forming galaxies into those above and those below the median sSFR for each stellar mass bin. This method creates two star-forming samples with identical stellar mass distributions, allowing us to compare the clustering of star-forming galaxies with above average verses below average sSFRs at fixed stellar mass, and likewise for the quiescent population. The samples above and below the star-forming main sequence have mean stellar masses of $\log(M_*/\mathrm{M}_\odot) = 9.87$, and respective mean sSFRs of $\log(\mathrm{sSFR}/\mathrm{yr}^{-1}) = -9.87$ and -10.37. The samples above and below the quiescent sequence have mean stellar masses of $\log(M_*/\mathrm{M}_\odot) = 10.42$, with mean sSFRs of $\log(\mathrm{sSFR}/\mathrm{yr}^{-1}) = -11.60$ and -12.14, respectively.

sSFR cuts. Here we use cuts in sSFR to divide the parent sample into six subsamples, three spanning the star-forming population and three spanning the quiescent population. The star-forming samples are limited to $\log(M_*/\mathrm{M}_\odot) > 9.25$ with sSFR cut lower bounds at $\log(\mathrm{sSFR}/\mathrm{yr}^{-1}) = -10.0$, -10.4, and -10.8. The quiescent samples are limited to $\log(M_*/\mathrm{M}_\odot) > 9.75$ with sSFR cut upper bounds at $\log(\mathrm{sSFR}/\mathrm{yr}^{-1}) = -10.8$, -11.5, and -12.1. While all of these samples are stellar mass complete, unlike the previous set of samples the mean stellar mass varies by ~ 0.5 dex within the three star-forming subsamples, from ~ 9.6 to ~ 10.1. Within the quiescent subsamples the mean stellar mass ranges from ~ 10.3 to ~ 10.7.

Stellar mass/sSFR grid. The final set of subsamples is designed to allow us to measure both the clustering dependence on stellar mass at fixed sSFR, and on sSFR at fixed stellar mass. For these subsamples we divide the stellar mass–sSFR plane into three stellar mass bins with lower bounds at $\log(M_*/\mathrm{M}_\odot) = 9.25$, 9.75, and 10.4, and four bins in sSFR with cuts at $\log(\mathrm{sSFR}/\mathrm{yr}^{-1}) = -10.0$, -10.8, and -11.7. Of the 12 regions in the stellar mass–sSFR plane defined by these cuts, nine contain sufficient numbers of galaxies to be included in our analysis. These nine regions are by design are comparable to C17's divisions of PRIMUS data at $0.2 < z < 0.7$, although the precise values of the bin edges are offset from those used at higher redshift to better align with the distribution of SDSS data in the stellar mass–sSFR plane.

Table 4.1: SDSS galaxy samples. All samples span $0.02 < z < 0.0435$ and have median redshift $z_{\rm med} \simeq 0.033$. One-halo bias is measured on scales of $0.1\ h^{-1}\,{\rm Mpc} < r_{\rm p} < 1\ h^{-1}\,{\rm Mpc}$ and two-halo bias on scales of $1\ h^{-1}\,{\rm Mpc} < r_{\rm p} < 10\ h^{-1}\,{\rm Mpc}$.

Run	Sample	$N_{\rm gal}$	$\log(M_*/{\rm M}_\odot)$			$\log({\rm sSFR/yr}^{-1})$			Bias	
			min	mean	max	min	mean	max	one-halo	two-halo
SF/Q split	**blue**	11009	9.75	10.08	10.50	-11.14	-10.23	-8.41	0.78 (0.03)	1.19 (0.05)
	red	7751	9.75	10.15	10.50	-13.40	-11.69	-10.80	2.26 (0.06)	1.97 (0.06)
Main sequence split	**dark blue**	12582	9.25	9.87	11.35	-11.20	-9.87	-8.41	0.69 (0.03)	1.08 (0.05)
	light blue	12604	9.25	9.87	11.43	-11.54	-10.37	-9.77	0.92 (0.03)	1.33 (0.05)
	light red	6712	9.75	10.42	11.59	-12.70	-11.60	-10.80	1.63 (0.05)	1.72 (0.06)
	red	6732	9.75	10.42	11.75	-13.40	-12.14	-11.40	2.37 (0.06)	1.99 (0.05)
sSFR cuts	**dark blue**	10695	9.25	9.63	11.15	-10.00	-9.76	-9.00	0.67 (0.03)	1.05 (0.05)
	blue	8452	9.25	9.91	11.24	-10.40	-10.19	-10.00	0.82 (0.03)	1.22 (0.05)
	light blue	4879	9.25	10.09	11.35	-10.80	-10.58	-10.40	1.11 (0.04)	1.49 (0.05)
	light green	4342	9.75	10.27	11.57	-11.50	-11.16	-10.80	1.51 (0.05)	1.68 (0.06)
	light red	6134	9.75	10.36	11.55	-12.10	-11.83	-11.50	2.08 (0.05)	1.90 (0.06)
	red	4462	9.76	10.70	12.00	-13.40	-12.32	-12.10	2.00 (0.05)	1.82 (0.05)
M_*/sSFR grid	**black**	7599	9.25	9.47	9.75	-10.00	-9.74	-8.60	0.65 (0.03)	1.04 (0.05)
	blue	4401	9.25	9.51	9.75	-10.80	-10.28	-10.00	1.17 (0.03)	1.51 (0.05)
	dark blue	2846	9.75	9.98	10.40	-10.00	-9.82	-8.41	0.73 (0.03)	1.05 (0.05)
	light blue	6668	9.75	10.06	10.40	-10.80	-10.33	-10.00	0.79 (0.03)	1.23 (0.05)
	light green	3940	9.75	10.06	10.40	-11.70	-11.29	-10.80	1.87 (0.05)	1.89 (0.06)
	red	3104	9.75	10.15	10.40	-13.40	-11.97	-11.70	2.82 (0.07)	2.11 (0.06)
	cyan	2262	10.40	10.61	11.35	-10.80	-10.44	-10.00	0.86 (0.03)	1.21 (0.05)
	dark green	2037	10.40	10.68	11.43	-11.70	-11.26	-10.80	1.15 (0.04)	1.47 (0.06)
	light red	5842	10.40	10.75	11.50	-13.36	-12.19	-11.70	1.69 (0.04)	1.72 (0.05)

Mock Galaxy Samples

We define galaxy samples in mock catalogs at $z = 0$ to compare to our SDSS results, and at $z = 0.45$ and $z = 0.9$ to compare to C17's results for PRIMUS data at $0.2 < z < 0.7$ and $0.7 < z < 1.2$, respectively. The mock galaxy sample cuts are given in Table 4.2. These are the same as the cuts that subdivide the corresponding data samples, except for the cut that distinguishes star-forming from quiescent galaxies at each mock redshift (Equation 4.3). Our SDSS and especially C17's PRIMUS data samples span a range of redshifts and are classified as star-forming or quiescent based on Equation 4.2 (for SDSS data) and C17's Equation 1 (for PRIMUS data), both of which evolve linearly with redshift. As our mock catalogs are snapshots at single redshifts, Equation 4.3 does not contain any redshift dependence beyond having a single version for each mock.

Table 4.2: Mock galaxy samples. Bias measurements are on two-halo scales.

Run	Sample	$N_{\rm gal}$	$\log(M_*/{\rm M}_\odot)$			$\log({\rm sSFR/yr}^{-1})$			Satellite fraction	Bias
			min	mean	max	min	mean	max		
					$z = 0$					
SF/Q split	**blue**	49946	9.75	10.08	10.50	-11.07	-10.21	-8.84	0.24	1.21 (0.07)
	red	38107	9.75	10.16	10.50	-12.89	-11.68	-10.73	0.46	1.64 (0.07)
Main sequence split	**dark blue**	55321	9.25	9.88	11.40	-11.16	-9.87	-8.72	0.26	1.30 (0.05)
	light blue	55343	9.25	9.89	11.42	-11.41	-10.36	-9.78	0.24	1.19 (0.07)
	light red	31422	9.75	10.41	11.65	-12.62	-11.54	-10.73	0.39	1.59 (0.04)
	red	31439	9.75	10.41	11.65	-13.24	-12.11	-11.36	0.50	1.76 (0.09)
sSFR cuts	**dark blue**	46367	9.25	9.65	11.15	-10.00	-9.77	-9.0	0.28	1.26 (0.04)
	blue	38815	9.25	9.92	11.26	-10.40	-10.19	-10.0	0.23	1.18 (0.07)
	light blue	21041	9.25	10.15	11.37	-10.80	-10.57	-10.4	0.21	1.19 (0.08)
	light green	19976	9.75	10.28	11.54	-11.50	-11.17	-10.8	0.34	1.44 (0.03)
	light red	30157	9.75	10.37	11.46	-12.10	-11.83	-11.5	0.44	1.67 (0.05)
	red	17726	9.75	10.67	11.99	-13.24	-12.32	-12.1	0.49	1.82 (0.12)
M_*/sSFR grid	**black**	31878	9.25	9.48	9.75	-10.00	-9.74	-8.72	0.29	1.27 (0.04)
	blue	18243	9.25	9.53	9.75	-10.80	-10.24	-10.0	0.25	1.14 (0.07)
	dark blue	13296	9.75	9.98	10.40	-10.00	-9.82	-8.84	0.25	1.22 (0.03)
	light blue	30953	9.75	10.06	10.40	-10.80	-10.33	-10.0	0.23	1.19 (0.08)
	light green	18301	9.75	10.07	10.40	-11.70	-11.30	-10.8	0.41	1.52 (0.03)
	red	15265	9.75	10.16	10.40	-12.89	-11.98	-11.7	0.51	1.72 (0.11)
	cyan	10660	10.4	10.62	11.37	-10.80	-10.44	-10.0	0.19	1.22 (0.09)
	dark green	9714	10.4	10.68	11.47	-11.70	-11.27	-10.8	0.28	1.41 (0.03)
	light red	24528	10.4	10.74	11.50	-13.24	-12.16	-11.7	0.45	1.79 (0.08)

Continued on next page

Table 4.2 — *continued from previous page*

Run	Sample	$N_{\rm gal}$	$\log(M_*/{\rm M}_\odot)$			$\log({\rm sSFR/yr}^{-1})$			Satellite fraction	Bias
			min	mean	max	min	mean	max		
					$z = 0.45$					
SF/Q split	**blue**	117645	10.5	10.71	11.00	-10.82	-10.01	-8.57	0.21	1.20 (0.02)
	red	116897	10.5	10.72	11.00	-12.53	-11.68	-10.74	0.38	1.65 (0.05)
Main sequence split	**dark blue**	484447	8.5	9.6	10.50	-9.85	-9.19	-8.1	0.28	1.12 (0.02)
	light blue	484462	8.5	9.61	10.50	-10.70	-9.66	-8.78	0.34	1.20 (0.02)
	light red	116975	10.1	10.64	11.60	-11.84	-11.36	-10.62	0.33	1.54 (0.05)
	red	116983	10.1	10.64	11.60	-12.53	-11.88	-11.42	0.44	1.75 (0.10)
sSFR cuts	**dark blue**	119453	8.5	9.17	10.50	-9.00	-8.81	-8.1	0.27	1.04 (0.02)
	blue	541553	8.5	9.53	10.50	-9.60	-9.32	-9.0	0.32	1.19 (0.01)
	light blue	307452	8.57	9.91	10.50	-10.60	-9.84	-9.6	0.32	1.21 (0.02)
	light green	38552	10.0	10.55	11.50	-11.20	-10.98	-10.6	0.31	1.45 (0.03)
	light red	139955	10.0	10.56	11.50	-11.80	-11.52	-11.2	0.38	1.58 (0.06)
	red	75249	10.0	10.77	11.50	-12.53	-12.00	-11.8	0.44	1.79 (0.09)
M_*/sSFR grid	**black**	194019	8.5	9.1	9.50	-9.20	-8.96	-8.2	0.31	1.10 (0.01)
	blue	226615	8.53	9.26	9.50	-10.20	-9.46	-9.2	0.36	1.19 (0.03)
	dark blue	69657	9.5	9.78	10.50	-9.20	-9.04	-8.2	0.24	1.07 (0.03)
	light blue	463458	9.5	9.95	10.50	-10.20	-9.63	-9.2	0.30	1.18 (0.02)
	light green	45038	9.5	10.1	10.50	-11.20	-10.82	-10.2	0.42	1.42 (0.05)
	red	95546	9.5	10.21	10.50	-12.20	-11.54	-11.2	0.47	1.57 (0.09)
	cyan	90503	10.5	10.72	11.50	-10.20	-9.88	-9.2	0.20	1.17 (0.02)
	dark green	57092	10.5	10.84	11.50	-11.20	-10.56	-10.2	0.23	1.35 (0.03)
	light red	127046	10.5	10.82	11.50	-12.20	-11.71	-11.2	0.36	1.67 (0.07)
					$z = 0.9$					
SF/Q split	**blue**	44044	10.5	10.72	11.00	-10.46	-9.64	-8.13	0.24	1.48 (0.03)
	red	62842	10.5	10.76	11.00	-11.90	-11.29	-10.38	0.27	1.82 (0.06)
Main sequence split	**dark blue**	106422	8.88	9.87	10.50	-9.49	-8.91	-7.98	0.27	1.30 (0.04)
	light blue	106430	8.88	9.88	10.50	-10.36	-9.31	-8.25	0.34	1.38 (0.05)
	light red	48400	10.1	10.81	11.60	-11.59	-11.07	-10.36	0.23	1.80 (0.08)
	red	48410	10.1	10.81	11.60	-11.90	-11.51	-10.82	0.28	1.91 (0.08)
sSFR cuts	**dark blue**	56452	9.0	9.58	11.00	-8.90	-8.66	-8.0	0.24	1.16 (0.04)
	blue	158677	9.01	10.04	11.00	-9.60	-9.25	-8.9	0.32	1.40 (0.04)
	light blue	39763	9.51	10.55	11.00	-10.20	-9.78	-9.6	0.29	1.45 (0.06)
	light green	8828	10.2	10.72	11.69	-10.80	-10.58	-10.2	0.25	1.63 (0.07)
	light red	26630	10.2	10.72	11.65	-11.20	-11.03	-10.8	0.24	1.75 (0.07)
	red	60417	10.2	10.86	11.69	-11.80	-11.46	-11.2	0.26	1.92 (0.09)
M_*/sSFR grid	**black**	29931	8.88	9.33	9.50	-9.20	-8.67	-8.2	0.26	1.12 (0.03)
	dark blue	89738	9.5	9.84	10.50	-9.20	-8.95	-8.2	0.30	1.34 (0.06)
	light blue	90797	9.5	10.1	10.50	-10.20	-9.44	-9.2	0.34	1.39 (0.03)
	light green	9133	9.73	10.33	10.50	-11.20	-10.86	-10.2	0.33	1.58 (0.05)
	cyan	48638	10.5	10.79	11.50	-10.20	-9.69	-9.2	0.23	1.50 (0.03)
	dark green	27713	10.5	10.81	11.50	-11.20	-10.93	-10.2	0.23	1.76 (0.04)
	light red	59321	10.5	10.89	11.50	-11.90	-11.48	-11.2	0.26	1.93 (0.10)

4.3 Methods

In this section we describe the methods used to measure the projected correlation functions and bias values of galaxy samples in both SDSS data and mock galaxy catalogs. We also describe how we estimate the errors of these measurements, including uncertainties due to cosmic variance.

4.3.1 Clustering Measurements

To measure projected two-point clustering in SDSS, $\omega_{\rm p}(r_{\rm p})$, we use the `correl` program in UNIVERSEMACHINE. The program uses the Landy & Szalay (1993) estimator $(DD - 2DR + RR)$ to compute the redshift-space correlation function, $\xi(r_{\rm p}, \pi)$, which is then integrated over $|\pi| < 20$ h^{-1} Mpc to compute the projected correlation function $\omega_{\rm p}(r_{\rm p})$. The code uses 10^6 random points drawn from the same mask region with uniform volume distribution to compute *DR*, while *RR* is computed via Monte Carlo integration. Jackknife resampling is used to estimate errors, giving us an estimate for the lower bound of samples with volumes $V_{\rm eff} = 0.3{\rm Gpc}^3$.

In the mock catalogs, to reduce the Poisson errors we estimate the two-point correlation function $\xi(r)$ of mock galaxy samples by measuring the autocorrelation function (ACF) of all mock galaxies, and the cross-correlation function (CCF) between each sample and all galaxies in the mock. We then infer the ACF of each sample as described below.

For ACF and CCF measurements we use the `Halotools` (Hearin et al., 2017) function `wp_jackknife` with the Davis & Peebles (1983) estimator: $\xi(r) = DD(r)/DR(r) - 1$. For ACF measurements $DD(r)$ counts pair separations among all galaxies in a given sample, while for CCF measurements $DD(r)$ is a count of pair separations between the galaxy sample of interest and a "tracer" galaxy sample consisting of the entire mock catalog.

We measure $\xi(r)$ separately both perpendicular to ($r_{\rm p}$) and along (π) the mock catalog's line-of-sight dimension, then integrate $\xi(r_{\rm p}, \pi)$ over the line-of-sight to a given value of $\pi_{\rm max}$ to obtain the projected correlation function $\omega_{\rm p}(r_{\rm p})$. For each mock we use the same $\pi_{\rm max}$ value

used for $\omega_p(r_p)$ measurements in the corresponding dataset: $\pi_{max} = 20\ h^{-1}\,\mathrm{Mpc}$ for the $z = 0$ mock and SDSS data,[2] and $\pi_{max} = 40\ h^{-1}\,\mathrm{Mpc}$ for the $z = 0.45$ and $z = 0.9$ mocks. The latter is consistent with C17 and their clustering measurements of PRIMUS galaxy samples.

The inferred projected ACF $\omega_p(r_p)$ for each mock galaxy sample is

$$\omega_p(r_p) = \frac{\omega_{GT}^2(r_p)}{\omega_{TT}(r_p)}, \tag{4.4}$$

where $\omega_{GT}(r_p)$ is the projected galaxy–tracer CCF, and $\omega_{TT}(r_p)$ is the projected tracer–tracer ACF. Inferring the ACF in this way reduces the error on $\omega_p(r_p)$, especially for smaller galaxy samples.

The `wp_jackknife` function estimates the error of $\omega_p(r_p)$ by dividing the mock volume N times along each dimension to define $N_j = (N+1)^3$ equal subvolumes and creates the same number of jackknife samples, where each jackknife sample is the entire mock volume excluding one subvolume. The error of $\omega_p(r_p)$ is then $[\sigma^2_{\omega_p}(N_j - 1)/N_j]^{1/2}$, where $\sigma^2_{\omega_p}$ is the variance of $\omega_p(r_p)$ across the jackknife samples.

4.3.2 Absolute and Relative Bias Measurements

We measure the absolute bias of both SDSS and mock galaxy samples using the projected correlation function $\omega_p(r_p)$ of each sample. Absolute bias is a measure of the clustering strength of a particular galaxy sample compared to that of dark matter, and is defined as $\sqrt{\omega_G/\omega_{DM}}$, where ω_G and ω_{DM} are the galaxy and dark matter projected correlation functions, respectively, averaged over "two-halo" scales of $1\ h^{-1}\,\mathrm{Mpc} < r_p < 10\ h^{-1}\,\mathrm{Mpc}$. To estimate ω_{DM} we use the publicly available code of Smith et al. (2003) to calculate ξ_{DM} at the median redshift of the relevant galaxy sample, then integrate ξ_{DM} to the same value of π_{max} used for the corresponding galaxy sample.

[2]For SDSS data we tested both $\pi_{max} = 20$ and $40\ h^{-1}\,\mathrm{Mpc}$ and found that the signal-to-noise of individual $\omega_p(r_p)$ measurements is almost universally larger for $\pi_{max} = 20\ h^{-1}\,\mathrm{Mpc}$.

The relative bias of two galaxy samples is the square root of the ratio of their respective projected correlation functions, averaged over a given length scale, and compares the clustering strengths of the two samples on that scale. We measure the relative bias as a function of scale between pairs of SDSS galaxy samples and pairs of mock galaxy samples as $\sqrt{\omega_1(r_p)/\omega_2(r_p)}$, where $\omega_1(r_p)$ and $\omega_2(r_p)$ are the projected correlation functions of the two samples. We then estimate the relative bias at a given redshift on "one-halo" ($0.1\ h^{-1}\,\mathrm{Mpc} < r_p < 1\ h^{-1}\,\mathrm{Mpc}$) and "two-halo" ($1\ h^{-1}\,\mathrm{Mpc} < r_p < 10\ h^{-1}\,\mathrm{Mpc}$) scales by averaging $\sqrt{\omega_1(r_p)/\omega_2(r_p)}$ over the length scale of interest.

To estimate the error on absolute and relative bias measurements of SDSS galaxy samples we calculate the bias b for *each* jackknife sample and compute the variance of the relevant bias itself across all the jackknife samples. The error of that bias measurement is then $\sqrt{(N_j - 1/N_j)\,\sigma_b^2}$, where N_j is again the total number of jackknife samples, and σ_b^2 is the variance of b across the samples. This method does not use the error on $\omega_p(r_p)$ described in the previous section, and instead estimates the uncertainty on the relative bias directly, accounting for cosmic variance across jackknife samples.

4.4 Correlation Functions and Bias of Galaxy Samples in Data and Mocks

In this section we present measurements of $\omega_p(r_p)$, and of absolute and relative bias versus stellar mass and sSFR, for our SDSS galaxy samples. We also present the same measurements for mock galaxy catalogs at $z = 0$, 0.45, and 0.9, and compare these results to the corresponding data at each redshift.

4.4.1 SDSS Clustering Dependence on Stellar Mass and sSFR

Figure 4.1 shows the stellar mass and sSFR distributions of all SDSS galaxy samples, as well as the projected correlation function $\omega_p(r_p)$ of each sample. Table 4.1 provides the bias on one-halo ($0.1\ h^{-1}\,\mathrm{Mpc} < r_p < 1\ h^{-1}\,\mathrm{Mpc}$) and two-halo ($1\ h^{-1}\,\mathrm{Mpc} < r_p < 10\ h^{-1}\,\mathrm{Mpc}$) scales for each sample.

The star-forming/quiescent split samples clearly show that quiescent galaxies are more

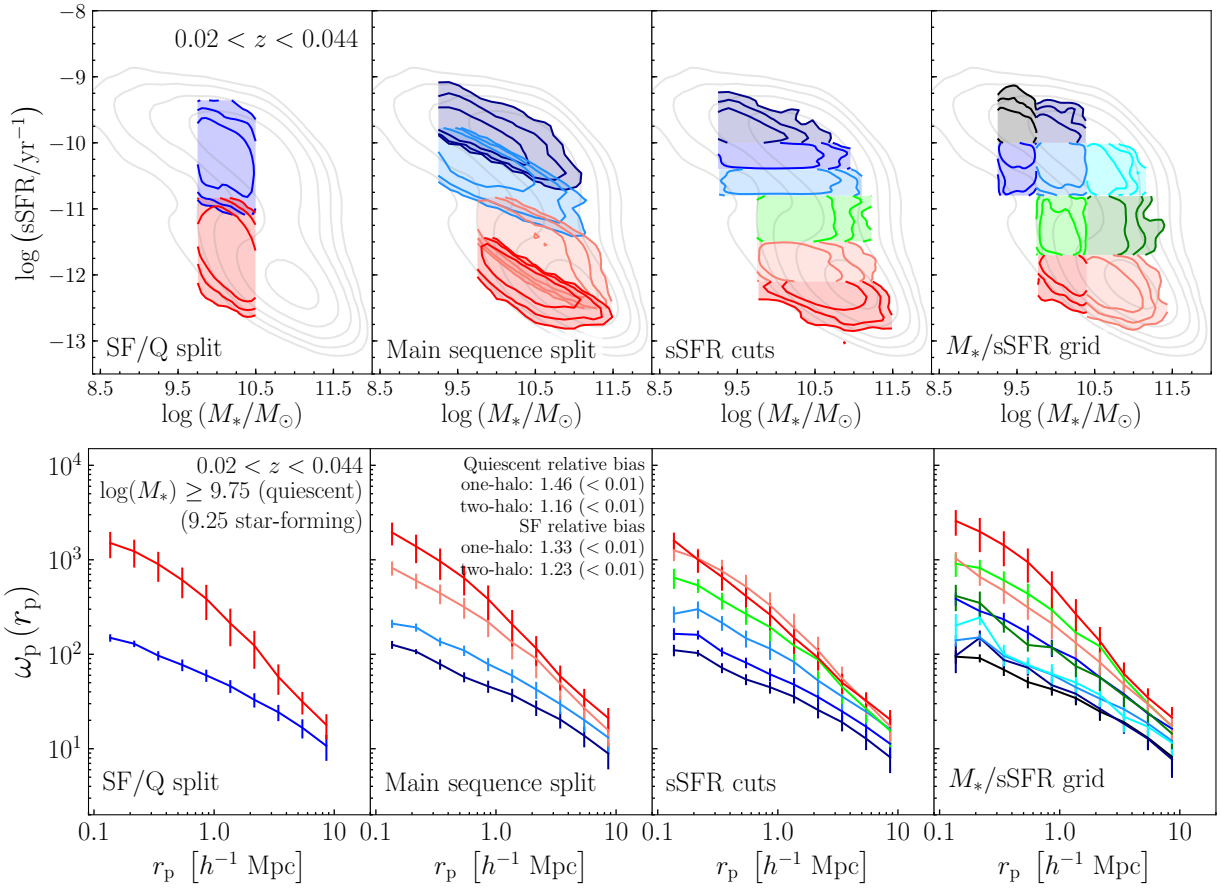

Figure 4.1: Top row: Specific star formation rate (sSFR) versus stellar mass for all SDSS galaxy samples used here. From left to right galaxies are divided into (i) star-forming versus quiescent ("SF/Q split"), (ii) above versus below the star-forming and quiescent main sequences ("main sequence split"), (iii) cuts in sSFR ("sSFR cuts"), and (iv) cuts in both sSFR and stellar mass ("M_*/sSFR grid"). All samples are stellar mass complete, with $\log(M_*/\mathrm{M}_\odot) > 9.25$ for star-forming and $\log(M_*/\mathrm{M}_\odot) > 9.75$ for quiescent galaxy samples (see text for details). Bottom row: The projected correlation function $\omega_p(r_p)$ for each of the galaxy samples shown in the top row. The relative biases (see §4.3.2) on one-halo and two-halo scales of "main sequence split" samples are given. Errors on $\omega_p(r_p)$ are estimated by jackknife resampling.

strongly clustered than star-forming galaxies at fixed stellar mass. This confirms previous studies of the dependence of SDSS clustering on galaxy color (e.g. Heinis et al., 2009; Hearin et al., 2014; Watson et al., 2015), often used as a proxy for SFR.

The "main sequence split" samples in Figure 4.1 (second column) show that clustering strength is correlated with sSFR at fixed stellar mass *within* both the star-forming and quiescent populations. Within the star-forming main sequence, galaxies below the sequence are substantially more strongly clustered than galaxies above the sequence. The relative bias between these samples is 1.33 ± 0.02 on one-halo scales and 1.23 ± 0.03 on two-halo scales. We find similar results within the quiescent population, where galaxies below the quiescent sequence are more clustered than galaxies above the sequence, which have higher sSFR at a given stellar mass. This is the first time this has been shown in SDSS and reflects the trends seen at higher redshift in Mostek et al. (2013) and C17.

The third set of samples ("sSFR cuts") display an anticorrelation between sSFR and clustering strength across the full galaxy population, although the trend is more pronounced for star-forming galaxies. In the lower panel of the third column of Figure 4.1 the amplitude of $\omega_{\rm p}(r_{\rm p})$ increases smoothly as sSFR decreases across five of the six samples, from the highest sSFR sample (dark blue) to the second lowest sSFR sample (light red). The lowest sSFR sample (red) is similar to that of the next lowest sSFR sample (light red); within the errors $\omega_{\rm p}(r_{\rm p})$ is the same for these two samples on both one-halo and two-halo scales. The lack of differentiation of $\omega_{\rm p}(r_{\rm p})$ for the two lowest sSFR samples could be due in part to the difficulty of estimating robust SFRs for galaxies with very low star formation rates.

The final set of samples ("stellar mass/sSFR grid") are most easily interpreted by considering separately subsets confined to either a given stellar mass or sSFR bin. Following C17, these samples are used primarily to fill out the range of stellar mass and sSFR *ratios* over which we explore the dependence of clustering on sSFR at fixed stellar mass and on stellar mass at fixed sSFR in the following sections.

4.4.2 Projected Correlation Functions in Mocks

In this section we compare the clustering measurements in SDSS and PRIMUS data to equivalent measurements in mock galaxy catalogs at $z = 0$, $z = 0.45$, and $z = 0.9$. Table 4.2 lists the details and two-halo bias measurements of all mock galaxy samples.

The UNIVERSEMACHINE model is observationally constrained in part by measurements of stellar mass-complete clustering in SDSS data (at $z \sim 0$) and PRIMUS data (at $z \sim 0.45$). The model utilizes clustering measurements of star-forming and quiescent galaxies separately,

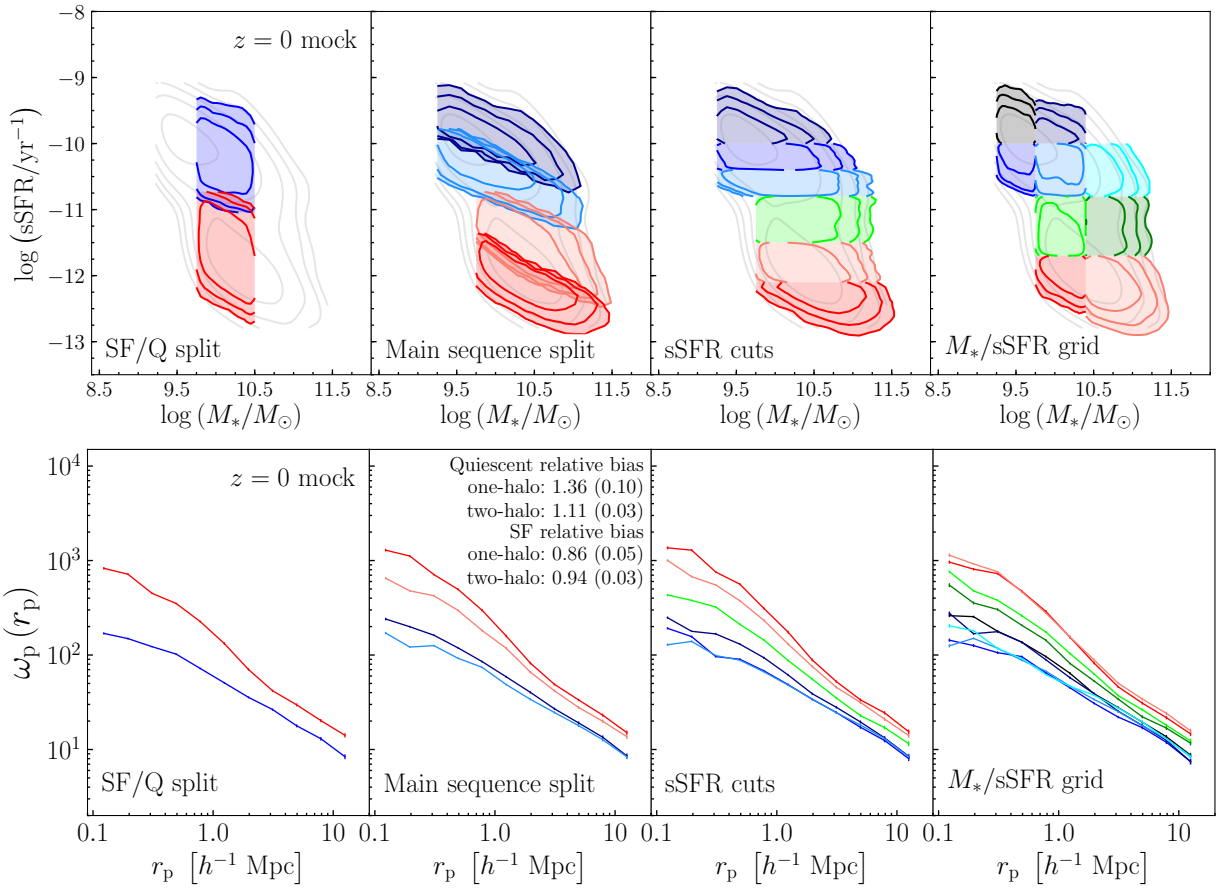

Figure 4.2: Analogous to Figure 4.1 but for the $z = 0$ mock galaxy catalog. The top row shows mock galaxy sample distributions in the sSFR-stellar mass plane. All samples are stellar mass complete, as described in the text. The bottom row shows the projected correlation function $\omega_p(r_p)$ for each sample show in the top row, and the relative biases (see §4.3.2) on one-halo and two-halo scales of "main sequence split" samples are given in the second panel.

but does *not* directly incorporate measurements of clustering dependence in narrower bins in sSFR or the intra-sequence relative bias previously observed in PRIMUS. A natural question is whether and to what extent does UNIVERSEMACHINE reproduce the variation in clustering strength with sSFR observed *within* the star-forming and quiescent galaxy populations in both SDSS and PRIMUS data?

Figure 4.2 is analogous to Figure 4.1 and shows the sSFR and stellar mass distributions and projected correlation functions of galaxy samples in the $z = 0$ mock described above in §4.2. There is excellent agreement between SDSS and the $z = 0$ mock for the star-forming/quiescent split galaxy samples, largely by design. The amplitude of the $\omega_p(r_p)$ one-halo term for quiescent mock galaxies is smaller than for the analogous SDSS galaxy sample. However, it is known that the clustering amplitude of SDSS galaxies is higher at $z < 0.05$ (e.g. Figure C5 of Behroozi et al. (2019) and the associated discussion).

Clustering in the SDSS data and the $z = 0$ mock further diverge when we consider the "main sequence split" samples. The relative bias within the star-forming $z = 0$ mock galaxy population—i.e. the bias ratio of galaxies with above average to below average sSFRs—is less than unity on both one-halo and two-halo scales, while in the data it is greater than unity. We discuss this reversal below in §4.5.

Two differences between the $z = 0$ mock and SDSS data are present in the third set of samples ("sSFR cuts"), which divide the galaxy population into six bins in sSFR. In the mock the clustering strength of the three samples spanning the quiescent sequence correlates with sSFR, especially on one-halo scales. The lowest sSFR quiescent sample (red) has the largest $\omega_p(r_p)$, followed by the next lowest sSFR sample (light red). The highest sSFR quiescent sample (light green) is the least strongly clustered of the three quiescent mock samples, and splits the difference in $\omega_p(r_p)$ amplitude between the other quiescent samples and the three star-forming samples. In contrast, the quiescent "sSFR cuts" samples in SDSS data are less differentiated in terms of relative clustering strength than the corresponding mock samples. The projected correlation

functions of lowest and second lowest sSFR samples agree within the errors, on both one-halo and two-halo scales. As previously discussed in §4.4.1, the lack of differentiation in $\omega_{\rm p}(r_{\rm p})$ between the two lowest sSFR samples in SDSS may be at least partly be due to the difficulty of robustly inferring SFRs for SDSS galaxies with the lowest rates of star formation.

At higher redshift we compare our clustering results in mock catalogs to C17's clustering measurements of analogous galaxy samples in PRIMUS data at $0.2 < z < 0.7$ (which we compare to the $z = 0.45$ mock) and at $0.7 < z < 1.2$ (which we compare to the $z = 0.9$ mock). Interestingly, there are different trends in terms of agreement between the higher redshift mocks and PRIMUS data than for the $z = 0$ mock and SDSS data.

As expected, the star-forming/quiescent split mock samples at both $z = 0.45$ (Figure 4.3) and $z = 0.9$ agree with what C17 finds in PRIMUS data at $0.2 < z < 0.7$ and $0.7 < z < 1.2$: quiescent galaxies are more strongly clustered than star-forming galaxies at fixed stellar mass. This agreement is unsurprising, as the star-forming/quiescent split sample results at $z \sim 0.45$ from C17 serve as constraints for the UNIVERSEMACHINE model.

The "main sequence split" mock samples divide the star-forming and quiescent populations each into two samples with identical stellar mass distributions, allowing us to compare the clustering of star-forming galaxies with above average and below average sSFRs, independent of stellar mass, and likewise for quiescent galaxies. We find a correlation between clustering amplitude and sSFR *within* both the star-forming and quiescent sequences at $z = 0.45$ and $z = 0.9$, although the magnitude of the effect is stronger at $z = 0.45$, particularly for the quiescent population. These results again agree with what C17 find in PRIMUS data: on both one-halo and two-halo scales star-forming galaxies with the highest sSFRs are less clustered than those with sSFRs below the SFMS. Similarly, quiescent galaxies with the lowest sSFRs are more clustered than those with above average sSFRs.

The third set of galaxy samples ("sSFR cuts") also display qualitative agreement between the mocks and the corresponding PRIMUS data samples at both $0.2 < z < 0.7$ and $0.7 < z < 1.2$,

although direct comparisons of $\omega_p(r_p)$ for the $0.7 < z < 1.2$ data samples and $z = 0.9$ are complicated by the higher noise in the data samples. At $0.2 < z < 0.7$ C17 find a general decline in the amplitude of $\omega_p(r_p)$ with increasing sSFR, although the two lowest sSFR samples have the same one-halo clustering amplitude within the errors, and two of the three star-forming samples have nearly identical clustering strengths on two-halo scales. In the $z = 0.45$ mock the corresponding two star-forming samples also have nearly identical clustering amplitudes on both one-halo and two-halo scales. The highest sSFR star-forming mock sample has the lowest clustering amplitude, which C17 also find for PRIMUS data. While in the $z = 0.45$ mock we see a clear decline in clustering strength with increasing sSFR across the three quiescent samples, this distinction is less prominent in the corresponding quiescent data samples.

At $0.7 < z < 1.2$ the projected correlation functions of the PRIMUS "sSFR cuts" samples are noisier, and a more useful comparison to the corresponding mock is made by comparing the absolute and relative biases, as performed in the following subsections.

4.4.3 Absolute Bias of Galaxy Samples in Data and Mocks

Figure 4.4 shows the absolute bias on two-halo scales of the "main sequence split" and "sSFR cuts" galaxy samples for both data and mocks at $z \sim 0$, $z \sim 0.45$, and $z \sim 0.9$. At $z \sim 0$ there is an overall normalization difference between the data and mock that is not present at higher redshift: the bias values in the mock samples are generally lower than in the corresponding data sample. However it is known that SDSS data exhibits a clustering excess at $z < 0.05$ (see Figure C5 of Behroozi et al., 2019), which aligns with the redshift range used here, and is consistent with the bias offsets between the data and $z = 0$ mock galaxy samples shown in Figure 4.4.

As an additional check we also tested using time-averaged (versus instantaneous) SFRs for the $z = 0$ mock. While this did slightly improve agreement with the data, the overall trends were the same as using those found using instantaneous SFRs.

Up to the overall normalization difference discussed above, the data and $z = 0$ mock

agree well for quiescent galaxy samples (red, light red, and green points in Figure 4.4). The one exception is the two "sSFR cuts" samples with the lowest sSFRs (red and light red), which are reversed from the general trend: the lowest sSFR sample is less biased than the next lowest sSFR sample. As discussed in §4.4.1 above, this may be due to the difficulty of robustly estimating SFRs for galaxies with the lowest rates of star formation with sufficient accuracy to meaningfully differentiate between the galaxies in these two samples.

For star-forming galaxy samples (light blue, blue, and dark blue points in Figure 4.4, highlighted by the two gray circles in the lower left panels) the data and $z = 0$ mock do not agree. In the data the bias decreases monotonically with increasing sSFR, while in the mock the highest

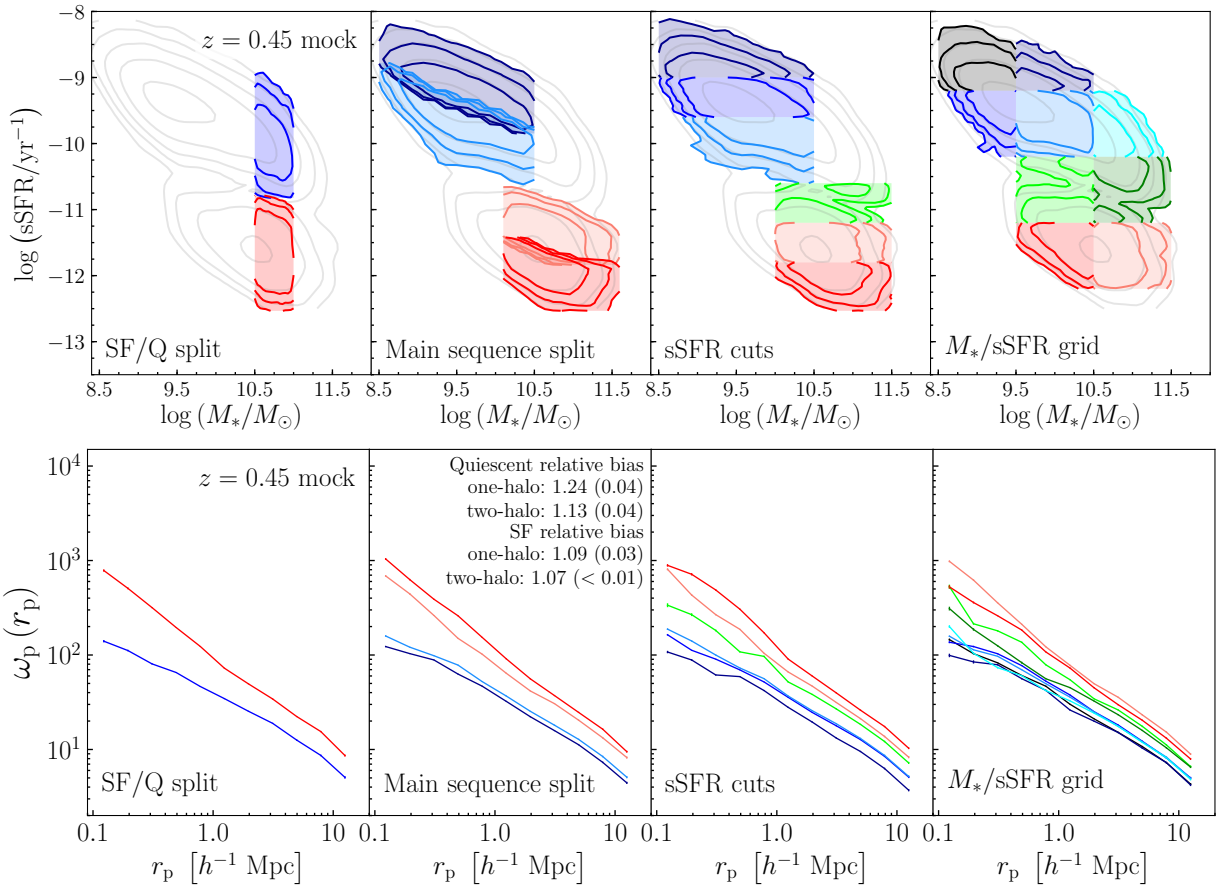

Figure 4.3: Same as Figure 4.2 but for the $z = 0.45$ mock galaxy catalog. Only the star-forming/quiescent split samples (first column) are stellar mass complete. We compare these results to Figure 2 of C17, which shows analogous measurements for PRIMUS galaxy samples at $0.2 < z < 0.7$ and $0.7 < z < 1.2$.

sSFR samples are *more* biased than star-forming galaxies with lower sSFRs, i.e. the opposite trend. This discrepancy is not seen at the higher redshifts.

Agreement between the data and corresponding mock is strongest at $z \sim 0.45$, where the data and mock values match within the errors for every galaxy sample. The $z = 0.9$ mock samples also agree well with the corresponding data samples, particularly for star-forming galaxies. Within the quiescent population the lowest sSFR data sample is substantially more biased in the data than in the mock, both when quiescent galaxies are split into two samples above and below the quiescent main sequence in the stellar mass–sSFR plane, and into three samples using simple cuts in sSFR. As noted above, at these higher redshifts the PRIMUS results are noisier, due to smaller sample sizes.

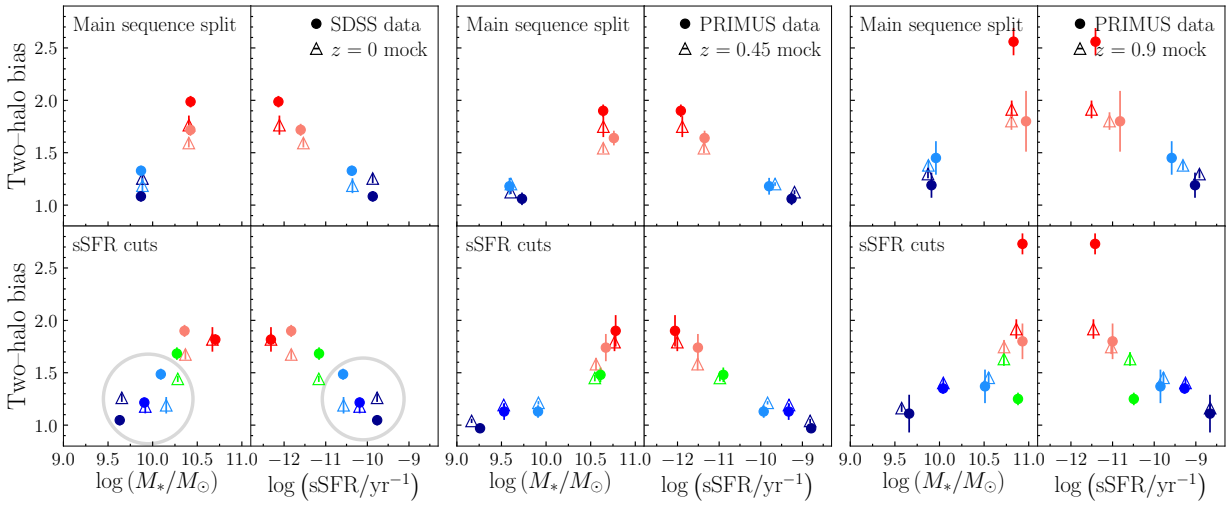

Figure 4.4: Absolute bias measured on two-halo scales as a function of mean stellar mass (left column in each set of panels) and mean sSFR (right column in each set of panels) for data (filled circles) and mock (open triangles) galaxy samples. Shown are the "main sequence split" (top row) and "sSFR cuts" (bottom row) samples for $z = 0$ (left panels), $z = 0.45$ (middle panels), and $z = 0.9$ (right panels). The colors used are the same as in Figures 4.1, 4.2, and 4.3. Errors are estimated by jackknife resampling. Gray circles highlight the area of disagreement between the data and model at $z = 0$, discussed further in the text.

4.4.4 Relative Bias of Galaxy Samples in Data and Mocks

We now compare the *relative* biases between pairs of galaxy samples in SDSS and PRIMUS data to the corresponding galaxy sample pairs in mocks. The relative clustering strengths of galaxy samples within the same volume can have smaller uncertainty than the absolute biases because cosmic variance largely cancels out in relative bias measurements.

Berti et al. (2019) refer to the clustering strength dependence on sSFR *within* the star-forming or quiescent sequence as "intra-sequence relative bias" (ISRB). We adopt that term here to refer to the relative biases of our "main sequence split" galaxy samples in data and mocks.

The ISRB of quiescent galaxies in the $z = 0$ mock agrees well with SDSS data within the errors: the relative bias between quiescent mock galaxies with above average versus below average sSFRs is 1.24 ± 0.03 on one-halo scales and 1.13 ± 0.03 on two-halo scales, which is $\sim 9\%$ and $\sim 4\%$ lower than in SDSS data, respectively. This agreement disappears for the star-forming population, however, where in the $z = 0$ mock star-forming galaxies with below average sSFRs are *less* strongly clustered than those with above average sSFRs, the opposite of what we find in SDSS data. On both one-halo and two-halo scales the ISRB within the star-forming $z = 0$ mock galaxy population is less than unity on both one-halo and two-halo scales, while it is greater than unity in the data.

At higher redshift there is good qualitative agreement between the mocks and PRIMUS data at both $z = 0.45$ and $z = 0.9$. The ISRB C17 find in quiescent and star-forming PRIMUS galaxies on both one-halo and two-halo scales, at both $0.2 < z < 0.7$ and $0.7 < z < 1.2$, is also present in the $z = 0.45$ and $z = 0.9$ mocks, although the *magnitude* of the ISRB present in the mocks differs somewhat from the corresponding PRIMUS data.

In the $z = 0.45$ mock the ISRB values are generally $\sim 10\%$ lower than in the data, with the exception of the quiescent one-halo term, which is $\sim 5\%$ greater in the mock than in the data. The ISRB in the $z = 0.9$ mock is $\sim 20\%$ to 40% lower than in the data with the exception of the one-halo term for star-forming galaxies, which agrees precisely with the PRIMUS data value.

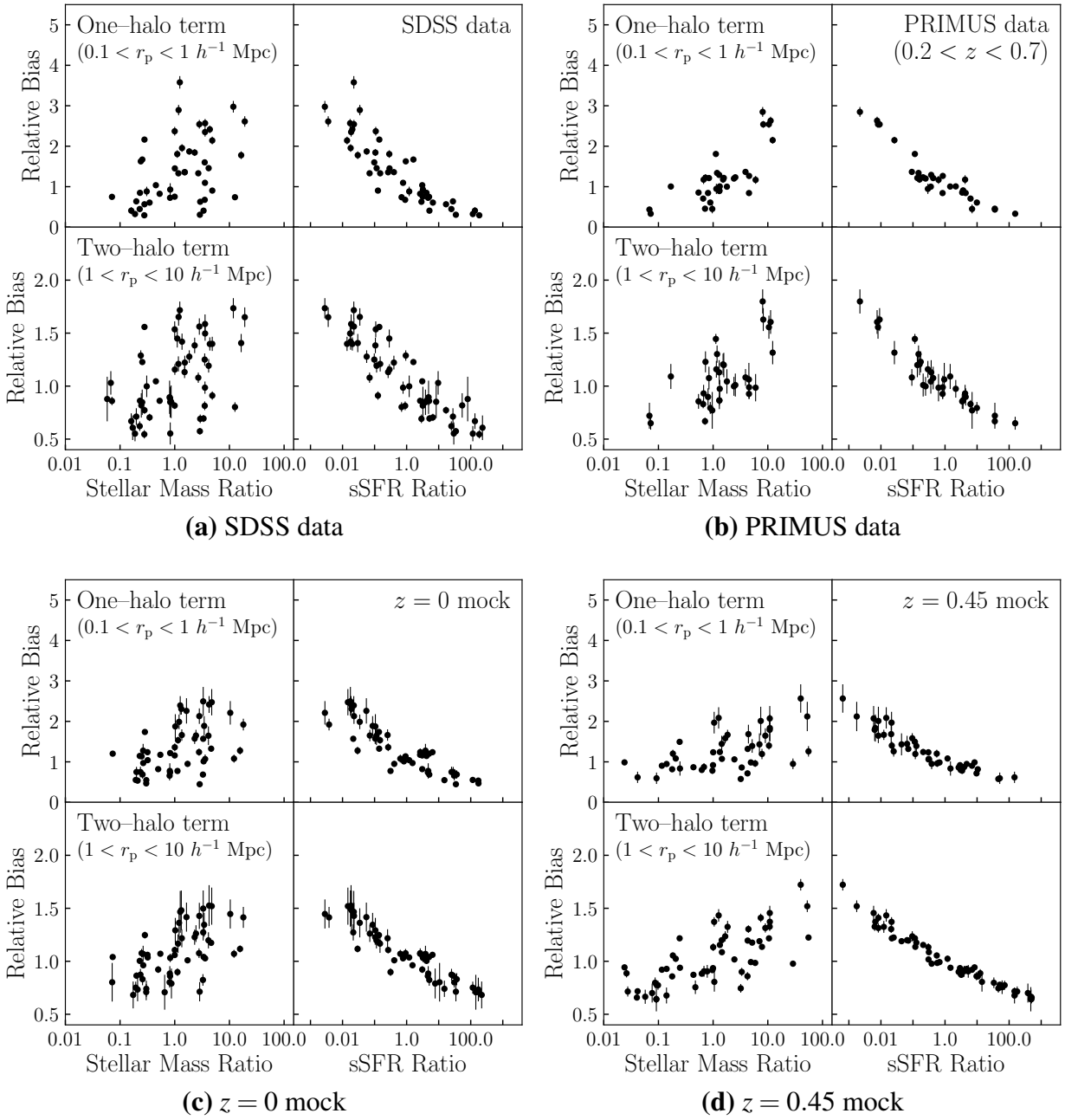

Figure 4.5: (a) Relative biases of pairs of SDSS galaxy samples as a function of each pair's stellar mass ratio (left column) and sSFR ratio (right column). The top and bottom rows show results one one-halo and two-halo scales, respectively. (b) Relative biases of pairs of $z = 0$ mock galaxy samples as a function of each pair's stellar mass ratio and sSFR ratio. (c) Same as panel (a) but for PRIMUS galaxy samples at $0.2 < z < 0.7$ (recreated from data previously published in C17). (d) Same as panel (b) but for the $z = 0.45$ mock.

Following the presentation in C17, Figure 4.5 shows the relative bias between pairs of galaxy samples in SDSS of PRIMUS data (panels (a) and (b),[3] respectively), and between corresponding pairs of galaxy samples in the relevant mock (panels (c) and (d)), as functions of the stellar mass *ratio* and sSFR *ratio* of each pair of galaxy samples. In other words, the data points in Figure 4.5 are a set of unique pairs taken from each of the galaxy samples we create in the stellar mass–sSFR plane. For example, the two "star-forming/quiescent split" samples yield one pair: "red/blue". Relative bias is shown versus stellar mass ratio on the left of each of the four panels, and verses sSFR ratio on the right. The top of each panel shows results on one-halo scales, while two-halo scales are shown on the bottom of each panel.

All possible galaxy sample pairs are not shown in panel (b) of Figure 4.5 because C17 include only pairs of PRIMUS data samples for which the one-halo relative bias error is less than 25%. In essence, the larger sample sizes provided by SDSS allow us to fill this parameter space more completely at $z \sim 0$. We show results for $z \sim 0$ and $z \sim 0.45$; the results at $z \sim 0.9$ are very similar.

We find similar trends at $z \sim 0$ compared to C17's results at higher redshift. On both one-halo and two-halo scales the correlation between relative bias and sSFR ratio clearly has less scatter than the trend with stellar mass ratio. A quick comparison of the the right columns of panels (a) and (b) may seem to suggest the correlation of relative bias with sSFR is tighter at higher redshift, but this could also be due to the lower signal-to-noise of PRIMUS data at $0.2 < z < 0.7$ compared to SDSS data.

Panels (c) and (d) of Figure 4.5 present the same same analysis in the $z = 0$ and $z = 0.45$ mocks. The mocks at both redshifts display a similar relatively tight dependence of relative bias on sSFR ratio that we see in the data. There is little to no correlation between relative bias and stellar mass ratio at either redshift, in qualitative agreement with the $z \sim 0$ data. For clarity Figure 4.5 does not show results for the $z = 0.9$ data or mock, but the trends agree with our results

[3]Panel (b) of Figure 4.5 is recreated with permission from results previously published in C17.

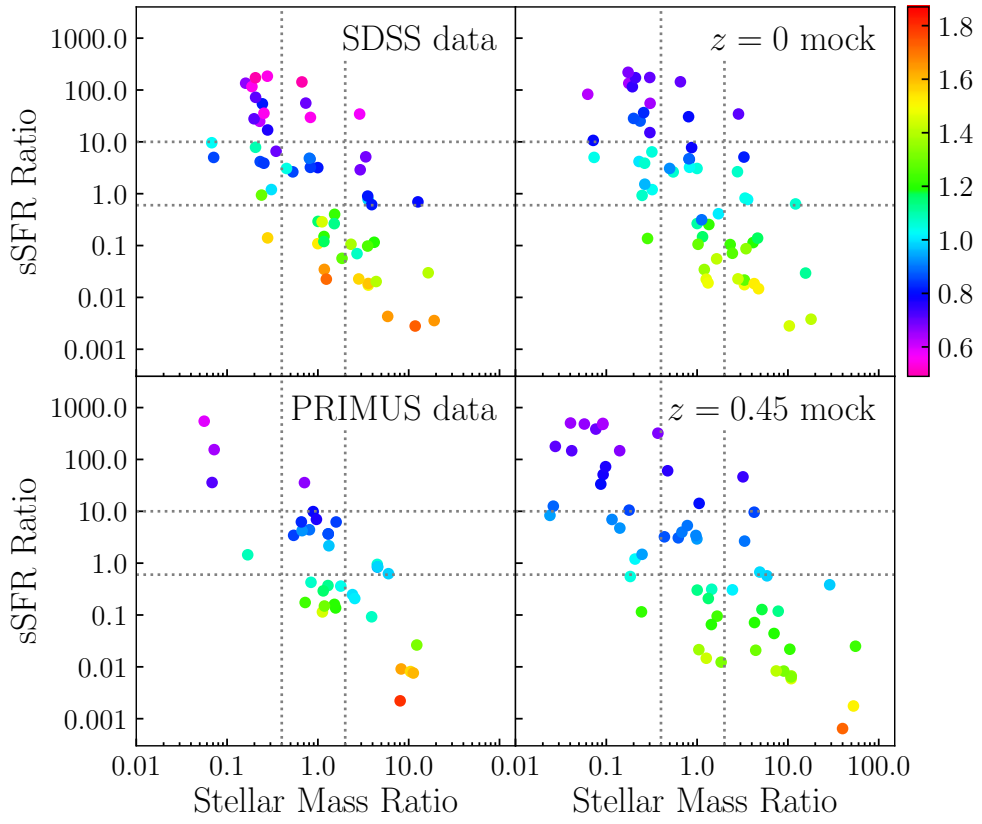

Figure 4.6: Two-halo relative bias of pairs of galaxy samples the data (left column) and corresponding mock (right column) at $z = 0$ (top row) and $z = 0.45$ (bottom row), shown as a joint function of the stellar mass ratio and sSFR ratio of each sample pair. The color of each point represents the magnitude of that pair's relative bias, as shown in the color bar. The dotted lines highlight regions of fixed stellar mass ratio or sSFR ratio where our galaxy samples probe several orders of magnitude in the ratio of the other parameter. Variations in sSFR ratio at fixed stellar mass ratio correspond to strong differences in relative bias, while variations in stellar mass ratio at fixed sSFR ratio do not result in substantially different relative bias values.

at lower redshift.

4.4.5 The Joint Dependence of Relative Bias on Stellar Mass and sSFR

Again following C17, in Figure 4.6 we present a way to understand the *joint* dependence of relative bias on both stellar mass ratio and sSFR ratio at in both the data and corresponding mocks. Figure 4.6 shows the relative bias on two-halo scales of pairs of galaxy samples in the data (left column) and corresponding mock (right column) as a joint function of each pair's stellar mass

ratio and sSFR ratio, with the magnitude of the relative bias represented by the color bar in the figure. The dotted lines bracket regions of either fixed stellar mass ratio or sSFR ratio where our samples probe several of magnitude in the ratio of the other parameter. The vertical dotted lines highlight sample pairs with stellar mass ratios of 0.6–2 and sSFR ratios from $\sim 10^{-3}$ to $\sim 10^{2}$. The relative biases of these sample pairs span the full range of relative bias values observed, from ~ 1.6 for the smallest sSFR ratios to ~ 0.6 for the largest sSFR ratios. For comparison, the horizontal dotted lines highlight sample pairs with sSFR ratios of 0.9–10, across three orders of magnitude in stellar mass ratio, and show little variation in relative bias across the range of stellar mass ratios probed by our samples. These results confirm at $z \sim 0$ the trends observed by C17 in PRIMUS data at $0.2 < z < 1.2$, namely that sSFR ratio is more relevant for determining the relative bias of two galaxy samples than stellar mass ratio. This implies that clustering amplitude is more fundamentally linked to sSFR than to stellar mass.

4.5 Modifying the Mock Galaxy Catalog at Low Redshift

As noted in §4.4.3 there is less agreement between the data and corresponding mock at $z \sim 0$ than at either $z \sim 0.45$ or $z \sim 0.9$, particularly within the SFMS, where sSFR in the $z = 0$ mock is anticorrelated with clustering strength (left panels of Figure 4.4). This anticorrelation does *not* appear in the data at any of the redshifts studied here, nor is it present in the $z = 0.45$ or $z = 0.9$ mock. This arises in the UNIVERSEMACHINE because there is a redshift-dependent parameter $(\sigma_{\rm SF,uncorr}(z))$ that determines the scatter between SFR in the main sequence and halo accretion rate. Specifically, the proxy used for halo accretion rate is $\Delta V_{\rm max}$, the change in the maximum circular velocity of a halo over the last dynamical time, $\tau_{\rm dyn} \equiv \left(4/3\,\pi G \rho_{\rm vir}\right)^{-1/2}$, where $\rho_{\rm vir}$ is the virial overdensity (Bryan & Norman, 1998).[4]

The $\sigma_{\rm SF,uncorr}(z)$ parameter has no direct constraints from any of the observations used as

[4]In detail, we use the larger of $\tau_{\rm dyn}$ or $\tau_{\rm M_{peak}}$, the time at which the halo reached its peak mass, to account for sustained quenching of extremely stripped (sub)halos. See §3.1 of Behroozi et al. (2019) for additional details.

inputs to the UNIVERSEMACHINE, however, and so functions as a nuisance parameter to capture uncertainty in the underlying galaxy–halo relationship. In the current best-fit UNIVERSEMACHINE model, this parameter apparently results in a moderate correlation strength between main sequence SFR and halo accretion at $z \gtrsim 0.5$ and a negligible correlation strength at $z = 0$, causing the behavior seen in Figure 4.4.

Evidently, the new SDSS measurements presented here have the constraining power to directly measure this previously-unknown correlation strength. Motivated by this additional constraining power, we examine how the strength of this galaxy–halo correlation can be better understood through the full, two-dimensional dependence of clustering upon stellar mass and sSFR.

Rather than rerunning the full UNIVERSEMACHINE machinery while including these new measurements, which is beyond the scope of this chapter, here we carry out a targeted study of this effect by creating a "modified" $z = 0$ mock with an imposed stronger correlation between galaxy SFR and halo mass accretion rate (using $\Delta V_{\rm max}$ at fixed $V_{\rm max}$ at $M_{\rm peak}$[5] as a proxy). We created this mock by re-running the UNIVERSEMACHINE with the best-fit parameter set, except that we lowered $\sigma_{\rm SF,uncorr}$ at $z = 0$ so that the correlation between main sequence SFR and halo accretion was effectively the same ($r = 0.5$) as at higher redshifts.

Figure 4.7 demonstrates this modification visually, showing the SFR versus halo accretion rate[6] for star-forming galaxies in the default mocks at $z = 0$, 0.45, and 0.9, and for the "modified" $z = 0$ mock. In the default model the SFR–halo accretion rate correlation for star-forming galaxies is strongest in the $z = 0.9$ mock and declines to a very shallow trend at $z = 0$. In our "modified" $z = 0$ mock this correlation is boosted to be as strong as it is at higher redshift in the default model.

In Figure 4.8 we repeat the analysis of Figures 4.4 and 4.6 for the "modified" $z = 0$ mock. The left panels show absolute bias on two-halo scales as a function of mean stellar mass and

[5] $V_{\rm max}$ at $M_{\rm peak}$ is the maximum circular halo velocity at $M_{\rm peak}$, the peak historical mass achieved by a halo.

[6] Specifically, Figure 4.7 shows the relationship between rank-ordered SFR and rank-ordered halo accretion rate.

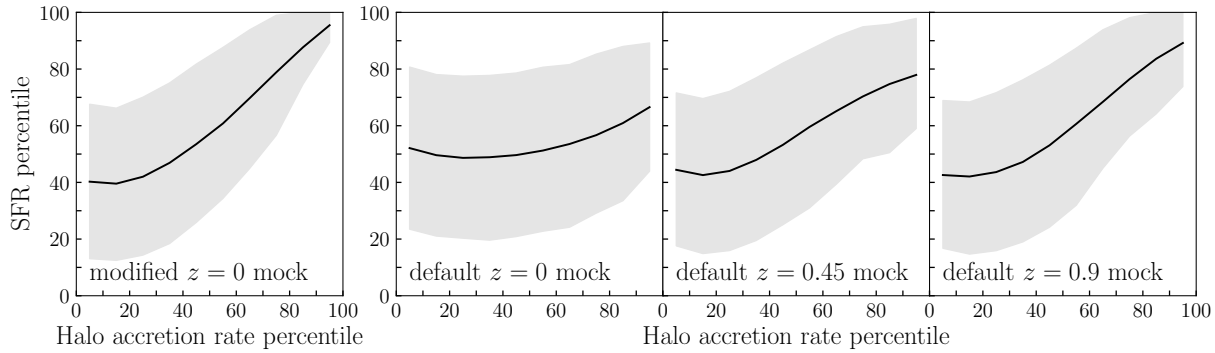

Figure 4.7: Mean galaxy SFR percentile rank versus halo accretion rate percentile rank for star-forming mock galaxies in the modified $z = 0$ mock (left panel) and the default mocks at $z = 0$, 0.45, and 0.9 (right three panels). In the "modified" $z = 0$ mock the correlation between SFR and halo accretion rate for star-forming galaxies is increased to ~ 0.5 from the default value of ~ 0. The shaded gray regions show 1σ deviation on the mean SFR.

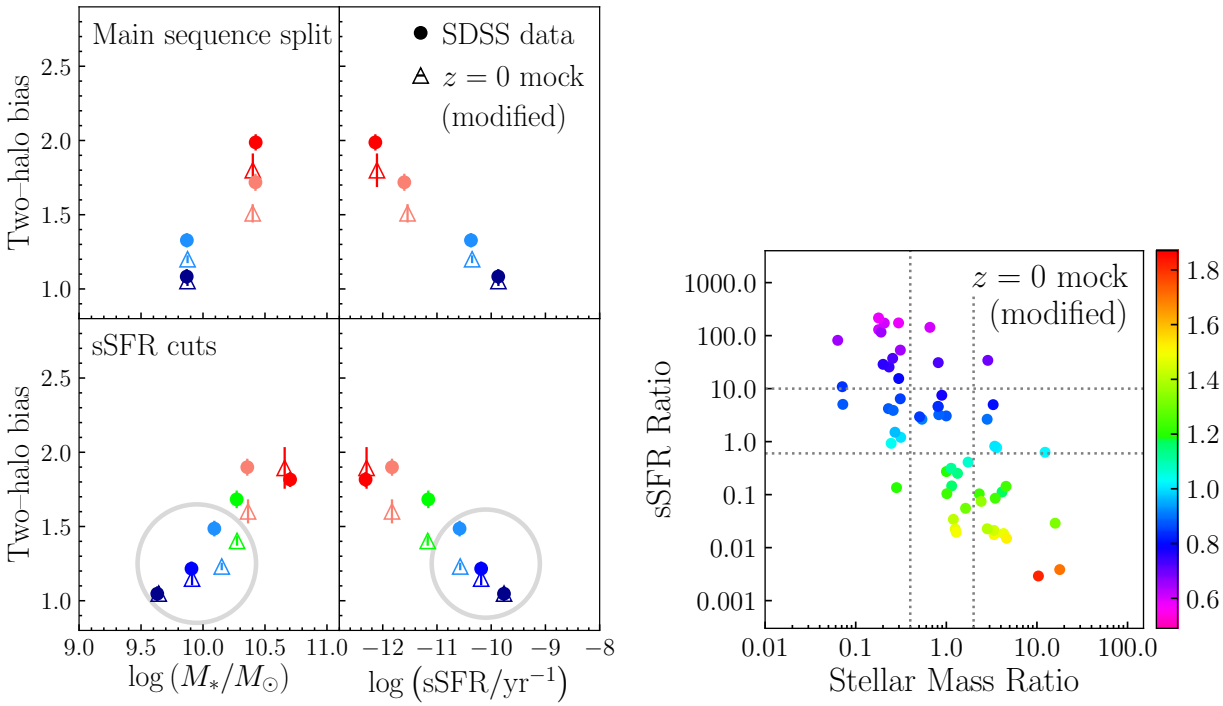

Figure 4.8: Left: Same as the left four panels of Figure 4.4 but for the "modified" $z = 0$ mock, which reproduces bias as a function of sSFR for star-forming SDSS galaxies better than the default model, as highlighted by the gray circles. Right: Same as the upper right panel of Figure 4.6 but for the "modified" $z = 0$ mock. Shown is the relative bias on two-halo scales of mock galaxy sample pairs as a joint function of stellar mass ratio and sSFR ratio; the color of each point indicates the relative bias value. The correlation between relative bias and sSFR ratio at fixed stellar mass is stronger than in the default $z = 0$ mock, which also makes this model a better fit to SDSS data (upper left panel of Figure 4.6) than the default.

mean sSFR for SDSS data and the "modified" $z = 0$ mock for the "main sequence split" (top row) and "sSFR cuts" (bottom row) sets of galaxy samples. The gray circles highlight bias values for star-forming samples, which for the "modified" mock agree with SDSS data much better than the default model: although the slope is shallower than in the data, bias increases with decreasing sSFR for the star-forming samples in this mock (as well as for quiescent samples, which is unchanged from the default $z = 0$ mock).

The right panel of Figure 4.8 is the same as the upper right panel of the Figure 4.6, but for the "modified" $z = 0$ mock: two-halo relative bias of galaxy sample pairs as a joint function of the stellar mass ratio and sSFR ratio of each pair. The difference between the default and "modified" $z = 0$ mocks is the range of relative bias values. In the default $z = 0$ mock the two-halo relative bias varies from 0.63 at the smallest sSFR ratios to 1.53 at the largest. This expands to 0.58–1.81 in the "modified" $z = 0$ mock over the same range of sSFR ratios, which is a better match to the range seen in SDSS data of 0.49–1.73. These results highlight the constraining power of both the absolute bias as a function of sSFR and the relative bias as a function of sSFR ratio for pairs of galaxy samples in constraining empirical models of galaxy evolution. In the following section we use exclusively the "modified" $z = 0$ mock and the default mocks at $z = 0.45$ and $z = 0.9$.

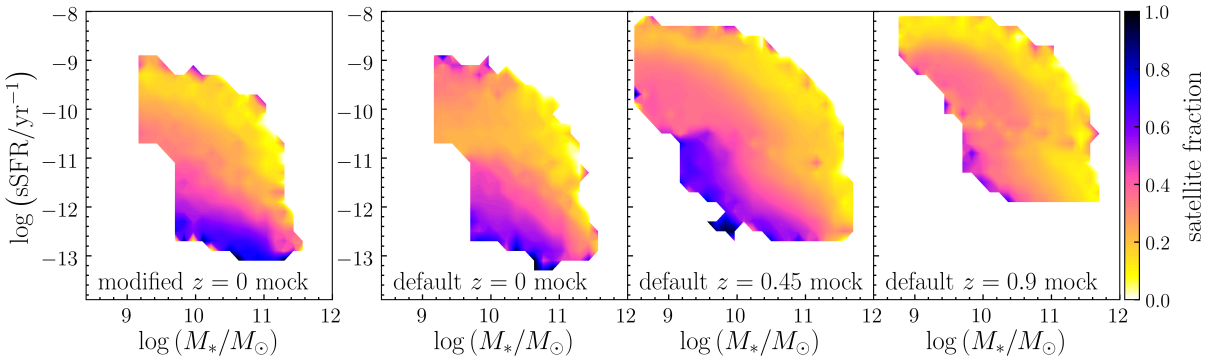

Figure 4.9: Satellite galaxy fraction as a function of stellar mass and sSFR for the "modified" $z = 0$ mock (left panel) and the default mocks at $z = 0$, 0.45, and 0.9 (right three panels). The modified $z = 0$ mock brings the satellite fraction distribution into closer agreement with the default mocks at higher redshift.

4.6 Contribution of Central Galaxies to Intra-sequence Relative Bias

In this section we use the mock galaxy catalogs to investigate the relative contributions of central and satellite galaxies to the result of §4.4 that galaxy clustering is a stronger function of sSFR at a given stellar mass than of stellar mass at fixed sSFR. Here we use exclusively the "modified" $z = 0$ mock and the default mocks at $z = 0.45$ and $z = 0.9$.

4.6.1 Relative Bias of Mock Central and Satellite Galaxies

Having shown agreement between data and mocks when considering various galaxy samples drawn from the full galaxy population, we now divide each mock galaxy sample into

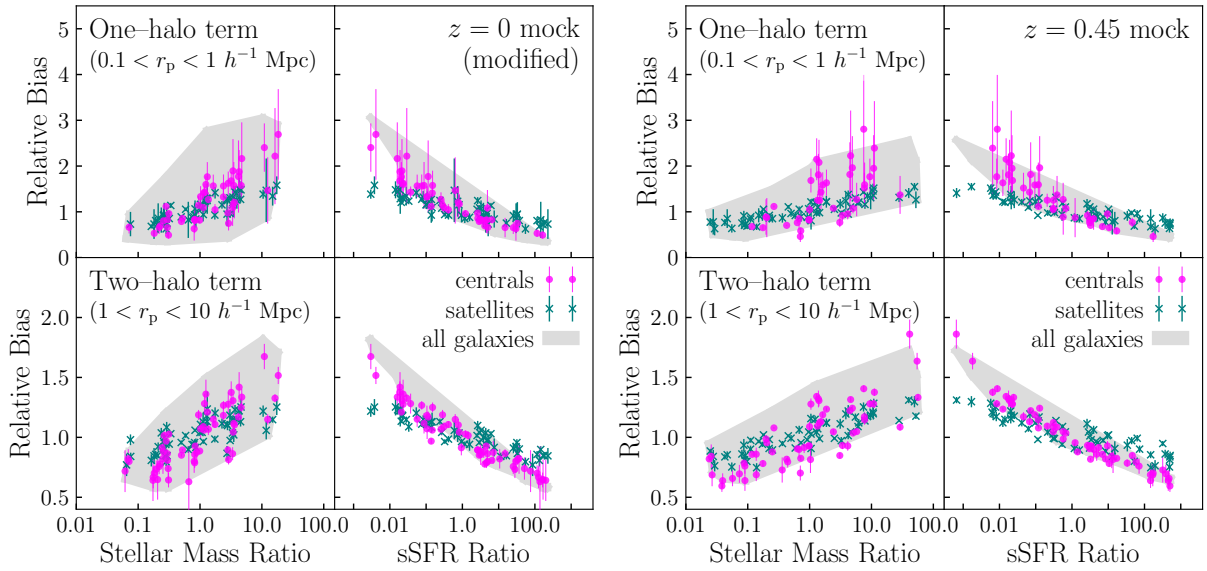

(a) $z = 0$ mock **(b)** $z = 0.45$ mock

Figure 4.10: (a) Relative biases of sample pairs of $z = 0$ mock galaxies as a function of each pair's stellar mass ratio and sSFR ratio, divided into centrals (magenta circles) and satellites (green × symbols). The grey shaded region is the result for all mock galaxies (i.e. without distinguishing centrals from satellites, as shown in panels (c) and (d) of Figure 4.5.) For clarity only points with errors less than 50% of the relative bias value are shown. (b) Same as panel (a) but for the $z = 0.45$ mock. Results at $z = 0.9$ are not shown but exhibit the same trends as those seen at lower redshifts: the correlations between relative bias and both sSFR and stellar mass ratio are due predominantly to central galaxies.

central and satellite components to determine the contribution of each to the trends seen in Figures 4.5 and 4.6. Figure 4.9 shows how the satellite galaxy fraction in the mocks changes with both stellar mass and sSFR. Like the presentation in Figure 4.7, the set of three panels on the right shows the default mocks, while the leftmost panel shows the "modified" $z = 0$ mock. The satellite fraction distribution is qualitatively different for star-forming galaxies in the default $z = 0$ mock compared to the default at higher redshift. In the "modified" $z = 0$ the satellite fraction distribution more closely resembles that of the higher redshift default mocks: within the SFMS the satellite fraction is lowest ($\lesssim 10\%$) for the highest sSFR galaxies and increases fairly smoothly across the main sequence to $\sim 40\%$ for the lowest sSFR star-forming galaxies. In the default $z = 0$ mock this trend is reversed across the lower-mass end of the SFMS.

Results showing the dependence of the relative bias as a function of stellar mass ratio and sSFR ratio separated in the mock samples into centrals and satellites are shown in Figure 4.10; centrals are represented by magenta circles and satellites by green $\times$ symbols. The gray shaded region is the result for all mock galaxies shown in panels (c) and (d) of Figure 4.5. We focus on the two-halo relative bias (bottom row of Figure 4.10) as this is the length scale at which central galaxy relative bias is well defined, and therefore also the scale at which meaningful comparisons can be made between centrals and satellites. The same trends are seen on smaller scales (top row), but the errors are larger for the central galaxy relative bias.

In both the $z = 0$ and $z = 0.45$ mocks the correlation between relative bias and sSFR ratio is driven by central galaxies. This can be clearly seen in the lower right sections of both panels (a) and (b) of Figure 4.10. In the $z = 0$ mock the two-halo relative bias of central galaxies increases from ~ 0.6 to ~ 1.7 with decreasing sSFR ratio across the nearly five orders of magnitude in sSFR ratio probed here. Over the same range in sSFR ratio the two-halo relative bias of mock satellites spans the narrower range of ~ 0.8 to ~ 1.3. At $z = 0.45$ the two-halo relative bias of mock centrals is again anticorrelated with sSFR ratio across five orders of magnitude, from ~ 0.6 at the largest sSFR ratios to ~ 1.8 at the smallest sSFR ratios (lower right of panel (b) in

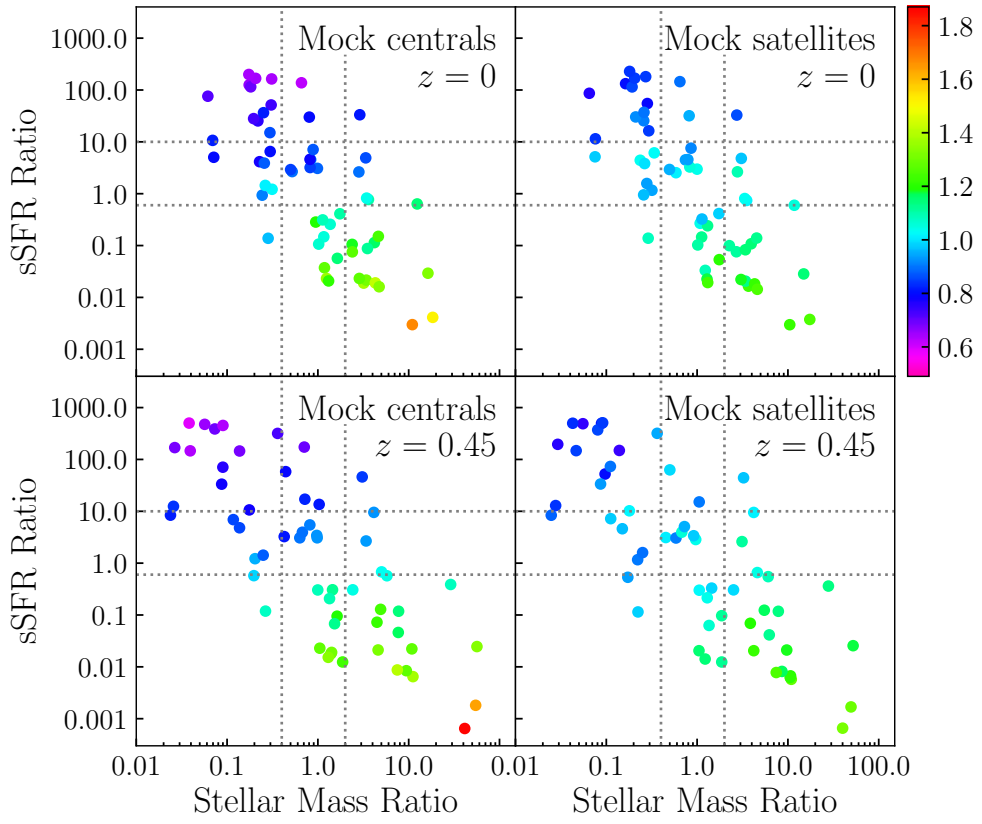

Figure 4.11: Similar to Figure 4.6 for the $z = 0$ (top row) and $z = 0.45$ mocks (bottom row): two-halo relative bias of mock galaxy sample pairs, shown as a joint function of stellar mass ratio and sSFR ratio, and divided into central and satellite galaxies (left and right columns, respectively). For clarity results for the $z = 0.9$ mock are not shown, but follow the same trends seen in the $z = 0$ and $z = 0.45$ mocks. Dotted lines highlight regions of fixed stellar mass ratio or sSFR ratio where our galaxy samples probe several orders of magnitude in the ratio of the other parameter. The dependence of relative bias on sSFR ratio at fixed stellar mass ratio (and not vice versa) is due predominantly to centrals; pairs of central galaxy samples span a larger range of relative biases compared to the range for satellite galaxies over the same span of sSFR ratios.

Figure 4.10). There is a shallower anticorrelation with slightly larger scatter between relative bias and sSFR ratio for mock satellites over the same range of sSFR ratios. We also note that in stellar mass ratio space the division between central and satellite galaxies is not as clean as in sSFR ratio space.

Figure 4.11 illustrates the difference between the trends for mock centrals and satellites differently (similar to the presentation of Figure 4.6), showing the relative bias of pairs of central galaxy samples (left column) and pairs of satellite galaxy samples (right column) as a joint

function of each pair's stellar mass ratio and sSFR ratio. In other words, to make this figure we remeasure the clustering and bias of each mock galaxy sample, first keeping only the central galaxies in each sample, then keeping only the satellites. We then calculate the relative bias of pairs of central-only samples, and likewise for satellite-only samples.[7]

The top and bottom rows of Figure 4.11 show results for $z = 0$ and $z = 0.45$ mocks, respectively. At both $z = 0$ and $z = 0.45$ the relative biases of central galaxies span nearly the entire range of the color bar, from magenta at the low end (~ 0.6) to orange near the high end (~ 1.8). In contrast, the relative biases of satellites at both redshifts span a narrower section of the color bar, from dark blue (~ 0.8) to light green (~ 1.3). We do not include the $z = 0.9$ mock in Figure 4.11, but the results follow the same trends seen in mocks at lower redshift.

In summary, we find that sSFR ratio—not stellar mass ratio—is the key factor influencing the clustering amplitude differences between galaxy samples. Moreover, this relationship is driven primarily by central galaxies.

4.6.2 Intra-sequence Clustering Differences

Next we use the simulations from which the mock catalogs are drawn to investigate the extent that ISRB is due to central galaxies alone, as opposed to an effect of different satellite fractions above and below each sequence.

Figure 4.12 shows the normalized two-point correlation functions (in three spatial dimensions, not projected onto the plane of the sky) of galaxy samples selected from the full outputs of the UNIVERSEMACHINE model. These samples use stellar mass and sSFR cuts identical to those that define the mock galaxy samples used in previous sections, but these samples are *not* subject to the observational effects applied to the simulation to create mock galaxy catalogs that mimic observational data (see §4.2.3).

[7]The stellar mass and sSFR ratios of both sets of samples are the same by design, as centrals and satellites are selected from the same parent samples (see Table 4.2).

The left column of Figure 4.12 shows the distribution of these galaxy samples in the stellar mass–sSFR plane, as in Figures 4.2 and 4.3 above. The remaining panels in each row show $\xi(r)$ for each sample divided by $\xi(r)$ of all galaxies *of the relevant type* (centrals, satellites, or both types together), which we call $\xi_{\rm norm}$. We measure $\xi(r)$ instead of $\omega_{\rm p}(r_{\rm p})$ for these galaxy samples because they do not have added line-of-sight position uncertainties. Our aim is to compare the normalized 3D clustering amplitudes of galaxy samples with different sSFRs, such that any variation in amplitude is purely a prediction of the model and not influenced by added observational effects.

As seen in Figure 4.12, normalized clustering amplitude decreases smoothly with increasing sSFR, both *within* the star-forming and quiescent populations, and *across* the entire galaxy population. This trend is present for all galaxies (centrals and satellites), and for just centrals. The one exception is star-forming satellite galaxies, where the trend is reversed at both $z = 0$ and $z = 0.45$: star-forming satellites with above average sSFR are *more* clustered than those with below average sSFR. This trend is present for star-forming satellites on both one-halo and two-halo scales, although the one-halo term is stronger.

To quantify the results of Figure 4.12 we compute the two-halo intra-sequence relative bias of star-forming and of quiescent mock galaxies, $b_{\rm rel}$, as the mean of $\sqrt{\xi_1(r)/\xi_2(r)}$ over $1\ h^{-1}\,{\rm Mpc} < r_{\rm p} < 10\ h^{-1}\,{\rm Mpc}$, where $\xi_1(r)$ and $\xi_2(r)$ are either for the light blue and dark blue "main sequence split" samples, respectively, or the red and light red "main sequence split" samples, respectively, as shown in the figure. We measure $b_{\rm rel}$ separately for all mock galaxies, just mock centrals, and just mock satellites.

Within the quiescent population the relative bias at $z = 0$ is 1.65 for all galaxies, 1.29 for centrals, and 1.17 for satellites. At $z = 0.45$ the values are lower, but the overall trend is the same: quiescent ISRB is greatest for all galaxies (1.42), lower for centrals (1.20), and lowest for satellites (1.10) We emphasize that the two "main sequence split" samples within each population (star-forming and quiescent) have the same stellar mass distribution by design.

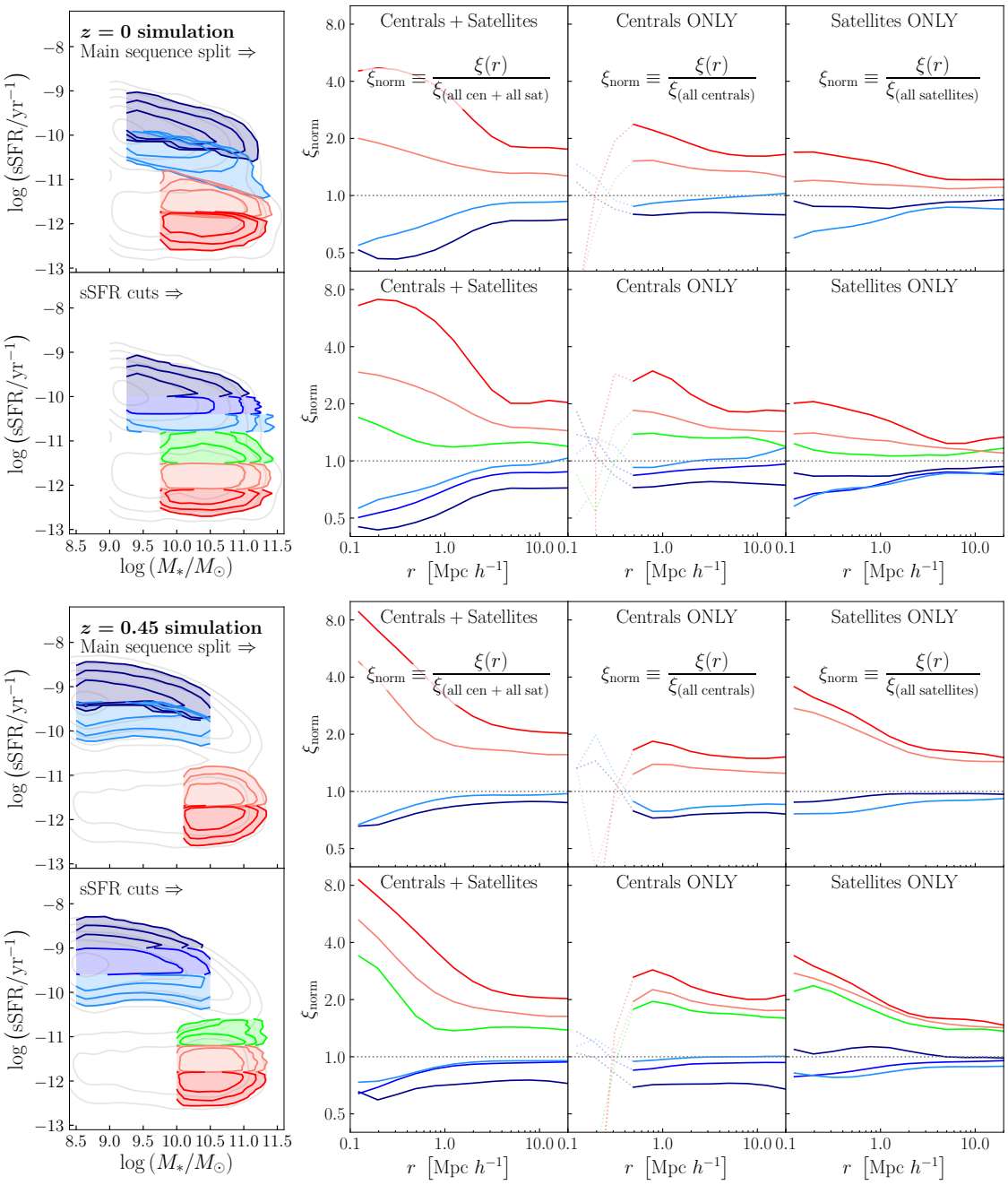

Figure 4.12: Normalized $\xi(r)$ for the "main sequence split" and "sSFR cuts" samples selected from the $z = 0$ (top two rows) and $z = 0.45$ (bottom two rows) simulations. For each sample $\xi_{\rm norm}$ is $\xi(r)$ for that sample divided by the correlation function for all simulated galaxies *of the relevant galaxy type*, i.e. centrals + satellites (second column), centrals only (third column), or satellites only (last column), as indicated in the relevant panels. The first column shows the stellar mass-sSFR distributions of the relevant samples in each row. While the stellar mass and sSFR cuts defining these samples are identical to those used to select mock galaxy samples used in previous sections, the samples shown here are taken from the full UNIVERSEMACHINE model output, i.e. these samples are *not* subject to observational effects such as magnitude limits or redshift errors. Note the $\log_2$ scale of the $\xi_{\rm norm}$ axis.

For star-forming mock galaxies at $z = 0$ the ISRB is 1.29 for all galaxies, 1.19 for centrals, and 0.93 for satellites, reflecting the greater clustering of star-forming satellites above the SFMS compared to those below the SFMS. Similarly, at $z = 0.45$ the ISRB is 1.10 for all star-forming mock galaxies, 1.09 for centrals, and 0.90 for satellites. While not shown in Figure 4.12, the trends at $z = 0.9$ again follow those at lower redshift.

4.7 Summary

In this chapter we present new measurements of the clustering of stellar mass-complete samples of SDSS galaxies at $z \sim 0.03$ as a joint function of stellar mass and sSFR. We split star-forming galaxies into samples above and below the SFMS with equivalent stellar mass distributions, and likewise for quiescent galaxies. We compare our SDSS results and C17's comparable measurements at intermediate redshift to mock galaxy catalogs at $z = 0$, 0.45, and 0.9 based on the empirical UNIVERSEMACHINE galaxy evolution model of Behroozi et al. (2019), focusing on the relative bias of various galaxy samples with different sSFR and stellar mass ratios. We show that this model fits PRIMUS and DEEP2 clustering data well, but the agreement with SDSS is not as strong. Our primary results are:

1. Galaxy clustering is a stronger function of sSFR at fixed stellar mass than of stellar mass at fixed sSFR. Galaxies above the SFMS (with higher sSFR) are less clustered than those below the SFMS (with lower sSFR), at a given stellar mass. We refer to this as *intra-sequence relative bias* (ISRB). A similar trend is present within the quiescent galaxy population. This result has been shown at $z \sim 0.7$ by C17 and we demonstrate here that it is also true at $z \sim 0$. This shows that the scatter observed in the main sequence scatter is real, in that there are distinct clustering properties for galaxies above and below the sequence.

2. Central galaxies are the driver of our result that sSFR ratio (and not stellar mass ratio) is the key factor influencing the clustering differences between galaxy samples. While this effect

is also present for satellite galaxies, the correlation between sSFR and clustering amplitude is stronger for centrals. This is consistent with central galaxy assembly bias and/or different stellar-to-halo mass relations for star-forming and quiescent (central) galaxies.

3. The empirical model of Behroozi et al. (2019) fits combined PRIMUS and DEEP2 clustering data well at intermediate redshift ($z \sim 0.45$ and $z \sim 0.9$), i.e. galaxy bias increases smoothly with decreasing sSFR in the model as well as in the data. At low redshift ($z \sim 0$) the model does not reproduce SDSS data; we show that increasing the correlation between galaxy SFR and halo accretion rate improves the agreement.

4. Measurements of galaxy bias as a function of sSFR, and of relative bias versus sSFR ratio for different galaxy samples, are highly constraining for models of galaxy evolution. Forward modeling with mock galaxy catalogs based on empirical models, as performed here, allows for comparisons of data and models at intermediate redshift without the need for stellar mass-complete galaxy samples, which are currently restricted to high mass at such redshifts.

Acknowledgements

Funding for SDSS-III has been provided by the Alfred P. Sloan Foundation, the Participating Institutions, the National Science Foundation, and the U.S. Department of Energy Office of Science. The SDSS-III website is http://www.sdss3.org/. SDSS-III is managed by the Astrophysical Research Consortium for the Participating Institutions of the SDSS-III Collaboration including the University of Arizona, the Brazilian Participation Group, Brookhaven National Laboratory, Carnegie Mellon University, University of Florida, the French Participation Group, the German Participation Group, Harvard University, the Instituto de Astrofisica de Canarias, the Michigan State/Notre Dame/JINA Participation Group, Johns Hopkins University, Lawrence Berkeley National Laboratory, Max Planck Institute for Astrophysics, Max Planck Institute

for Extraterrestrial Physics, New Mexico State University, New York University, Ohio State University, Pennsylvania State University, University of Portsmouth, Princeton University, the Spanish Participation Group, University of Tokyo, University of Utah, Vanderbilt University, University of Virginia, University of Washington, and Yale University.

The CosmoSim database used in this work is a service by the Leibniz-Institute for Astrophysics Potsdam (AIP). The MultiDark database was developed in cooperation with the Spanish MultiDark Consolider Project CSD2009-00064. The authors gratefully acknowledge the Gauss Centre for Supercomputing e.V. (www.gauss-centre.eu) and the Partnership for Advanced Supercomputing in Europe (PRACE, www.prace-ri.eu) for funding the MultiDark simulation project by providing computing time on the GCS Supercomputer SuperMUC at Leibniz Supercomputing Centre (LRZ, www.lrz.de). The Bolshoi simulations have been performed within the Bolshoi project of the University of California High-Performance AstroComputing Center (UC-HiPACC) and were run at the NASA Ames Research Center. AMB and ALC acknowledge support from the Ingrid and Joseph W. Hibben endowed chair at UC San Diego.

Chapter 4, in part, is currently being prepared for submission for publication in The Astrophysical Journal as "Main Sequence Scatter is Real: The Joint Dependence of Galaxy Clustering on Star Formation and Stellar Mass" by A. M. Berti, A. L. Coil, A. P. Hearin, and P. S. Behroozi. The dissertation author was the primary investigator and author of this material.

Appendix to Chapter 4:
Uniform Stellar Mass Complete SDSS Galaxy Samples

Here we present measurements of $\omega_p(r_p)$ for SDSS galaxy samples that use a single stellar mass completeness cut. These samples are nearly identical to the samples described in §4.2.4 and used for the results presented in §4.4, but are limited to $\log(M_*/M_\odot) > 9.75$ for both star-forming and quiescent galaxies so as to be better suited for comparisons with theoretical models.

As in the main text, the four sets of galaxy samples are (1) "star-forming/quiescent split," in which galaxies are divided into star-forming and quiescent samples by Eq. 4.2; (2) "main

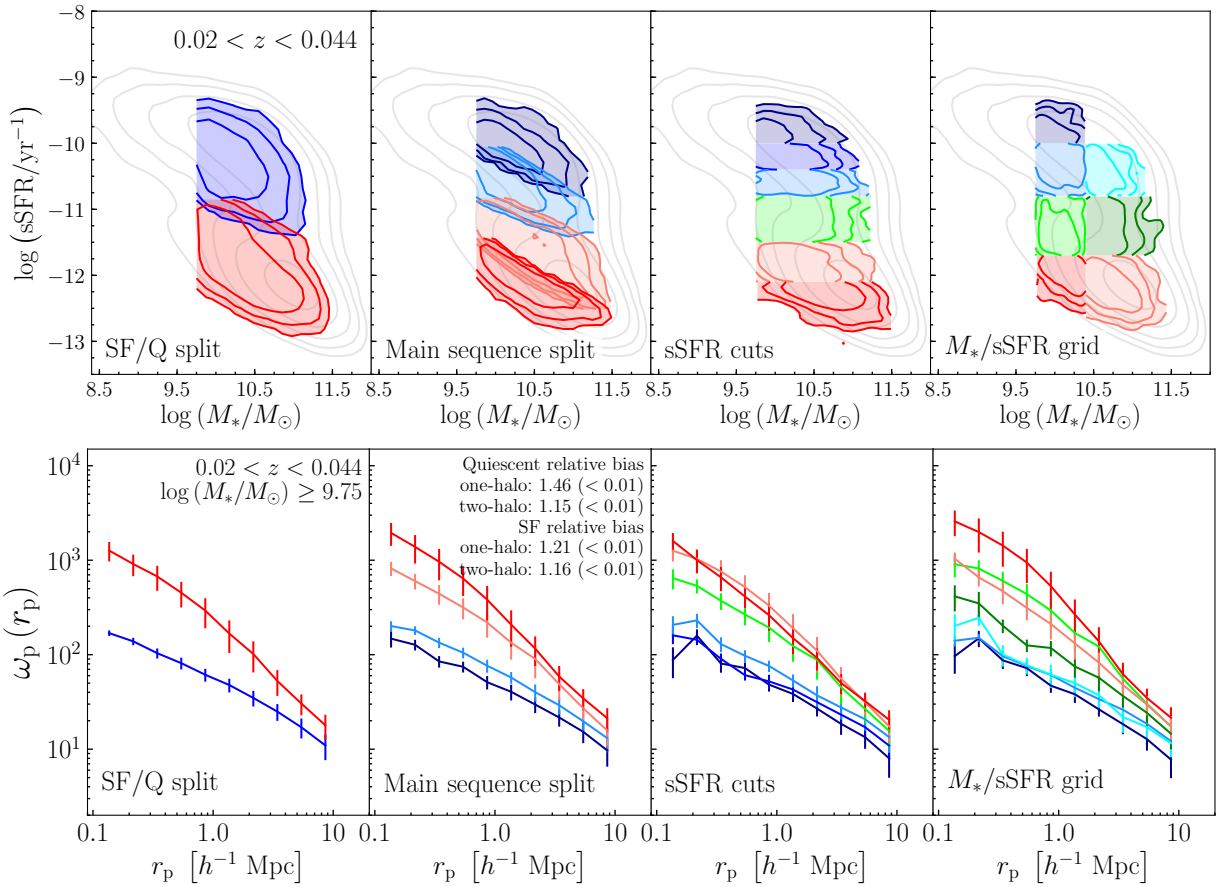

Figure 4.13: Same as Figure 4.1 but using a stellar mass limit of $\log(M_*/M_\odot) \geq 9.75$ for all galaxy samples.

sequence split," in which the star-forming and quiescent populations are split into samples above and below each population's main sequence; (3) "sSFR cuts," in which galaxies are split into six bins in sSFR; and (4) "stellar mass/sSFR grid," in which galaxies are divided into seven samples using two bins in stellar mass and four bins in sSFR.

The top row of Figure 4.13 shows the distribution of all galaxy samples in the stellar mass–sSFR plane; $\omega_p(r_p)$ for each sample is shown in the bottom row. Table 4.3 lists the stellar mass and sSFR cuts used for each sample, and Table 4.4 contains $\omega_p(r_p)$ for each sample for 10 logarithmic bins in r_p between $\log(r_p/(h^{-1}\,\mathrm{Mpc})) = -0.8$ and $\log(r_p/(h^{-1}\,\mathrm{Mpc})) = 1.2$.

Table 4.3: Uniform stellar mass complete SDSS galaxy samples ($\log(M_*/\mathrm{M}_\odot) \geq 9.75$). All samples span $0.02 < z < 0.0435$ and have median redshift $z_{\mathrm{med}} \simeq 0.033$.

Run	Sample	N_{gal}	$\log(M_*/\mathrm{M}_\odot)$			$\log(\mathrm{sSFR/yr}^{-1})$		
			min	mean	max	min	mean	max
SF/Q split	**blue**	13548	9.75	10.20	11.98	-11.64	-10.30	-8.41
	red	13449	9.75	10.42	12.42	-13.40	-11.87	-10.80
Main sequence split	**dark blue**	6762	9.75	10.20	11.35	-11.20	-10.03	-8.41
	light blue	6779	9.75	10.20	11.43	-11.54	-10.57	-10.05
	light red	6712	9.75	10.42	11.59	-12.70	-11.60	-10.80
	red	6732	9.75	10.42	11.75	-13.40	-12.14	-11.40
sSFR cuts	**dark blue**	3109	9.75	10.03	11.15	-10.00	-9.82	-9.01
	blue	5272	9.75	10.15	11.24	-10.40	-10.20	-10.00
	light blue	3658	9.75	10.28	11.35	-10.80	-10.58	-10.40
	light green	4342	9.75	10.27	11.57	-11.50	-11.16	-10.80
	light red	6134	9.75	10.36	11.55	-12.10	-11.83	-11.50
	red	4462	9.76	10.70	12.00	-13.40	-12.32	-12.10
M_*/sSFR grid	**dark blue**	2846	9.75	9.98	10.40	-10.00	-9.82	-8.41
	light blue	6668	9.75	10.06	10.40	-10.80	-10.33	-10.00
	light green	3940	9.75	10.06	10.40	-11.70	-11.29	-10.80
	red	3104	9.75	10.15	10.40	-13.40	-11.97	-11.70
	cyan	2262	10.40	10.61	11.35	-10.80	-10.44	-10.00
	dark green	2037	10.40	10.68	11.43	-11.70	-11.26	-10.80
	light red	5842	10.40	10.75	11.50	-13.36	-12.19	-11.70

Table 4.4: $\omega_p(r_p)$ for uniform stellar mass complete SDSS galaxy samples ($\log(M_*/M_\odot) > 9.75$). Values of r_p are bin centers in units of h^{-1} Mpc for 10 logarithmic bins between -0.8 and 1.2. The units of $\omega_p(r_p)$ are h^{-1} Mpc. Sample parameters are presented in Table 4.3.

Star-forming/quiescent split			Main sequence split				
r_p	**blue**	**red**	r_p	**dark blue**	**light blue**	**light red**	**red**
0.136	169.2 (4.5)	1264.9 (38.9)	0.136	147.9 (4.4)	201.1 (8.2)	820.0 (22.3)	1947.3 (69.9)
0.216	138.4 (3.5)	911.8 (32.0)	0.216	127.3 (3.7)	180.6 (5.2)	601.2 (19.5)	1383.6 (66.3)
0.343	103.8 (3.4)	673.3 (27.4)	0.343	84.9 (3.1)	134.1 (4.5)	442.1 (17.0)	964.3 (54.9)
0.543	81.4 (2.7)	452.7 (19.7)	0.543	74.5 (2.4)	105.0 (3.6)	316.2 (14.3)	640.2 (33.0)
0.861	61.3 (2.4)	293.0 (16.0)	0.861	51.2 (2.2)	76.4 (2.9)	219.2 (12.2)	382.7 (25.1)
1.364	47.8 (2.0)	167.4 (9.9)	1.364	40.5 (1.9)	57.4 (2.0)	133.9 (7.8)	207.8 (14.8)
2.162	34.9 (1.6)	101.7 (5.8)	2.162	29.7 (1.5)	40.2 (1.8)	90.2 (5.9)	116.0 (6.7)
3.426	25.0 (1.3)	52.6 (2.3)	3.426	21.6 (1.2)	29.2 (1.4)	48.7 (2.5)	58.7 (2.7)
5.431	17.0 (1.1)	30.4 (1.7)	5.431	15.3 (1.1)	19.7 (1.1)	27.1 (1.5)	34.5 (1.9)
8.607	11.0 (0.9)	17.9 (1.3)	8.607	9.7 (1.0)	13.1 (0.9)	15.8 (1.3)	21.2 (1.3)

sSFR cuts						
r_p	**dark blue**	**blue**	**light blue**	**light green**	**light red**	**red**
0.136	88.0 (7.3)	160.3 (6.1)	206.7 (14.3)	646.2 (30.6)	1261.0 (34.2)	1599.6 (50.1)
0.216	159.1 (5.7)	143.8 (4.2)	230.9 (10.7)	535.4 (19.5)	1033.3 (39.1)	1002.8 (48.8)
0.343	80.7 (3.9)	90.3 (3.6)	129.5 (5.7)	372.2 (18.4)	760.2 (33.9)	658.8 (32.0)
0.543	72.2 (3.0)	60.7 (2.0)	97.4 (3.8)	266.2 (13.7)	519.7 (26.2)	412.7 (19.3)
0.861	48.2 (2.2)	52.2 (2.0)	76.0 (2.8)	193.4 (11.0)	330.6 (19.5)	262.0 (14.3)
1.364	38.4 (2.1)	42.7 (1.8)	53.3 (1.9)	123.4 (8.2)	190.7 (13.5)	149.6 (7.6)
2.162	26.9 (1.4)	31.5 (1.5)	37.1 (1.7)	88.1 (6.5)	110.1 (7.0)	92.2 (4.2)
3.426	18.5 (1.1)	23.2 (1.2)	27.6 (1.4)	45.3 (2.7)	55.7 (2.6)	50.1 (2.1)
5.431	13.4 (1.0)	17.1 (1.1)	20.7 (1.2)	26.6 (1.7)	31.5 (1.8)	32.3 (1.7)
8.607	8.0 (1.0)	10.9 (0.9)	13.5 (1.0)	15.6 (1.3)	17.4 (1.3)	20.5 (1.3)

Stellar mass/sSFR grid							
r_p	**dark blue**	**light blue**	**light green**	**red**	**cyan**	**dark green**	**light red**
0.136	96.5 (8.9)	140.6 (5.6)	906.9 (35.3)	2577.9 (138.0)	201.7 (16.1)	414.5 (29.5)	1035.2 (32.7)
0.216	149.3 (5.6)	151.0 (4.6)	817.3 (31.7)	1986.5 (128.9)	245.6 (11.6)	349.0 (32.2)	659.0 (21.5)
0.343	87.1 (4.3)	96.6 (3.2)	603.9 (28.5)	1427.8 (91.6)	100.4 (5.4)	202.5 (8.5)	469.5 (19.4)
0.543	72.1 (3.0)	75.7 (2.5)	437.6 (22.3)	944.5 (55.1)	77.4 (3.7)	125.5 (4.5)	312.6 (12.4)
0.861	47.0 (2.3)	61.0 (2.2)	293.2 (16.4)	531.0 (35.7)	61.4 (3.9)	117.8 (4.6)	211.3 (10.8)
1.364	38.1 (2.1)	44.7 (1.7)	169.7 (10.8)	266.3 (21.1)	50.1 (3.3)	74.8 (4.3)	131.7 (6.8)
2.162	26.4 (1.3)	33.9 (1.4)	121.9 (9.1)	138.4 (10.4)	37.1 (2.3)	57.1 (3.3)	82.3 (3.8)
3.426	18.4 (1.1)	26.1 (1.2)	55.8 (3.0)	62.1 (3.1)	21.9 (1.8)	36.6 (2.1)	48.0 (2.1)
5.431	12.8 (0.9)	18.5 (1.0)	30.2 (1.6)	34.8 (1.9)	17.1 (1.2)	24.2 (1.8)	29.6 (1.6)
8.607	7.8 (0.9)	12.1 (0.9)	17.4 (1.3)	21.5 (1.4)	11.6 (1.0)	14.6 (1.3)	17.5 (1.2)

5 Future Directions

One of the biggest obstacles currently facing studies of galaxy evolution is a lack of cosmological-scale, spectroscopic data at $z > 0.2$. Additional spectroscopic surveys at intermediate redshift are needed to compliment PRIMUS and DEEP2, as are PRIMUS-like surveys at $z > 1$ to fill in the first several billion years of galaxy evolution. Larger datasets are needed to achieve greater signal-to-noise for statistical measurements, such as those featured in this dissertation, as well as to further subdivide the galaxy population simultaneously along multiple axes.

On the theory and modeling side, computing efficiency continues to increase, expanding the limits of the volumes (on the high end) and particle mass resolution (on the low end) accessible by cosmological *N*-body simulations. A potential danger here is a proliferation of predictions that are untestable with existing data and likely to remain so indefinitely. This issue is similar to problems currently facing fundamental particle physics, where attempts at reconciling the incompatibility of general relativity and quantum mechanics have produced many novel theories that either don't make testable predictions, or whose predictions require experiments so technologically advanced as to be impractical or impossible (e.g. a particle accelerator with a diameter larger than that of Earth).

The results presented in this dissertation have demonstrated the critical importance of several features any galaxy redshift survey should have to be effectively suitable for studies of galaxy evolution:

1. **Spectroscopic redshifts precise enough for clustering and other statistical measurements.** While spectroscopic redshift surveys are more time-consuming and expensive

than obtaining large numbers of photometric redshifts, the smaller errors of spectroscopic redshifts are essential for three-dimensional precision mapping of the galaxy spatial distribution. The good news is that PRIMUS has shown that low-resolution ($\Delta\lambda/\lambda \sim 40$) spectra obtained from dispersion by a simple prism, combined with multi-wavelength photometry, is sufficient for the task. Moreover, the error of PRIMUS redshifts was originally estimated to be $\sigma_z \sim 0.005\,(1+z)$, but has since been shown by Behroozi et al. (2019) to be closer to $\sigma_z \sim 0.0033\,(1+z)$.

2. **Multiple fields and large survey volume, both in terms of depth and area on the sky.** This requirement serves several purposes: (i) to account for cosmic variance and avoid results dominated by a statistical outlier field (e.g. the effect of the COSMOS field discussed in §2.3.5), and to have sufficiently large sample sizes to ensure (ii) Poisson errors are subdominant and (iii) we can subdivide the galaxy population along multiple axes (redshift, stellar mass, etc.) to measure the dependence of statistical signals like conformity and clustering in joint spaces.

3. **Include statistically complete samples of galaxies below the break in the stellar mass function.** This point is related to survey volume, as depth is required to observe lower-mass galaxies, and breadth is necessary ensure large sample sizes of galaxies across the spectrum of stellar mass. Sampling galaxies below $M_* \sim 10^{10}$ $M_\odot$ is also essential for identifying central galaxies and assessing differences between the physical processes important for the evolution of satellite galaxies versus centrals.

Unfortunately none of the upcoming spectroscopic galaxy redshift surveys meet all of the above criteria, but a few come close. The recently completed Baryon Oscillation Spectroscopic Survey (BOSS; Dawson et al., 2013) contains 1.5 million spectroscopic galaxy redshifts to $z \sim 0.7$, covering a volume larger than that of all previous spectroscopic surveys of large-scale structure combined. But, as its main goal is to study baryon acoustic oscillations, BOSS targeted bright

galaxies and contains almost no galaxies with stellar masses below $\sim 10^{10.5}$ $M_\odot$ (Maraston et al., 2013).

The Dark Energy Spectroscopic Instrument (DESI; Flaugher & Bebek, 2014) installed on the Mayall 4-meter telescope at Kitt Peak National Observatory in Arizona saw its first light in late 2019. DESI is capable of observing $5,000$ spectra simultaneously, and uses the relatively new technology of motorized arms to quickly and individually reposition the $5,000$ fibre optic cables that receive light from targeted galaxies. Previously spectroscopic surveys like SDSS and PRIMUS used machined plates with fixed slit positions to obtain spectra, which had to be continually swapped out. DESI's robotic arm technology represents a significant improvement in the "down time" required between different target positions.

The DESI Bright Galaxy Survey (BGS) will in some sense be the next generation of the SDSS's mapping of galaxies across one-third of the sky to $z \sim 0.2$. The BGS will obtain a nearly complete sample of some one million redshifts over a similarly large area to $z \sim 0.4$, or over 4 Gyr of cosmic history. This is a $\sim 75\%$ increase in the history of the universe covered by the SDSS. However, as its name suggests, the BGS is limited to bright galaxies and will not probe to stellar masses low enough to expand on much of the work presented here. Other DESI surveys such as the Luminous Red Galaxy (LRG) and Emission Line Galaxy (ELG) surveys will reach higher redshifts, but with the usual tradeoff of greater luminosity thresholds with increasing redshift.

Just a few months into its multiyear observing schedule the DESI survey was halted in March 2020 by the global novel coronavirus pandemic. As of this writing the timeline for resuming observations remains uncertain, but in the best case scenario operations at Kitt Peak could restart in a limited capacity in October 2020.

Finally, the Prime Focus Spectrograph (PFS, Takada et al., 2014) on the 8.2-meter Subaru telescope at Hawaii's Mauna Kea Observatory has a similar design to DESI, using robotic arms to quickly reconfigure its $2,394$ fibre optic cables. Designed for optical and near-infrared spectroscopy, the PFS will have a minimum resolution of at least $\Delta\lambda/\lambda \sim 2,000$, fifty times

that of PRIMUS. As of December 2018 commissioning was scheduled to begin in 2020, with science operations starting in 2022. The Subaru PFS will obtain a statistically complete sample of galaxies and AGN with stellar masses greater than $\sim 10^{10}$ $M_{\odot}$ to $z \sim 2$ over an area three times larger than that of the PRIMUS data used in this work.

These upcoming surveys will greatly expand the cosmological volume over which we have mapped large-scale structure to the resolution obtainable with spectra of more massive galaxies. Combined with the PFS's ability to target typical galaxies, these new observations will substantially increase our understanding of how galaxies evolve over the bulk of cosmic time.

Bibliography

Ahn, C. P., Alexandroff, R., Prieto, C. A., Anders, F., Anderson, S. F., Anderton, T., Andrews, B. H., Aubourg, É., Bailey, S., Bastien, F. A., Bautista, J. E., Beers, T. C., Beifiori, A., Bender, C. F., Berlind, A. A., Beutler, F., Bhardwaj, V., Bird, J. C., Bizyaev, D., Blake, C. H., Blanton, M. R., Blomqvist, M., Bochanski, J. J., Bolton, A. S., Borde, A., Bovy, J., Bradley, A. S., Brandt, W. N., Brauer, D., Brinkmann, J., Brownstein, J. R., Busca, N. G., Carithers, W., Carlberg, J. K., Carnero, A. R., Carr, M. A., Chiappini, C., Chojnowski, S. D., Chuang, C.-H., Comparat, J., Crepp, J. R., Cristiani, S., Croft, R. A. C., Cuesta, A. J., Cunha, K., da Costa, L. N., Dawson, K. S., Lee, N. D., Dean, J. D. R., Delubac, T., Deshpande, R., Dhital, S., Ealet, A., Ebelke, G. L., Edmondson, E. M., Eisenstein, D. J., Epstein, C. R., Escoffier, S., Esposito, M., Evans, M. L., Fabbian, D., Fan, X., Favole, G., Castellá, B. F., Alvar, E. F., Feuillet, D., Ak, N. F., Finley, H., Fleming, S. W., Font-Ribera, A., Frinchaboy, P. M., Galbraith-Frew, J. G., García-Hernández, D. A., Pérez, A. E. G., Ge, J., Génova-Santos, R., Gillespie, B. A., Girardi, L., Hernández, J. I. G., Gott, J. R., Gunn, J. E., Guo, H., Halverson, S., Harding, P., Harris, D. W., Hasselquist, S., Hawley, S. L., Hayden, M., Hearty, F. R., Davó, A. H., Ho, S., Hogg, D. W., Holtzman, J. A., Honscheid, K., Huehnerhoff, J., Ivans, I. I., Jackson, K. M., Jiang, P., Johnson, J. A., Kinemuchi, K., Kirkby, D., Klaene, M. A., Kneib, J.-P., Koesterke, L., Lan, T.-W., Lang, D., Goff, J.-M. L., Leauthaud, A., Lee, K.-G., Lee, Y. S., Long, D. C., Loomis, C. P., Lucatello, S., Lupton, R. H., Ma, B., Mack, C. E., Mahadevan, S., Maia, M. A. G., Majewski, S. R., Malanushenko, E., Malanushenko, V., Manchado, A., Manera, M., Maraston, C., Margala, D., Martell, S. L., Masters, K. L., McBride, C. K., McGreer, I. D., McMahon, R. G., Ménard, B., Mészáros, S., Miralda-Escudé, J., Miyatake, H., Montero-Dorta, A. D., Montesano, F., More, S., Morrison, H. L., Muna, D., Munn, J. A., Myers, A. D., Nguyen, D. C., Nichol, R. C., Nidever, D. L., Noterdaeme, P., Nuza, S. E., O'Connell, J. E., O'Connell, R. W., O'Connell, R., Olmstead, M. D., Oravetz, D. J., Owen, R., Padmanabhan, N., Palanque-Delabrouille, N., Pan, K., Parejko, J. K., Parihar, P., Pâris, I., Pepper, J., Percival, W. J., Pérez-Ràfols, I., Perottoni, H. D., Petitjean, P., Pieri, M. M., Pinsonneault, M. H., Prada, F., Price-Whelan, A. M., Raddick, M. J., Rahman, M., Rebolo, R., Reid, B. A., Richards, J. C., Riffel, R., Robin, A. C., Rocha-Pinto, H. J., Rockosi, C. M., Roe, N. A., Ross, A. J., Ross, N. P., Rossi, G., Roy, A., Rubiño-Martin, J. A., Sabiu, C. G., Sánchez, A. G., Santiago, B., Sayres, C., Schiavon, R. P., Schlegel, D. J., Schlesinger, K. J., Schmidt, S. J., Schneider, D. P., Schultheis, M., Sellgren, K., Seo, H.-J., Shen, Y., Shetrone, M., Shu, Y., Simmons, A. E., Skrutskie, M. F., Slosar, A., Smith, V. V., Snedden, S. A., Sobeck, J. S., Sobreira, F., Stassun, K. G., Steinmetz, M., Strauss, M. A., Streblyanska, A., Suzuki, N., Swanson, M. E. C., Terrien, R. C., Thakar, A. R., Thomas, D., Thompson, B. A., Tinker, J. L., Tojeiro, R., Troup, N. W., Vandenberg, J., Magaña, M. V., Viel, M., Vogt, N. P., Wake, D. A., Weaver, B. A., Weinberg, D. H., Weiner, B. J., White, M., White, S. D. M., Wilson, J. C., Wisniewski, J. P., Wood-Vasey, W. M., Yèche, C., York, D. G., Zamora, O., Zasowski, G., Zehavi, I., Zhao, G.-B., Zheng, Z., & Zhu, G. 2014, ApJS, 211, 17 129

Anderson, M. E., Gaspari, M., White, S. D. M., Wang, W., & Dai, X. 2015, MNRAS, 449, 3806 119

Baldry, I. K., Glazebrook, K., Brinkmann, J., Ivezić, Ž., Lupton, R. H., Nichol, R. C., & Szalay, A. S. 2004, ApJ, 600, 681 11, 20

Balogh, M. L., Baldry, I. K., Nichol, R., Miller, C., Bower, R., & Glazebrook, K. 2004, ApJL, 615, L101 11, 20

Barton, E. J., Arnold, J. A., Zentner, A. R., Bullock, J. S., & Wechsler, R. H. 2007, ApJ, 671, 1538 121

Becker, M. R. 2015, arXiv e-prints 85, 119

Behroozi, P., Wechsler, R. H., Hearin, A. P., & Conroy, C. 2019, MNRAS 68, 71, 85, 99, 118, 119, 123, 127, 128, 132, 133, 146, 148, 155, 165, 166, 172

Behroozi, P. S., Conroy, C., & Wechsler, R. H. 2010, ApJ, 717, 379 125

Behroozi, P. S., Wechsler, R. H., & Conroy, C. 2013, ApJ, 770, 57 110, 128, 132

Behroozi, P. S., Zhu, G., Ferguson, H. C., Hearin, A. P., Lotz, J., Silk, J., Kassin, S., Lu, Y., Croton, D., Somerville, R. S., & Watson, D. F. 2015, MNRAS, 450, 1546 128, 129, 130

Benoist, C., Maurogordato, S., da Costa, L. N., Cappi, A., & Schaeffer, R. 1996, ApJ, 472, 452 125

Benson, A. J. 2012, arXiv e-prints, 17, 175 85, 119

Benson, A. J., Cole, S., Frenk, C. S., Baugh, C. M., & Lacey, C. G. 2000, MNRAS, 311, 793 15, 124

Berlind, A. A. & Weinberg, D. H. 2002, ApJ, 575, 587 15, 21, 69, 124

Berlind, A. A., Blanton, M. R., Hogg, D. W., Weinberg, D. H., Dave, R., Eisenstein, D. J., & Katz, N. 2005, ApJ, 629, 625 16

Berlind, A. A., Frieman, J., Weinberg, D. H., Blanton, M. R., Warren, M. S., Abazajian, K., Scranton, R., Hogg, D. W., Scoccimarro, R., Bahcall, N. A., Brinkmann, J., III, J. R. G., Kleinman, S. J., Krzesinski, J., Lee, B. C., Miller, C. J., Nitta, A., Schneider, D. P., Tucker, D. L., & Zehavi, I. 2006, ApJS, 167, 1 121

Berti, A. M., Coil, A. L., Behroozi, P. S., Eisenstein, D. J., Bray, A. D., Cool, R. J., & Moustakas, J. 2017, ApJ, 834, 87 78, 80, 81, 116, 121, 127

Berti, A. M., Coil, A. L., Hearin, A. P., & Moustakas, J. 2019, ApJ, 884, 76 127, 133, 151

Bigelow, B. C. & Dressler, A. M. 2003, in Society of Photo-Optical Instrumentation Engineers (SPIE) Conference Series, ed. M. Iye & A. F. M. Moorwood, Vol. 4841, 1727–1738 26, 72, 131

Blanton, M. R., Schlegel, D. J., Strauss, M. A., Brinkmann, J., Finkbeiner, D., Fukugita, M., Gunn, J. E., Hogg, D. W., Ivezić, Ž., Knapp, G. R., Lupton, R. H., Munn, J. A., Schneider, D. P., Tegmark, M., & Zehavi, I. 2005, AJ, 129, 2562 133

Bray, A. D., Pillepich, A., Sales, L. V., Zhu, E., Genel, S., Rodriguez-Gomez, V., Torrey, P., Nelson, D., Vogelsberger, M., Springel, V., Eisenstein, D. J., & Hernquist, L. 2016, MNRAS, 455, 185 23

Brinchmann, J., Charlot, S., White, S. D. M., Tremonti, C., Kauffmann, G., Heckman, T., & Brinkmann, J. 2004, MNRAS, 351, 1151 129

Bruzual, G. & Charlot, S. 2003, MNRAS, 344, 1000 132

Bryan, G. L. & Norman, M. L. 1998, ApJ, 495, 80 155

Cacciato, M., van den Bosch, F. C., More, S., Mo, H., & Yang, X. 2013, MNRAS, 430, 767 69

Calderon, V. F., Berlind, A. A., & Sinha, M. 2018, MNRAS, 480, 2031 121

Campbell, D., van den Bosch, F. C., Hearin, A., Padmanabhan, N., Berlind, A., Mo, H. J., Tinker, J., & Yang, X. 2015, MNRAS, 452, 444 16, 24, 34, 121

Chabrier, G. 2003, PASP, 115, 763 77, 132

Chen, J., Kravtsov, A. V., Prada, F., Sheldon, E. S., Klypin, A. A., Blanton, M. R., Brinkmann, J., & Thakar, A. R. 2006, ApJ, 647, 86 59

Cohn, J. D. 2017, MNRAS, 466, 2718 85

Coil, A. L., Davis, M., Madgwick, D. S., Newman, J. A., Conselice, C. J., Cooper, M., Ellis, R. S., Faber, S. M., Finkbeiner, D. P., Guhathakurta, P., Kaiser, N., Koo, D. C., Phillips, A. C., Steidel, C. C., Weiner, B. J., Willmer, C. N. A., & Yan, R. 2004, ApJ, 609, 525 125

Coil, A. L., Newman, J. A., Cooper, M. C., Davis, M., Faber, S. M., Koo, D. C., & Willmer, C. N. A. 2006, ApJ, 644, 671 12, 13, 69, 125

Coil, A. L., Newman, J. A., Croton, D., Cooper, M. C., Davis, M., Faber, S. M., Gerke, B. F., Koo, D. C., Padmanabhan, N., Wechsler, R. H., & Weiner, B. J. 2008, ApJ, 672, 153 12, 13, 69, 125

Coil, A. L., Blanton, M. R., Burles, S. M., Cool, R. J., Eisenstein, D. J., Moustakas, J., Wong, K. C., Zhu, G., Aird, J., Bernstein, R. A., Bolton, A. S., & Hogg, D. W. 2011, ApJ, 741, 8 4, 25, 26, 27, 76, 80, 131, 133

Coil, A. L., Mendez, A. J., Eisenstein, D. J., & Moustakas, J. 2017, ApJ, 838, 87 12, 70, 71, 81, 87, 93, 94, 95, 100, 101, 104, 118, 123, 125

Colless, M., Dalton, G., Maddox, S., Sutherland, W., Norberg, P., Cole, S., Bland-Hawthorn, J., Bridges, T., Cannon, R., Collins, C., Couch, W., Cross, N., Deeley, K., de Propris, R., Driver, S. P., Efstathiou, G., Ellis, R. S., Frenk, C. S., Glazebrook, K., Jackson, C., Lahav, O., Lewis, I., Lumsden, S., Madgwick, D., Peacock, J. A., Peterson, B. A., Price, I., Seaborne, M., & Taylor, K. 2001, MNRAS, 328, 1039 4

Conroy, C., Wechsler, R. H., & Kravtsov, A. V. 2006, ApJ, 647, 201 69

Cool, R. J., Moustakas, J., Blanton, M. R., Burles, S. M., Coil, A. L., Eisenstein, D. J., Wong, K. C., Zhu, G., Aird, J., Bernstein, R. A., Bolton, A. S., Hogg, D. W., & Mendez, A. J. 2013, ApJ, 767, 118 4, 25, 26, 27, 29, 72, 76, 77, 131

Cooper, M. C., Newman, J. A., Coil, A. L., Croton, D. J., Gerke, B. F., Yan, R., Davis, M., Faber, S. M., Guhathakurta, P., Koo, D. C., Weiner, B. J., & Willmer, C. N. A. 2007, MNRAS, 376, 1445 63

Croton, D. J., Gao, L., & White, S. D. M. 2007, MNRAS, 374, 1303 14, 21

Croton, D. J., Springel, V., White, S. D. M., De Lucia, G., Frenk, C. S., Gao, L., Jenkins, A., Kauffmann, G., Navarro, J. F., & Yoshida, N. 2006, MNRAS, 365, 11 11, 20

Dalal, N., Doré, O., Huterer, D., & Shirokov, A. 2008, Phys. Rev. D, 77, 123514 21, 70, 126

Darvish, B., Mobasher, B., Sobral, D., Rettura, A., Scoville, N., Faisst, A., & Capak, P. 2016, ApJ, 825, 113 63

Davis, M. & Peebles, P. J. E. 1983, ApJ, 267, 465 9, 93, 140

Davis, M., Huchra, J., Latham, D. W., & Tonry, J. 1982, ApJ, 253, 423 2

Dawson, K. S., Schlegel, D. J., Ahn, C. P., Anderson, S. F., Aubourg, É., Bailey, S., Barkhouser, R. H., Bautista, J. E., Beifiori, A., Berlind, A. A., Bhardwaj, V., Bizyaev, D., Blake, C. H., Blanton, M. R., Blomqvist, M., Bolton, A. S., Borde, A., Bovy, J., Brandt, W. N., Brewington, H., Brinkmann, J., Brown, P. J., Brownstein, J. R., Bundy, K., Busca, N. G., Carithers, W., Carnero, A. R., Carr, M. A., Chen, Y., Comparat, J., Connolly, N., Cope, F., Croft, R. A. C., Cuesta, A. J., da Costa, L. N., Davenport, J. R. A., Delubac, T., de Putter, R., Dhital, S., Ealet, A., Ebelke, G. L., Eisenstein, D. J., Escoffier, S., Fan, X., Filiz Ak, N., Finley, H., Font-Ribera, A., Génova-Santos, R., Gunn, J. E., Guo, H., Haggard, D., Hall, P. B., Hamilton, J.-C., Harris, B., Harris, D. W., Ho, S., Hogg, D. W., Holder, D., Honscheid, K., Huehnerhoff, J., Jordan, B., Jordan, W. P., Kauffmann, G., Kazin, E. A., Kirkby, D., Klaene, M. A., Kneib, J.-P., Le Goff, J.-M., Lee, K.-G., Long, D. C., Loomis, C. P., Lundgren, B., Lupton, R. H., Maia, M. A. G., Makler, M., Malanushenko, E., Malanushenko, V., Mandelbaum, R., Manera, M., Maraston, C., Margala, D., Masters, K. L., McBride, C. K., McDonald, P., McGreer, I. D., McMahon, R. G., Mena, O., Miralda-Escudé, J., Montero-Dorta, A. D., Montesano, F., Muna, D., Myers, A. D., Naugle, T., Nichol, R. C., Noterdaeme, P., Nuza, S. E., Olmstead, M. D., Oravetz, A., Oravetz, D. J., Owen, R., Padmanabhan, N., Palanque-Delabrouille, N., Pan, K., Parejko, J. K., Pâris, I., Percival, W. J., Pérez-Fournon, I., Pérez-Ràfols, I., Petitjean, P., Pfaffenberger, R., Pforr, J., Pieri, M. M., Prada, F., Price-Whelan, A. M., Raddick, M. J., Rebolo, R., Rich, J., Richards, G. T., Rockosi, C. M., Roe, N. A., Ross, A. J., Ross, N. P., Rossi, G., Rubiño-Martin, J. A., Samushia, L., Sánchez, A. G., Sayres, C., Schmidt, S. J., Schneider, D. P., Scóccola, C. G., Seo, H.-J., Shelden, A., Sheldon, E., Shen, Y., Shu, Y., Slosar, A., Smee, S. A., Snedden, S. A., Stauffer, F., Steele, O., Strauss, M. A., Streblyanska, A., Suzuki, N., Swanson, M. E. C., Tal, T., Tanaka, M., Thomas, D., Tinker, J. L., Tojeiro, R., Tremonti, C. A., Vargas Magaña, M., Verde, L., Viel, M., Wake, D. A., Watson, M., Weaver, B. A., Weinberg, D. H., Weiner, B. J., West, A. A., White, M., Wood-Vasey, W. M., Yeche, C., Zehavi, I., Zhao, G.-B., & Zheng, Z. 2013, AJ, 145, 10 64, 172

Dekel, A. & Birnboim, Y. 2006, MNRAS, 368, 2 20

Duarte, M. & Mamon, G. A. 2014, MNRAS, 440, 1763 121

Durkalec, A., Le Fèvre, O., de la Torre, S., Pollo, A., Cassata, P., Garilli, B., Le Brun, V., Lemaux, B. C., Maccagni, D., Pentericci, L., Tasca, L. A. M., Thomas, R., Vanzella, E., Zamorani, G., Zucca, E., Amorín, R., Bardelli, S., Cassarà, L. P., Castellano, M., Cimatti, A., Cucciati, O., Fontana, A., Giavalisco, M., Grazian, A., Hathi, N. P., Ilbert, O., Paltani, S., Ribeiro, B., Schaerer, D., Scodeggio, M., Sommariva, V., Talia, M., Tresse, L., Vergani, D., Capak, P., Charlot, S., Contini, T., Cuby, J. G., Dunlop,

J., Fotopoulou, S., Koekemoer, A., López-Sanjuan, C., Mellier, Y., Pforr, J., Salvato, M., Scoville, N., Taniguchi, Y., & Wang, P. W. 2015, A&A, 576, L7 125

Eisenstein, D. & DESI Collaboration. 2015, in American Astronomical Society Meeting Series, Vol. 225, 336.05 64

Faber, S. M., Phillips, A. C., Kibrick, R. I., Alcott, B., Allen, S. L., Burrous, J., Cantrall, T., Clarke, D., Coil, A. L., Cowley, D. J., Davis, M., Deich, W. T. S., Dietsch, K., Gilmore, D. K., Harper, C. A., Hilyard, D. F., Lewis, J. P., McVeigh, M., Newman, J., Osborne, J., Schiavon, R., Stover, R. J., Tucker, D., Wallace, V., Wei, M., Wirth, G., & Wright, C. A. 2003, in Instrument Design and Performance for Optical/Infrared Ground-based Telescopes, ed. M. Iye & A. F. M. Moorwood, Vol. 4841 (SPIE), 1657 131

Fazio, G. G., Hora, J. L., Allen, L. E., Ashby, M. L. N., Barmby, P., Deutsch, L. K., Huang, J.-S., Kleiner, S., Marengo, M., Megeath, S. T., Melnick, G. J., Pahre, M. A., Patten, B. M., Polizotti, J., Smith, H. A., Taylor, R. S., Wang, Z., Willner, S. P., Hoffmann, W. F., Pipher, J. L., Forrest, W. J., McMurty, C. W., McCreight, C. R., McKelvey, M. E., McMurray, R. E., Koch, D. G., Moseley, S. H., Arendt, R. G., Mentzell, J. E., Marx, C. T., Losch, P., Mayman, P., Eichhorn, W., Krebs, D., Jhabvala, M., Gezari, D. Y., Fixsen, D. J., Flores, J., Shakoorzadeh, K., Jungo, R., Hakun, C., Workman, L., Karpati, G., Kichak, R., Whitley, R., Mann, S., Tollestrup, E. V., Eisenhardt, P., Stern, D., Gorjian, V., Bhattacharya, B., Carey, S., Nelson, B. O., Glaccum, W. J., Lacy, M., Lowrance, P. J., Laine, S., Reach, W. T., Stauffer, J. A., Surace, J. A., Wilson, G., Wright, E. L., Hoffman, A., Domingo, G., & Cohen, M. 2004, ApJS, 154, 10 26, 73

Fisher, K. B., Davis, M., Strauss, M. A., Yahil, A., & Huchra, J. P. 1994, MNRAS, 267, 927 9

Flaugher, B. & Bebek, C. 2014, in Proceedings of SPIE, Vol. 9147, Ground-based and Airborne Instrumentation for Astronomy V, 91470S 64, 173

Fry, J. N. & Peebles, P. J. E. 1978, ApJ, 221, 19 2

Furusawa, H., Kosugi, G., Akiyama, M., Takata, T., Sekiguchi, K., & Furusawa, J. 2008, in Astronomical Society of the Pacific Conference Series, Vol. 399, Panoramic Views of Galaxy Formation and Evolution, ed. T. Kodama, T. Yamada, & K. Aoki, 131 26, 76

Gao, L., Springel, V., & White, S. D. M. 2005, MNRAS, 363, L66 14, 21, 70, 126

Gao, L. & White, S. D. M. 2007, MNRAS, 377, L5 14, 21

Gregory, S. A. & Thompson, L. A. 1978, ApJ, 222, 784 2

Groth, E. J. & Peebles, P. J. E. 1977, ApJ, 217, 385 2

Hahn, O., Porciani, C., Dekel, A., & Carollo, C. M. 2009, MNRAS, 398, 1742 14, 22

Hamilton, A. J. S. 1993, ApJ, 417, 19 9

Hartley, W. G., Conselice, C. J., Mortlock, A., Foucaud, S., & Simpson, C. 2015, MNRAS, 451, 1613 24, 59, 60, 61, 116, 119, 121

Hauser, M. G. & Peebles, P. J. E. 1973, ApJ, 185, 757 2

Hearin, A. P., Behroozi, P. S., & van den Bosch, F. C. 2016, MNRAS, 461, 2135 22, 23, 24, 48, 51, 52, 57, 59, 63

Hearin, A. P. & Watson, D. F. 2013, MNRAS, 435, 1313 15

Hearin, A. P., Watson, D. F., & van den Bosch, F. C. 2015, MNRAS, 452, 1958 21, 22, 25, 127

Hearin, A. P., Zentner, A. R., Berlind, A. A., & Newman, J. A. 2013, MNRAS, 433, 659 127

Hearin, A. P., Watson, D. F., Becker, M. R., Reyes, R., Berlind, A. A., & Zentner, A. R. 2014, MNRAS, 444, 729 15, 87, 144

Hearin, A. P., Campbell, D., Tollerud, E., Behroozi, P., Diemer, B., Goldbaum, N. J., Jennings, E., Leauthaud, A., Mao, Y.-Y., More, S., Parejko, J., Sinha, M., Sipöcz, B., & Zentner, A. 2017, ApJ, 154, 190 87, 140

Heinis, S., Budavári, T., Szalay, A. S., Arnouts, S., Aragón-Calvo, M. A., Wyder, T. K., Barlow, T. A., Foster, K., Peter, F. G., Martin, D. C., Morrissey, P., Neff, S. G., Schiminovich, D., Seibert, M., Bianchi, L., Donas, J., Heckman, T. M., Lee, Y.-W., Madore, B. F., Milliard, B., Rich, R. M., & Yi, S. K. 2009, ApJ, 698, 1838 125, 144

Henriques, B. M. B., White, S. D. M., Thomas, P. A., Angulo, R. E., Guo, Q., Lemson, G., & Wang, W. 2017, MNRAS, 469, 2626 119

Hogg, D. W., Blanton, M. R., Eisenstein, D. J., Gunn, J. E., Schlegel, D. J., Zehavi, I., Bahcall, N. A., Brinkmann, J., Csabai, I., Schneider, D. P., Weinberg, D. H., & York, D. G. 2003, ApJ, 585, L5 125

Hopkins, P. F., Hernquist, L., Cox, T. J., Matteo, T. D., Robertson, B., & Springel, V. 2006, ApJS, 163, 1 11, 20

Hubble, E. P. 1926, ApJ, 64 1

Hubble, E. P. 1934, ApJ, 79, 8 2

Jôeveer, M., Einasto, J., & Tago, E. 1978, MNRAS, 185, 357 2

Johnson, J. W., Maller, A. H., Berlind, A. A., Sinha, M., & Holley-Bockelmann, J. K. 2018, arXiv e-prints 14, 70, 126

Kauffmann, G. 2015, MNRAS, 454, 1840 23, 24

Kauffmann, G., White, S. D. M., & Guiderdoni, B. 1993, MNRAS, 264, 201 85

Kauffmann, G., Heckman, T. M., White, S. D. M., Charlot, S., Tremonti, C., Brinchmann, J., Bruzual, G., Peng, E. W., Seibert, M., Bernardi, M., Blanton, M., Brinkmann, J., Castander, F., Csábai, I., Fukugita, M., Ivezic, Z., Munn, J. A., Nichol, R. C., Padmanabhan, N., Thakar, A. R., Weinberg, D. H., & York, D. 2003, MNRAS, 341, 33 11, 20, 129

Kauffmann, G., Li, C., Zhang, W., & Weinmann, S. 2013, MNRAS, 430, 1447 21, 22, 23, 31, 58, 59, 63, 79, 116, 121, 127

Kawinwanichakij, L., Quadri, R. F., Papovich, C., Kacprzak, G. G., Labbé, I., Spitler, L. R., Straatman, C. M. S., Tran, K.-V. H., Allen, R., Behroozi, P., Cowley, M., Dekel, A., Glazebrook, K., Hartley, W. G., Kelson, D. D., Koo, D. C., Lee, S.-K., Lu, Y., Nanayakkara, T., Persson, S. E., Primack, J., Tilvi, V., Tomczak, A. R., & van Dokkum, P. 2016, ApJ, 817, 9 24, 59, 60, 61, 116, 121

Klypin, A., Yepes, G., Gottlöber, S., Prada, F., & Heß, S. 2016, MNRAS, 457, 4340 85, 132

Klypin, A. A., Trujillo-Gomez, S., & Primack, J. 2011, ApJ, 740, 102 22, 132

Kovač, K., Lilly, S. J., Cucciati, O., Porciani, C., Iovino, A., Zamorani, G., Oesch, P., Bolzonella, M., Knobel, C., Finoguenov, A., Peng, Y., Carollo, C. M., Pozzetti, L., Caputi, K., Silverman, J. D., Tasca, L. A. M., Scodeggio, M., Vergani, D., Scoville, N. Z., Capak, P., Contini, T., Kneib, J.-P., Fèvre, O. L., Mainieri, V., Renzini, A., Bardelli, S., Bongiorno, A., Coppa, G., de la Torre, S., de Ravel, L., Franzetti, P., Garilli, B., Guzzo, L., Kampczyk, P., Lamareille, F., Borgne, J.-F. L., Brun, V. L., Maier, C., Mignoli, M., Pello, R., Montero, E. P., Ricciardelli, E., Tanaka, M., Tresse, L., Zucca, E., Abbas, U., Bottini, D., Cappi, A., Cassata, P., Cimatti, A., Fumana, M., Koekemoer, A. M., Maccagni, D., Marinoni, C., McCracken, H. J., Memeo, P., Meneux, B., & Scaramella, R. 2010, ApJ, 708, 505 51

Kravtsov, A. V., Berlind, A. A., Wechsler, R. H., Klypin, A. A., Gottlöber, S., Allgood, B., & Primack, J. R. 2004, ApJ, 609, 35 15, 21, 69, 124

Lacerna, I. & Padilla, N. 2011, MNRAS, 412, 1283 14

Lacerna, I. & Padilla, N. 2012, MNRAS, 426, L26 14

Lacey, C. G., Baugh, C. M., Frenk, C. S., Benson, A. J., Bower, R. G., Cole, S., Gonzalez-Perez, V., Helly, J. C., Lagos, C. D. P., & Mitchell, P. D. 2016, MNRAS, 462, 3854 119

Landy, S. D. & Szalay, A. S. 1993, ApJ, 412, 64 9, 94, 140

Lawrence, A., Warren, S. J., Almaini, O., Edge, A. C., Hambly, N. C., Jameson, R. F., Lucas, P., Casali, M., Adamson, A., Dye, S., Emerson, J. P., Foucaud, S., Hewett, P., Hirst, P., Hodgkin, S. T., Irwin, M. J., Lodieu, N., McMahon, R. G., Simpson, C., Smail, I., Mortlock, D., & Folger, M. 2007, MNRAS, 379, 1599 59, 60

Leauthaud, A., Tinker, J., Behroozi, P. S., Busha, M. T., & Wechsler, R. H. 2011, ApJ, 738, 45 125

Leauthaud, A., Tinker, J., Bundy, K., Behroozi, P. S., Massey, R., Rhodes, J., George, M. R., Kneib, J.-P., Benson, A., Wechsler, R. H., Busha, M. T., Capak, P., Cortês, M., Ilbert, O., Koekemoer, A. M., Le Fèvre, O., Lilly, S., McCracken, H. J., Salvato, M., Schrabback, T., Scoville, N., Smith, T., & Taylor, J. E. 2012, ApJ, 744, 159 69, 98, 125

Lee, C. T., Primack, J. R., Behroozi, P., Rodríguez-Puebla, A., Hellinger, D., & Dekel, A. 2017, MNRAS, 466, 3834 14, 120

Lemaître, A. G. 1931, MNRAS, 91, 483 1

Li, C., Kauffmann, G., Jing, Y. P., White, S. D. M., Börner, G., & Cheng, F. Z. 2006, MNRAS, 368, 21 12, 125

Lin, Y.-T., Mandelbaum, R., Huang, Y.-H., Huang, H.-J., Dalal, N., Diemer, B., Jian, H.-Y., & Kravtsov, A. 2016, ApJ, 819, 119 121

Lonsdale, C. J., Smith, H. E., Rowan-Robinson, M., Surace, J., Shupe, D., Xu, C., Oliver, S., Padgett, D., Fang, F., Conrow, T., Franceschini, A., Gautier, N., Griffin, M., Hacking, P., Masci, F., Morrison, G., O'Linger, J., Owen, F., Pérez-Fournon, I., Pierre, M., Puetter, R., Stacey, G., Castro, S., Polletta, M. d. C., Farrah, D., Jarrett, T., Frayer, D., Siana, B., Babbedge, T., Dye, S., Fox, M., Gonzalez-Solares, E., Salaman, M., Berta, S., Condon, J. J., Dole, H., & Serjeant, S. 2003, PASP, 115, 897 26, 73

Lynds, R. & Petrosian, V. 1989, ApJ, 336, 1 6

Madgwick, D. S., Hawkins, E., Lahav, O., Maddox, S., Norberg, P., Peacock, J. A., Baldry, I. K., Baugh, C. M., Bland-Hawthorn, J., Bridges, T., Cannon, R., Cole, S., Colless, M., Collins, C., Couch, W., Dalton, G., de Propris, R., Driver, S. P., Efstathiou, G., Ellis, R. S., Frenk, C. S., Glazebrook, K., Jackson, C., Lewis, I., Lumsden, S., Peterson, B. A., Sutherland, W., Taylor, K., & 2dFGRS Team, T. 2003, MNRAS, 344, 847 12

Mandelbaum, R., Zu, Y., Wang, W., White, S., Henriques, B., & More, S. 2016, MNRAS, 457, 3200 69, 70, 99, 119

Mansfield, P. & Kravtsov, A. V. 2019, arXiv e-prints 14, 70, 120, 126

Mao, Y.-Y., Zentner, A. R., & Wechsler, R. H. 2018, MNRAS, 474, 5143 14, 70, 126

Maraston, C., Pforr, J., Henriques, B. M., Thomas, D., Wake, D., Brownstein, J. R., Capozzi, D., Tinker, J., Bundy, K., Skibba, R. A., Beifiori, A., Nichol, R. C., Edmondson, E., Schneider, D. P., Chen, Y., Masters, K. L., Steele, O., Bolton, A. S., York, D. G., Weaver, B. A., Higgs, T., Bizyaev, D., Brewington, H., Malanushenko, E., Malanushenko, V., Snedden, S., Oravetz, D., Pan, K., Shelden, A., & Simmons, A. 2013, MNRAS, 435, 2764 64, 173

Martin, D. C., Fanson, J., Schiminovich, D., Morrissey, P., Friedman, P. G., Barlow, T. A., Conrow, T., Grange, R., Jelinsky, P. N., Milliard, B., Siegmund, O. H. W., Bianchi, L., Byun, Y.-I., Donas, J., Forster, K., Heckman, T. M., Lee, Y.-W., Madore, B. F., Malina, R. F., Neff, S. G., Rich, R. M., Small, T., Surber, F., Szalay, A. S., Welsh, B., & Wyder, T. K. 2005, ApJL, 619, L1 26, 73

Marulli, F., Bolzonella, M., Branchini, E., Davidzon, I., de la Torre, S., Granett, B. R., Guzzo, L., Iovino, A., Moscardini, L., Pollo, A., Abbas, U., Adami, C., Arnouts, S., Bel, J., Bottini, D., Cappi, A., Coupon, J., Cucciati, O., De Lucia, G., Fritz, A., Franzetti, P., Fumana, M., Garilli, B., Ilbert, O., Krywult, J., Le Brun, V., Le Fèvre, O., Maccagni, D., Malek, K., McCracken, H. J., Paioro, L., Polletta, M., Schlagenhaufer, H., Scodeggio, M., Tasca, L. A. M., Tojeiro, R., Vergani, D., Zanichelli, A., Burden, A., Di Porto, C., Marchetti, A., Marinoni, C., Mellier, Y., Nichol, R. C., Peacock, J. A., Percival, W. J., Phleps, S., Wolk, M., & Zamorani, G. 2013, A&A, 557, A17 125

McCracken, H. J., Peacock, J. A., Guzzo, L., Capak, P., Porciani, C., Scoville, N., Aussel, H., Finoguenov, A., James, J. B., Kitzbichler, M. G., Koekemoer, A., Leauthaud, A., Fèvre, O. L., Massey, R., Mellier, Y., Mobasher, B., Norberg, P., Rhodes, J., Sanders, D. B., Sasaki, S. S., Taniguchi, Y., Thompson, D. J., White, S. D. M., & El-Zant, A. 2007, ApJS, 172, 314 51

McCracken, H. J., Milvang-Jensen, B., Dunlop, J., Franx, M., Fynbo, J. P. U., Le Fèvre, O., Holt, J., Caputi, K. I., Goranova, Y., Buitrago, F., Emerson, J. P., Freudling, W., Hudelot, P., López-Sanjuan, C., Magnard, F., Mellier, Y., Møller, P., Nilsson, K. K., Sutherland, W., Tasca, L., & Zabl, J. 2012, A&A, 544, A156 60

Meneux, B., Guzzo, L., de la Torre, S., Porciani, C., Zamorani, G., Abbas, U., Bolzonella, M., Garilli, B., Iovino, A., Pozzetti, L., Zucca, E., Lilly, S. J., Le Fèvre, O., Kneib, J.-P., Carollo, C. M., Contini, T., Mainieri, V., Renzini, A., Scodeggio, M., Bardelli, S., Bongiorno, A., Caputi, K., Coppa, G., Cucciati, O., de Ravel, L., Franzetti, P., Kampczyk, P., Knobel, C., Kovač, K., Lamareille, F., Le Borgne, J.-F., Le Brun, V., Maier, C., Pellò, R., Peng, Y., Perez Montero, E., Ricciardelli, E., Silverman, J. D., Tanaka, M., Tasca, L., Tresse, L., Vergani, D., Bottini, D., Cappi, A., Cimatti, A., Cassata, P., Fumana, M., Koekemoer, A. M., Leauthaud, A., Maccagni, D., Marinoni, C., McCracken, H. J., Memeo, P., Oesch, P., & Scaramella, R. 2009, A&A, 505, 463 51, 125

Meneux, B., Le Fèvre, O., Guzzo, L., Pollo, A., Cappi, A., Ilbert, O., Iovino, A., Marinoni, C., McCracken, H. J., Bottini, D., Garilli, B., Le Brun, V., Maccagni, D., Picat, J. P., Scaramella, R., Scodeggio, M., Tresse, L., Vettolani, G., Zanichelli, A., Adami, C., Arnouts, S., Arnaboldi, M., Bardelli, S., Bolzonella, M., Charlot, S., Ciliegi, P., Contini, T., Foucaud, S., Franzetti, P., Gavignaud, I., Marano, B., Mazure, A., Merighi, R., Paltani, S., Pellò, R., Pozzetti, L., Radovich, M., Zamorani, G., Zucca, E., Bondi, M., Bongiorno, A., Busarello, G., Cucciati, O., Gregorini, L., Lamareille, F., Mathez, G., Mellier, Y., Merluzzi, P., Ripepi, V., & Rizzo, D. 2006, A&A, 452, 387 125

Meneux, B., Guzzo, L., Garilli, B., Le Fèvre, O., Pollo, A., Blaizot, J., De Lucia, G., Bolzonella, M., Lamareille, F., Pozzetti, L., Cappi, A., Iovino, A., Marinoni, C., McCracken, H. J., de la Torre, S., Bottini, D., Le Brun, V., Maccagni, D., Picat, J. P., Scaramella, R., Scodeggio, M., Tresse, L., Vettolani, G., Zanichelli, A., Abbas, U., Adami, C., Arnouts, S., Bardelli, S., Bongiorno, A., Charlot, S., Ciliegi, P., Contini, T., Cucciati, O., Foucaud, S., Franzetti, P., Gavignaud, I., Ilbert, O., Marano, B., Mazure, A., Merighi, R., Paltani, S., Pellò, R., Radovich, M., Vergani, D., Zamorani, G., & Zucca, E. 2008, A&A, 478, 299 125

Merritt, D. 1983, ApJ, 264, 24 12

Milgrom, M. 1983, ApJ, 270, 365 7

Moore, B., Katz, N., Lake, G., Dressler, A., & Oemler, A. 1996, Nature, 379, 613 20

Mostek, N., Coil, A. L., Cooper, M., Davis, M., Newman, J. A., & Weiner, B. J. 2013, ApJ, 767, 89 12, 125, 144

Moster, B. P., Naab, T., & White, S. D. M. 2013, MNRAS, 428, 3121 110

Moster, B. P., Naab, T., & White, S. D. M. 2018, MNRAS, 477, 1822 85, 119

Moster, B. P., Somerville, R. S., Maulbetsch, C., van den Bosch, F. C., Macciò, A. V., Naab, T., & Oser, L. 2010, ApJ, 710, 903 125

Moustakas, J., Coil, A. L., Aird, J., Blanton, M. R., Cool, R. J., Eisenstein, D. J., Mendez, A. J., Wong, K. C., Zhu, G., & Arnouts, S. 2013, ApJ, 767, 50 29, 32, 33, 35, 38, 39, 77, 79, 80, 82, 131, 132

Navarro, J. F., Frenk, C. S., & White, S. D. M. 1997, ApJ, 490, 493 7, 15

Newman, J. A., Cooper, M. C., Davis, M., Faber, S. M., Coil, A. L., Guhathakurta, P., Koo, D. C., Phillips, A. C., Conroy, C., Dutton, A. A., Finkbeiner, D. P., Gerke, B. F., Rosario, D. J., Weiner, B. J., Willmer, C. N. A., Yan, R., Harker, J. J., Kassin, S. A., Konidaris, N. P., Lai, K., Madgwick, D. S., Noeske, K. G., Wirth, G. D., Connolly, A. J., Kaiser, N., Kirby, E. N., Lemaux, B. C., Lin, L., Lotz, J. M., Luppino, G. A., Marinoni, C., Matthews, D. J., Metevier, A., & Schiavon, R. P. 2013, ApJS, 208, 5 4, 26, 131

Noeske, K. G., Faber, S. M., Weiner, B. J., Koo, D. C., Primack, J. R., Dekel, A., Papovich, C., Conselice, C. J., Le Floc'h, E., Rieke, G. H., Coil, A. L., Lotz, J. M., Somerville, R. S., & Bundy, K. 2007, ApJL, 660, L47 30, 78

Norberg, P., Baugh, C. M., Hawkins, E., Maddox, S., Peacock, J. A., Cole, S., Frenk, C. S., Bland-Hawthorn, J., Bridges, T., Cannon, R., Colless, M., Collins, C., Couch, W., Dalton, G., De Propris, R., Driver, S. P., Efstathiou, G., Ellis, R. S., Glazebrook, K., Jackson, C., Lahav, O., Lewis, I., Lumsden, S., Madgwick, D., Peterson, B. A., Sutherland, W., & Taylor, K. 2001, MNRAS, 328, 64 12, 125

Norberg, P., Baugh, C. M., Hawkins, E., Maddox, S., Madgwick, D., Lahav, O., Cole, S., Frenk, C. S., Baldry, I., Bland-Hawthorn, J., Bridges, T., Cannon, R., Colless, M., Collins, C., Couch, W., Dalton, G., De Propris, R., Driver, S. P., Efstathiou, G., Ellis, R. S., Glazebrook, K., Jackson, C., Lewis, I., Lumsden, S., Peacock, J. A., Peterson, B. A., Sutherland, W., & Taylor, K. 2002, MNRAS, 332, 827 12, 125

Oliver, S., Rowan-Robinson, M., Alexander, D. M., Almaini, O., Balcells, M., Baker, A. C., Barcons, X., Barden, M., Bellas-Velidis, I., Cabrera-Guerra, F., Carballo, R., Cesarsky, C. J., Ciliegi, P., Clements, D. L., Crockett, H., Danese, L., Dapergolas, A., Drolias, B., Eaton, N., Efstathiou, A., Egami, E., Elbaz, D., Fadda, D., Fox, M., Franceschini, A., Genzel, R., Goldschmidt, P., Graham, M., Gonzalez-Serrano, J. I., Gonzalez-Solares, E. A., Granato, G. L., Gruppioni, C., Herbstmeier, U., Héraudeau, P., Joshi, M., Kontizas, E., Kontizas, M., Kotilainen, J. K., Kunze, D., La Franca, F., Lari, C., Lawrence, A., Lemke, D., Linden-Vørnle, M. J. D., Mann, R. G., Márquez, I., Masegosa, J., Mattila, K., McMahon, R. G., Miley, G., Missoulis, V., Mobasher, B., Morel, T., Nørgaard-Nielsen, H., Omont, A., Papadopoulos, P., Perez-Fournon, I., Puget, J.-L., Rigopoulou, D., Rocca-Volmerange, B., Serjeant, S., Silva, L., Sumner, T., Surace, C., Vaisanen, P., van der Werf, P. P., Verma, A., Vigroux, L., Villar-Martin, M., & Willott, C. J. 2000, MNRAS, 316, 749 26, 73

Paranjape, A., Kovač, K., Hartley, W. G., & Pahwa, I. 2015, MNRAS, 454, 3030 23, 24

Peacock, J. A. & Smith, R. E. 2000, MNRAS, 318, 1144 7, 15, 69, 124

Peebles, P. J. E. 1973, ApJ, 185, 413 2

Perlmutter, S., Aldering, G., Goldhaber, G., Knop, R. A., Nugent, P., Castro, P. G., Deustua, S., Fabbro, S., Goobar, A., Groom, D. E., Hook, I. M., Kim, A. G., Kim, M. Y., Lee, J. C., Nunes, N. J., Pain, R., Pennypacker, C. R., Quimby, R., Lidman, C., Ellis, R. S., Irwin, M., McMahon, R. G., Ruiz-Lapuente, P., Walton, N., Schaefer, B., Boyle, B. J., Filippenko, A. V., Matheson, T., Fruchter, A. S., Panagia, N., Newberg, H. J. M., Couch, W. J., & Project, T. S. C. 1999, ApJ, 517, 565 7

Pierre, M., Valtchanov, I., Altieri, B., Andreon, S., Bolzonella, M., Bremer, M., Disseau, L., Dos Santos, S., Gandhi, P., Jean, C., Pacaud, F., Read, A., Refregier, A., Willis, J., Adami, C., Alloin, D., Birkinshaw, M., Chiappetti, L., Cohen, A., Detal, A., Duc, P.-A., Gosset, E., Hjorth, J., Jones, L., Le Fèvre, O., Lonsdale, C., Maccagni, D., Mazure, A., McBreen, B., McCracken, H., Mellier, Y., Ponman, T., Quintana, H., Rottgering, H., Smette, A., Surdej, J., Starck, J.-L., Vigroux, L., & White, S. 2004, JCAP, 9, 011 26, 73

Planck Collaboration, Ade, P. A. R., Aghanim, N., Arnaud, M., Ashdown, M., Atrio-Barandela, F., Aumont, J., Baccigalupi, C., Balbi, A., Banday, A. J., & et al. 2013, A&A, 557, A52 119

Planck Collaboration, Ade, P. A. R., Aghanim, N., Arnaud, M., Ashdown, M., Aumont, J., Baccigalupi, C., Banday, A. J., Barreiro, R. B., Bartlett, J. G., Bartolo, N., Battaner, E., Battye, R., Benabed, K., Benoît, A., Benoit-Lévy, A., Bernard, J.-P., Bersanelli, M., Bielewicz, P., Bock, J. J., Bonaldi, A., Bonavera, L., Bond, J. R., Borrill, J., Bouchet, F. R., Boulanger, F., Bucher, M., Burigana, C., Butler, R. C., Calabrese, E., Cardoso, J.-F., Catalano, A., Challinor, A., Chamballu, A., Chary, R.-R., Chiang, H. C., Chluba, J., Christensen, P. R., Church, S., Clements, D. L., Colombi, S., Colombo, L. P. L., Combet, C., Coulais, A., Crill, B. P., Curto, A., Cuttaia, F., Danese, L., Davies, R. D., Davis, R. J., de Bernardis, P., de Rosa, A., de Zotti, G., Delabrouille, J., Désert, F.-X., Di Valentino, E., Dickinson, C., Diego, J. M., Dolag, K., Dole, H., Donzelli, S., Doré, O., Douspis, M., Ducout, A., Dunkley, J., Dupac, X., Efstathiou, G., Elsner, F., Enßlin, T. A., Eriksen, H. K., Farhang, M., Fergusson, J., Finelli, F., Forni, O., Frailis, M., Fraisse, A. A., Franceschi, E., Frejsel, A., Galeotta, S., Galli, S., Ganga, K., Gauthier, C., Gerbino, M., Ghosh, T., Giard, M., Giraud-Héraud, Y., Giusarma, E., Gjerløw, E., González-Nuevo, J., Górski, K. M., Gratton, S., Gregorio, A., Gruppuso, A., Gudmundsson, J. E., Hamann, J., Hansen, F. K., Hanson, D., Harrison, D. L., Helou, G., Henrot-Versillé, S., Hernández-Monteagudo, C., Herranz, D., Hildebrandt, S. R., Hivon, E., Hobson, M., Holmes, W. A., Hornstrup, A., Hovest, W., Huang, Z., Huffenberger, K. M., Hurier, G., Jaffe, A. H., Jaffe, T. R., Jones, W. C., Juvela, M., Keihänen, E., Keskitalo, R., Kisner, T. S., Kneissl, R., Knoche, J., Knox, L., Kunz, M., Kurki-Suonio, H., Lagache, G., Lähteenmäki, A., Lamarre, J.-M., Lasenby, A., Lattanzi, M., Lawrence, C. R., Leahy, J. P., Leonardi, R., Lesgourgues, J., Levrier, F., Lewis, A., Liguori, M., Lilje, P. B., Linden-Vørnle, M., López-Caniego, M., Lubin, P. M., Macías-Pérez, J. F., Maggio, G., Maino, D., Mandolesi, N., Mangilli, A., Marchini, A., Maris, M., Martin, P. G., Martinelli, M., Martínez-González, E., Masi, S., Matarrese, S., McGehee, P., Meinhold, P. R., Melchiorri, A., Melin, J.-B., Mendes, L., Mennella, A., Migliaccio, M., Millea, M., Mitra, S., Miville-Deschênes, M.-A., Moneti, A., Montier, L., Morgante, G., Mortlock, D., Moss, A., Munshi, D., Murphy, J. A., Naselsky, P., Nati, F., Natoli, P., Netterfield, C. B., Nørgaard-Nielsen, H. U., Noviello, F., Novikov, D., Novikov, I., Oxborrow, C. A., Paci, F., Pagano, L., Pajot, F., Paladini, R., Paoletti, D., Partridge, B., Pasian, F., Patanchon, G., Pearson, T. J., Perdereau, O., Perotto, L., Perrotta, F., Pettorino, V., Piacentini, F., Piat, M., Pierpaoli, E., Pietrobon, D., Plaszczynski, S., Pointecouteau, E., Polenta, G., Popa, L., Pratt, G. W., Prézeau, G., Prunet, S., Puget, J.-L., Rachen, J. P., Reach, W. T., Rebolo, R., Reinecke, M., Remazeilles, M., Renault, C., Renzi, A., Ristorcelli, I., Rocha, G., Rosset, C., Rossetti, M., Roudier, G., Rouillé d´Orfeuil, B., Rowan-Robinson, M., Rubiño-Martín, J. A., Rusholme, B., Said, N., Salvatelli, V., Salvati, L., Sandri, M., Santos, D., Savelainen, M., Savini, G., Scott, D., Seiffert, M. D., Serra, P., Shellard, E. P. S., Spencer, L. D., Spinelli, M., Stolyarov, V., Stompor, R., Sudiwala, R., Sunyaev, R., Sutton, D., Suur-Uski, A.-S., Sygnet, J.-F., Tauber, J. A., Terenzi, L., Toffolatti, L., Tomasi, M., Tristram, M., Trombetti, T., Tucci, M., Tuovinen, J., Türler, M., Umana, G., Valenziano, L., Valiviita, J., Van Tent, F., Vielva, P., Villa, F., Wade, L. A., Wandelt, B. D., Wehus, I. K., White, M., White, S. D. M., Wilkinson, A., Yvon, D., Zacchei, A., & Zonca, A. 2016, A&A, 594, A13 5, 7

Pollo, A., Guzzo, L., Le Fèvre, O., Meneux, B., Cappi, A., Franzetti, P., Iovino, A., McCracken, H. J., Marinoni, C., Zamorani, G., Bottini, D., Garilli, B., Le Brun, V., Maccagni, D., Picat, J. P., Scaramella, R., Scodeggio, M., Tresse, L., Vettolani, G., Zanichelli, A., Adami, C., Arnouts, S., Bardelli, S., Bolzonella, M., Charlot, S., Ciliegi, P., Contini, T., Foucaud, S., Gavignaud, I., Ilbert, O., Marano, B., Mazure, A., Merighi, R., Paltani, S., Pellò, R., Pozzetti, L., Radovich, M., Zucca, E., Bondi, M., Bongiorno, A., Busarello, G., Cucciati, O., Gregorini, L., Lamareille, F., Mathez, G., Mellier, Y., Merluzzi, P., Ripepi, V., & Rizzo, D. 2006, A&A, 451, 409 125

Reddick, R. M., Wechsler, R. H., Tinker, J. L., & Behroozi, P. S. 2013, ApJ, 771, 30 69

Riess, A. G., Filippenko, A. V., Challis, P., Clocchiatti, A., Diercks, A., Garnavich, P. M., Gilliland, R. L., Hogan, C. J., Jha, S., & Kirshner, R. P. 1998, AJ, 116, 1009 7

Rodriguez-Puebla, A., Avila-Reese, V., Yang, X., Foucaud, S., Drory, N., & Jing, Y. P. 2015, ApJ, 799, 130 70

Rubin, V. C., Ford, W. K., J., & Thonnard, N. 1978, ApJL, 225, L107 6

Rubin, V. C., Thonnard, N., Ford, W. K., J., & Roberts, M. S. 1976, AJ, 81, 719 6

Salcedo, A. N., Maller, A. H., Berlind, A. A., Sinha, M., McBride, C. K., Behroozi, P. S., Wechsler, R. H., & Weinberg, D. H. 2018, MNRAS, 475, 4411 14, 70, 126

Schechter, P. 1976, ApJ, 203, 297 12

Scoville, N., Aussel, H., Brusa, M., Capak, P., Carollo, C. M., Elvis, M., Giavalisco, M., Guzzo, L., Hasinger, G., Impey, C., Kneib, J.-P., LeFevre, O., Lilly, S. J., Mobasher, B., Renzini, A., Rich, R. M., Sanders, D. B., Schinnerer, E., Schminovich, D., Shopbell, P., Taniguchi, Y., & Tyson, N. D. 2007, ApJS, 172, 1 26, 73

Seldner, M. & Peebles, P. J. E. 1977, ApJ, 215, 703 2

Seldner, M., Siebers, B., Groth, E. J., & Peebles, P. J. E. 1977, ApJ, 82, 249 2

Seljak, U. 2000, MNRAS, 318, 203 69

Shane, C. D. & Wirtanen, C. A. 1967, Publ. Lick Obs., 22 2

Shapley, H. & Ames, A. 1932, Annals of Harvard College Obs., 88, 41 2

Sheth, R. K. & Tormen, G. 1999, MNRAS, 308, 119 14

Skibba, R. A., Smith, M. S. M., Coil, A. L., Moustakas, J., Aird, J., Blanton, M. R., Bray, A. D., Cool, R. J., Eisenstein, D. J., Mendez, A. J., Wong, K. C., & Zhu, G. 2014, ApJ, 784, 128 12, 27, 29, 77, 125

Skibba, R. A., Coil, A. L., Mendez, A. J., Blanton, M. R., Bray, A. D., Cool, R. J., Eisenstein, D. J., Guo, H., Miyaji, T., Moustakas, J., & Zhu, G. 2015, ApJ, 807, 152 125

Smith, R. E., Peacock, J. A., Jenkins, A., White, S. D. M., Frenk, C. S., Pearce, F. R., Thomas, P. A., Efstathiou, G., & Couchman, H. M. P. 2003, MNRAS, 341, 1311 7, 141

Somerville, R. S. & Davé, R. 2015, ARA&A, 53, 51 85

Somerville, R. S. & Primack, J. R. 1999, MNRAS, 310, 1087 85

Spergel, D. N. & Steinhardt, P. J. 2000, Phys. Rev. Lett., 84, 3760 14

Spitler, L. R., Labbé, I., Glazebrook, K., Persson, S. E., Monson, A., Papovich, C., Tran, K.-V. H., Poole, G. B., Quadri, R., van Dokkum, P., Kelson, D. D., Kacprzak, G. G., McCarthy, P. J., Murphy, D., Straatman, C. M. S., & Tilvi, V. 2012, ApJL, 748, L21 60

Springel, V., White, S. D. M., Jenkins, A., Frenk, C. S., Yoshida, N., Gao, L., Navarro, J., Thacker, R., Croton, D., & Helly, J. 2005, Nature, 435, 629 14

Strateva, I., Ivezić, Ž., Knapp, G. R., Narayanan, V. K., Strauss, M. A., Gunn, J. E., Lupton, R. H., Schlegel, D., Bahcall, N. A., Brinkmann, J., Brunner, R. J., Budavári, T., Csabai, I., Castander, F. J., Doi, M., Fukugita, M., Győry, Z., Hamabe, M., Hennessy, G., Ichikawa, T., Kunszt, P. Z., Lamb, D. Q., McKay, T. A., Okamura, S., Racusin, J., Sekiguchi, M., Schneider, D. P., Shimasaku, K., & York, D. 2001, ApJ, 122, 1861 11, 20

Sunayama, T., Hearin, A. P., Padmanabhan, N., & Leauthaud, A. 2016, MNRAS, 458, 1510 14, 21

Takada, M., Ellis, R. S., Chiba, M., Greene, J. E., Aihara, H., Arimoto, N., Bundy, K., Cohen, J., Doré, O., Graves, G., Gunn, J. E., Heckman, T., Hirata, C. M., Ho, P., Kneib, J.-P., Fèvre, O. L., Lin, L., More, S., Murayama, H., Nagao, T., Ouchi, M., Seiffert, M., Silverman, J. D., Sodré, L., Spergel, D. N., Strauss, M. A., Sugai, H., Suto, Y., Takami, H., & Wyse, R. 2014, PASJ, 66, R1 64, 173

Tal, T., van Dokkum, P. G., Franx, M., Leja, J., Wake, D. A., & Whitaker, K. E. 2013, ApJ, 769, 31 119

Tinker, J., Kravtsov, A. V., Klypin, A., Abazajian, K., Warren, M., Yepes, G., Gottlöber, S., & Holz, D. E. 2008, ApJ, 688, 709 14, 21

Tinker, J. L. & Wetzel, A. R. 2010, ApJ, 719, 88 20

Tinker, J. L., Weinberg, D. H., Zheng, Z., & Zehavi, I. 2005, ApJ, 631, 41 69

Tinker, J. L., Leauthaud, A., Bundy, K., George, M. R., Behroozi, P., Massey, R., Rhodes, J., & Wechsler, R. H. 2013, ApJ, 778, 93 70, 98

Tinker, J. L., Hahn, C., Mao, Y.-Y., Wetzel, A. R., & Conroy, C. 2018, MNRAS, 477, 935 121

Vale, A. & Ostriker, J. P. 2004, MNRAS, 353, 189 15, 124

Vale, A. & Ostriker, J. P. 2006, MNRAS, 371, 1173 124

van den Bosch, F. C., Yang, X., & Mo, H. J. 2003, MNRAS, 340, 771 15, 70

Velander, M., Rowe, B., Heymans, C., Bonnett, C., van Uitert, E., Semboloni, E., Hildebrandt, H., Hoekstra, H., Coupon, J., Kuijken, K., Miller, L., Fu, L., Van Waerbeke, L., Hudson, M. J., Giodini, S., Erben, T., Kitching, T. D., Schrabback, T., & Mellier, Y. 2013, MNRAS, 437, 2111 70

Villarreal, A. S., Zentner, A. R., Mao, Y.-Y., Purcell, C. W., van den Bosch, F. C., Diemer, B., Lange, J. U., Wang, K., & Campbell, D. 2017, MNRAS, 472, 1088 14, 70, 126

Vogelsberger, M., Genel, S., Springel, V., Torrey, P., Sijacki, D., Xu, D., Snyder, G., Nelson, D., & Hernquist, L. 2014, MNRAS, 444, 1518 23

Wake, D. A., Whitaker, K. E., Labbé, I., van Dokkum, P. G., Franx, M., Quadri, R., Brammer, G., Kriek, M., Lundgren, B. F., Marchesini, D., & Muzzin, A. 2011, ApJ, 728, 46 69, 125

Walsh, D., Carswell, R. F., & Weymann, R. J. 1979, Nature, 279, 381 6

Watson, D. F. & Conroy, C. 2013, ApJ, 772, 139 15, 71, 126

Watson, D. F., Hearin, A. P., Berlind, A. A., Becker, M. R., Behroozi, P. S., Skibba, R. A., Reyes, R., Zentner, A. R., & van den Bosch, F. C. 2015, MNRAS, 446, 651 70, 87, 127, 144

Wechsler, R. H. & Tinker, J. L. 2018, ARA&A, 56, 435 70, 126

Wechsler, R. H., Zentner, A. R., Bullock, J. S., Kravtsov, A. V., & Allgood, B. 2006, ApJ, 652, 71 14, 21, 70, 126

Weinmann, S. M., van den Bosch, F. C., Yang, X., & Mo, H. J. 2006, MNRAS, 366, 2 17, 20, 21, 57, 58, 63, 121

Werner, M. W., Roellig, T. L., Low, F. J., Rieke, G. H., Rieke, M., Hoffmann, W. F., Young, E., Houck, J. R., Brandl, B., Fazio, G. G., Hora, J. L., Gehrz, R. D., Helou, G., Soifer, B. T., Stauffer, J., Keene, J., Eisenhardt, P., Gallagher, D., Gautier, T. N., Irace, W., Lawrence, C. R., Simmons, L., Van Cleve, J. E., Jura, M., Wright, E. L., & Cruikshank, D. P. 2004, ApJS, 154, 1 26, 73

Wetzel, A. R. & Nagai, D. 2015, ApJ, 808, 40 22

Wetzel, A. R., Tinker, J. L., & Conroy, C. 2012, MNRAS, 424, 232 71, 127

Wetzel, A. R., Tinker, J. L., Conroy, C., & van den Bosch, F. C. 2013, MNRAS, 432, 336 20, 22

White, S. D. M. & Rees, M. J. 1978, MNRAS, 183, 341 12, 20, 69

Wittman, D. M., Tyson, J. A., Dell'Antonio, I. P., Becker, A., Margoniner, V., Cohen, J. G., Norman, D., Loomba, D., Squires, G., Wilson, G., Stubbs, C. W., Hennawi, J., Spergel, D. N., Boeshaar, P., Clocchiatti, A., Hamuy, M., Bernstein, G., Gonzalez, A., Guhathakurta, P., Hu, W., Seljak, U., & Zaritsky, D. 2002, in Proceedings of SPIE, Vol. 4836, Survey and Other Telescope Technologies and Discoveries, ed. J. A. Tyson & S. Wolff, 73–82 26

Yang, X., Mo, H. J., & van den Bosch, F. C. 2003, MNRAS, 339, 1057 15, 69, 124

Yang, X., Mo, H. J., & van den Bosch, F. C. 2008, ApJ, 676, 248 121

Yang, X., Mo, H. J., van den Bosch, F. C., & Jing, Y. P. 2005, MNRAS, 356, 1293 20, 121

York, D. G., Adelman, J., John E. Anderson, J., Anderson, S. F., Annis, J., Bahcall, N. A., Bakken, J. A., Barkhouser, R., Bastian, S., Berman, E., Boroski, W. N., Bracker, S., Briegel, C., Briggs, J. W., Brinkmann, J., Brunner, R., Burles, S., Carey, L., Carr, M. A., Castander, F. J., Chen, B., Colestock, P. L., Connolly, A. J., Crocker, J. H., Csabai, I., Czarapata, P. C., Davis, J. E., Doi, M., Dombeck, T., Eisenstein, D., Ellman, N., Elms, B. R., Evans, M. L., Fan, X., Federwitz, G. R., Fiscelli, L., Friedman, S., Frieman, J. A., Fukugita, M., Gillespie, B., Gunn, J. E., Gurbani, V. K., de Haas, E., Haldeman, M., Harris, F. H., Hayes, J., Heckman, T. M., Hennessy, G. S., Hindsley, R. B., Holm, S., Holmgren, D. J., hao Huang, C., Hull, C., Husby, D., Ichikawa, S.-I., Ichikawa, T., Ivezić, Ž., Kent, S., Kim, R. S. J., Kinney, E., Klaene, M., Kleinman, A. N., Kleinman, S., Knapp, G. R., Korienek, J., Kron, R. G., Kunszt, P. Z., Lamb, D. Q., Lee, B., Leger, R. F., Limmongkol, S., Lindenmeyer, C., Long, D. C., Loomis, C., Loveday, J., Lucinio, R., Lupton, R. H., MacKinnon, B., Mannery, E. J., Mantsch, P. M., Margon, B., McGehee, P., McKay, T. A., Meiksin, A., Merelli, A., Monet, D. G., Munn, J. A., Narayanan, V. K., Nash, T., Neilsen, E., Neswold, R., Newberg, H. J., Nichol, R. C., Nicinski, T., Nonino, M., Okada, N., Okamura, S., Ostriker, J. P., Owen, R., Pauls, A. G., Peoples, J., Peterson, R. L., Petravick, D., Pier, J. R., Pope, A., Pordes, R., Prosapio, A., Rechenmacher, R., Quinn, T. R., Richards, G. T., Richmond, M. W., Rivetta, C. H., Rockosi, C. M., Ruthmansdorfer, K., Sandford, D., Schlegel, D. J., Schneider, D. P., Sekiguchi, M., Sergey, G., Shimasaku, K., Siegmund, W. A., Smee, S., Smith, J. A., Snedden, S., Stone, R., Stoughton, C., Strauss, M. A., Stubbs, C., SubbaRao, M., Szalay, A. S., Szapudi, I., Szokoly, G. P., Thakar, A. R., Tremonti, C., Tucker, D. L., Uomoto, A., Berk, D. V., Vogeley, M. S., Waddell, P., i Wang, S., Watanabe, M., Weinberg, D. H., Yanny, B., & Yasuda, N. 2000, ApJ, 120, 1579 4, 20, 133

Zehavi, I., Blanton, M. R., Frieman, J. A., Weinberg, D. H., Mo, H. J., Strauss, M. A., Anderson, S. F., Annis, J., Bahcall, N. A., Bernardi, M., Briggs, J. W., Brinkmann, J., Burles, S., Carey, L., Castander, F. J., Connolly, A. J., Csabai, I., Dalcanton, J. J., Dodelson, S., Doi, M., Eisenstein, D., Evans, M. L., Finkbeiner, D. P., Friedman, S., Fukugita, M., Gunn, J. E., Hennessy, G. S., Hindsley, R. B., Ivezić, Ž., Kent, S., Knapp, G. R., Kron, R., Kunszt, P., Lamb, D. Q., Leger, R. F., Long, D. C., Loveday, J., Lupton, R. H., McKay, T., Meiksin, A., Merrelli, A., Munn, J. A., Narayanan, V., Newcomb, M., Nichol, R. C., Owen, R., Peoples, J., Pope, A., Rockosi, C. M., Schlegel, D., Schneider, D. P., Scoccimarro, R., Sheth, R. K., Siegmund, W., Smee, S., Snir, Y., Stebbins, A., Stoughton, C., SubbaRao, M., Szalay, A. S., Szapudi, I., Tegmark, M., Tucker, D. L., Uomoto, A., Vanden Berk, D., Vogeley, M. S., Waddell, P., Yanny, B., & York, D. G. 2002, ApJ, 571, 172 12

Zehavi, I., Weinberg, D. H., Zheng, Z., Berlind, A. A., Frieman, J. A., Scoccimarro, R., Sheth, R. K., Blanton, M. R., Tegmark, M., Mo, H. J., Bahcall, N. A., Brinkmann, J., Burles, S., Csabai, I., Fukugita, M., Gunn, J. E., Lamb, D. Q., Loveday, J., Lupton, R. H., Meiksin, A., Munn, J. A., Nichol, R. C., Schlegel, D., Schneider, D. P., SubbaRao, M., Szalay, A. S., Uomoto, A., & and, D. G. Y. 2004, ApJ, 608, 16 15, 16

Zehavi, I., Zheng, Z., Weinberg, D. H., Frieman, J. A., Berlind, A. A., Blanton, M. R., Scoccimarro, R., Sheth, R. K., Strauss, M. A., Kayo, I., Suto, Y., Fukugita, M., Nakamura, O., Bahcall, N. A., Brinkmann, J., Gunn, J. E., Hennessy, G. S., Ivezić, Ž., Knapp, G. R., Loveday, J., Meiksin, A., Schlegel, D. J., Schneider, D. P., Szapudi, I., Tegmark, M., Vogeley, M. S., York, D. G., & SDSS Collaboration. 2005, ApJ, 630, 1 12, 69, 98, 125

Zehavi, I., Zheng, Z., Weinberg, D. H., Blanton, M. R., Bahcall, N. A., Berlind, A. A., Brinkmann, J.,

Frieman, J. A., Gunn, J. E., Lupton, R. H., Nichol, R. C., Percival, W. J., Schneider, D. P., Skibba, R. A., Strauss, M. A., Tegmark, M., & York, D. G. 2011, ApJ, 736, 59 12, 16, 69, 70, 125

Zentner, A. R. 2007, IJMPD, 16, 763 14, 21

Zentner, A. R., Hearin, A. P., & van den Bosch, F. C. 2014, MNRAS, 443, 3044 16

Zentner, A. R., Hearin, A., van den Bosch, F. C., Lange, J. U., & Villarreal, A. 2016, arXiv e-prints 70, 126

Zu, Y. & Mandelbaum, R. 2015, MNRAS, 454, 1161 16

Zu, Y. & Mandelbaum, R. 2016, MNRAS, 457, 4360 70

Zu, Y., Mandelbaum, R., Simet, M., Rozo, E., & Rykoff, E. S. 2017, MNRAS, 551 104

Zwicky, F. 1933, Helv. Phys. Acta, 6, 138 5